Material properties of hybrid lipid/polymer vesicles and incorporation of membrane proteins within these structures for robust applications in bionanotechnology

Rashmi Hiranya Seneviratne

Submitted in accordance with the requirements
for the degree of Doctor of Philosophy

The University of Leeds
The School of Chemistry
August 2021

For Thaththi

Declaration

The candidate confirms that the work submitted is her own, except where work which has formed part of jointly authored publications has been included. The contribution of the candidate and the other authors to this work has been explicitly indicated below. The candidate confirms that appropriate credit has been given within the thesis where reference has been made to the work of others.

The details of membrane proton permeability in Chapter 4 has appeared in the publication: Seneviratne, R., Khan, S., Moscrop, E., Rappolt, M., Muench, S. P., Jeuken, L. J., and Beales, P. A. A reconstitution method for integral membrane proteins in hybrid lipid-polymer vesicles for enhanced functional durability. *Methods*. 2018, **147**, pp.142-149.

Contributions of the authors:

- Seneviratne, R.H.: Collected and analysed the data and drafted the manuscript.
- Khan, S.: Collected and analysed the data and drafted the manuscript.
- Moscrop, E.: Collected the data.
- Rappolt, M.: Provided supervision, edited and proofread the manuscript.
- Muench, S.: Edited and proofread the manuscript.
- Jeuken,L.J.C.: Provided supervision, edited and proofread the manuscript.
- Beales, P.A.: Provided supervision, edited and proofread the manuscript.

The details of vesicle sterilisation and preservation methods in Chapter 8 has appeared in the publication: Seneviratne, R., Jeuken, L. J., Rappolt, M., and Beales, P. A. Hybrid Vesicle Stability under Sterilisation and Preservation Processes Used in the Manufacture of Medicinal Formulations. *Polymers*. 2020, **12**(4), p.914.

Contributions of the authors:

- Seneviratne, R.H.: Collected and analysed the data and drafted the manuscript.
- Rappolt, M.: Provided supervision, edited and proofread the manuscript.
- Jeuken,L.J.C.: Provided supervision, edited and proofread the manuscript.
- Beales, P.A.: Provided supervision, edited and proofread the manuscript.

Acknowledgements

I would first like to thank my supervisors Dr. Paul Beales, Prof. Lars Jeuken and Prof. Michael Rappolt for their invaluable guidance and patience throughout the PhD, especially Paul who has supported me so much both academically and personally. I am also grateful to Dr. Rebecca Thompson, Dr. Arwen Tyler and Dr. Amin Sadeghpour for all the time and effort they have spent helping me with either electron microscopy or SAXS.

This journey could not have been completed without the encouragement and support of other researchers based in Chemistry and Lab 3.14, in particular, David Fogarty, Dr. Andrew Booth, Dr. Sanobar Khan, Marcos Arribas Perez, Zexi Xu, Simran Channa, Jason Rowley and David Martin. It has been a pleasure working with you all and I will sorely miss our discussions, academic or otherwise! I am also fortunate enough to be part of Cohort 3 in the SOFI CDT who made the transition into PhD life so much easier and have been an excellent support system since the beginning, especially Dale Diamond, Dan Day, Sophie Ayscough, Natasha Rigby, Andrew Christy and David Crosby.

I could not have got this far without the comfort, sacrifices and unwavering belief from my Ammi, Thaththi and sister, Indunee. Although Thaththi passed away in the middle of my project, this PhD would not have been started, nor the thesis completed, if not for him. Thanks also goes to my Chuti Thaththi who sparked my interest in science, and my Aunty Wendy and Aunty Ramani, cousins Pre-Akki, Pata, Marque Aiya and Prabhu Aiya, and cousin-niece and nephews, Kuki, Sean, Chuti and Prashi, for their interest and encouragement.

Last, but definitely not least, Liam, whose never-ending patience and understanding has supported me through both the good times and the bad. I have been very lucky to have you by my side.

Thank you all for your kindness.

Abstract

Vesicles have many applications from acting as microreactors and sensors to drug delivery vectors. While pure lipid and pure polymer vesicles have been used in the past for these applications, there are some disadvantages: although biocompatible, lipid membranes have poor long-term stability while the opposite is true of polymer membranes. A previous study showed that by blending POPC lipid with poly 1,2-butadiene-block-polyethylene oxide (PBd-b-PEO) diblock copolymer to form a hybrid vesicle, the durability from the polymers can be combined with the biocompatibility of lipids (1). However, while the biocompatibility of PBd-b-PEO/POPC blend has been established, relatively little is known about membrane properties of this lipid-polymer mixture.

A combination of techniques was used to probe the material properties and structure of hybrid POPC lipid combined with PBd_{22}-PEO_{14} or PBd_{12}-PEO_{11} polymer membranes. Overall, increasing the polymer fractions in PBd_{22}-PEO_{14}/POPC vesicles decreased proton permeability, but increased permeability in PBd_{12}-PEO_{11}/POPC vesicles.

Cryogenic-electron tomography, single particle analysis and small angle x-ray scattering were utilised in conjunction to obtain an electron density profile of the lipid-polymer membrane compositions. These profiles imply PBd_{22}-PEO_{14}/POPC vesicles form homogenous, symmetric membranes. Bilayer thickness measurements were also found to increase with increasing polymer fraction, however two membrane thickness populations were revealed within the PBd_{22}-PEO_{14} hybrid samples. Steep increases in bilayer measurements of PBd_{12}-PEO_{11} hybrid vesicles imply differences in material rigidity may cause PBd_{12}-PEO_{11} polymers to favour extension. Automated analysis confirmed individual hybrid vesicles within each thickness population were homogenous. While these populations could be perceived as polymer-rich and lipid-rich vesicles with hybrid lipid-polymer samples, it could also be indicative of the polymer forming membranes with either interdigitated or bilayer conformations.

Intensity contributions of fluorescently labelled lipid and polymer within mixed GUV membranes confirm membrane homogeneity within the hybrids and show there are no pure polymer or pure lipid vesicle populations within hybrid vesicle compositions. Diffusion of the fluorescent lipid through hybrid GUV membranes was found to decrease with increasing polymer fraction. However, the diffusion coefficients for the fluorescent polymer in hybrid membranes did not change with increasing polymer content, suggesting that while increasing polymer fraction reduces movement of lipid through a polymer-rich matrix, the polymer diffusion is unaffected. These blends of lipid and polymers also appear to result in a hydrated, disordered membrane, with a marginal increase in order as the

polymer fraction increases in GUVs membranes.

This characterisation of the material properties of a hybrid vesicle could help design vesicles for bionanotechnology applications with controlled encapsulation and release. Hybrid vesicles composed of this lipid-polymer blend have already been found to retain encapsulated cargo after several filtration and freeze-thaw cycles (2). However, for many bionanotechnology applications it is also desirable for the system to incorporate biofunctional molecules for biomimetic membrane-based technologies. This hybrid lipid-polymer blend could be developed further to provide a stable, durable, homogenous environment for certain membrane proteins to create artificial cells.

Contents

Abbreviations

ATP Adenosine triphosphate.

CF 5(6)- carboxyfluorescein.

CONTIN Constrained regularization method for inverting data.

COSY-NMR Correlated spectroscopy - nuclear magnetic resonance.

cryo-TEM Cryogenic transmission electron microscopy.

cryo-ET Cryogenic electron tomography.

DiO 3,3′-dioctadecyloxacarbocyanine perchlorate.

DLS Dynamic light scattering.

DMAP Anhydrous 4- Dimethylaminopyridine.

DOPC Dipalmitoylphosphatidylcholine.

DPPC 1,2-dipalmitoyl-sn-glycero-3-phosphocholine.

DSC Differential scanning calorimetry.

EDP Electron density profile.

FIJI (Fiji is Just) ImageJ.

FLIM Fluorescence lifetime imaging microscopy.

FRAP Fluorescence recovery after photobleaching.

FRET Förster resonance energy transfer.

FWHM Full width half maximum.

GP Generalised polarisation.

GUV Giant unilamellar vesicles.

H-NMR Hydrogen nuclear magnetic resonance.

HCl Hydrochloric acid.

HEPES 4-(2-hydroxyethyl) -1- piperazine ethanesulfonic acid.

HPTS 8-hydroxypyrene-1,3,6-trisulfonic acid trisodium salt.

IR Infrared.

ITO Indium titanium oxide.

Laurdan 6-Dodecanoyl -2- Dimethylaminonaphthalene.

LC-MS Liquid chromatography - mass spectroscopy.

LUV Large unilamellar vesicles.

MD Molecular dynamics.

MLV Multi-lamellar vesicles.

NA Numerical aperture.

NaCl Sodium chloride.

NaOH Sodium hydroxide.

OTF Optical transfer function.

PBd_{12}-PEO_{11} Poly 1,2- butadiene(650)-block-polyethylene oxide(500).

PBd_{22}-PEO_{14}-TMR Poly 1,2-butadiene(1200)-block-polyethylene oxide(600) with 5-(and-6-)-((N-(5-aminopentyl) amino) carbonyl) tetramethylrhodamine fluorescent tag.

PBd_{22}-PEO_{14} Poly 1,2- butadiene(1200)-block-polyethylene oxide(600).

PBd-b-PEO Poly 1,2- butadiene -block- polyethylene oxide.

PC Phosphatidylcholine.

PCS Photocorrelation spectroscopy.

PDI Polydispersity index.

PDMS-g-PEO Poly dimethyl siloxane -graft- polyethylene oxide.

PE Phosphatidylethanolamine.

PEG Polyethylene gylcol.

PMOXA-b-PDMS-b-PMOXA Poly (2- methyloxazoline -block- dimethyl siloxane -block- 2-methyloxazoline).

POPC 1- palmitoyl -2- oleoyl -sn- glycero -3- phosphocholine.

PS Phosphatidylserine.

PSF Point spread function.

QCM-D Quartz crystal microbalance with dissipation.

Rh-PE 1,2- dioleoyl -sn- glycero -3- phosphoethanolamine -N- (lissamine rhodamine B sulfonyl) (ammonium salt).

SANS Small angle neutron scattering.

SAXS Small angle x-ray scattering.

SIRT Simultaneous iterative reconstruction technique.

SPA Single particle analysis.

SSL Strong segregation limit.

TEM Transmission electron microscopy.

tetramethylrhodamine cadaverine 5-(and-6-)- ((N- (5-aminopentyl) amino) carbonyl) tetra methylrhodamine.

VPP Volta phase plate.

WAXS Wide angle x-ray scattering.

WBP Weighted back projection.

List of Figures

List of Tables

1. Introduction

Vesicles have many applications from acting as microreactors (3, 4, 5) and sensors (6, 7, 8), to drug delivery vectors (9, 10, 11, 12, 13) and models for a cell membrane (14, 15) as shown in Figure 1.1. Biological membranes usually comprise a mixture of lipids and their composition controls essential cell membrane properties such as fluidity, mechanical stability and membrane protein function (16). However, they also contain of a mixture of glycoproteins, glycolipids and membrane proteins, making this environment very difficult to replicate in artificial membrane models (17, 18). For many bionanotechnology applications, it is desirable for the system to incorporate biofunctional molecules to develop artificial cells and other biomimetic membrane-based technologies. Membrane proteins in biological membranes perform a specific function and their functionality depends on their environment. To successfully retain their functionality, reconstituting the membrane protein requires a native-like membrane environment (19, 20).

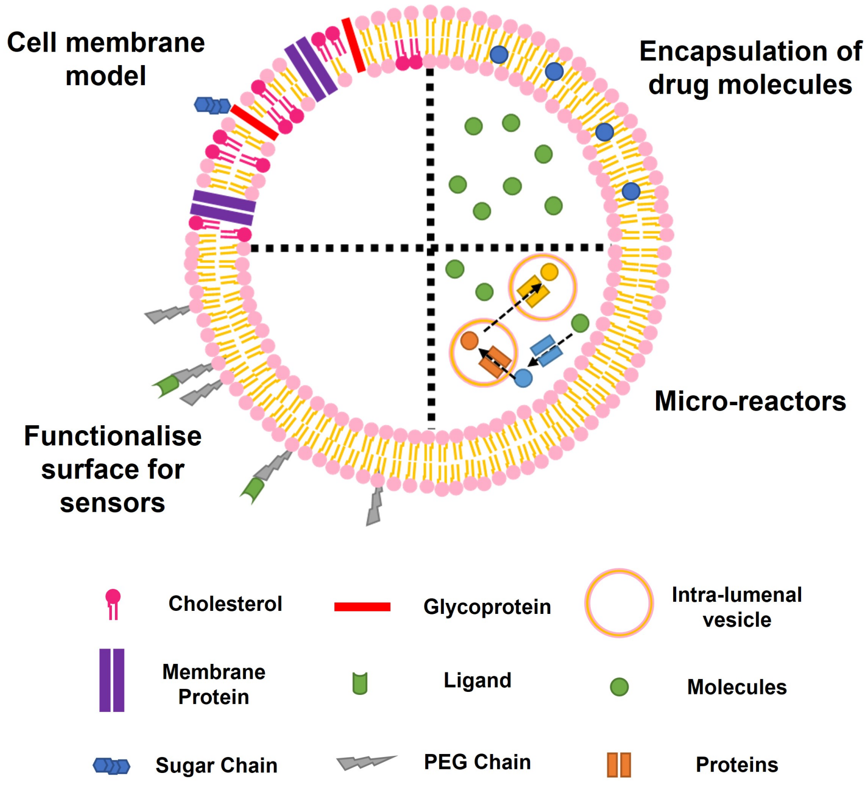

Figure 1.1: Potential applications for vesicles. Vesicles have many applications from acting as a drug delivery vector, to a micro-reactor for compartmentalized chemistry, sensors if the surface is functionalised, or as a cell membrane model.

Lipids and amphiphilic block copolymers are common materials for fabrication of synthetic membrane vesicles in the form of lipid vesicles and polymersomes, respectively. Liposomes have been used as models for biological cells since the sixties (21) as their structure and chemistry are similar to a natural bilayer (14), making them an excellent tool for understanding biological cell processes such as cell adhesion, signal transduction and endocytosis (22). More recently, lipid vesicles have been used for membrane protein reconstitution, which has applications in targeted drug delivery and release: because they are biodegradable and non-toxic, liposomes can be easily internalized by living cells and are able to encapsulate both hydrophilic and hydrophobic materials. However, lipid vesicles have poor mechanical stability and high permeability, making them ill-suited for some applications. While these membrane properties can be modified to increase their resistance to shear by grafting polyethylene glycol (PEG) molecules to a liposome surface, this modification can lower lipid cohesion and affect the vesicle stability (22, 23). Due to their fluidity, lipid bilayers can also have long-term structural instabilities such as transient pore formation which could lead to membrane rupture (24, 25, 26). The liposome lifetime therefore impacts the stability of proteins embedded within the membrane (27) making them a poor choice for drug delivery applications over an extended time period.

Amphiphilic copolymers have also been used to generate artificial membranes and are increasingly used in drug delivery as their membranes can be functionalised, and usually the polymersomes have outstanding stability (22). Copolymers can be created to alter membrane properties such as membrane stiffness and thickness, induce lateral segregation or volume changes, or even introduce new properties such as hydrophilicity and fluorescence (28). Functional groups can even be added to the copolymers to make stimuli-responsive polymersomes that respond to changes in the environment (29). Polymersomes have also been used for protein reconstitution despite the difference in material properties to lipids, such as membrane fluidity and membrane thickness (30, 31, 32, 33). However, little is known about their potential toxicity and long-term accumulation for *in vivo* applications, making a pure polymer vesicle a poor choice for some applications.

Although lipids are biocompatible, their major drawback is their low mechanical stability and high permeability, while the converse is true for polymer membranes. An approach to circumvent the issues present in the pure systems is to combine lipid and polymers into a hybrid vesicle. This takes advantage of the robustness and chemical versatility of a polymer membrane as well as the biocompatibility and softness provided by a lipid bilayer (22, 34).

1.1 Amphiphile geometry and self-assembly

Physical properties of lipids are dependent on their structure (28). Phospholipids are an amphiphilic molecule found in bilayers. They have a polar, hydrophilic head group and two hydrophobic hydrocarbon tails. Typical lengths for the tail group range from 14-20 carbons and the head groups can also have a variety of sizes, leading to different possibilities for membrane structure, shape, properties and function (35). The molecular structure of the phospholipid POPC is shown in Figure 1.2a.

Amphiphilic copolymers with different morphologies have been used to successfully form vesicles. Diblock copolymers comprising an AB conformation of a hydrophilic block (A) and a hydrophobic block (B) can have hydrophobic core thicknesses between 8.0 - 21.0 nm as determined by simulation (36) or from cryogenic transmission electron microscopy (cryo-TEM) and small angle x-ray scattering (SAXS) measurements (37). The molecular structure of amphiphilic diblock copolymer Poly 1,2- butadiene -block- polyethylene oxide (PBd-b-PEO) is shown in Figure 1.2b.

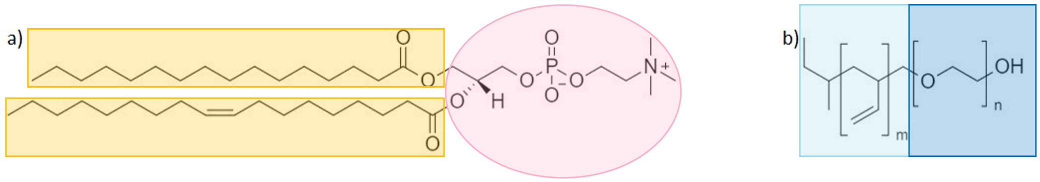

Figure 1.2: Molecular structure of POPC and PBd-b-PEO. Lipids such as a) POPC have a polar hydrophilic head group (pink) and two hydrophobic hydrocarbon tails (yellow). Amphiphilic diblock copolymers with an AB conformation like b) PBd-b-PEO diblock copolymer have *m* number of hydrophobic poly 1,2-butadiene monomers (light blue) and *n* number of polyethylene oxide monomers (dark blue.

The final geometry favoured by an amphiphile depends on their molecular geometry as shown by Figure 1.3. The packing arrangement of amphiphilic molecules is characterised by a shape factor: $\frac{v}{al}$ where a is the interface area occupied by the head group; v is the volume occupied by the hydrophobic chains; and l the length of the hydrocarbon region. Bilayers are favoured when (38):

$$\frac{1}{2} < \frac{v}{al} < 1 \tag{1.1}$$

Generally, lipids that have a similar polar head group and hydrophobic region cross-sectional areas, such as dual chain lipids, preferentially form bilayers. Thus the mean spacing between lipid molecules is minimised, reinforcing the formation of a bilayer (39). Other structures can form from different amphiphile geometries as shown in Figure 1.3.

Typically, when the interface area a is larger than v/l, $\frac{v}{al} < \frac{1}{3}$, which corresponds to a conical shape and formation of a spherical micelle, while cylindrical micelles are more likely when $\frac{v}{al}$ is between $\frac{1}{3} < \frac{v}{al} < \frac{1}{2}$. When the hydrocarbon volume v is larger than al, the amphiphiles have a truncated cone shape and inverted micelle structure is favoured (39, 40).

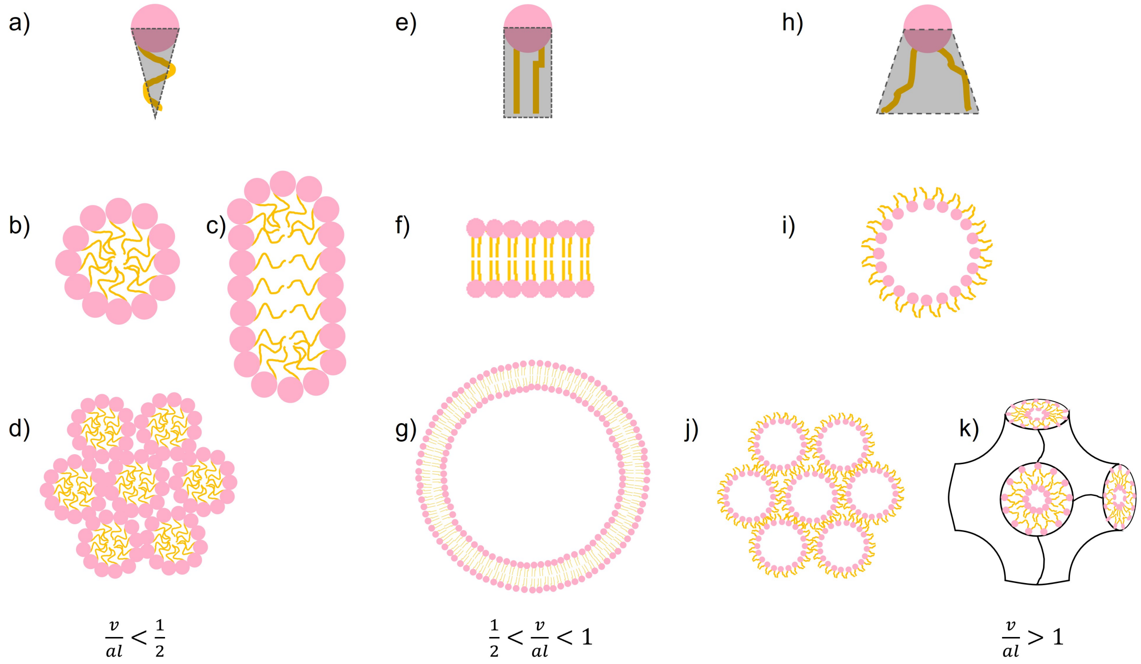

Figure 1.3: Lipid geometry and subsequent structures. Lipids that have a molecular shape similar to an a) inverted cone induce a positive curvature strain and favour the formation of b) spherical c) worm-like or d) tubular micelles (HI). Lipids that have e) similar hydrophilic and hydrophobic cross-sectional areas have cylindrical geometry and form f) a bilayer (lamellar phase), which can close to to give g) vesicles (39, 40, 41). Lipids with a h) small polar head have a molecular shape that resembles a truncated cone, which induces a negative curvature strain and preferentially arranges into i) inverted micelles, which would exist in a continuous oil phase, and then either j) and inverted hexagonal phase (HII) or k) cubic (bicontinuous) structures (35, 40).

The formation of bilayers from dual-chain amphiphilic molecules like phospholipids are due to van der Waals forces, hydrogen bonding, hydrophobic and screened electrostatic interactions. Therefore a change in solution conditions, such as the pH or electrolyte concentration, of a suspension of amphiphilic molecules will affect the interactions and intermolecular forces between and within each aggregate, thus modifying the size, shape and type of the final structures formed (38). The hydrophobic and hydrophilic balance of the amphiphiles will also govern the interactions between amphiphiles (42).

The resultant morphology of both lipid and polymers is also controlled by several factors: the hydrophilic/hydrophobic ratio, lipid or polymer concentration, salt concentration, solution pH and temperature (43). For polymers the volume ratio of the hydrophilic to hydrophobic block is believed to be an important parameter for self-assembly into vesicles. Generally, copolymers with a hydrophilic to hydrophobic ratio of less than 1:2 favour vesicle formation (43, 44). Ultimately, the balance between all the free energy contributions to the self-assembly and also kinetic factors determine the final morphology (44).

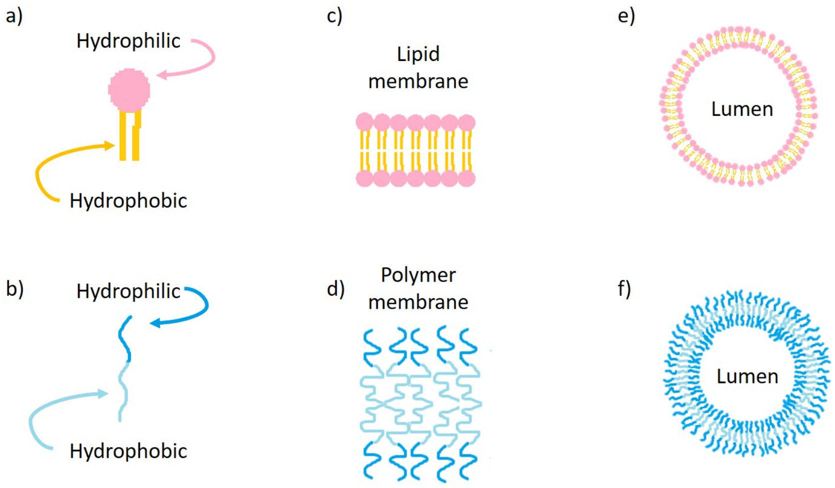

Figure 1.4: Phospholipid and diblock copolymer bilayers. a) Phosopholipids and b) amphiphilic block copolymers have a hydrophilic group and hydrophobic region that self-assemble into a c) lipid bilayer and d) polymer membrane to reduce interaction between the hydrophobic region and an aqueous environment. e) Liposomes and f) polymersomes form to reduce edge tension.

At low concentrations amphiphiles, such as lipids and block copolymers, will be dispersed in water until the saturation point, commonly in the 10^{-3} M range. At concentrations higher than this saturation point, the amphiphiles can form bilayers, and then vesicles, in aqueous solution if their concentration is above the critical micelle concentration - the minimum number of molecules required for aggregation. The driving force for bilayer self-assembly is the unfavourable interaction between the hydrophobic region of the amphiphile and water. To reduce this interaction, the hydrophilic head groups form an interface with the aqueous environment resulting in the formation of a bilayer to reduce the contact energy between the hydrophobic chains and an aqueous environment (39, 45, 46).

1.2 Membrane energies

1.2.1 Tension

The competition between bending resistance and edge tension is what compels a flat bilayer membrane to form a closed sphere. Lipids energetically prefer a parallel molecular arrangement. At low lipid concentrations, these disks of parallel lipid sheets are so large that it is more favourable for the sheet to close than to remain in a disk configuration. The circular rim of the bilayer disk of radius R_D gives rise to a line energy E_{disk} :

$$E_{disk} = 2\pi R_D \gamma_l \tag{1.2}$$

where γ_l is the line tension (interfacial energy at the edge of a membrane). Bending energy, E_{sphere}, is required to bend a flat membrane into a closed vesicle, given by

$$E_{sphere} = 4\pi(2\kappa_b + \kappa_G) \tag{1.3}$$

where κ_b and κ_G are the bending modulus and Gaussian rigidities respectively. Note that the bending energy of a sphere, E_{sphere}, is independent of the sphere radius (47). The balance between line tension and bending energy therefore defines the minimal radius of a vesicle, R_v. When R_v is small, the disk configuration is favoured, however as the disk perimeter increases, the sphere becomes the preferred structure for radii above (39)

$$R_v = \frac{2\kappa_b + \kappa_G}{\gamma_l} \tag{1.4}$$

Recent studies have highlighted the importance of tension in maintaining shape, and overall membrane area, as well as controlling complex transitions in cell motility and polarization. Biological membrane tension is defined by two main components: the in-plane tension in the lipid bilayer, mainly due to hydrostatic pressure; and membrane – cytoskeleton adhesion, conciliated by phospholipid-binding proteins. However, the relative magnitude of each contribution depends on the cell state and remains unclear because they are interdependent (48).

For non-equilibrium vesicles, spherical vesicles are only one example of possible shapes. The shape of a vesicle is one that minimizes the bending energy when there is a difference in the number of amphiphiles in the inner and outer leaflets, which itself depends on vesicle preparation method. The shapes can be parameterised by the volume-to-area ratio v and the area difference between the inner and outer bilayer leaflets $\Delta A = A_{in} - A_{out}$.

Spherical vesicles have a maximum value of $v = 1$, the highest possible volume-to-area ratio. A large area difference, $\Delta A > 1$, causes the membrane to curve outwards, while $\Delta A < 1$ leads to shapes that curve inwards. Changes in v can be induced by changes to solute concentrations, while changes in ΔA occur by transverse diffusion (flip-flop). Temperature can also affect both v and ΔA. For vesicles at equilibrium however, v is adjusted by permeation of solvent through the bilayer and ΔA modified by rapid exchange of lipids between the layers and different vesicles, which is why most vesicles are spherical (47, 49). Although most vesicles are spherical, their the intrinsic membrane curvature can be very close to zero, as is the case in GUVs.

During self-assembly, the membrane structures, such as free lamellar phases, can equilibrate to a local minimum in free energy as a function of membrane surface area, causing surface tension to vanish (35). The surface tension γ is related to the Gibbs free energy dG by:

$$\frac{dG}{dA} = \gamma \tag{1.5}$$

where A is the membrane surface area.

However, a vesicle generally does not have a vanishing surface tension. A vesicle will have an enclosed internal volume and contain a certain number of molecules in the bilayer. Changes in the membrane shape will cause a change in surface area to maintain the total number of molecules in the bilayer and the enclosed volume. These constraints lead to a surface tension related to area changes and pressure differences. A vesicle shape can then be found by examining the fluctuations in the free energy of the system G:

$$G = G_0 - \tilde{\gamma} A - pV \tag{1.6}$$

where G_0 is the bulk free energy. The frame tension, $\widetilde{\gamma}$, and shape factor, p, enforce the total membrane surface area, A, (assuming no stretching) and enclosed volume, V. Frame tension is caused by the constraints placed on the membrane shape and can be tuned by osmotically changing the vesicle volume.

Surface tension, γ, has mathematically the same role as frame tension, $\widetilde{\gamma}$. The surface tension regulates the addition of more lipid to the membrane at the expense of other forms of lipid, such as free monomers, while the frame tension specifies the work done in increasing the area against a specific form of external constraint. Both surface and frame tension physically lead to the same effects.

$$d\gamma + \Sigma_i c_i d\mu_i = 0 \tag{1.7}$$

where c_i is the concentration of the species on the surface and μ_i is the monomer chemical potential (35).

1.2.2 Stretching

As phospholipid bilayers are fluid-like at physiological conditions, shear does not need to be taken into account (50). However, stretching in biological membranes does cost energy and directly affects the structure and function of the membrane. Most biological membranes will only stretch a small amount before the membrane ruptures and the cell bursts. For strong in-plane deformations, the large hydrophobic cost of exposing the phospholipid acyl tail groups results in a large stretching modulus to resist change in the area per head group (35). The energy, $E_{stretch}$, is given by:

$$E_{stretch} = \frac{1}{2}\kappa_s(\frac{A - A_0}{A_0})^2 \tag{1.8}$$

where κ_s is the stretching modulus, A_0 is the original area and A is the area after deformation. The stretching modulus of an interface is determined by the variation in surface tension, γ with a changing area (35):

$$\kappa_s = 2A\frac{\delta\gamma}{\delta A} \tag{1.9}$$

In a single-component system the relationship between the area stretching modulus, κ_s, and interfacial tension, γ_{if} is (36, 37):

$$\kappa_s = 4\gamma_{if} \tag{1.10}$$

However, large thermal undulations can complicate measurements of the stretching modulus, κ_s. Factors affecting κ_s include hydrophobic interactions, counterion pairing in zwitterionic amphiphiles or even the presence of small molecules, in the membrane (37). Insertion of small molecules into the head group region of the membrane leads to increased level of undulations and overall softening of the membrane (51).

1.2.3 Bending

Biological bilayers have asymmetry caused by different chemical environments, ionic strengths, species, concentration of proteins and dynamic interactions. Therefore, it is likely that most membrane compositions are asymmetric across the two leaflets in a bilayer, resulting in spontaneous curvature (35). Compelling two lipid monolayers, each with their own preferred curvature, to form a flat symmetric bilayer also has an energy cost, leading to a curvature elastic stress in the resultant membrane (52). The tendency of a material to resist bending is known as the bending modulus, κ_b. In the case of a lipid membrane, it is the energy required to deform the bilayer from its original curvature to a different curvature. It is believed to play an important role in many biological cell processes such as endocytosis, membrane trafficking and membrane fusion (53).

Using the Helfrich theory of membrane bending, a lipid bilayer can be modelled as a two-dimensional elastic sheet, expressing the curvature energy per unit area, E as:

$$E = \frac{\kappa_b}{2}(J - J_s)^2 + K\bar{k} \tag{1.11}$$

J is the total curvature, J_s is the spontaneous curvature, K is the Gaussian curvature and $\bar{k}$ is the Gaussian modulus. The Helfrich model is an approximation for bilayer surfaces with small curvature as higher terms are assumed to be negligible to prevent the introduction of the membrane stresses from Gaussian curvature, K (35). The relationship between stretching and bending modulus for lipid bilayers is thought to be:

$$\kappa_b = \kappa_s \beta h^2 \tag{1.12}$$

where h is the thickness of hydrophobic segment, and β is the coupling factor. If the bilayer is completely coupled, and rigid β has a value of $\frac{1}{12}$, however for a bilayer that is free to slide over one another β assumes a value of $\frac{1}{48}$ (36). While this model is commonly used for bilayers, it can be valid for monolayers as well (54).

Bilayers in a fluid state will undergo thermal undulations, leading to local displacements. The thermal undulations can be expressed in terms of plane waves: a vertical displacement, $u(r)$ at each point of the membrane, r, with respect to the horizontal plane of the flat membrane. Assuming that the membrane behaves as if it were flat, and that the equatorial plane of the GUV is imaged, a model for thermal undulations can be created. Working in the reciprocal space and taking the wavevector, $q(= 2pi/l)$ along the length of the GUV contour, l, in to account, the power spectrum $\langle \mid u_q^2 \mid \rangle$ can be found:

$$\langle \mid u_q^2 \mid \rangle = \frac{k_B T}{A(\kappa_b q^4 + \sigma q^2)} \tag{1.13}$$

Where A being the area of a squared section of membrane, σ is the membrane tension, k_B is the Boltzmann constant and T is the temperature. When the tension is negligible, the only parameter left is κ_b, giving the starting point of the most common experimental and numerical methods used to determine the bending modulus from a thermal undulation spectrum (53).

1.3 Membrane phases

Because the phospholipid membrane is a dynamic structure, it is under equilibrium and can undergo reversible transitions such as domain formation and thermotropic transitions (38).

Phospholipid bilayers experience reversible thermotropic transitions, where the phospholipid membrane switches between the highly ordered solid-like gel phase (L_β) to the more disordered liquid crystalline phase (L_α), at the main transition temperature, T_m, as shown in Figure 1.5. The most common phospholipids include phosphatidylcholine (PC), phosphatidylethanolamine (PE) and phosphatidylserine (PS). In these lipids, one of the tails is fully saturated, while the other generally has one or more double bonds. Fully saturated chains are less fluid and crystalline (gel) at higher temperatures than unsaturated hydrocarbons, therefore the main transition (melting) temperature can be controlled by utilising a suitable blend of lipids (35).

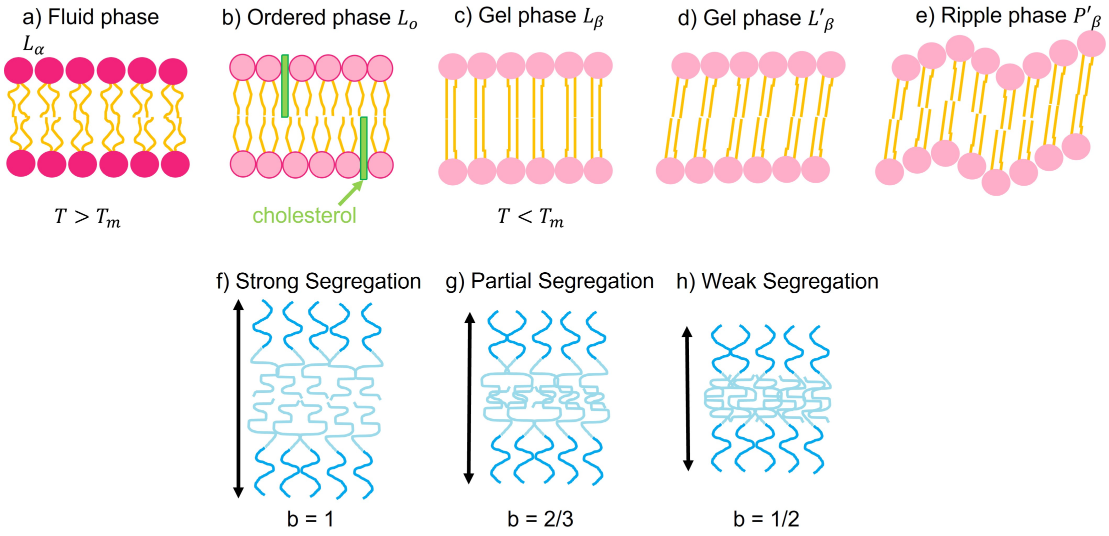

Figure 1.5: Phospholipid and diblock copolymer phases. Some lipid bilayers can perform a reversible transition from the a) fluid-phase (liquid disordered) to b) liquid ordered and then c) gel-phase. The liquid ordered phase usually forms in mixtures of lipid and cholesterol (or other similar molecules). The gel phase can also become d) tilted if the lipid head group is too large for efficient packing and e) ripple. Diblock copolymers also have different membrane conformations: f) a strongly segregated bilayer, g) partially segregated with some interdigitation and h) weakly segregated, interdigiting membrane.

Pure lipid bilayers are fluid at temperatures above the main transition temperature T_m and solidify at temperatures $< T_m$. The lipids in the bilayers can form different phases. For example, in fluid or liquid disordered phases L_α or L_d, the lipid hydrocarbon tails are liquid and disordered at high temperatures while in gel phase, L_β, the tails attempt to be crystalline. If the head group is too large for efficient packing, the amphiphiles may form the tilted phase, L'_β, where the amphiphiles are tilted relative to the midplane (35, 55). A liquid ordered phase L_o lies between the L_d and L_β. L_o has solid-like qualities similar to L_β while retaining the high rate of lateral diffusion typically found in L_d phases (56). The tilted L'_β phase can also transition into the asymmetric ripple phase P'_β (35).

Lateral phase separation can occur in mixed phospholipid membranes if the respective chain length of the phospholipid components differs by more than two carbons, or if the lipid head groups are different. Domains could also be triggered by external stimuli such as temperature, lateral pressure, differences in the degree of saturation, or integration of macromolecules and membrane proteins, in the bilayer (22).

Although the behaviour of amphiphilic block copolymers is similar to that of a lipids, the similarities may be inappropriate at molecular weights greater than a typical lipid. Amphiphile self-assembly has been attributed to the two main contributions to free energy: interfacial tension at the hydrophobic/hydrophilic edge and the entropic loss that occurs when polymer chains are forced into more ordered structures (57). Two limiting regimes are believed to exist in diblock copolymer membranes. At the strong segregation limit (SSL) there is disparity between the interfacial tension and the entropic stretching penalty so minimising the interfacial surface influences association thermodynamics and induces separation and stretching between the hydrophilic and hydrophobic segments of a diblock copolymer chain (57, 58). For copolymer membranes, the strength of segregation can be estimated based on how the membrane thickness t varies with the degree of polymerisation in the hydrophobic segment (the number of hydrophobic units) N using exponent b:

$$t \sim N^b \tag{1.14}$$

So for fully stretched, strongly segregated copolymer chains, $b = 1$, which is also the theoretical limit approached by phospholipids (57). The other limiting regime is called the weak segregation limit where the interactions between the hydrophilic and hydrophobic segments are weak enough that the individual chains are unperturbed. In this case $b = \frac{1}{2}$. For the intermediate condition, the interfacial tension and chain entropy are balanced and the exponent is $b = \frac{2}{3}$ as shown by Figure 1.5 (37, 57).

Conformation of block copolymer molecules in a membrane changes with the molecular weight due to the SSL at the hydrophilic/hydrophobic segment interface (57). In low molecular weight diblock copolymers (hydrophobic block <1000 $\mathrm{g\,mol^{-1}}$), the repulsion between the hydrophilic and the hydrophobic block causes a more stretched chain conformation (59). In contrast, an increase in block copolymer molecular weight causes an increase in the entropic energy contribution, leading to stronger interdigitation and entanglement of the polymer chains within the membrane (57). Because higher molecular weight copolymers form larger membrane thicknesses they experience less segregation force from an increase in chain flexibility. This leads to more coiled and denser structure, reflected in interdigitation of the leaflets (60).

The conformation of copolymers is determined by three factors: overall degree of polymerisation, N; the overall volume fraction of each component f_A and f_B, and the Flory-Huggins segment-segment interaction parameter χ (58). For diblock copolymers, which have no strong interactions such as hydrogen bonding, χ is generally positive and small, and varies inversely with temperature (45). The copolymer conformation is dictated by χN. The weak segregation limit is associated with $\chi N \sim 10$, while $\chi N >> 10$ is believed to correspond to the strong segregation limit. As with one-component diblock copolymers, in two-component blends the morphologies can also be approximated by χN and f only if the diblock copolymers have similar values of N (61). Other polymer architectures have also been studied using self-consistent field theory. The study concluded that for all two-component copolymers, the morphology behaviours (lamellar, cylindrical, spherical) are similar, however occurrence of the structures significantly depends on the individual copolymer component fraction f (62).

Mixed lipid vesicles, mixed polymer vesicles and hybrid lipid/block copolymer vesicles can de-mix to create typically bilayer domains of different shapes and sizes, depending on the composition and cooling rate (63, 64), or in the case of polymers, the compatibility of the hydrophobic blocks (65).

Domains existing within biological membranes can play a role in biological cell process such as cell adhesion, signal transduction or endocytosis (66) as well as membrane tension regulation (67, 68).

Domains can form within the bilayer membrane through diffusion. While a lipid in one of the two layers of a membrane bilayer can "flip-flop" from one layer to the other to redistribute the lipids as shown in Figure 1.6, to maintain asymmetry low flip-flop rates are required (39). Phospholipid movements are generally restricted to lateral diffusion, because the crossing of the phospholipid from one leaflet to the other requires the energetically unfavourable momentary contact of their hydrophilic head with the hydrophobic region (18). In lateral diffusion molecules only move within a leaflet, rather than across them as shown in Figure 1.6 (16), and generate membrane domains.

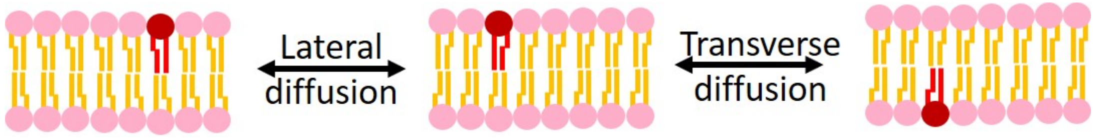

Figure 1.6: Diffusion in phospholipid bilayers. Amphiphiles can diffuse through a membrane by diffusing laterally and along the same leaf of the bilayer or by flipping from one bilayer leaflet to another during transverse diffusion. However, ”flip-flopping” is unfavourable and low flip-flop rates of rapid active processes are required to maintain asymmetry, so phospholipid movement is generally restricted to lateral diffusion.

Nanoscale domains are energetically unlikely because of the anticipated high interfacial line tension of matching a liquid ordered lipid with a liquid disordered lipid (69) or polymer rich membrane domain to a phospholipid rich membrane domain as their hydrophobic thickness are so different. This mismatch in thickness could lead to a large interfacial energy cost at the domain boundaries as a result of water molecules potentially accessing the hydrophobic region of the polymer membrane. Thermodynamically, the line tension tends to favour domain coalescence to minimize boundary length, but as a consequence domains could grow with time into a single large domain within the membrane (34). The energetically unfavourable mismatched thickness configuration could be avoided by having a mixed interfacial region at the domain boundaries that allow a more gradual change in the membrane thickness. Such a region would maintain the isolation of the hydrophobic residues from directly contacting the aqueous phase.

Typically, the thickness for a hydrated phospholipid bilayer is between 3-5 nm (70, 71), while for polymers, the thickness can vary from 5-50 nm (72). In hybrid lipid-polymer membranes, these large differences in hydrophobic region size can lead to a pronounced hydrophobic mismatch at the polymer/lipid boundaries, which could lead to the exposure of hydrophobic groups to the aqueous environment with significant energetic cost. Gradual reduction of the hydrophobic region in the interfacial zone might involve polymer interdigitation to attain a thinner membrane structure (29) as shown in Figure 1.7.

Domain instability is driven by a balance between the bending energy of a domain and the line tension at the boundaries. Edge energy can be decreased by reducing the perimeter of the circular domain and increasing the bending energy. When the energetic cost of the line tension is higher than the membrane bending energy required for fission, the vesicles can split into separate vesicles. This phenomenon has been observed in hybrid membranes above a critical lipid weight fraction leading to separated liposomes and polymersomes (34).

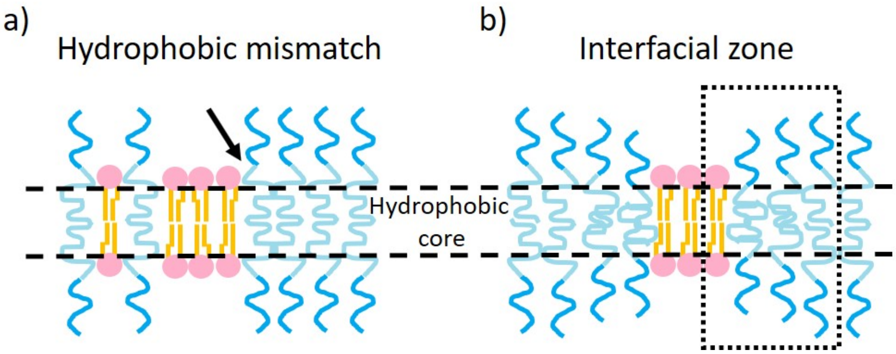

Figure 1.7: Interfacial region in phospholipid and diblock copolymer hybrid membranes. Domains with a) a mismatch in hydrophobic core thickness are unfavourable and can be avoided by having a b) mixed interfacial region that has a more gradual change between the different membrane thickness.

1.4 Vesicle preparation

Vesicles are not at thermodynamic equilibrium but in a kinetically trapped state for which the energy barrier is so high that thermodynamic equilibrium cannot be easily reached (23). Since the vesicle formation process is driven by kinetics, particular membrane morphologies could form in multi-component vesicles and then become trapped in that arrangement. Once formed, the time vesicles remain in the kinetically stable state may be hours, days or even weeks depending on their preparation procedure. Various initial experimental conditions such as concentration, temperature, and preparation method have been shown to influence vesicle size and lamellarity (23). The actual size of the vesicle depends less on thermodynamics and more on the non-equilibrium aspects of the formation process, allowing the diameters to be tailored using different preparation procedures (47).

There are a variety of methods available to generate hybrid lipid-polymer vesicles, from bulk techniques such as electroformation (73, 74, 75), hydration (65), and droplet phase transfer (76) for GUVs, extrusion (74, 77, 78, 79) for LUVs to more automated and high-throughput technologies such as droplet microfluidics (80).

Electroformation shown in Figure 1.8a is most commonly used in the formation of giant unilamellar vesicles (GUV) as it is a rapid technique (81) and generates a homogenous vesicle populations with sizes $> 5\mu m$ (72, 82). Extrusion shown in Figure 1.8b on the other hand, allows generation of large unilamellar vesicles (LUV) with reproducible homogenous size distributions > 100 nm (83, 84). By altering the flow rate, membrane pore size and temperature during the extrusion process, the average size and homogeneity of the vesicles can be controlled (84). Multiple extrusion steps are also suspected to allow more thorough mixing of the amphiphiles compared to electroformation, perhaps reflecting the structures formed during electroformation are in a non-equilibrium state (82).

The effect of buffers on membranes has not been fully explored due to the assumption that buffers are too hydrophilic to substantially interact with a lipid bilayer. However, HEPES and PIPES buffers were found to have a membrane softening effect on DPPC bilayer, believed to be caused by an interaction between the buffer molecules and the lipid head group. As changes to the hydrophilic region are thought to alter membrane elasticity, the relationship between buffer and lipid needs to be kept in mind when planning experiments (51). Other factors that could influence lipid and polymer vesicle formation include amphiphile composition, electrostatic interactions, electrolyte concentration and interactions with polymers (47, 85).

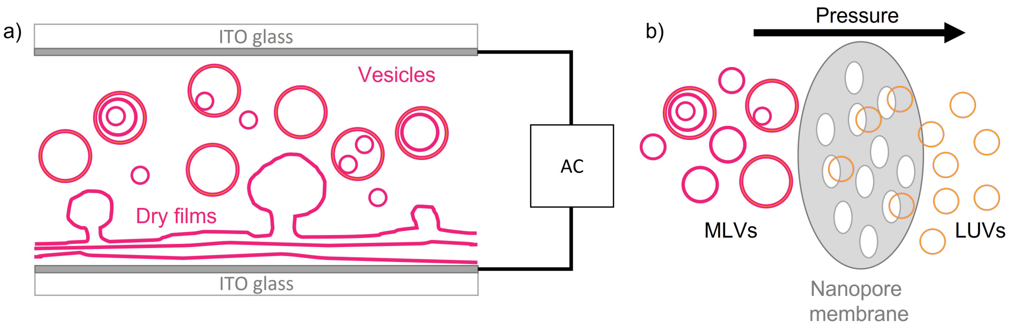

Figure 1.8: Vesicle preparation methods. Vesicles can be prepared using the a) electroformation method of GUVs and b) extrusion method for LUVs.

1.5 Recent advances for hybrid lipid/polymer vesicles

Recent work is starting to uncover important advantages in using hybrid vesicles for membrane protein reconstitution, including enhanced protein folding and significantly extended functional lifetime: hybrid vesicles have already been used to reconstitute a model membrane protein. POPC has been blended withPBd_{22}-PEO_{14}, and reconstituted with cytochrome *bo*$_3$. The protein function in a range of compositions was monitored using a spectroscopic decylubiquinone oxidation assay. All the hybrid compositions were found to maintain $>$ 40% protein activity after 41 days (1).

A combination of PBd_{22}-PEO_{14} and POPC or *E. coli* extracted lipids were also used to reconstitute two adenosine triphosphate (ATP) binding cassette membrane proteins, permeability glycoportein (P-gp) or *Novosphingobium aromaticivorans* Atm1 (NaAtm1). The choice of detergent during reconstitution was found to play an important role in final protein-to-lipid-polymer ratio. Ultimately, the complex lipid mixture in the *E. coli* lipids extract provided the environment for successful incorporation of P-gp protein into a hybrid *E. coli*-PBd_{22}-PEO_{14} membrane. The vesicles were also visualised using cryogenic transmission electron microscopy (cryo-TEM), and size characterised with dynamic light scattering (DLS). Membrane proton permeability over time was measured and found pure polymer and hybrid lipid-polymer membranes had higher permeability coefficients than pure lipid membranes (77).

Soy phosphatidylcholine (PC) was also combined with PBd_{22}-PEO_{14} or polydimethyl siloxane-graft-polyethylene oxide (PDMS-g-PEO) to form a hybrid vesicle. Another an ATP synthase, alongside bacteriorhodopsin, was reconstituted into the hybrid vesicles and retained activity of $> 50\%$ over 42 days in 50 mol% PBd_{22}-PEO_{14}/POPC and 70 mol% PDMS-g-PEO/POPC vesicles. Vesicle size distributions using DLS found all hybrid vesicles were uniform in size, however passive proton permeability indicated that membrane composition played a role in permeability (78).

Ionophores have also been reconstituted into hybrid dipalmitoylphosphatidycholine (DOPC) and PBd_{37}-PEO_{22} membranes. Using a proton permeability assay to determine enzyme activity, it was found that the addition of ionophores increased the dissipation rate of externally imposed pH gradients and increased the transport of potassium ions. Again, size was characterised by DLS and vesicular structure confirmed using cryo-TEM (86).

Poly(1,4-isoprene)-block-polyethlene oxide (PIPEO) diblock copolymer was synthesised using hydrophilic/hydrophobic block ratios known to foster polymeric bilayer formation. In combination with 1,2-dipalmitoyl-sn-glycero-3-phosphocholine (DPPC) lipids, giant unilamellar vesicles (GUV) were prepared by electroformation. $PIPEO_{3188}$ molecular weight appeared to have no effect on vesicle formation despite differences in hydrophobic mismatch between the lipid and polymer as shown by cryo-TEM in Figure 1.9. However, hybrid DPPC/$PIPEO_{3188}$ vesicles did have a heterogeneous distribution of a fluorescent lipid above 50 mol% DPPC. Outer membrane protein F , OmpF, was successfully integrated into these membranes and the activity confirmed by measuring transmembrane currents, although the probability of OmpF insertion into the hybrid vesicles was lower than into DPPC bilayers (73).

Longer triblock copolymers also form stable vesicles via self-assembly. Although the hydrophobic thickness of triblock copolymers was anticipated to be much greater, the membrane protein acetylcholinesterase (AChE) was successfully incorporated into hybrid poly(2-methyloxazoline-block-dimethyl siloxane-block- 2-methyloxazoline) (PMOXA-b-PDMS-b-PMOXA) and phosphatidylethanolamine (PE) or phosphatidylserine (PS) vesicles. Fluorescently labelled lipids and fluorescence quenching techniques revealed these hybrid blends form mixed vesicles and a non-aggregative distribution of lipids - the membranes were homogenous. The hybrids also appear to have intermediary properties between pure lipid and pure PMOXA-b-PDMS-b-PMOXA systems, where the hybrids retain stability against dehydration, but have reduced loading capacities by freeze-thaw processes due to transient pore formation (87).

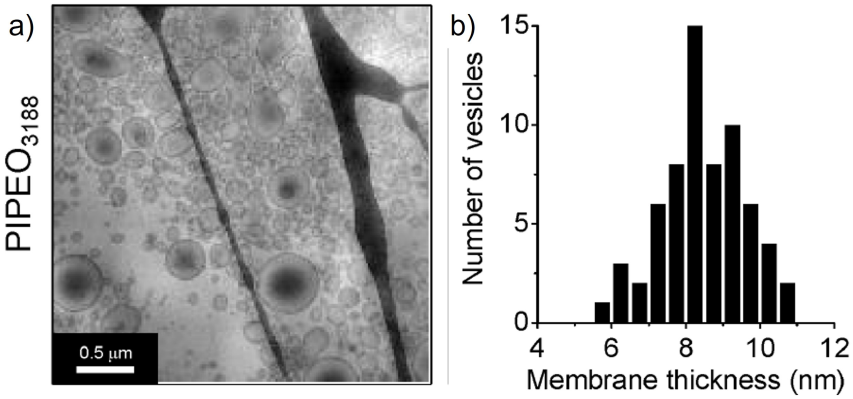

Figure 1.9: Thickness of pure $PIPEO_{3188}$ membranes determined by cryo electron microscopy. a) Micrographs of polymersomes formed by $PIPEO_{3188}$ in vitreous ice. (b) Histogram of the membrane thickness of individual polymersomes made of $PIPEO_{3188}$ based on the analysis of 65 vesicles. Image was taken from (73).

Both cytochrome bo_3 and ATP synthase membrane proteins were also successfully reconstituted into graft copolymer PDMS-g-PEO and soy PC large unilamellar hybrid vesicles (LUV). DLS was used to determine vesicle size, and cryo-TEM to confirm the unilamellar vesicular structure. Observations with fluorescence microscopy showed phase separation occurring in hybrid PDMS-g-PEO and soy PC membranes at polymer concentrations lower than 70 mol%. Here, a fluorescent polymer marker was synthesised specifically to determine mixing behaviours of this polymer-lipid blend. The protein functionality was measured by observing changes in oxygen concentration within the samples, with 75 mol% polymer hybrid sample maintaining a protein activity of 92%, similar to a pure lipid system (88).

Overall, the activity of these membrane proteins reconstituted into these hybrid membranes appears to be dependent on copolymer architecture and bilayer composition. Membrane proteins have been successfully incorporated into diblock, triblock and graft copolymer/lipid vesicles, with the lipids used for these hybrid vesicles generally having a low melting transition temperature. Some investigations have included membrane permeability or release studies to complement the enzyme activity results and confirmed vesicle size or structure using DLS or cryo-TEM (1, 78, 86). However, relatively few have completed experiments incrementally increasing the copolymer fraction within hybrid vesicles to monitor enzyme activity and determine membrane properties, and then relating membrane composition to those results.

In order to make them viable products for biomedical applications, it is essential to understand how the composition of a membrane affects its properties. Discovering which properties govern protein folding, structure and stability, would allow these hybrid membranes to be tuned to enhance a particular membrane protein and alter durability in artificial systems depending on the purpose. Previous studies combining block-copolymers and lipids exploring mixing behaviours and domain formation in the hybrid vesicle membrane could provide insight into hybrid vesicle component choices and membrane properties.

Phase separation due to changes in temperature has been explored using anisotropy and general polarisation (GP) experiments on hybrid DPPC and PBd_{11}-PEO_8 membranes, using Förster resonance energy transfer (FRET) on LUVs, which found the hybrid membranes could contain both solid and fluid phases across all compositions at room temperature. Although the Hildebrande solubility parameters for polybutadiene and alkane chains typically found in lipids are similar, GUVs of this copolymer lipid blend displayed phase separation (79).

Mixtures of diblock copolymer polybutadiene-block-polyethylene, PBd_{46}-PEO_{30} and either phospholipids POPC or DPPC were made into GUVs by electroformation, with demixing controlled by adding cholesterol and varying the cooling rate. The domain size was found to be affected by the cooling rate: faster cooling rates resulted in formation of smaller domains while the domain shape was determined by the lipid composition (63).

Although POPC was integrated into thick PBd_{46}-PEO_{30} -rich membranes, it appeared to be less energetically favourable for the PBd_{46}-PEO_{30} molecules to be incorporated into the thinner, lipid-rich membrane environment, resulting in poor hybrid lipid polymer GUV formation. Diffusion of the copolymer in polymersome membranes, determined by fluorescence recovery after photobleaching (FRAP), was found to be much slower than lipid diffusion through fluid liposome membranes implying polymer-rich domains are likely to diffuse more rapidly through a lipid-rich membrane matrix than lipid-rich domains through a polymer-rich matrix as domain mobility is dependent on the viscosity of the continuous phase. Micropipette aspiration revealed the thick, entangled copolymer membranes were more robust than POPC membranes, and had a higher lysis stress and strain (89).

PBd_{42}-PEO_{20} and DPPC hybrid vesicles generated phase separated, irregular shaped

GUVs (90, 91). A microfluidic device allowed the relationship between mechanical stress and vesicle deformation to be observed by controlling the pressure difference, and thus the flow, through the trap on the device. As shown in Figure 1.10, in hybrid vesicles of 65 mol% PBd_{42}-PEO_{20}, polymer mechanical properties dominated as the polymer was above its glass transition temperature and the vesicles were able to flow through the trap. For vesicles with 35 mol% PBd_{42}-PEO_{20}, some vesicles deformed like the polymer systems, while others flattened against the trap like pure DPPC vesicles. Small angle neutron scattering (SANS) performed on this hybrid blend suggested the coexistence of pure DPPC and PBd_{42}-PEO_{20} vesicles as well as hybrid cylindrical micelle structures within the samples, further confirmed using cryo-TEM. The difference in membrane surface morphology was attributed to the difference between thermodynamic stabilisation and kinetic control of the preparation techniques used to form GUVs and LUVs (91).

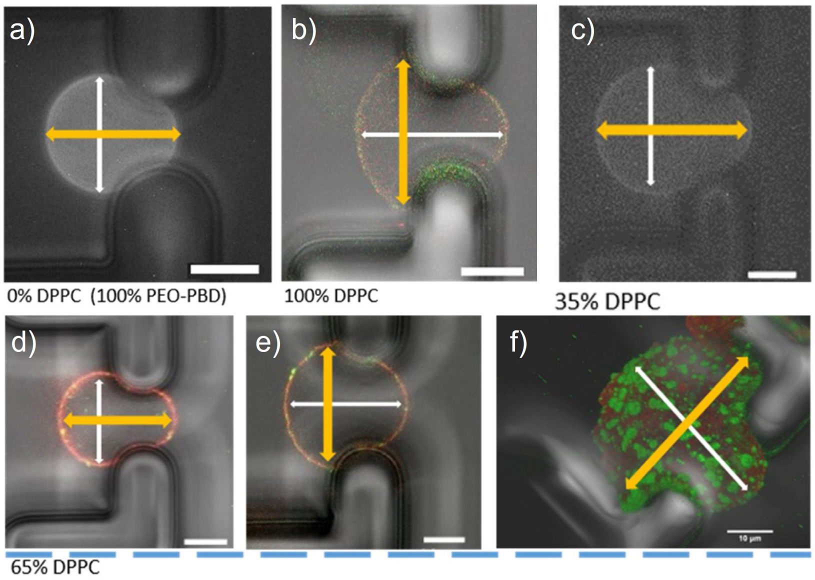

Figure 1.10: Microfluidics of PBd_{42}-PEO_{20} and DPPC GUVs. The GUVs become deformed as they flow through the device. a) Pure polymer vesicles deform along the flow while b) pure lipid vesicles deform perpendicular to the flow. c) In hybrid samples, 35 mol% DPPC GUVs deform along the flow, whereas for d-f) 65 mol% DPPC GUVs, different behaviours are observed. Scale bar 10 µm. Images taken from (91).

Hybrid vesicles containing polymers of lower molecular weight PBd_{22}-PEO_{14} on the other hand, showed a higher tendency to form hybrid vesicles when mixed with POPC. The GUVs were labelled with both a fluorescently labelled polymer and a fluorescent lipid to show both homogenous mixed hybrid vesicles as well as pure liposomes and polymersomes in the 50 mol% PBd_{22}-PEO_{14} sample. Overall, increasing PBd_{22}-PEO_{14}

mol% reduced the encapsulation efficiency and content release behaviours of hybrid nanoscale PBd-b-PEO and POPC membranes (82).

Cryogenic electron tomography (cryo-ET) of hybrid PBd_{22}-PEO_{14} and POPC samples discovered both tubular and spherical vesicles existing in samples with 15-85 mol% polymer component as shown in Figure 1.11. Cylindrical vesicles were thought to form due to asymmetric membrane composition, confirmed by the reduction in quenching of fluorescently labelled lipids, and the inhibition of a phospholipase. The results suggested that a large fraction of the polymer accumulated in the outer leaflet, while the lipid was found in the inner bilayer leaflet (92).

Building on this previous study, hybrid PBd_{22}-PEO_{14}/POPC membranes were compared with polylactic acid-polyethylene oxide (PLA-PEO)/POPC and polycaprolactone-polyethylene oxide (PCL-PEO)/POPC membranes using calcein leakage and enzymatic assays as well as cryo-TEM and confocal microscopy. Electron density profiles from cryo-TEM images suggest interdigitation in PCL-PEO/POPC and PLA-PEO/POPC membranes. Although surface morphologies in GUVs of PCL-PEO/POPC membranes indicated microdomains, the other block copolymer hybrids appeared homogeneous. The enzymatic assay also revealed the surface topography was lipid-like, and enzymatic digestion could be modulated by changing the polymer component (93).

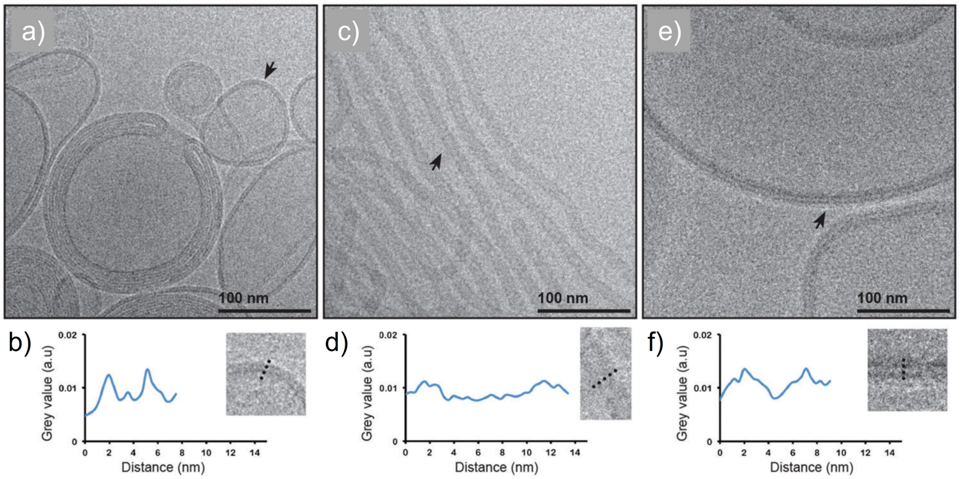

Figure 1.11: Polymorphism of aqueous suspensions of lipid–polymer mixtures. Cryo-EM images of nanostructures formed from thin film rehydration of phospholipid a) POPC, b) 50 mol% PBd_{22}-PEO_{14}/POPC mixtures and c) PBd_{22}-PEO_{14}. The images show that tubular morphology co-exists with vesicular structures in the hybrid sample. Scale bars indicates 100 nanometers. Arrows in a), c) and e) indicate line-scan regions of b) POPC, d) 50 mol% PBd_{22}-PEO_{14}/POPC mixtures and f) PBd_{22}-PEO_{14}. Images taken from (92).

While PCL-PEO/POPC hybrids were confirmed to have poor passive encapsulation and colloidal stability, PLA-PEO/POPC had improved encapsulation, comparable to pure POPC and were stable over 3 weeks. Increasing PLA-PEO mol% reduced the initial burst release of encapsulated carboxyfluorescein (CF) and reduced the long term release rate (10).

Hybrid GUV membranes containing DPPC with 20-28 mol% of polyisobutylene-polyethylene oxide PIB_{87}-PEO_{17} block copolymer generated by electroformation were also observed to experience domain formation. The morphology of DPPC/PIB-PEO GUVs was significantly affected by the initial mixing ratio as well as the PIB-PEO block compositions. Incorporation of 16-60 mol% PIB_{87}-PEO_{17} copolymer into DPPC liposomes was believed to disturb lipid packing in the bilayer, leading to smooth membranes from the faceted surface typically found in pure DPPC membranes. Hybrid PIB_{37}-PEO_{48} and DPPC vesicles on the other hand exhibited a more ragged surface than pure DPPC membranes, with larger holes and lacerated edges. PIB_{37}-PEO_{48} hybrids were also much larger, at 200 μm, compared to 50 μm of PIB_{87}-PEO_{17} hybrids (28).

Polydimethylsiloxane-block-polyethylene oxide, PDMS-b-PEO, diblock copolymers of various molar masses and hydrophobic weight fraction were synthesised and combined with 10 wt% POPC to form GUVs. Mixing behaviours were observed using a fluorescently labelled polymer and lipid while mechanical properties of these hybrid GUVs were evaluated using micropipette aspiration. The polymer was thought to form weakly segregated membranes (bilayer conformation) and hybrid vesicles were found to have intermediary mechanical properties between pure liposomes and polymersomes (74).

POPC/PDMS-b-PEO mixtures were also compared to POPC/PEO-PDMS-PEO triblock copolymer blends to determine structural and mechanical property differences in different copolymer architectures. For all compositions and architectures, homogeneous membranes were formed at low POPC contents until the limit fraction for each composition was reached - where phase separation and then budding and fission were favoured. However, the diblock PDMS-b-PEO/POPC composition membranes displayed greater toughness, especially at high molar masses, compared to the triblock PEO-PDMS-PEO/POPC vesicles, which were considered even more fragile than pure POPC (94).

Hybrid lipid/diblock copolymer membranes have even been simulated by molecular dynamics (MD), which found phase separation was driven by incompatibility between lipids and copolymers and thickness mismatch. Lipid diffusivity also appeared to depend on the state of the hybrid membrane, as resistance to lipid motion was suggested to come mainly from component interactions and interdigitation (95).

Lateral diffusion of PEO-PDMS-PEO/POPC GUV membranes of different molecular weights and compositions was also compared to their mechanical properties. For the higher molecular weight PEO-PDMS-PEO polymer, increasing the polymer fraction decreased the diffusion coefficient, while for the lower molecular weight copolymer, the diffusion coefficient increased with increasing copolymer fraction. This difference in membrane diffusion and viscosity was attributed to the membrane conformation of these triblock copolymers as lipid diffusion seemed insensitive to vesicle composition. Micropipette aspiration measurements also indicate triblock copolymer architecture gives a tougher membrane compared to grafted copolymers of the same hydrophobic molar mass (96).

The stability of DOPC and poly(2-methyloxazoline -block- dimethyl siloxane -block-2-methyloxazoline) (PMOXA-b-PDMS-b-PMOXA) symmetric triblock copolymer large unilamellar vesicles (LUVs) over time was characterised using DLS and quartz crystal microbalance with dissipation (QCM-D). Stability and resistance to surface rupture was shown to be enhanced after the incorporation of the copolymers. Stopped flow and differential scanning calorimetry (DSC) experiments suggested copolymer incorporation modified the bilayer structure so the hydrophilic block stretched into the solution while the hydrophobic block filled the voids in the lipid (97).

Studies on GUVs of polydimethylsiloxane-graft-polyethylene oxide (PDMS-g-PEO) or triblock copolymer PEO-PDMS-PEO of different molecular weights and POPC or DPPC blends were conducted to examine the membrane mixing behaviour and mechanical properties with copolymers of different architectures and increasing molecular weight at a range of compositions and temperatures. Using a combination of fluorescence lifetime imaging microscopy (FLIM) and FRET, evidence for the presence of stable nanodomains in hybrid GUVs was found. As shown by Figure 1.12 the cooling rate impacted domain morphology within 20 mol% DPPC/ 80 mol% PEO-PDMS-PEO GUVs. Modulation of the line tension and bending rigidity was shown to affect hybrid vesicle surface morphology in compositions containing POPC (34).

Triblock copolymer PEO-PDMS-PEO of different molecular weights was also blended with POPC or DPPC to form hybrid LUVs and evaluated against PDMS-g-PEO/POPC hybrid vesicles using cryo-TEM, FRET and SANS techniques. Changing the copolymer architecture from graft to triblock led to more efficient mixing of the lipid and polymer indicating line tension can be modified by changes to the architecture of the copolymer. Decreasing the molar mass of the triblock copolymer also promoted hybrid vesicle formation and resulted in disappearance of worm-like micelles in PEO-PDMS-PEO/DPPC mixtures (98).

FRET allowed the mixing behaviours and domain formation of hybrid LUV membranes containing PDMS-g-PEO with phospholipids DPPC or POPC to be explored. Mixtures of the polymers with each of the phospholipids were found to have low thickness mismatch as determined by SANS and cryo-TEM. There was no evidence of budding and fission phenomenon occurring in the LUVs, unlike for GUVs with the same composition, suggesting that membrane curvature could play a role in the stabilisation of domains (99).

Binary-lipid membranes containing DPPC (high melting transition temperature) and DOPC (low melting transition temperature) phospholipids were compared to PDMS-g-PEO and DPPC hybrid membranes. Although only a fluorescent lipid was used, domain formation could be clearly observed as shown in Figure 1.12. In both systems DPPC could be manipulated to solidify into stripy or patchy domains by altering the membrane tension through changes in temperature. The shape of the domains was suggested to be due to the polymorph that DPPC formed while cooling, with the size thought to be controlled by the proportion of DPPC used to form the vesicle. Vesicle stress and strain were characterised by micropipette aspiration, which revealed tension played a dominant role in the morphology of membrane domains (75).

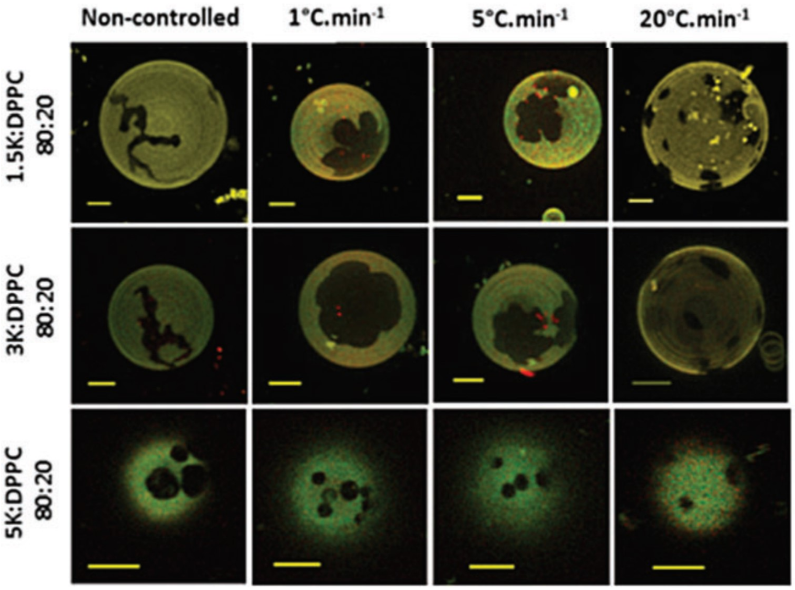

Figure 1.12: Fluorescence microscopy images showing the impact of the cooling rate on 20 mol% DPPC/ 80 mol% PEO-PDMS-PEO GUVs. Three different molecular weights (1500, 3000 and 5000 $\mathrm{g\,mol^{-1}}$) of the triblock PEO-PDMS-PEO polymer were combined with DPPC to form heterogeneous 20 mol% DPPC/ 80 mol% PEO-PDMS-PEO GUVs. DPPC-rhodamine (red channel), expected to partition into the lipid phase, and PEO-PDMS-PEO-FITC (green channel), expected to partition into the polymer phase, were used as probes. The cooling rate was controlled to observe domain morphology within these hybrid membranes. Scale bar is 5 μm and the image was taken from (34).

Hybrid GUVs of PDMS-g-PEO and DPPC or POPC membranes were obtained using the electroformation procedure, including both a fluorescently labelled lipid and polymer to determine mixing behaviours. Over time, domains, budding, and finally fission occurred in hybrid PDMS-g-PEO/POPC vesicles, with stable, homogenous membranes obtained only when the polymer was the major component (60-90 mol%) as shown in Figure 1.13. DPPC/ PDMS-g-PEO mixtures formed heterogeneous vesicles at copolymer $>$ 50 mol%, which unlike their POPC counterparts, were stable for several days. Copolymer interaction with the lipid was believed to impact the enthalpy and the melting temperature for fractions as low as 10 mol% PDMS-g-PEO, providing evidence that part of the copolymer chains were dispersed in the lipid phase. Further additions of copolymer did not alter the melting transition, suggesting a copolymer saturation point in the lipid phase (22).

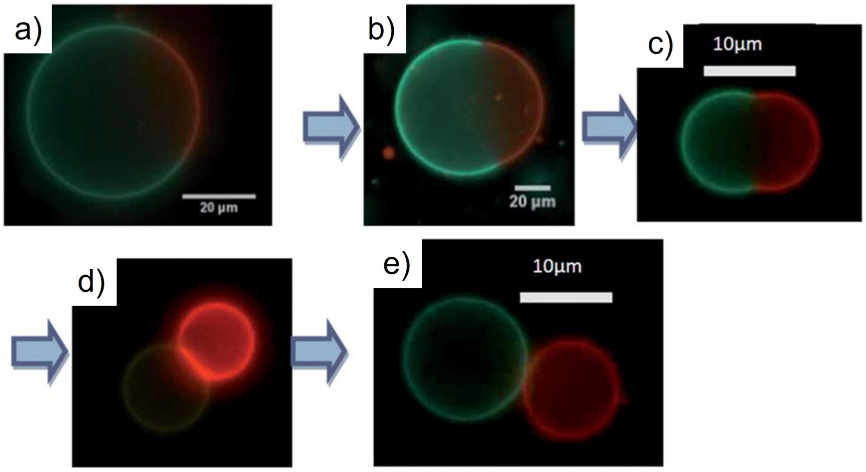

Figure 1.13: Fluorescence microscopy images of heterogeneous hybrid 75 mol% POPC/ 25 mol% PDMS-g-PEO GUVs. Rh-PE (red channel), expected to partition into the lipid phase, and PDMS-g-PEO-fluorescein (teal channel), expected to partition into the polymer phase, were used as probes. Initially, 75 mol% PDMS-g-PEO sample has a) spherical, biphasic vesicles which then b) and c) begin to present different curvatures within the same vesicle. d) A flat contact area appears between the two adhering, but separated, vesicles before e) the vesicles become completely distinct. Image taken from (22).

The majority of studies use a combination of fluorescence microscopy and fluorescence spectroscopy to observe phase separation within hybrid lipid-polymer membranes. Investigations show the existence lipid-rich and polymer-rich phases within hybrid vesicles, although this is dependent on copolymer architecture, the mean the ratio of lipid to polymer and the specific lipid and polymer used. Homogeneous distribution within lipid-polymer hybrid GUV membranes is favoured provided the lipid component is in a fluid state, and typically at a low fraction (22, 29, 90, 98). Although not fully investigated, it appears that above a threshold lipid fraction, microdomains start to appear and begin budding and fission processes depending on the line tension at the lipid domain boundaries. The line tension seems to be partially modulated by the hydrophobic thickness mismatch, and therefore the molar mass of the hydrophobic block of the components, at the lipid-polymer interface. Studies on PDMS-based copolymer/lipid hybrid membranes have even reported formation of stable nanodomains (98).

In terms of membrane properties, studies focus on membrane permeability and release experiments (10, 78, 82, 86, 97). However it is difficult to extract properties such as diffusion across the membrane as both systems and loaded molecules differed between studies and membrane structure was not known. However, few studies have focussed on the influence of membrane structure on the properties of copolymer/lipid hybrid membranes. Majority of studies use DLS for size characterisation, and SAXS, SANS or cryo-TEM used merely to confirm vesicle morphology rather than to their full potential (34, 92). In order to tune hybrid lipid-polymer vesicles for particular applications, the parameters that govern membrane structure must also be understood.

Although PC/PBd-b-PEO ($< 3000\ \mathrm{g\,mol^{-1}}$) hybrid membranes have been shown to extend functional lifetimes of incorporated membrane proteins (1, 77, 78, 86), relatively few investigations have completed experiments incrementally increasing the copolymer fraction within hybrid vesicles to determine surface morphologies (membrane homogeneity or phase separation) and membrane properties, and then relating membrane composition to those results. Therefore there is a need to systematically investigate PC/PBd-b-PEO ($< 3000\ \mathrm{g\,mol^{-1}}$) membrane compositions.

1.6 Research aims and objectives

In the past, pure lipids and polymer vesicles have been used to act as microreactors for compartmentalised chemistry, sensors from functionalising the membrane surface, and drug delivery vectors by encapsulation within the vesicle lumen or membrane. However these pure systems have disadvantages, making hybrid lipid-polymer vesicle systems more attractive as it is believed the advantages from both components can be retained. Hybrid lipid-polymer vesicles are quickly gaining interest due to their increased robustness and colloidal stability as well as their reduced permeability compared to pure lipid vesicles. Previous investigations have also shown membrane proteins can be integrated into the hybrid vesicle membrane and their enzymatic activity maintained over time.

One study in particular showed that by blending POPC lipid with poly 1,2-butadiene(1200)-block-polyethylene oxide(600) (PBd_{22}-PEO_{14}) diblock copolymer into 50 mol% and 75 mol%

PBd_{22}-PEO_{14} the enzymatic activity for an integrated membrane protein could be retained for over 500 days - far longer than a POPC liposome (1). While the biocompatibility of PBd_{22}-PEO_{14}/POPC blend has been established, relatively little is known about membrane properties and structure of this lipid-polymer mixture. Reasons for this sustained activity, the orientation of the integrated membrane protein, and whether the vesicles form a homogenous or phase-separated membranes and thus which environment the enzyme might prefer, is also unknown.

The main aim of this project is to understand the structure, dynamics and physical properties of hybrid lipid polymer vesicles made from POPC phospholipids, and two different molecular weights of PBd-b-PEO copolymer. A numerical estimate for the degree of interaction and solubility between nonpolar materials such as polymers is given by the Hildebrande solubility parameter. A PBd-b-PEO amphiphilic block copolymer was used because it has a similar Hildebrande solubility parameter (15.9 $(\mathrm{J\,cm^{-3}})^{\frac{1}{2}}$) to alkanes typically found in lipids like POPC ($\sim$ 14-16 $(\mathrm{J\,cm^{-3}})^{\frac{1}{2}}$) (100, 101). Butadiene mimics the long alkyl chains of a phospholipid, while ethylene oxide is hydrophilic like a typical phosphate head group of phospholipids (102). PEO is also known to improve the pharmacokinetic properties of vesicles due to a stealth effect it causes that hinders recognition of the vesicle as a foreign body by the immune system (91). Polymer molecular weight is thought to control the membrane thickness and therefore the membrane mechanical properties (103).

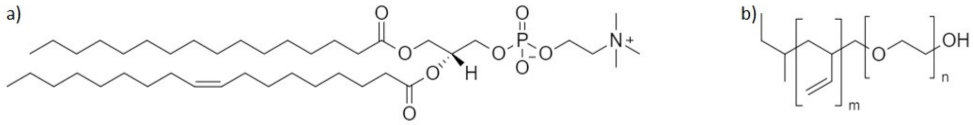

Figure 1.14: Component structures. Structures of a) POPC b) PBd-b-PEO diblock copolymer with *m* number of hydrophobic poly 1,2-butadiene monomers and *n* number of polyethylene oxide monomers.

Membrane properties of large unilamellar vesicles LUV will be determined using a variety of techniques: the permeability and contents release of different compositions of membranes will be investigated using fluorescent probes. Small angle x-ray scattering (SAXS) will be used in conjunction with cryogenic electron tomography (cryo-ET) to find structural information, such as electron density profiles, and morphological changes of vesicles with different membrane compositions. Finally, the mechanical and rheological properties of giant unilamellar vesicles (GUV) membranes will be explored using Flicker spectroscopy and fluorescence recovery after photobleaching (FRAP) and results compared with the membrane hydration determined using Laurdan fluorescent membrane probe.

2. Techniques

2.1 Fluorescence

Fluorescent dyes (fluorophores) have often been used to probe vesicle properties such as ion permeability (86), contents encapsulation and release (10), phase separation (98, 99), membrane viscosity (29) and membrane packing (79).

Fluorescence in fluorophores is a multi-stage process as shown in Figure 2.1. First the molecule absorbs photons which promotes the molecule from the ground state, S_0 to an excited state, $S_1, S_2, ..S_n$ (104). This excited molecule can collide with surrounding molecules, dissipating some of its energy. However, the surrounding molecules may not be able to accept all the energy needed for the molecule to return to its ground state - instead this excess energy can be emitted as a photon as the molecule relaxes from S_1 to S_0 states. Due to the energy dissipation while the molecule was excited, the energy of the emitted photon is lower, and therefore of a longer wavelength, than the photon initially absorbed.

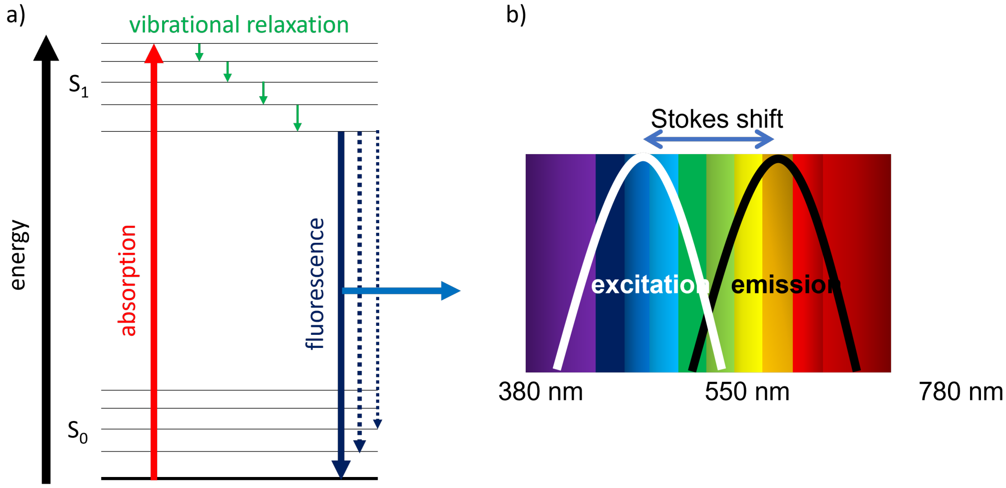

Figure 2.1: The Jablonksi diagram. a) The electronic states of a molecule and the transitions between them are arranged vertically by energy. The Stokes shift b) is the difference in nanometres between the excitation peak and the emission peak wavelengths.

This difference in energy and wavelength between the absorbed and emitted photon is known as the Stokes shift. Each fluorophore has a distinct and individual Stokes shift (105, 106). The magnitude of the Stokes shift depends on the fluorophore and its environment. When excited, the dipole moment of the fluorophore changes, however the surrounding solvent molecules may not adjust as quickly. In more polar solvents such as water an methanol, the fluorophore dipole moment interacts with the polar solvent molecules to reduce the energy of the excited state. Generally, more polar solvents such as water and methanol give larger Stokes shifts compared to non-polar solvents such as hexane and toluene, which have no dipole moment (107).

A fluorometer (or fluorimeter) measures the the intensity and wavelength distribution of the emission spectrum of a sample after excitation of the sample by a specific wavelength; these parameters are then used to determine the number of fluorophores present in the sample.

2.1.1 Environment sensitivity: proton permeability

HPTS is a hydrophilic pyranine polyanion that is often used to observe the proton permeability of vesicles (86, 108, 109) as the pyranine's fluorescence intensity is sensitive to changes in hydrogen ion concentration, making HPTS suitable for exploring passive and facilitated proton fluxes and thus allowing continuous steady-state measurements of the internal hydrogen ion concentration in neutral and anionic vesicles after gel filtration (110). Because the pyranine molecule is anionic, encapsulated HPTS does not bind to the internal phospholipid bilayer, does not readily leak, and molecules are free in solution of the internal aqueous phase (86).

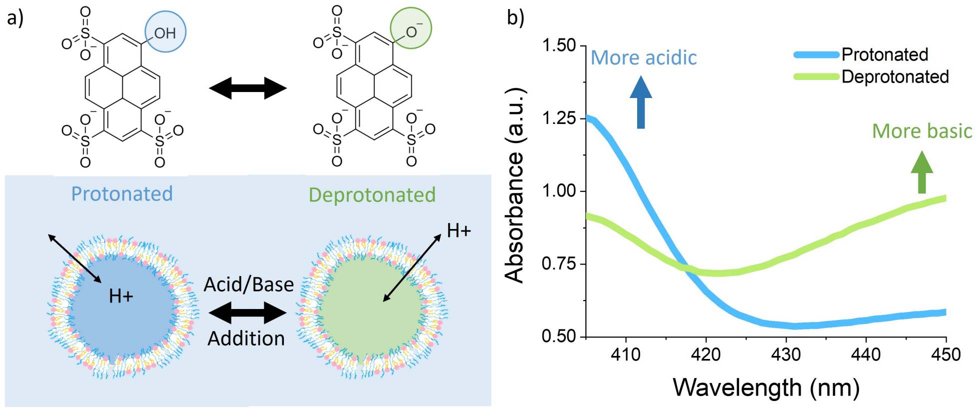

Figure 2.2: a) HPTS in protonated and deprotonated form. b) shows how the HPTS absorbance profile changes as the pH chances. When the solution is more acidic,the absorbance at 405 nm increases, while if the solution is more basic, the absorbance at 445 nm increases.

As shown in Figure 2.2, the ionisation of the pyranine group of HPTS by a pH change has a pronounced red shift in the fluorescence excitation maximum, from 400 nm (at pH 4) to 450 nm (at pH 10) while the fluorescence emission maximum of 510 nm remains unchanged (110). This red shift can also be observed as a colour change that can be measured using a UV-vis spectrometer or fluorometer.

2.1.2 Fluorescence quenching: contents release

Previously carboxyfluorescein (CF) has been used to determine encapsulation efficiency and release in vesicles (10). At high concentrations ($>$ 40 mM) this dye self-quenches (11, 111); fluorescence is lost due to the higher probability of collision between CF molecules. The excitation and emission wavelengths do not change (492 nm and 519 nm respectively) and only the fluorescence signal is reduced, so once CF is diluted to a lower concentration, fluorescence returns.

This is useful when measuring the encapsulation efficiency and release from vesicles. Initially the CF is trapped in the vesicle lumen at high concentrations and has low fluorescence emission intensity. Excess CF in the bulk aqueous phase is removed by gel filtration. Fluorescence in the initial sample can then be measured before the vesicles are then be destabilised, thus diluting the CF concentration, and final CF fluorescence recorded. Encapsulation efficiency can then be calculated by comparing the initial fluorescence against the final emission.

2.1.3 Confocal microscopy: imaging fluorescent vesicles

Confocal microscopy is commonly used to obtain high resolution images of giant unilamellar hybrid lipid-polymer vesicles, specifically to determine whether phase separation has occurred (29, 79, 88, 90, 99). Confocal microscopy offers several advantages over conventional optical microscopy, including the control over depth of field, and a reduction of background information not in the focal plane, that can cause image degradation.

Traditional optical microscopes use an arrangement of lenses to magnify and view objects that are otherwise too small to be seen. A high resolution is also important as objects can be viewed with greater detail. In bright-field microscopes, visible light is passed through the sample and used to form the image directly, without any alterations to enhance the contrast and clarity of the image.

For high resolution imaging, this out-of-focus information that could contaminate image analysis, has to be removed (112). Instead of using a wide field light source, the beam can be focused to a small point (defined by the microscope point spread function), which in turn illuminates a single point inside the sample, and weakly illuminates the rest of the sample. To remove the contribution from weakly lit, out-of-focus objects, a pinhole is placed on the image plane, which allows only light from the bright part of the image to pass. The detector now registers the object illuminated by the focused light and ignores the rest of the sample (113, 114).

This is the basis of confocal microscopy: a focused laser is used to excite fluorescent molecules within the sample and, with help of a pinhole, only emissions from the targeted area are used to produce a sharp image without interference from fluorescent molecules in the surrounding environment as demonstrated in Figure 2.3a. The illuminating beam can be moved across the sample to allow different areas to be imaged, and microscope will discriminate points near (next to, above and below) the focal area, a feature known as optical sectioning. This allows a thin section of the sample to be imaged and then combined with other optical sections into a three-dimensional display (114).

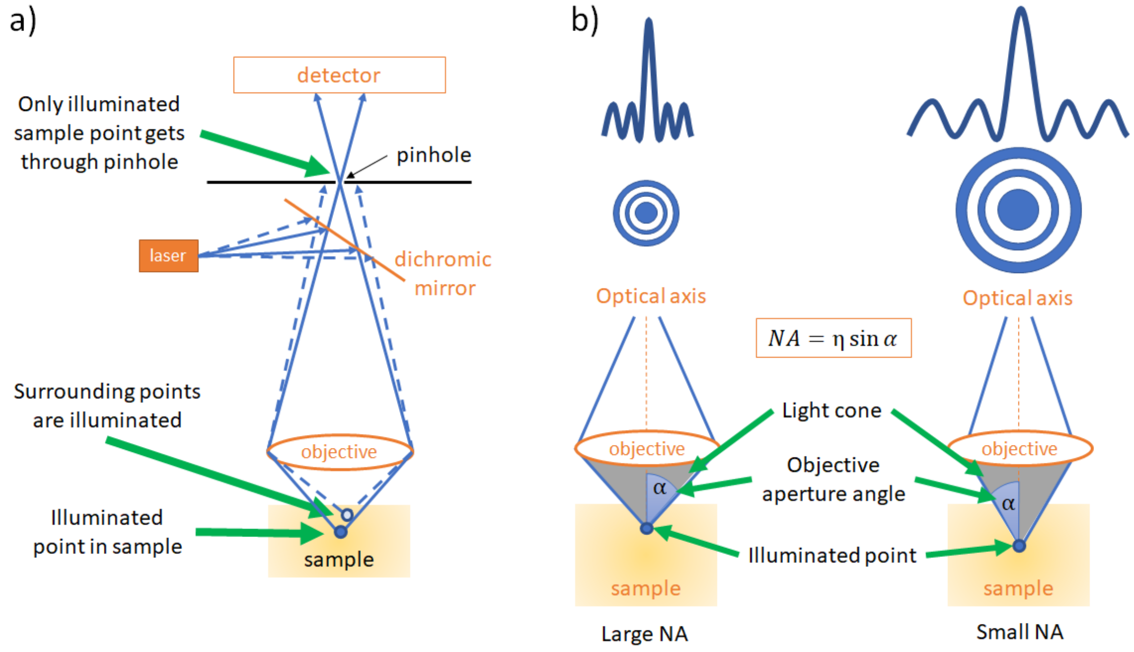

Figure 2.3: Confocal microscopy and the point spread function. a) When a fluorescent sample is illuminated, the excited fluorophores will emit photons. The surrounding area will also be illuminated, however the pinhole will block the light from the proximate points, while allowing the point of interest to be imaged. b) The emitted photons are diffracted by the optical components of the microscope and the point of interest appears as spaced rings by the detector. The number of photons that can be collected depends on the size of the objective aperture angle. The PSF appears as regular rings, also known as an Airy pattern. The larger the numerical aperture, the greater the collection angle, and the more photons are collected, generating a smaller airy disk and producing images with greater resolution (115).

The key properties of the microscope, the magnification and the resolution, are dictated by the objective lens. The resolution is defined as the minimal distance, d, at which two objects within a sample are seen separately. The minimal distance imaged using a regular bright-field microscope depends on the sine of the half angle (α) of the cone of light accepted by the objective lens or emerging from the condenser lens, $\sin\alpha$, the wavelength λ of the incident light and the refractive index η of the media between the frontal lens and the sample. The product of $\sin\alpha$ and the refractive index, η, gives the numerical aperture (NA) for the objective (NA_{obj}) or condenser (NA_{con}) lens. In fluorescence microscopy the objective is the condenser so NA_{con} is equal to NA_{obj} (104, 116):

$$d_{min} = \frac{\lambda}{NA_{con} + NA_{obj}} = \frac{\lambda}{2NA} \tag{2.1}$$

where d_{min} is the minimal distance between two points. The resolution limit of a microscope depends on the diffraction of light, which blurs any point object into a certain size and shape. This degradation is due to the microscope's point spread function (PSF), or it's Fourier transform, the optical transfer function (OTF) (112). An illuminated fluorescent sample will emit photons which are diffracted by the optical components of the microscope. The number of photons that can be collected depends on the size of the objective aperture angle. The PSF appears as regular rings and varies depending on the wavelength and the numerical aperture of the objective lens: short wavelengths and a high NA objective results in a smaller PSF, while long wavelengths and a low NA objective gives a larger PSF as depicted in Figure 2.3b.

Environment sensitivity: membrane packing

Laurdan (6-dodecanoyl-N,N-dimethyl-2-naphthylamine) is a fluorophore that been used in the past to monitor the structure and polarity of a membrane (117, 118, 119, 120, 121, 122). It has a hydrophobic fatty acid tail that allows the Laurdan to be soluble in the lipid bilayer, while the fluorescent napthalene group of the molecule rests towards the aqueous environment between the glycerol backbones of the phospholipid membrane.

While in the bilayer, Laurdan can be excited between 350-400 nm wavelengths, increasing the dipole moment of its napthalene moiety and causing the reorientation of surrounding solvent dipoles (121). Then as Laurdan relaxes, photons are emitted. Photon emission at approximately 440 nm indicates an ordered lipid bilayer, while emission at approximately 490 nm implies a disordered lipid bilayer (117, 118, 119, 120, 121, 122). By comparing the fluorescence emission intensities from images of vesicles at 440 nm and 490 nm, a change in the environment of a lipid bilayer, such as hydration state, can be monitored using confocal microscopy.

The shift in emission between different membrane phases is used to calculate the generalised polarisation (GP), a relative quantitative measure for lipid packing. Generalised polarisation is calculated by:

$$GP = \frac{I_{440} - I_{490}}{I_{440} + I_{490}} \tag{2.2}$$

Where I_{440} and I_{490} are the fluorescence emission intensities at 440 and 490 nm respectively (118). Generalized polarization values vary from 1 indicating little or no solvent effect, to -1 where the Laurdan is completely exposed to the bulk media, which in this case is water (121).

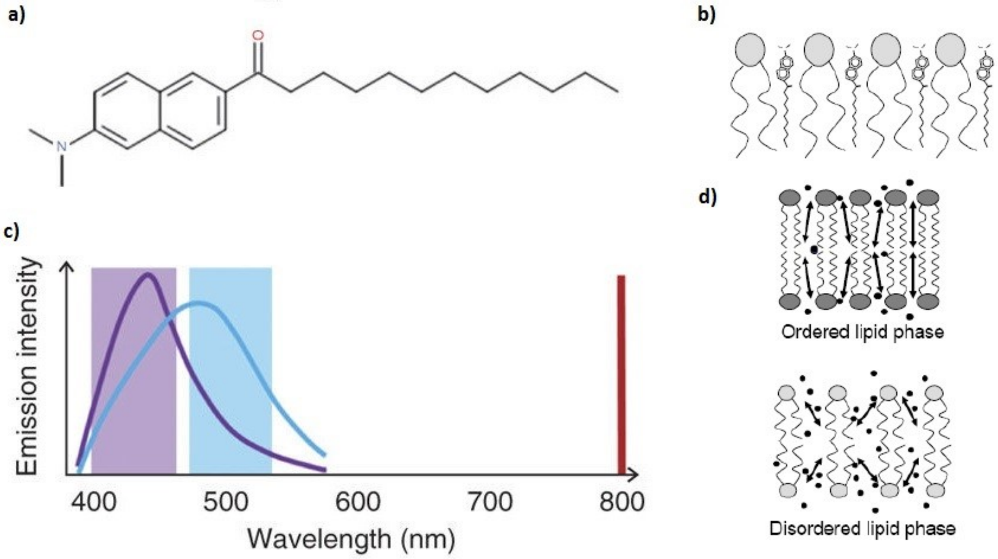

Figure 2.4: Laurdan excitation and emission. a) Laurdan has a hydrophobic fatty acid tail that allows b) the Laurdan to be soluble in the lipid bilayer, while the fluorescent napthalene group of the molecule rests towards the aqueous environment between the glycerol backbones of the phospholipid membrane. Laurdan is excited between 350-400 nm and a) emits at wavelengths between 400-540 nm. Photon emission at 440 nm (violet line) indicates a b) liquid ordered membrane, while emission at 490 nm (blue line) indicates c) liquid disordered. The rearrangement of water molecules (black dots) around the Laurdan dipole (arrows) causes the shift between different phases. Image was adapted from (121, 122).

Photobleaching: membrane viscosity

Fluorescence recovery after photobleaching (FRAP) has been used previously to determine lateral diffusion coefficients of fluorophores through a hybrid lipid-polymer membrane

(90). Fluorescent molecules used for FRAP experiments must be chosen with care. The fluorophores need to be soluble in the membrane, so generally fluorescently labelled lipids or polymers that can partition into the membrane components are used to conduct FRAP in pure lipid or pure polymer membranes (29, 88).

To perform FRAP, the top pole of vesicles containing fluorescently labelled amphiphiles are imaged using a confocal microscope and then a small area is irradiated with a high intensity laser. The extent of photobleaching is dependent on the duration and intensity of exposure to excitation light. The fluorophore is irreversibly destroyed in the excited state and loss of fluorescence signal is irreversible if the bleached fluorophore population is not replenished. However, vesicle membranes are assumed to be dynamic environments, so fluorescence signal returns to the bleached area by lateral diffusion of fluorophores from non-bleached areas (123) as shown in Figure 2.5. The rate at which the fluorescence signal returns can be used to determine membrane viscosity: fluorophores diffusion through a viscous membrane is expected to be slow, while fluorophores would be anticipated to diffuse easily through a fluid membrane.

The recovery curves can then be fitted to find a diffusion coefficient, D, for the fluorescently labelled lipid or polymer through the membrane:

$$D = \frac{r^2}{4\tau_D} \tag{2.3}$$

Where r is the radius of the bleached region and τ_D is the half recovery time.

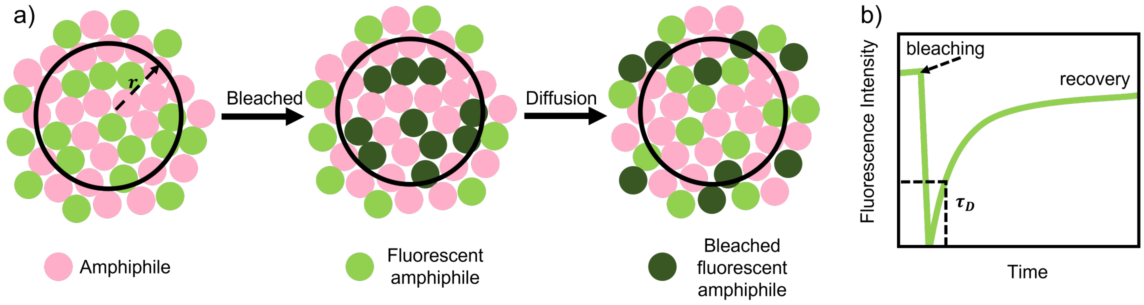

Figure 2.5: Fluorescence recovery after photobleaching. a) vesicles containing fluorescently labelled lipids or polymers are imaged and then a small area is irradiated with a high intensity laser. The fluorescent amphiphile is irreversibly destroyed, however fluorescence returns the bleached area by lateral diffusion of fluorophores through the membrane. The return of fluorescence is recorded as a b) recovery curve that can be fitted to find the diffusion coefficient of the fluorescently labelled amphiphile through the membrane.

Vesicle flickering: membrane thermal undulations

Lipid membranes exhibit thermal membrane undulations that are governed by the bending elasticity of the membrane. These membrane undulations can be analysed to find the membrane bending rigidity κ_b and membrane tension, σ, by imaging the equatorial plane of a fluorescently labelled giant unilamellar vesicle (GUV) using a confocal microscope (124).

With aid from fluorescent probes, an image sequence of a fluctuating GUV membrane over time (flicker spectrum) can show that the apparent membrane position does not always correspond to its equatorial contour. Imaging the equatorial plane allows fluorescence to be captured from a greater area of membrane, and allow changes in the radial membrane distribution to reflect the underlying membrane flickering. This flicker spectrum can then be used to track membrane undulations, resulting in a power spectrum of the mean square amplitude of a given vibrational mode, $\langle | u_q^2 | \rangle$, against wavenumber, q. The power spectrum is fitted with:

$$\langle | u_q^2 | \rangle = \frac{k_B T}{2\sigma} \left(\frac{1}{q} - \frac{1}{\sqrt{\frac{\sigma}{\kappa_b} + q^2}} \right) \tag{2.4}$$

where k_B is the Boltzmann constant and T is the temperature, allows κ_b and σ to be quantified.

2.2 Scattering

2.2.1 Dynamic light scattering: characterising vesicle size

Dynamic light scattering (DLS), also known as photocorrelation spectroscopy (PCS), is usually used to determine the diffusion behaviour of suspended particles in solution (125). It is also commonly used to characterise vesicle size distributions (10, 77, 78, 86, 88, 126). Previously, the vesicle diffusion coefficients from DLS were typically used to find size and polydispersity information. These coefficients depend on the particle size, temperature sample and solvent viscosity (125).

Macromolecules in solution are buffeted by solvent molecules in Brownian motion. When a beam of light hits the suspension, light scatters in all directions as function of size and shape of the macromolecules. Brownian motion imparts a randomness to the phase of the scattered light giving either constructive or destructive interference. This leads to time-dependent fluctuations in intensity of scattered light, which are directly related to the rate of diffusion of the molecule through the solvent, which in turn is related to the hydrodynamic radius of the particle. How rapidly the light scattering intensity fluctuates is related to diffusion behaviour of molecules: large molecules will diffuse slowly, so will have similar positions over time, while small particles will move much faster and won't have a specific position (125).

The intensity correlation function, $g_2(\tau)$, describes the movement of the particles, and after normalisation, is found by:

$$g_2(\tau) = \frac{\langle I(t)I(t+\tau)\rangle}{\langle I(t)^2\rangle} \tag{2.5}$$

where τ is the lag time between two time points, $I(t)$ is the intensity of the scattered light at time, t. The angle brackets indicate that the values are averaged over all t. This second-order correlation function depends on the shift of a duplicate intensity trace from the original before the averaging is performed.

The precise motion of each particle in a solution is not known, however the movement of particles relative to each other can be found using an electric field correlation function, which when normalised gives:

$$g_1(\tau) = \frac{\langle E(t)E(t+\tau)\rangle}{\langle E(t)^2\rangle} \tag{2.6}$$

where $E(t)$ and $E(t+\tau)$ give the scattered electric fields at time t and $t+\tau$.

Assuming that the photodetector detects only scattered light and that the counting is a random Gaussian process, the first- and second-order correlation functions, $g_1(\tau)$ and $g_2(\tau)$ respectively, can be combined (125):

$$g_2(\tau) = B + \beta|g_1(\tau)|^2 \tag{2.7}$$

where B is the baseline of the correlation function at infinite delay (∼1) (125, 127). The coherence factor, β, is also known as the correlation function amplitude at zero delay and is dependent on optical alignment, and scattering properties of macromolecules.

For particles undergoing Brownian motion, the electric field correlation factor, $g_1(\tau)$, decays. For monodisperse systems, the decay is exponential and dependent on the decay constant, Γ, while in a polydisperse system the decay is a distribution of decay rates (125). A non-linear least squares fitting algorithm can be used to fit the measured correlation function $g_2(\tau)$ shown in Figure 2.6 to retrieve the correlation function decay rate Γ. This decay constant, Γ is directly related to a particles' diffusion behaviour (D_τ):

$$\Gamma = -D_\tau q^2 \tag{2.8}$$

The Bragg wave vector, q, gives the magnitude of the scattering vector and is proportional to the solvent refractive index, n_0:

$$q = \frac{4\pi n_0}{\lambda_0} sin(\frac{\theta}{2}) \tag{2.9}$$

λ_0 is the vacuum wavelength of the incident light, and θ is the scattering angle (125, 127).

From this, the velocity of the Brownian motion and the particle size can then be determined using the Stokes-Einstein relationship:

$$D_\tau = \frac{kT}{6\pi\eta R_h} \tag{2.10}$$

where D_τ is the diffusion coefficient of a spherical particle of hydrodynamic radius R_h in a fluid of viscosity η at absolute temperature T, and k is the Boltzmann constant. The hydrodynamic radius R_h is defined as the radius of an equivalent hard sphere diffusing at the same rate as the molecule under observation, but more closely reflects the apparent size adopted by the solvated, tumbling molecule (125, 127).

Particle motion can then be connected to the measured scattering intensity fluctuations by:

$$g_2(\tau) = 1 + \beta \exp^{2D_\tau q^2 \tau} \tag{2.11}$$

DLS instruments will have a detector at either 90 °or a backscatter detection system at 173 °and 158 °, which is close to the incident light at 180 °. At high scattering angles ($> 90°$) the scattering contributions from rotational diffusion can be ignored and D_τ can be obtained. Backscattering detection would also allow for the measurement of D_τ in highly concentrated solutions as the light passes through a shorter path length, reducing light scattering from one particle being scattered by surrounding particles. The scattering contributions from large contaminating particles such as dust can also be avoided in a backscatter detecting system as these large contaminants scatter light in the forward direction, while smaller particles scatter light in both forward and backward directions (125).

The correlation function in Equation 2.11 has to be fitted in order to understand the information on the diffusion coefficient: the model used is dependent on whether the sample is mono- or polydisperse. In a monodisperse system, the size distribution is Gaussian-like distribution around a mean value, with the decay constant a single exponential function. In this case a cumulant analysis can be used (125, 128).

However for a polydisperse sample, polydispersity index (PDI) > 0.7, the correlation function is a sum of several decay functions with different decay rates so a non-monomodal distribution model is required. Constrained regularization method for inverting data (CONTIN) is a non-linear statistical technique that uses a Laplace transform to fit the correlation function (125). As with any fitting however, over parameterising a model can cause issues. During this research project, a maximum of three size distributions within a sample could be extracted using the CONTIN technique.

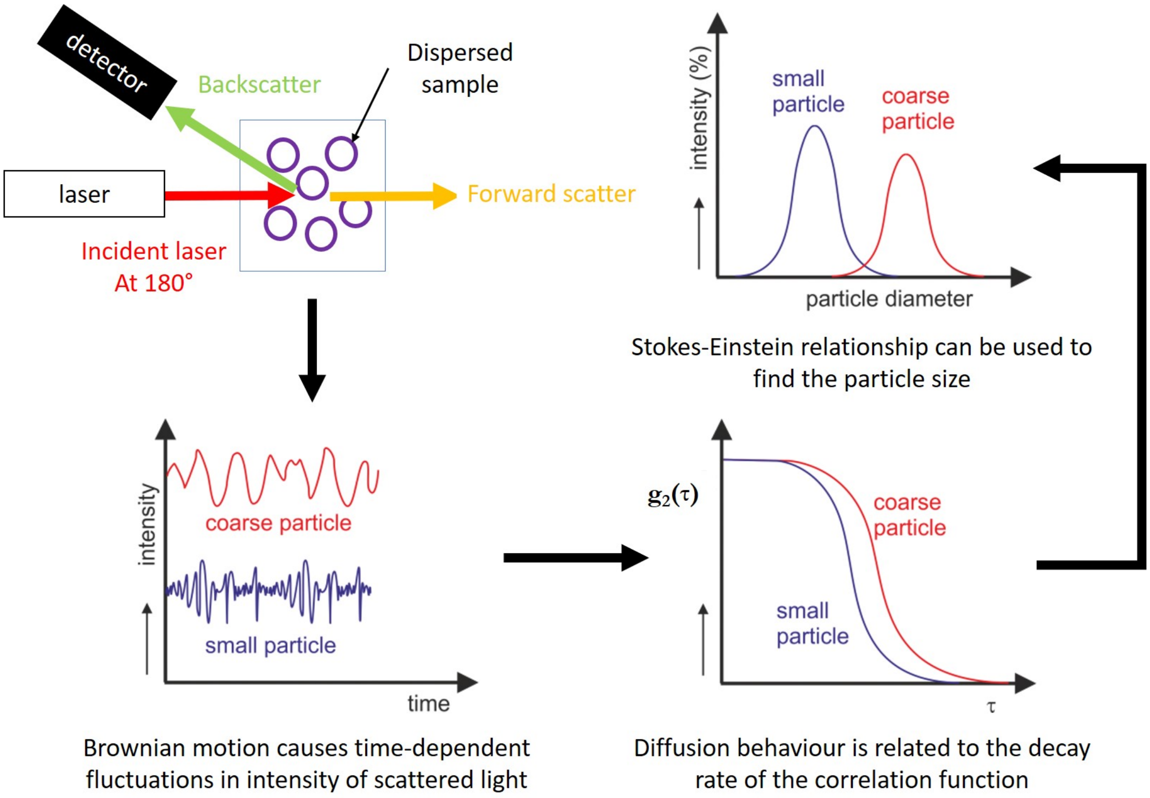

Figure 2.6: Size characterisation from intensity measurements using dynamic light scattering. Laser light is directed to a sample. The particles scatter the incident light, which is detected by photon detectors. Particle Brownian motion leads to time-dependent fluctuations in intensity of scattered light, which is related to the particles' diffusion. Using the Stokes-Einstein relationship, the velocity of Brownian motion and the particle size can be determined.

2.2.2 Small angle x-ray scattering: studying membrane structure

Small angle x-ray scattering (SAXS) is a non-destructive analytical method that can be used to accurately determine the average size and shape of particles in a sample. Applications for SAXS are broad and include structural determination of biological materials, polymers, colloids, nanocomposites, and pharmaceuticals. Unlike microscopy where a small part of the sample is magnified and investigated, in SAXS, the whole sample is illuminated and investigated at once, allowing the average structure to be obtained from all objects at different orientations within the sample. Small features will not be picked up unless they are present in the majority of the sample, and therefore are representative (129). In a typical SAXS set-up, particle sizes from 1 to 100 nm can be resolved, but this range can be extended by measuring at even smaller or larger scattering angles. At larger scattering angles, smaller details such as intermolecular distances are resolved, while at smaller scattering angles, larger particles and self-assembled systems can be observed (129, 130).

In SAXS the sample is irradiated with x-rays. The sample causes a fraction of the incoming x-ray radiation to scatter in all directions, giving rise to background radiation. Particles of clusters of atoms inside the sample will produce additional scattering. Other fractions of the incoming x-rays will either pass through the sample or be absorbed and transformed into other forms of energy (129). For example, in pure water most of the x-rays get absorbed (59%) and some do not interact at all (37%), so only a small number are scattered (4%) (131). To establish contrast, the particles in the sample must have an electron density that is different to the surrounding matrix material. Increasing exposure time and photon flux and using the high photon flux available at the synchrotron, helps improve the signal-to-noise ratio allowing even weakly scattering materials to be investigated (129). In this study, high electron density contrast to water results from the differences between phospholipid head groups and the methyl trough region within the lipid bilayer, and from the oxygen-rich polymer moieties and the hydrophobic core in polymer membranes.

Scattering can occur with or without loss of energy which means the scattering radiation can have either the same wavelength (elastic scattering) or different wavelengths (inelastic scattering) to the incident radiation. In elastic scattering, the electrons in the particles begin to oscillate at the same frequency as the incoming radiation. Due to this oscillation, the electrons emit radiation with the same frequency as the incoming radiation, producing interference patterns at the detector. At the detector, the intensities of the scattered x-rays are observed and the result is the square of all wave amplitudes that come from the sample volume. Only interfering x-rays can carry information on the structure. These interferences can be in-phase and constructive, out-of-phase and destructive, or in between the two, depending on the observation angle 2θ, and the distance between atoms, d. For constructive interference the reflected x-rays of wavelength λ must arrive at the detector in phase, with a path difference of integer multiple n as described by Bragg's law (129, 130):

$$n\lambda = 2d \sin\theta \tag{2.12}$$

Where n is the order of reflection ($n = 1, 2, 3...$), d is the distance between lattice planes, and 2θ is the scattering angle (130) as shown in Figure 2.7. Constructive interference causes intensity peaks on the scattering pattern, while destructive interference produces zero intensity regions. The resulting 2D interference pattern varies in intensity from position to position in terms of scattering angle 2θ and relative distances between atoms in the sample (129, 130).

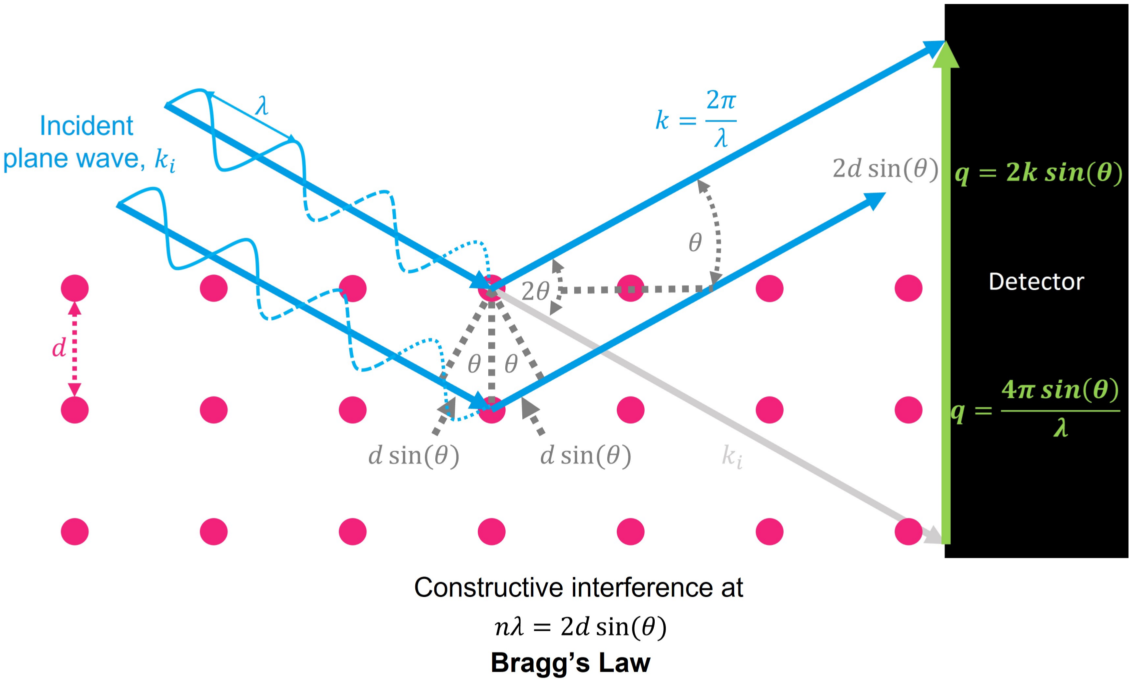

Figure 2.7: Bragg's law. Bragg's law states that when an incident x-ray hits a crystalline surface, its angle of incidence, θ , will be reflected at the same angle. Constructive interference will only occur when the path difference, $2dsin(\theta)$, is equal to a whole number, n , of wavelength λ. The incident beam k_i is scattered by a particle in solution. The scattered beam, k of wavelength λ is recorded by the detector and the scattering vector, q, is found from the scattering angle, 2θ.

Every distance is measured relative to the wavelength of the incoming radiation. To become independent from the wavelength, scattering patterns are commonly presented as functions of the scattering vector, q:

$$q = \frac{4\pi}{\lambda}\sin(\theta) \tag{2.13}$$

Scattering patterns show the structure in reciprocal space, so scattering vector q has dimensions nm^{-1}. The scattering pattern contains shape and density distribution information of the particles expressed as the square of the form factor, $F(q)$, and carries information about particle-particle interactions, which relates to the structure factor contribution, $S(q)$ (129).

If the particles in the sample are monodisperse in shape and size, and the sample is dilute, then the 2D scattering pattern corresponds to the product of the number of particles and their unique form factor only. In polydisperse samples, the scattering pattern is the sum of all the form factors of all particle sizes in the sample (129).

If the sample is concentrated, then the relative distances between particles is small enough that the particle scattering begins to interact with each other. This results in an additional interference pattern, known as the structure factor contribution, $S(q)$, and multiplies with the form factor squared to give the final scattering pattern.

$$\Delta I(q) \propto \frac{|F(q)|^2 S(q)}{q^2} \tag{2.14}$$

In the case of dilute system, $S(q) = 1$ so

$$\Delta I(q) \propto \frac{|F(q)|^2}{q^2} \tag{2.15}$$

A SAXS signal can be optimised by increasing the illuminated sample volume (scattering volume). However, samples that are too thick are undesirable due to the increased sample absorption, so to increase the scattering volume the beam dimensions can be widened, and the sample set to optimum sample thickness. For a given wavelength, the optimal sample thickness, t_{opt}, depends entirely on how easily the x-ray can penetrate the sample, which is characterised by the attenuation coefficient, μ_{sample} (131):

$$t_{opt} = \frac{1}{\mu_{sample}} \tag{2.16}$$

Most soft matter has an attenuation coefficient close to that of water, leading to an optimum sample thickness of 1 mm for water-based samples at $\lambda = 1.54$ Å (131).

Usually during a SAXS experiment of particles in a water-based suspension, scattering intensity curves of both the sample (particles within the matrix) and the matrix material in a cell are obtained. If the sample and the matrix have the same transmittance, $T_S = T_W$, where transmittance is the ratio of transmitted versus incident x-rays, then the scattering intensity from the water matrix can merely be subtracted from the sample to retrieve the scattering pattern from just the particles in the sample. If a material does not absorb x-rays, then transmittance is 1. However, if particles in the matrix (sample) absorb more than the matrix, $T_S < T_M$, then the scattering intensity of the sample will be reduced. Therefore the scattering intensity curves must be scaled by their respective transmittance values (129).

Measured intensity curves from the scatting pattern of particles in suspension will contain contributions from the particles, as well as the water and the cell. After normalisation, the empty cell scattering intensity I_C is subtracted from the sample scattering intensity, I_S and water scattering intensity I_W as follows:

$$I_S = \frac{I_{S+C}}{T_{S+C}} - \frac{I_C}{T_C} \tag{2.17}$$

$$I_W = \frac{I_{W+C}}{T_{W+C}} - \frac{I_C}{T_C} \tag{2.18}$$

where I_{S+C} and I_{W+C} are the scattering intensities from the sample and water and T_{S+C} and T_{W+C} are the transmissions from the sample and water, respectively (132). To retrieve the scattering from the particles only intensity, the scattering intensity of water I_W must be subtracted from the sample scattering intensity, I_S:

$$\Delta I(q) = I_S – I_W \tag{2.19}$$

To do this accurately however, variations in sample thickness must have been controlled. If the samples are also not dilute the excluded water volume has to be taken into account when applying Equation 2.19: for instance, from a 20 volume% dispersion only 0.8 I_W is subtracted from the sample scattering I_S. The resultant intensity curve can then be fitted with a model. However, the x-ray scattering pattern might be able to be fitted with an ensemble of different solutions, not all of which fully represent the particle structure, thus, any a prior knowledge of the sample structure is helpful in order to apply the most appropriate models when fitting the scattering curve.

Functionality in biological membranes strongly depends on the chemical properties and amphiphile geometry that make up the bilayer. Amphiphile organisation into membranes, and the resultant membrane permeability is dependent on the internal arrangement of the amphiphiles, so the electron density profile is an important parameter to know (129). SAXS is one of the best methods for determining bilayer thickness of lipid membranes in near-native conditions, providing information on the hydrocarbon chain region thickness of a membrane (130). Phospholipid bilayer membranes such as POPC, DOPC and DPPC have been extensively studied using SAXS to determine the electron density across their membranes, the bilayer thickness as well as fatty acid packing (133) and the membrane bending modulus (134).

The membrane electron density distribution can be found by performing a Fourier transform on the form factor $F(q)$. Membrane electron density profiles are commonly modelled by a strip-model, as shown in Figure 2.8. Using the "Bilayered Vesicle" model from the SASfit analysis program (135), the form factor, $F(q)_{BLV}$ for a unilamellar vesicle is given by:

$$\begin{aligned} F(q)_{BLV} =& (+K(q, R, \rho_W - \rho_C) + K(q, R + t_H, \rho_C - \rho_H) \\ &+ K(Q, R + t_H + t_C, \rho_H - \rho_C) + K(q, R + 2t_H + t_C, \rho_H - \rho_W)) \end{aligned} \tag{2.20}$$

With

$$K(q, R, \Delta\rho) = \frac{4}{3}\pi R^3 \Delta\rho 3 \frac{sin(qR) - (qR)cos(qR)}{(qR)^3} \tag{2.21}$$

Where R is the vesicle core radius, t_H is the thickness of the outer regions of the bilayer (headgroups), t_C is the thickness of the inner part of the bilayer (tail groups), ρ_W is the electron density of the matrix, ρ_H is the electron density of the head groups, and ρ_C is the electron density of the tail groups (136).

Previously the electron density profiles of fluid lipid bilayers have been modelled by a symmetric 3-Gaussian form factor, with two distinct Gaussians: one Gaussian representing the polar head groups at $\pm z_H$ and another Gaussian for the methyl groups at the centre of the lipid bilayer. The widths of the Gaussians representing the polar head groups and methyl trough are given by σ_H and σ_C, respectively. The fraction of the negative methyl group amplitude against the head group amplitude gives the minimum/maximum electron density contrast ratio, given as $\rho_R = \rho_C/\rho_H$. The water density can be set to zero, and since the electron density of the head group and the hydrophobic core are linear dependent, ρ_H can be set to 1 so only ρ_R can be used as a fitting parameter for the electron density. The following electron density profile has been used as a model for a pure lipid membrane:

$$\rho_{2G} = \exp(-\frac{(z - z_H)^2}{2\sigma_H^2}) + \exp(-\frac{(z + z_H)^2}{2\sigma_H^2}) - \rho_R \exp(-\frac{z^2}{2\sigma_C^2}) \tag{2.22}$$

The Fourier transform for this 2-Gaussian model gives the form factor, $F_{2G}(q)$, that can be used to fit the scattering intensity curves:

$$F_{2G}(q) = 2\pi(2\sigma_H \exp(-\frac{\sigma_H^2 q^2}{2}) \cos(qz_H) - \sigma_C \rho_R \exp(-\frac{\sigma_C^2 q^2}{2})) \tag{2.23}$$

This 2-Gaussian model can be made more complex by expanding to 3, or even 4-Gaussians and potentially also account for asymmetry (137) or other features within the membrane. For this symmetric 4-Gaussian model, the model can again be reduced to two Gaussians, where one Gaussian is used to represent the hydrophilic region at $+z_H$ and $-z_H$ of width σ_H, and the the hydrophobic core region is represented by two Gaussians at $\pm z_C$ with width σ_C. The minimum/maximum electron density contrast ratio here is given by $\rho_R = \rho_C/\rho_H$. The following electron density profile of a polymer membrane:

$$\begin{aligned}\rho_{4G} =& \exp(-\frac{(z-z_H)^2}{2\sigma_H^2}) + \exp(-\frac{(z+z_H)^2}{2\sigma_H^2}) \\ &- \rho_R \exp(-\frac{(z-z_C)^2}{2\sigma_C^2}) - \rho_R \exp(-\frac{(z+z_C)^2}{2\sigma_C^2})\end{aligned} \tag{2.24}$$

The Fourier transform for the 4-Gaussian electron density profile gives the form factor $F_{4G}(q)$:

$$\begin{aligned}F_{4G}(q) =& 2\pi(2\sigma_H \exp(-\frac{\sigma_H^2 q^2}{2}) \cos(q z_H) \\ &- 2\rho_R \sigma_C \exp(\sigma_C \exp(-\frac{\sigma_C^2 q^2}{2}) \cos(q z_C))\end{aligned} \tag{2.25}$$

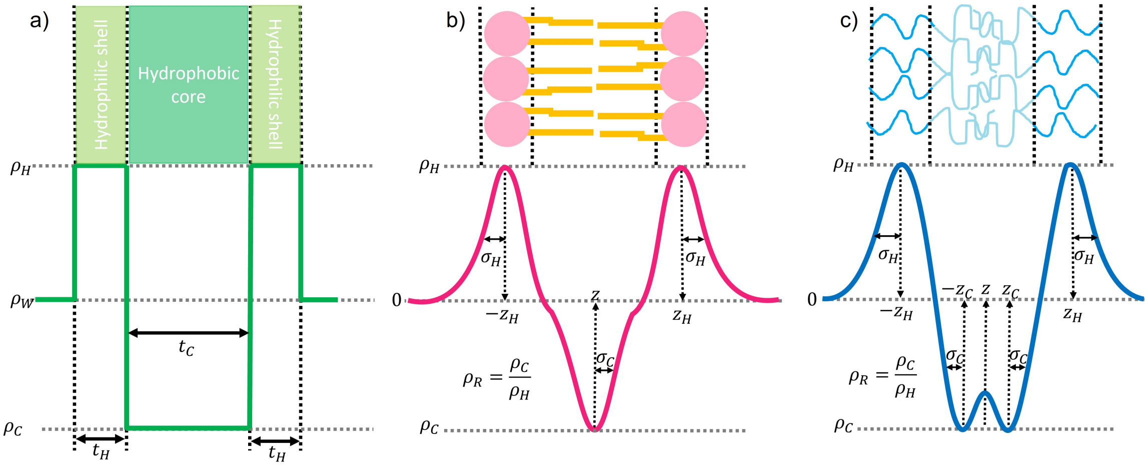

Figure 2.8: Electron density profile models from SAXS scattering patterns. The electron density profile of a lipid bilayer can be retrieved from scattering intensity curves obtained by SAXS. The curves can be fitted with either a a) strip-model as used in SASfit program or b) 2-Gaussian model. The 2-Gaussian model can be expanded into a c) 4-Gaussian model. The electron density profiles provide valuable insight into the structure of the membrane.

2.3 Electron microscopy

Transmission electron microscopes (TEM) allow the observation of very small samples that cannot be viewed using light or optical techniques such as confocal microscopy. The resolution of electron microscopes can go to 4 Å , while optical microscopes can only resolve to 2000 Å (138) because the resolution in traditional light microscopy is limited by the diffraction of light. While super-resolution optical microscopy can push the 2000 Å barrier, the resolution is still limited compared to electron microscopy. While electrons also have wave-particle duality, accelerated electrons have much smaller wavelengths than light (139), so are able to permeate between molecules. The resolution of the electron microscope has been improved over time with the development of electron sources that produce electron beams with smaller energy spreads and greater coherence (140). The energy of the accelerated electron can be used find the wavelength of the electron and therefore the resolving power of the microscope by using the de Broglie Equation 2.27.

$$E = \frac{1}{2}mv^2 \tag{2.26}$$

$$\lambda = \frac{h}{mv} \tag{2.27}$$

$$\lambda = \frac{h}{(2mE)^{\frac{1}{2}}} \tag{2.28}$$

In transmission electron microscopy (TEM), a parallel coherent beam of electrons is emitted from an electron gun through a sample grid contained in a chamber under high vacuum (140). As electrons are charged particles they can be focused using electromagnetic lenses that direct the electron waves towards the plane of the object (139, 140). This incident electron beam is a time-independent object wave with the equation

$$\psi(k) = A(r)e^{i\phi(r)} \tag{2.29}$$

where ψ denotes the wave function of the electrons, $A(r)$ is the amplitude of the wave in real space, and $\phi(r) = \frac{2\pi}{\lambda}$ is the wave vector in real space.

When the electrons pass through the sample they interact with the local atomic potential of the sample, which modifies the electrons' phase and produces scattering events (140). Electrons can interact with the sample in a variety of ways as shown in Figure 2.9. Phase contrast occurs when electron waves interfere with each other, while absorption of electrons or exclusion of scattered electrons results in intensity contrast in the projection image (141). Elastic interactions are when the electrons interact only slightly with the sample and deviate from the path a small amount giving rise to phase contrast (140). The interaction between the incident electron wave and the sample is modelled as the sum of atom and bond contributions:

$$v^{int}(r) = v_{atom}(r) + v_{bond}(r) \tag{2.30}$$

$$v_{atom}(r) = \Sigma_{j=1}^{m} v_{z_j}(r - R_j) \tag{2.31}$$

where $r = (x, y, z)$ is the position of the electron wave, v_{z_j} is the electrostatic potential of an isolated neutral atom with atomic number Z_j centred at R_j (142).

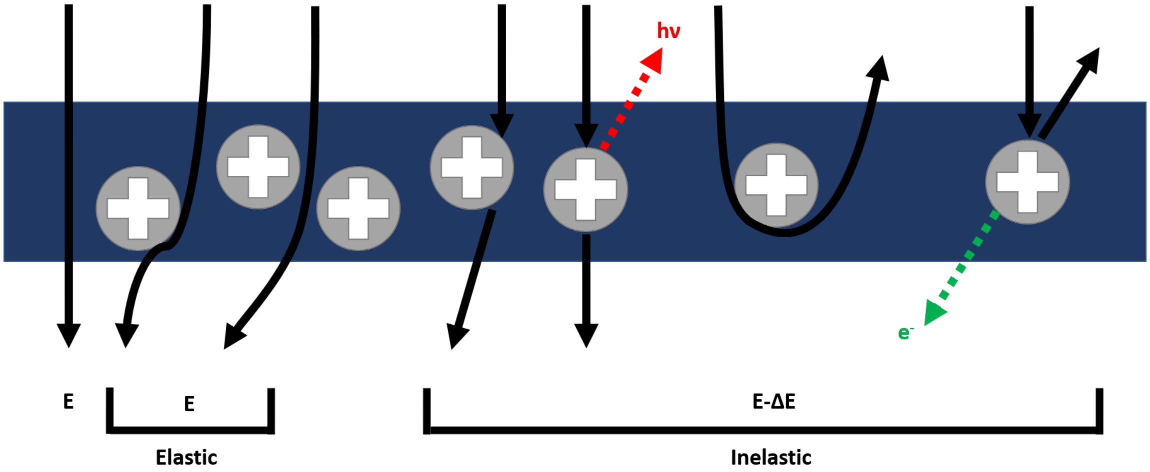

Figure 2.9: Electron scattering events. Electrons interact with the sample to produce elastic and inelastic scattering events.

Inelastic scattering occurs when the electrons collide directly with the sample resulting in either: energy deposited within the sample, thus causing radiation damage to the sample, ultimately destroying it; or energy being lost to the environment, causing a blurry image to be formed (140). Extensive damage results from electron-sample interactions as electron irradiation leads to the breaking of bonds and creation of free radicals, which can cause even further damage (138). This knock-on damage can be reduced if the accelerating voltage for the electrons is below the threshold for the given material (140). The amount of radiation damage increases rapidly as the microscope resolution is increased or as the specimen volume irradiated is decreased (139). Inelastic scattering is modelled as the imaginary part of the interaction potential:

$$v_{tot}^{int} = V_{ph} + iV_{ab} \tag{2.32}$$

where V_{ph} is the interaction potential that contributes to the phase contrast while V_{ab}

accounts for influences on the amplitude contrast.

Different features in a sample vary in electron potential (143). The electron wave that propagates through the sample is described by

$$\psi_{n+1} = \mathcal{F}^{-1}[P_n * \mathcal{F}(e^{i\sigma V_z}) * \psi_n] \tag{2.33}$$

where ψ_{n+1} is top plane of the specimen, $P_n = e^{-i\pi\lambda\delta z k^2}$ is the Fresnel propagator over a slice of thickness δz, k is the spatial frequency and V_z is the projected potential within a slice. When there is no sample in the path of the electrons, the incident plane wave is modelled by $\psi_0 = 1$ The propagation of the electron through each slice of the sample until the wave leaves the grid is ψ_{exit}(142).

When the electron wave exits the bottom surface of the grid, it contains information about the projected potential of the sample. This information is Fourier transformed by the objective lens to form an image so Equation 2.29 becomes

$$A(r) = \frac{1}{\sqrt{2\pi}} \int_{-\infty}^{\infty} \psi e^{-i\phi(r)} dx \tag{2.34}$$

The information undergoes a contrast transfer function (CTF), which measures the defocus of the image. The intermediate lens switches between imaging and diffraction modes and then the information is Fourier transformed back into Equation 2.29 by the projector lens, which magnifies the image. Obtaining the final image involves converting the electron wave intensity distribution into a digital signal by the detector.

A detector records the square magnitude, or intensity, of the transmitted electron wave (140, 144). The intensity in the image plane is the probability density function (142):

$$I_0 = \mid \mathcal{F}^{-1}[\mathcal{F}(\psi_{exit})CTF] \mid^2 \tag{2.35}$$

where I_0 is the intensity, ψ_{exit} is the electron wavefunction as the electron is emerging from the bottom surface of the grid, and $\mathcal{F}$ and $\mathcal{F}^{-1}$ represent Fourier transform and its inverse.

Charge coupled device (CCD) detectors and direct electron detectors (DED) can both be used to screen grids for desired features (145). However, while low dose sensitive CCD detectors are designed specifically for biological specimens, they are easily damaged by higher energy electrons. When the electrons hit the phosphor screen of the CCD, the incident electrons are either converted into photons, or are scattered which causes the information between the image pixels to become blurred. Using a DED produces a higher resolution and contrast image as the electrons are detected without the use of a phosphor screen (140, 145). The entire process must be kept under a high vacuum to prevent the high energy electrons from interacting with particles in the air within the chamber, giving a low signal-to-noise ratio (SNR).

The accuracy of the structure deduced from an image does improve as the resolution increases and structures of defects can then be examined individually(139). However, increasing the resolution does expose the sample to a greater dose of electrons, which can cause radiation damage, especially in biological macromolecules (140).

2.3.1 Cryogenic transmission electron microscopy: imaging vesicles

Many investigations into hybrid lipid-polymer vesicles use cryogenic transmission electron microscopy (cryo-TEM) rather than standard TEM to observe and confirm vesicle size and shape (1, 77, 86, 73, 88, 91, 93, 98, 99) as cryo-TEM allows samples to be examined in their hydrated native state.

Samples are fixed into their position by rapid freezing with liquid ethane, as shown by Figure 2.10 and then transferred to liquid nitrogen for storage (146). As the sample is embedded in buffer, potential artefacts from dehydration and chemical fixation are less likely to occur. Although biomaterials will exhibit low contrast as the scattering densities of the biomolecules and the solvent are similar, the image contrast can be enhanced by defocusing the image (140). This means that biological macromolecules can be viewed in their active state, which enables the study of complex biological systems. As the sample is frozen, the rate of radiation damage is also reduced from the low temperatures (140).

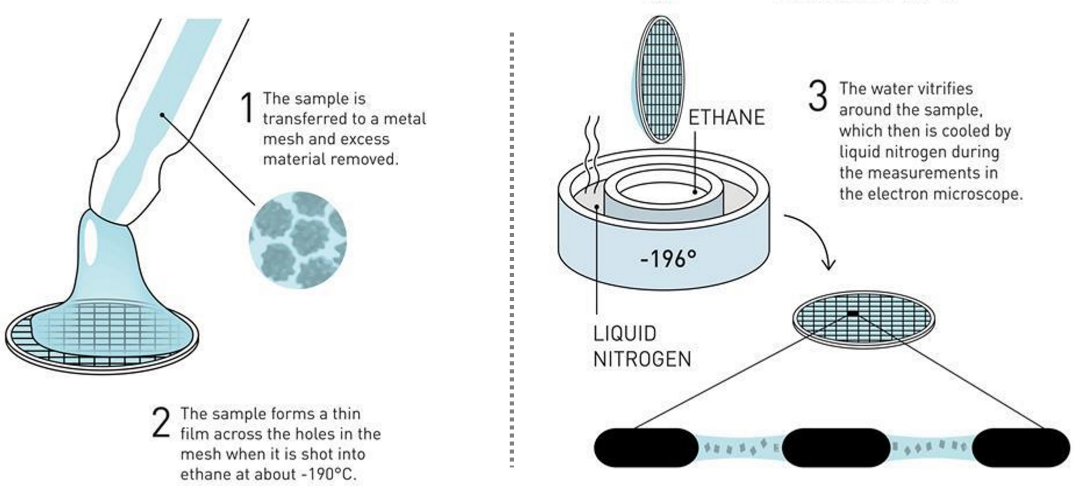

Figure 2.10: Vitrification method. The sample is placed onto a carbon coated metal grid and plunged into liquid ethane where the water vitrifies. The objects are fixed in the vitrified ice and can then be imaged using a cryogenic electron microscope. Image adapted from (146).

While resolving power has improved since the conception of electron microscopy, the resolution is limited by the dose that can be delivered to the sample before it becomes damaged by radiation, resulting in poor signal to noise. Biological samples can only withstand low doses, which reduces the resolution, whereas higher doses can be delivered to materials like metal, which gives rise to a greater resolution.

However resolution is also affected by physical lens aberrations. To overcome this, the accelerating voltage can be increased to reach small electron wavelengths, as shorter wavelengths give a higher attainable resolution (138), or corrections to the lens aberrations can be made. The lenses are needed to change the direction of the electron wave towards the plane of the object - an imperfect lens will cause the image plane to shift, adding an extra phase shift to the resultant image as shown in Figure 2.11.

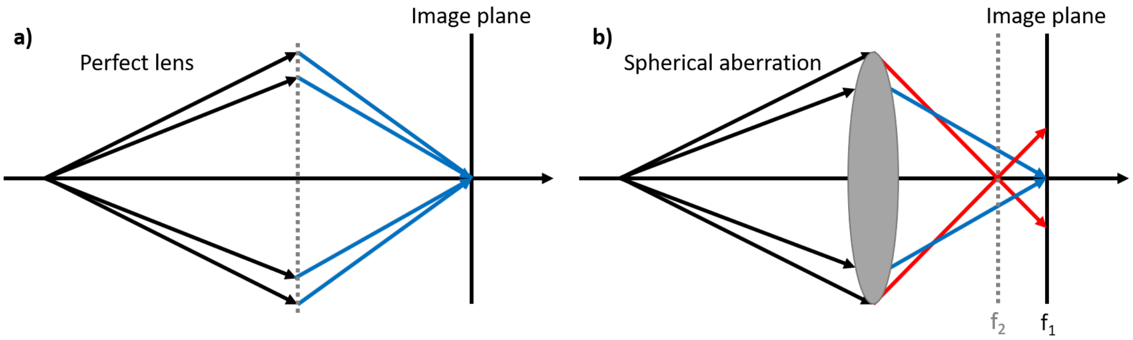

Figure 2.11: Spherical aberration in lenses. To change the direction of the wave, lenses are needed to focus the waves towards the plane of the object. For a) perfect lenses, incoming rays are focused to a single point, whereas for lenses with b) spherical aberrations, this will cause the image plane to shift and the incoming rays are focused to different points on the optical axis. This adds an extra phase shift.

Generally, biological specimens are comprised of light atoms that interact very weakly with electrons (138, 139, 140) so they only cause a weak phase shift in the incident electron beam resulting in low amplitude contrast. To generate amplitude contrast to see features in the specimen, a defocus is applied, which converts the weak phase shift into an amplitude varying signal by spreading the information from every position into adjacent sections of the image (140) as shown in Figure 2.12. Applying a small defocus (< 0µm) counters the effects of the spherical aberration, generating a larger phase shift between scattered and unscattered electrons, culminating in a stronger image contrast. The effect of the spherical aberration on the measured defocus is given by

$$\Delta z = C_s \beta^2 \tag{2.36}$$

where Δz is the defocus, C_s is the spherical aberration and β is the beam tilt angle. The defocus can be estimated by measuring the contrast transfer function (141).

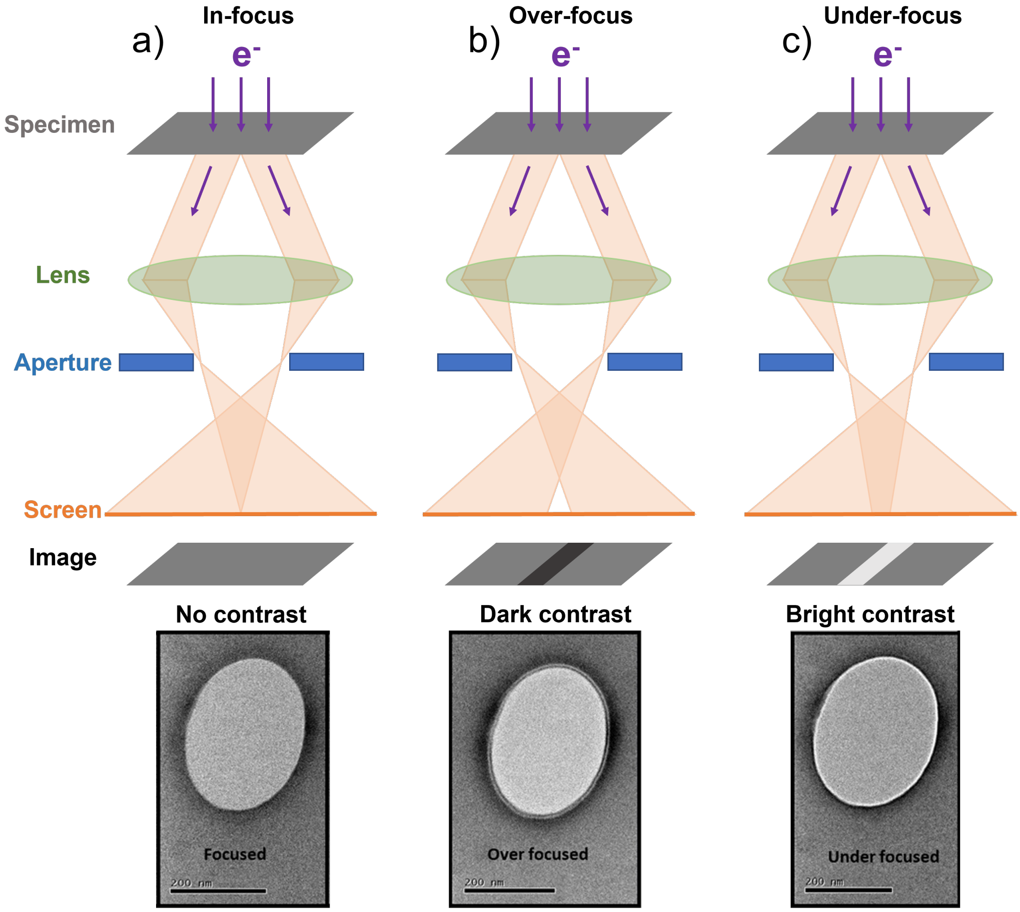

Figure 2.12: Focus conditions in an electron microscope. When correct focus a) is applied the deflected electrons are focused in the image plane so no contrast appears. In over focused conditions b) the aperture is small, leading to dark contrast, while in defocused conditions c) the electrons pass through a wide aperture and overlap near the detector, giving bright contrast. Scale bars indicate 2000 Å. The image was adapted from (147) and (148).

The contrast transfer function (CTF) mathematically describes how aberrations in TEM modify the image of the sample, providing a method to translate the exit wavefunction to a final image. CTF is an oscillating function with decreasing amplitude and increasing frequency showing how contrast generated varies with image resolution (140). The CTF is the Fourier transform of the point spread function (PSF) (144) and is described by

$$CTF(k) = E(k)sin(\pi\frac{1}{2}C_s\lambda^3k^4 - \pi\lambda\Delta zk^4) \tag{2.37}$$

where C_s is the spherical aberration coefficient, Δz is the applied defocus (negative for underfocus), k is the spatial frequency, λ is the electron wavelength and $E(k)$ is an envelope function describing high-resolution information degradation (149).

Depending on the defocus, certain features of the sample will appear enhanced or blurred in the image. This is because the CTF oscillates as the spatial frequency increases. Therefore the exact value of the zero crossings, where no contrast is transferred and information is lost, depends on the defocus setting. The CTF value is ideally held constant for all spatial frequencies however due to spherical aberrations, image drift, and ice thickness, the absolute value of CTF becomes less than one and is not held constant and fluctuates greatly at higher frequencies (150, 151) as shown in Figure 2.13.

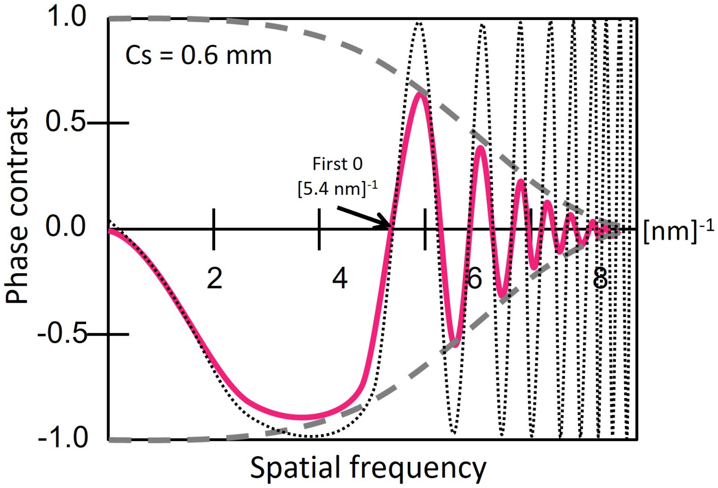

Figure 2.13: Contrast transfer function with spherical aberrations. Ideally the CTF is held constant for all spatial frequencies (black dotted line). However due to spherical aberrations, image drift, and ice thickness, the absolute value of CTF is damped by an envelope function (grey dashed line) resulting in the CTF fluctuating at higher frequencies (pink line). Image adapted from (152).

For high resolution three dimensional microscopy these effects have to be computationally corrected so the information returns to their initial position. Structural information of a specimen is transferred without contrast reversal until the first zero point, so the inverse of the frequency at this first zero gives the resolution of the structure in the image (140).

The CTF correction is shown in Figure 2.13, where the ideal CTF is corrected by using a damping envelope to obtain the true CTF.

Since the image contrast of biological specimens is very low, a high defocus condition is often used in order to observe the overall shape of macromolecules during data acquisition: the more defocus applied, the greater the micrograph contrast. However increasing the defocus reduces spatial resolution so a compromise between resolution and contrast has to be made. The defocus value is chosen when the frequency at the first minima of the CTF is higher than the targeted resolution (140).

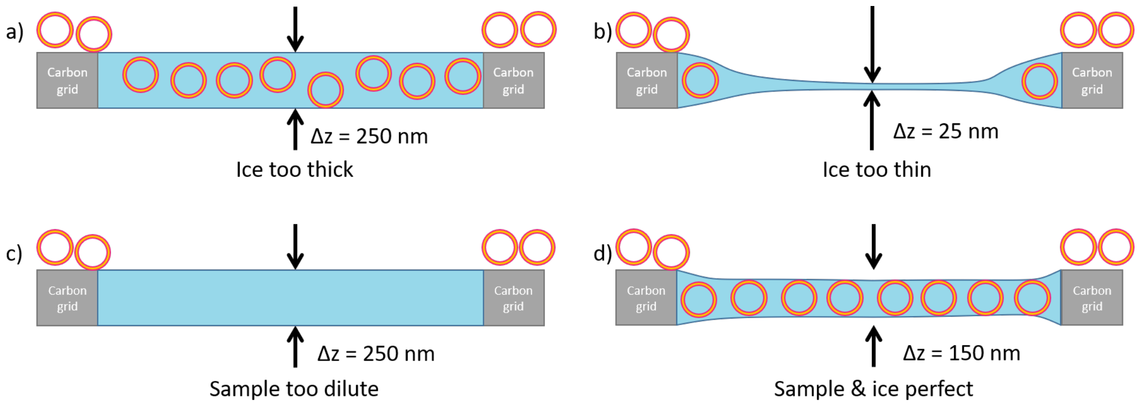

Figure 2.14: Ice thickness in cryo-TEM grids. If a) the ice is too thick the resultant images will be dark as no features can be seen. If b) the ice is too thin, the sample will wick to the sides of the carbon film, and radiation damage is more likely to have an effect. When c) the sample is too dilute there will be no sample in the grid holes. However, when d) there is a sufficient volume of ice and the sample is not too dilute, the ice will enclose the sample.

Artefacts are also inherent from data collection and data analysis methods making it difficult to identify features objectively. In cryo-TEM misleading artefacts are usually caused by the vitrification process and resulting thickness variation. Variations in thickness can sort the macromolecules by size, concentrating the larger molecules in thicker regions. This means that where the ice is thin, macromolecules protrude from the ice resulting in increased contrast in the corresponding area.

Macromolecules can also deform during grid preparation, which is caused by drying and accompanied increase in salt or osmolality as well as from an increase in surface tension from water flattening. Blotting is suggested to have no effect on sample composition or appearance but for this to be true the humidity and temperature have to be tuned to avoid drying and swelling of the sample during or after blotting (145). Electrons interact strongly with matter, therefore, in order to obtain sub-nanometre resolution as well as reduce the incident electron-sample interaction during electron transmission, the samples must also be dilute when applied to the grid (140). The grids prepared must be thin to prevent features from overlapping in the projected image. Thin ice also allows the sample to be seen in the microscope - if the ice too thick, the grid appears dark and no features can be seen (140).

The principles of cryo-TEM are the same as for TEM. However, as the specimen is fixed in a buffer, it is possible to determine the morphology of a macromolecule by taking multiple images of the specimen in its frozen state. There are four methods to obtain this 3D density map from 2D projections: single particle analysis SPA, tomography, diffraction and helical reconstruction.

The 2D images produced by the microscope are projections from the 3D structure of the sample. The third dimension is necessary to determine the functions of many structures, which is why 3D reconstruction techniques using 2D images were developed. The Fourier slice theorem is usually used to reconstruct 3D structures from 2D images. A 3D density map comprised of n^3 voxels has an equivalent Fourier transform, which is also an n^3 array of numerical values. The Fourier transform of the 3D density map contains all the information of the original map (153). The theorem states that if a projection image is obtained by projecting a 3D density map along a particular direction, then the values of the Fourier transform of that image will be identical to the Fourier transform of the 3D density map on a slice through that Fourier volume; the slice is taken on a plane that passes through the Fourier volume origin and is normal to the initial direction (153). This means that the Fourier transforms of a series of real space projections acquired at many angles can be used to fill in the objects' 3D Fourier transform, which is then inverted to produce a 3D reconstruction of the original object in real space (140).

2.3.2 Cryogenic electron tomography: 3D reconstruction

In cryo-ET, the specimen grid is tilted around a fixed eucentric axis from one extreme tilt angle to another while a series of 2D images at low electron doses are acquired at defined tilt increments. While it is possible to tilt 90° with specific microscopes that can image capillary tubes, for most TEM, the maximum tilt angle accessible is ± 70° (140) due to the shadowing of the specimen holder and space limitations in the specimen chamber.

All the images are then aligned and combined digitally to produce a representation of the original object. The resulting reconstruction consists of voxel intensities exhibiting the 3D distribution of the measured specimen. To do this requires the projection requirement to be fulfilled: image intensities must consistently provide monotonic measurement of a property of the sampled volume in every tilted projection (153). Reconstruction from a single axis tilt series exhibits anisotropic resolution because tomography inherently undersamples the object's structure. Resolution along the imaging axis perpendicular to the tilt axis is reduced due to the discrete number of projections acquired (140).

Alignment of low dose tilt images allows an accurate 3D reconstruction to be made. The missing wedge and artefacts in tilting have the biggest effects on the resolution. To fill in the wedge, larger rotation angles are required however the space between the focusing lenses near the sample and the sample holder do not allow for this. The missing information leads to distortion and elongation along the z-axis, but this can be corrected for by subtomographic averaging of repeated features within a tomogram. One solution would be to rotate the sample 90 °and then take another tilt series so the missing wedge is reduced to a missing cone of information (140). As the electron dose has to be limited to avoid sample damage, the signal to noise ratio of tomograms is low. This means that while larger features can be recognised, smaller macromolecules do require subtomogram averaging (145).

Fiducials are heavy metal markers that are applied to the sample to provide high contrast reference points for the determination of angles and positions in tilt images. Computational methods include cross correlation which calculates the coefficients among the tilt images. However this method depends on having a high density object in the image so for low contrast imaging, alignment using this method has a low accuracy (140).

ET is more tolerant of overexposure than single particle analysis because ET usually targets a lower resolution and the exposure is applied at a lower dose over a longer time(140). The severity of radiation damage is affected by sample temperature. Rate of reaction and molecular motion are influenced by the temperature so by combining ET with cryo-TEM it follows that low temperatures can slow down radiation damage. Although cooling does not entirely eliminate radiation damage it can reduce the motion of irradiated molecules. An exposure of 30-40 e^{-} Å^{-2} could generate bubbling caused by radiation damage from electrons in areas that are covered in very thin ice (1-30 nm). The areas with large volumes of ice suspended across a hole in the film bubble less. Additionally, large layers of ice provide an evenly flat sample area, which imparts a more even background contrast during tilting (140).

Phase plates can be used to enhance the contrast of a low dose image by introducing a phase shift between the scattered and unscattered waves at a diffraction plane. A Volta phase plate (VPP) is a continuous amorphous film which interacts with the central diffraction beam to create a phase shift. However the phase shift is not constant and increases proportionally to the accumulated dose, which has to be taken into account with acquiring images (141).

Limitations of ET are the resolution, the requirement of high defocus settings and the presence of detector noise. Issues with the sample itself like solvent background, stain effects, temperature related drift and sample surface charging can also lower the quality of the recorded images (140). During tilt series acquisition the sample stage suffers from various mechanical vibrations induced by gears motors and thermal expansion. As a result, the specimen central position (x,y) and the eucentric height (z) cannot be fixed throughout the collection of the tilt series. Automated data collection software attempts to compensate for these imperfections through computer algorithms by using a reference image before recentering the specimen for the next tilt image acquisition (140).

Large scale image distortion can limit the accuracy in determining the geometrical angles when using the whole image. Distortion can be induced by defocus, astigmatism, projector lens and the energy filter. This can then induce more errors when the structures are located near the edges of the images (140). As the tilt angles are usually limited, the structures reconstructed from the projection images tend to have a lower resolution in the z-direction (145). Missing information in Fourier space from the incomplete tilting scheme in real space distorts the features along the projection direction in the final reconstruction. Obtaining projection images at the highest tilt angle possible minimises the effect of this missing wedge information (140). Transforms can be used instead to reduce this distortion.

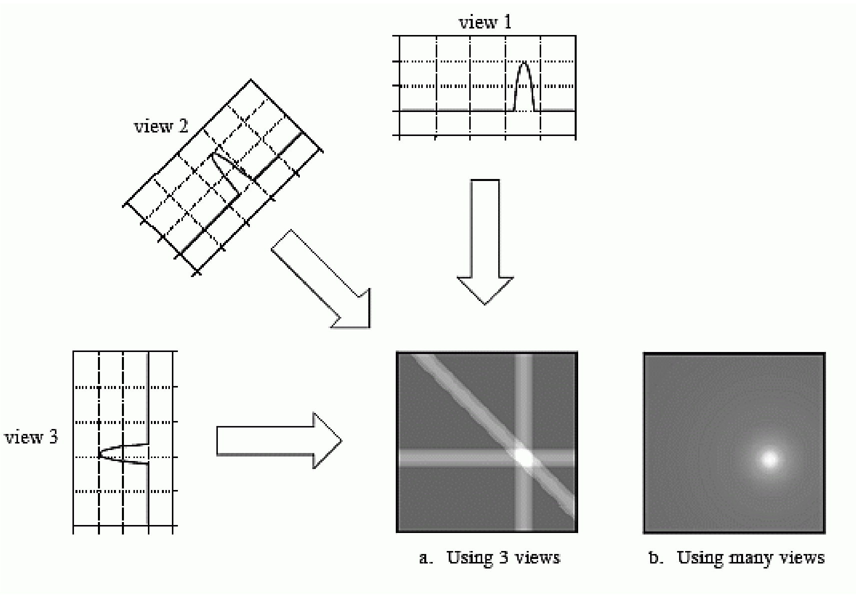

Figure 2.15: Tomogram generation by back projection method. A back projection is formed by following each view back through the image at the angle it was initially acquired. Image taken from (154).

The real space Radon transform is an alternative to Fourier transform. A forward Radon transform maps the 3D object into a 2D plane by calculating the line integrals (projections) of the objects density though all directions parallel to a given axis as shown by Figure 2.15. This means that incoherent electron scattering can be considered as a line integral of the specimen's density. All projection information is independent to the pixels perpendicular to the tilt axis and independent from neighbouring pixels because an object is rotated around a single axis. Radon transform is also known as back projection because the projected intensity in each pixel of a projection is linearly added into a 3D volume along a ray at the correct angle to build up 3D density. Both forward and inverse Radon transforms are performed completely in real space (140).

While back projection via inverse Radon transform avoids Fourier transforms and the errors associated with interpolation steps, using back projection typically gives blurred features (154) because the low frequency information near the zero-point of the axis is oversampled, or under sampled at high frequencies (140).

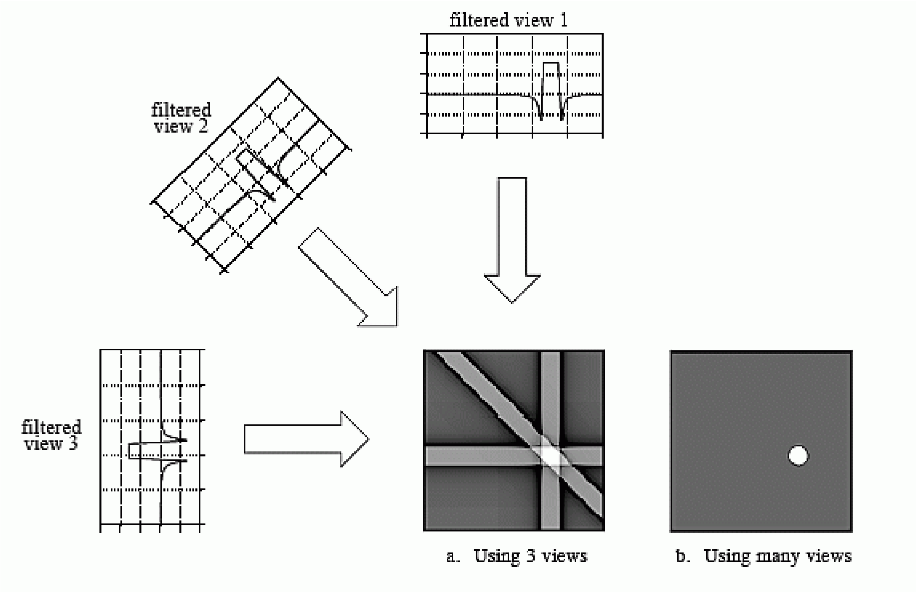

Figure 2.16: Tomogram generation by filtered back projection method. In filtered back projection, each view is filtered before back projection, reducing the blur otherwise seen in simple back projection. Image taken from (154).

Simultaneous iterative reconstruction technique (SIRT) iteratively improves the agreement between reconstructions and experimental projections: first, a trial tomogram is generated and images are superimposed at the stated angles and then the tomogram is adjusted for the differences between the original and the new projection positions. This reduces the production of reconstruction artefacts resulting in a reconstruction with low noise and high contrast. After 20-30 iterations the quality of the reconstruction decays. SIRT can be combined with back projections to give a weighted, or filtered, back projection. A linear relationship between projected density and image intensity is assumed.

Weighted back projection (WBP) combines the reconstruction with a radial weighting filter with an amplitude that increases linearly and is applied after the real space back projection. The filter smooths the uneven sampling distribution in Fourier space. This method is simple to use, quick and highly parallelisable but it does not take full advantage of the input data to refine the final reconstruction and also assumes a linear relationship between the projected density and image intensity (140).

Filtered back projection is similar to WBP however this method reconstructs the image by filtering each view before back projection as shown by Figure 2.16 (154).

2.3.3 Fourier transformations: obtaining a scattering profile from images

A scattering profile can be obtained from cryo-ET slices by using FIJI to perform a fast Fourier transform (FFT). Fourier transformation of a projection image produces an scattering pattern for the object from which a scattering curve can be extracted by taking a radial profile. The scattering profile obtained from the FFT image is comparable to the scattering curve of the object obtained using SAXS.

The tomogram slices have a set spatial calibration with units $\text{Å}\,\text{px}^{-1}$. Once a FFT of the slices has been performed, the FFT image has pixels labelled [units]/cycle(n), where [units] is the scale set in the original projection image, in this case Å. The cycle(n) is the radial pixel number in brackets, starting from the FFT image centre to the outer edge of the image as depicted in Figure 2.17. The central pixel is known as cycle 0 (Å/cycle(0) is infinite in the inverse space) and cycle(n) increases in number in x and y directions until the outermost edge pixel. For a 256 $\times$ 256 pixel FFT image, the outer edge pixel is cycle 128. In the x and y directions, the Å/cycle(n) value decreases linearly from the maximum Å/cycle(1).

After the image brightness and contrast is adjusted, and a threshold applied to reduce image background noise, a scattering profile can be extracted from the FFT image using FIJI. This radial profile plots the normalized integrated intensities in concentric circles as a function of distance from the central point in the image. In the profile, the intensity at any given distance from the central point represents the sum of the pixel intensity values in that cycle. The integrated intensity is divided by the number of pixels in the cycle that is also part of the image, yielding normalized comparable values.

Initially, the profile x-axis is in cycle number. To compare the scattering profile from an FFT image to the scattering curve obtained from SAXS, the x-axis (cycles) must be converted to q (Å^{-1}) using:

$$q = 2\pi \frac{cycle(n)}{\text{Å}/cycle(1)} \tag{2.38}$$

Differences in intensity are explained by the difference in flux, integration and interaction of photons or electrons between the SAXS and cryo-EM.

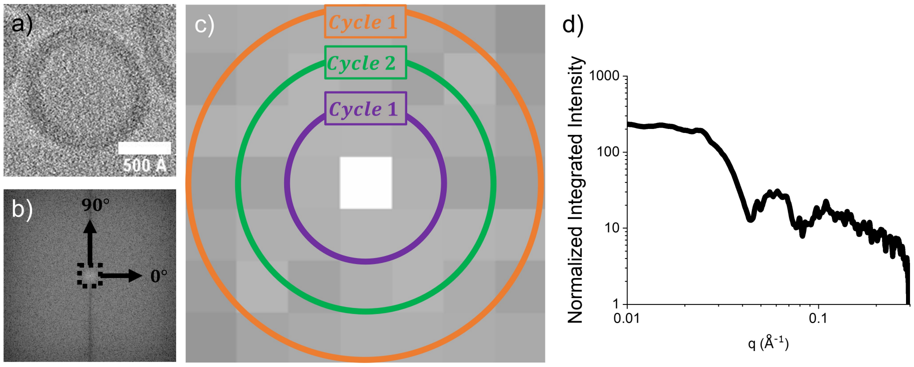

Figure 2.17: Interpreting the Fourier transform of an image. a) A tomogram slice with a spatial calibration of 8.06 Å px^{-1} is Fourier transformed to produce b) and FFT image. The black dotted box indicates the magnified area depicted in c). c) The pixels in the FFT image are labelled in Å/cycle(n). d) A scattering profile can then be extracted by taking a radial profile of the FFT image.

2.3.4 Single particle analysis: high resolution images

Generally, electron tomography shown in Figure 2.18a is conducted where there are a small number of macromolecules available on the specimen grid. When there are large number of macromolecules available on a specimen grid, single particle analysis (SPA) can be performed instead of electron tomography. When the sample is vitrified on the grid, the macromolecules within the sample usually exhibit a range of orientations, each resulting in different projection images. However, summation of projections is meaningless when the projections arise from different particle orientations. Instead, a statistical analysis is applied to classify images into groups (155). Therefore the goal of a single-particle analysis is to capture all relevant structural states through classification.

As shown by Figure 2.18b, for single particle analysis, the computer differentiates between the trace of the macromolecule and the noise in the background to identify similar traces, placing them in the same group. After sifting through thousands of projections, the computer generates a high resolution image from the group of projections and then calculates how the different images relate to each other to give a high resolution 3D structure (146). However, this technique requires a large number of sample projections as the final resolution of the sample 3D structure is directly related to the number of sample particles used to derive it (156, 157).

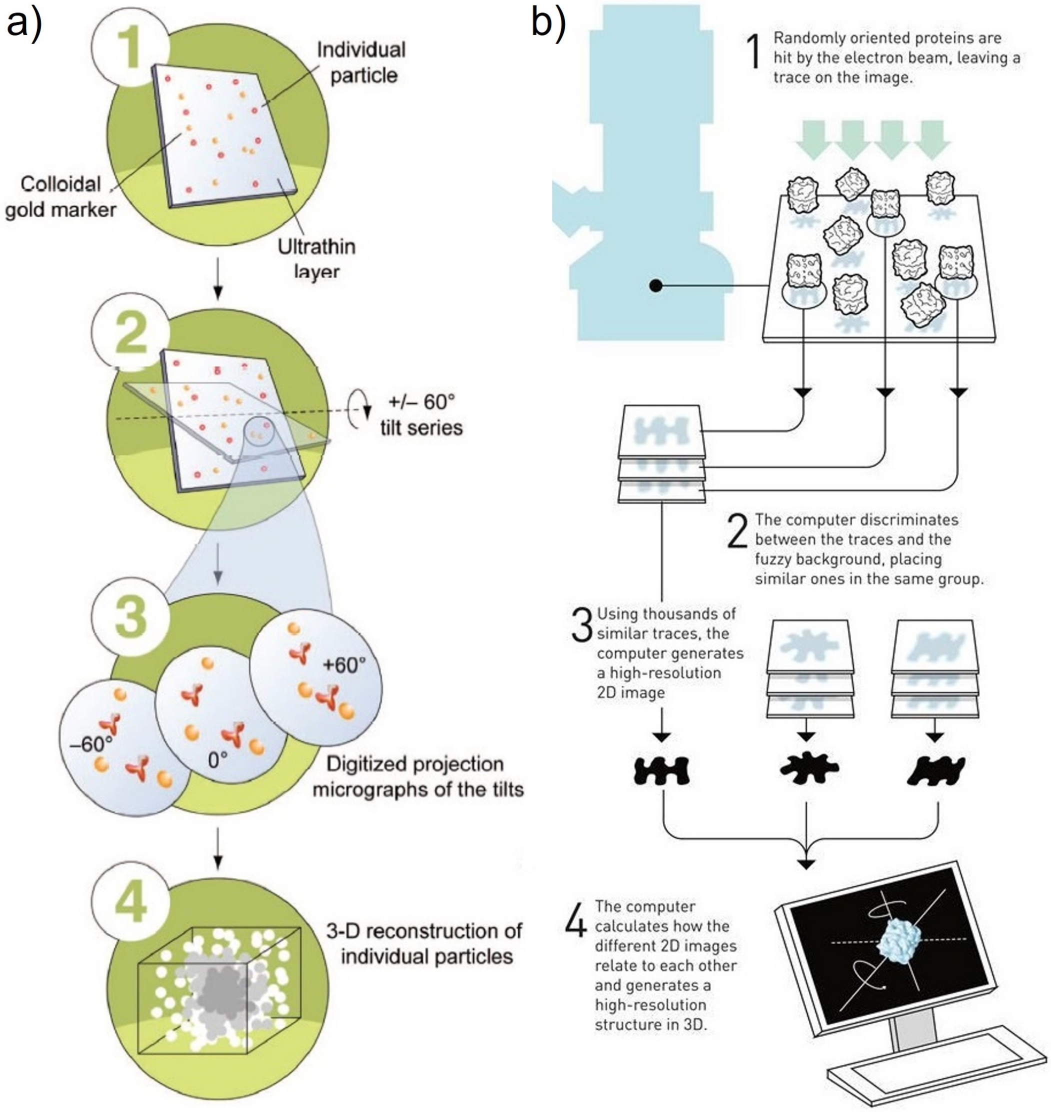

1 Randomly oriented proteins are hit by the electron beam, leaving a trace on the image.

2 The computer discriminates between the traces and the fuzzy background, placing similar ones in the same group.

3 Using thousands of similar traces, the computer generates a high-resolution 2D image

4 The computer calculates how the different 2D images relate to each other and generates a high-resolution structure in 3D.

Figure 2.18: Obtaining 3D structural information. Two of the methods to obtain this 3D density map from cryo-TEM 2D image projections are a) electron tomography and b) single particle analysis. Both techniques can be used to obtain a 3D electron density map of the sample. Image adapted from (146) and (158).

3. Materials and methods

3.1 Materials

The diblock copolymers poly 1,2-butadiene-block-polyethylene oxide (PBd-b-PEO) with total molecular weights of 1800 $\mathrm{g\,mol^{-1}}$ and 1150 $\mathrm{g\,mol^{-1}}$ were purchased from Polymer Source, Inc. (Montreal, Canada). Poly 1,2- butadiene(1200)-block-polyethylene oxide(600) (PBd_{22}-PEO_{14})(PDI 1.01) has a hydrophobic PBd block of 1200 $\mathrm{g\,mol^{-1}}$ ($>$ 85 % 1,2 addition) and a hydrophilic PEO block of 600 $\mathrm{g\,mol^{-1}}$ while Poly 1,2- butadiene(650)-block-polyethylene oxide(500) (PBd_{12}-PEO_{11})) (PDI 1.09) purchased from Polymer Source (Dorval, Montreal, Canada) has a hydrophobic PBd block of 650 $\mathrm{g\,mol^{-1}}$ (85 % 1,2 addition) and a hydrophilic PEO block of 500 $\mathrm{g\,mol^{-1}}$.

The 1- palmitoyl -2- oleoyl -sn- glycero -3- phosphocholine (POPC) and 1,2- dioleoyl -sn- glycero -3- phosphoethanolamine -N- (lissamine rhodamine B sulfonyl) (ammonium salt) (Rh-PE) in chloroform were purchased from Avanti Polar Lipids (Alabaster, AL, USA). 5(6)- carboxyfluorescein (CF) was purchased from Sigma Aldrich (St. Louis, MO, USA).

Other reagents purchased from Sigma Aldrich Ltd. (Gillingham, Dorset, UK) were Phosphorus standard solution (0.65 mM phosphorous), L-ascorbic acid, ammonium molybdate(IV) tetrahydrate 8-hydroxypyrene-1,3,6-trisulfonic acid trisodium salt (HPTS), 6-Dodecanoyl -2- Dimethylaminonaphthalene (Laurdan) and Anhydrous 4- Dimethylaminopyridine (DMAP).

5-(and-6-)- ((N- (5-aminopentyl) amino) carbonyl) tetra methylrhodamine (tetramethylrhodamine cadaverine) and protein A (10 nm colloidal gold) were purchased from Insight Biotechnology (Wembley, UK).

Sodium chloride (NaCl), Sodium hydroxide (NaOH) hydrogen peroxide, triton X-100, N,N- Disuccinimidyl carbonate and 4-(2-hydroxyethyl) -1- piperazine ethanesulfonic acid (HEPES) were bought from Thermo Fisher Scientific (Loughborough, Leicestershire, UK).

Anhydrous triethylamine was purchased from Fluorochem Ltd. (Hadfield, Derbyshire, UK).

The solvents chloroform, methanol, ethanol and dimethylformamide (DMF) were from VWR International Ltd. (Lutterworth, UK).

Filtered MilliQ water (filtered and deionised water 18.1 $\mathrm{m\Omega\,cm^{-1}}$ at 25°C) is referred to as water from hereon.

3.2 Sample preparation

3.2.1 Large unilamellar vesicle formation

Large unilamellar vesicles (LUV) were prepared by the thin film rehydration and extrusion method. To generate different hybrid vesicle compositions, relative volumes of POPC (32 mM) and the polymer (6.57 mM) in chloroform were measured using a Hamilton syringe into a glass vial. The solutions were dried in a vacuum desiccator to give a lipid-polymer film and then rehydrated with 1.0 mL of aqueous solution of 40 mM HEPES and 20 mM sodium chloride. The films were incubated at 50 °C for 5 min and vortexed for 1 min. The suspensions were then frozen in liquid nitrogen, thawed in a 60 °C water bath and vortexed for 10 s. This cycle was repeated 5 times. Suspensions were extruded 11 times though a polycarbonate membrane filters using a LiposoFast Basic Extruder. The samples were then kept at 4 °C until further analysis.

Table 3.1: Relative volumes of POPC (32 mM) and polymer (6.57 mM) used to prepare hybrid vesicle samples.

Sample	POPC volume (µL)	Polymer volume (µL)
0	200	0
25	150	250
50	100	500
75	50	750
100	0	1000

3.2.2 Removal of excess fluorescent dyes

The nanovesicle samples containing fluorescent dyes such as HPTS, CF or Rh-PE were run on a Sephadex G50 column under gravity using 40 mM HEPES and 20 mM sodium chloride buffered to pH 7.4 as the mobile phase to remove unencapsulated dye. The resulting 3 mL fractions were characterised using dynamic light scattering (DLS) for particle size distribution to confirm the presence of vesicles. The samples were then kept at 4°C until further analysis. 0.5 mL fractions containing reconstituted vesicles can be characterised using dynamic light scattering for particle size distribution and analysed for proton permeability with an HPTS assay or CF leakage assay.

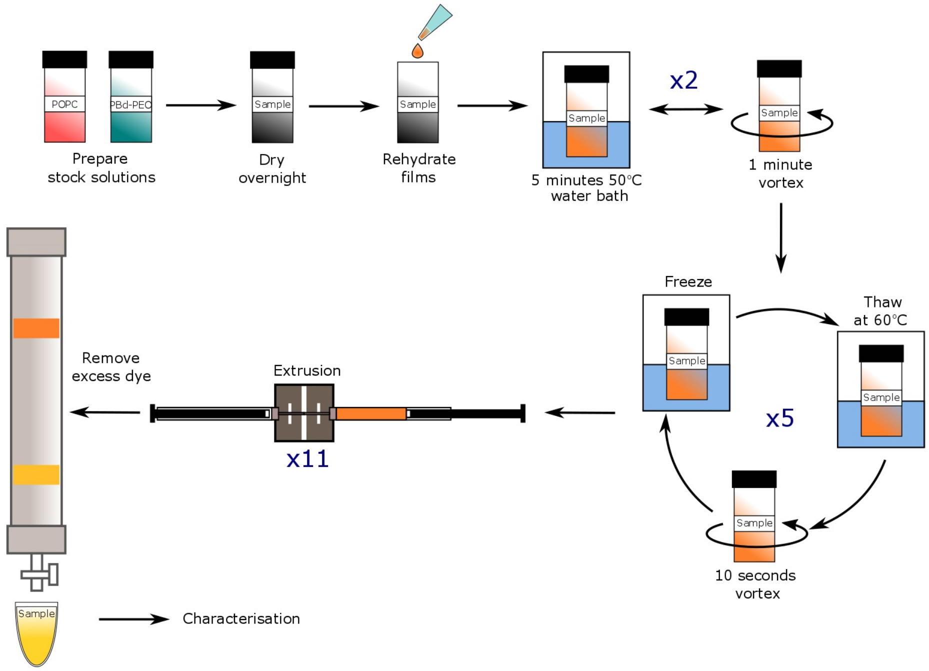

Figure 3.1: Method for forming large unilamellar vesicles. Large unilamellar vesicles were formed by rehydrating dried lipid-polymer films, followed by two 5 min water bath and 1 min vortex cycles and five freeze-thaw-vortex cycles. The solution was then extruded and if any dyes were added the excess dye was removed using a size exclusion column as detailed in Sections 3.2.1 and 3.2.2.

3.2.3 Characterising vesicle size using dynamic light scattering

The vesicles were characterised using a Malvern Zetasizer Nano ZSP (Malvern Panalytical Ltd, Malvern, UK) with scattering angle 173°. The Stokes-Einstein relationship

$$D = k_b T / 3\pi\eta d_h \tag{3.1}$$

was used to estimate the hydrodynamic diameter, d_h where k_b is the Boltzmann Constant and η is the solvent viscosity. Each hybrid vesicle was made and processed 3 times, so the results from three independent repeats were averaged.

3.2.4 Imaging vesicle samples using the cryo-electron microscope

Projection images

Large unilamellar vesicles were formed as outlined in Section 3.2.1. Quantifoil grids with 2 µm sized holes spaced every 2 µm were used to support the samples. The grids were glow discharged for 33 s at 10 mA using a Cressington 208 carbon coater to render the surface hydrophilic. Samples of 6.57 mM were placed directly on the grid using a FEI Vitrobot mkIV with a hold time of 40 s using a blot time of 6 s and blot force of 6. The samples were kept in closed pucs under nitrogen until required.

To image the grids, FEI Titan Krios microscope with an accelerating voltage of 300 kV was used, with defocussing of 6µm at a magnification of × 75000. The images obtained have high contrast due to the defocus of 6µm, which means some structural detail is lost. The resolution for these images are 1.069 $\text{Å}\,\text{px}^{-1}$.

Images were saved as .mrc files and processed using (Fiji is Just) ImageJ (FIJI) software. The images were adjusted for brightness and contrast and thresholded to reduce noise and display features more clearly. Radial distributions of the pixel intensity were taken from the centre of the vesicle to the outer rim, and then integrated by the measured segment of the vesicle to plot a normalised integrated intensity profile.

Tomograms

The cryo-transmission electron microscopy grids were prepared as detailed in Section 3.2.4 with a minor alteration. 10 nm gold nanoparticles to act as fiducial markers were added to the vesicle samples before this mixture was placed directly on the grid using a FEI Vitrobot mkIV using a blot time of 6 s and blot force of 6. The samples were kept in closed pucs under nitrogen until required.

To take tomograms of the grids a FEI Titan Krios microscope with a Volta phase plate was used with defocus set to 3 µm. The grids were exposed to an electron dose of 18 $e^{-}\,\text{Å}^{-2}\,s^{-1}$ and 61 images were taken at 2 ° increments to create the tomogram. The final resolution for these images were 5.39 $\text{Å}\,\text{px}^{-1}$.

The tomograms were reconstructed using eTomo program within the IMOD suite. Fiducial markers were registered and automatically tracked so that the images in the tomogram can be correctly aligned. The pixels in tomograms can also be binned to increase the contrast to see features more clearly, but at the cost of losing information and creating artefacts.

Tomogram processing and reconstruction was optimised iteratively for the samples. The final tomogram reconstruction method used consisted of a radial simultaneous iterative reconstruction technique (SIRT) filtered back projection with no pixel binning. The images were then saved as a sequence of .tif files for further analysis in FIJI. The $\text{Å}\,\text{px}^{-1}$ value was different for every tomogram reconstructed using this method but were between 5.39 - 11.49 $\text{Å}\,\text{px}^{-1}$.

3.2.5 Obtaining a scattering pattern using SAXS

Large unilamellar vesicles were formed as outlined in Section 3.2.1. Samples were transferred directly into quartz glass capillary tubes (0.01 mm wall thickness, 1.5 mm outside diameter) using a syringe and sealed with wax and epoxy resin for measurement in either the Diamond Light Source (Harwell Campus, Oxford, UK) I22 beamline at 17 keV with the detection camera at length 6.7 m.

3.2.6 Phosphorus assay

The phosphorus assay is used to determine the concentration of lipid in a sample. Standard tubes containing 0 µmol, as a blank, 0.0325µmol, 0.065µmol, 0.114µmol 0.163µmol and 0.228µmol phosphorus standard solution (0.65 mM) were prepared. The sample tube must contain approximately 0.1 µmol phosphorus and any solvent removed under nitrogen flow. The organic sample and standards were digested to inorganic phosphate using sulphuric acid (8.9N, 0.45 mL) and heating the tubes for 25 min at 200-215 °C. Hydrogen peroxide (150 µL) was added and the tubes were heated again at 200-215 °C for 30 min. Deionised water was added with both ammonium molybdate (VI) tetrahydrate solution (2.5 wt%, 0.5 mL) and ascorbic acid solution (10wt%, 0.5 mL) with vortexing between each addition. The tubes were heated again at 100 °C for 7 min. The absorbance of the standards were used to generate a calibration curve. The curve was then used to determine the concentration of phosphorus in the samples from their absorbance values.

3.2.7 Synthesis and purification of PBd$_{22}$-PEO$_{14}$ polymer tagged with tetramethylrhodamine cadaverine

PBd$_{22}$-PEO$_{14}$ was frozen at -20°C and dried in a vacuum desiccator to remove water. A Schlenk line was established and the reaction vessel was placed under nitrogen flow. All solvents and reactant materials were anhydrous and kept in sealed containers under nitrogen. The dried PBd$_{22}$-PEO$_{14}$ polymer (1800 $\mathrm{g\,mol^{-1}}$, 5 wt%, 50 $\mathrm{mg\,mL^{-1}}$, 0.0277 mmol, 50 mg) was dissolved in anhydrous dimethyl formamide (DMF, 5 mL). NN′ - Disuccinimidyl carbonate (256.17 $\mathrm{g\,mol^{-1}}$, 0.9 molar equivalents, 0.0249 mmol, 6.386 mg) was dissolved in DMF (5 mL) at 50°C. This was then combined with the polymer solution. Anhydrous 4- Dimethylaminopyridine (DMAP, 122.17 $\mathrm{g\,mol^{-1}}$, 0.1 molar equivalents, 0.00277 mmol, 0.3384mg) was dissolved in triethylamine (Hunig's base, 129.25 $\mathrm{g\,mol^{-1}}$, 3 molar equivalents, 0.0831 mmol) at 50°C. This was added to the polymer solution dropwise over a few minutes. The reaction mixture was left stirring overnight at 60°C under nitrogen flow. At this point the solution was a clear yellow colour. 5-(and-6-) - ((N- (5-

aminopentyl) amino) carbonyl) Tetramethylrhodamine (Tetramethylrhodamine cadaverine, 514.62 $\mathrm{g\,mol^{-1}}$, 1 molar equivalent, 0.0277 mmol, 14.254 mg) was dissolved in DMF at 50°C and added to the reaction mixture. The mixture became a clear orange solution. The reaction mixture was stirred continuously for 72 h until the solution consistently maintained an opaque brown colour. The final product was removed from the Schlenk line and dried using a GeneVac EZ2-Elite, producing a dark pink wax, which was then wrapped in foil and kept at 4°C until purification.

The wax was dissolved in water and run on a Sephadex G50 column under gravity. The first eluent was collected and freeze-dried on a VirTis Benchtop Pro Lyophiliser (Wolf Laboratories Ltd., York, UK) overnight. The fluorescently tagged polymer solid was kept at -20°C until use. The fluorescent polymer PBd$_{22}$-PEO$_{14}$-TMR was characterised using Infrared (IR)-spectroscopy, Liquid chromatography - mass spectroscopy (LC-MS) and Hydrogen nuclear magnetic resonance (H-NMR) spectroscopy. NMR and IR spectral data are available in JCAMP-DX format (.jdx files).

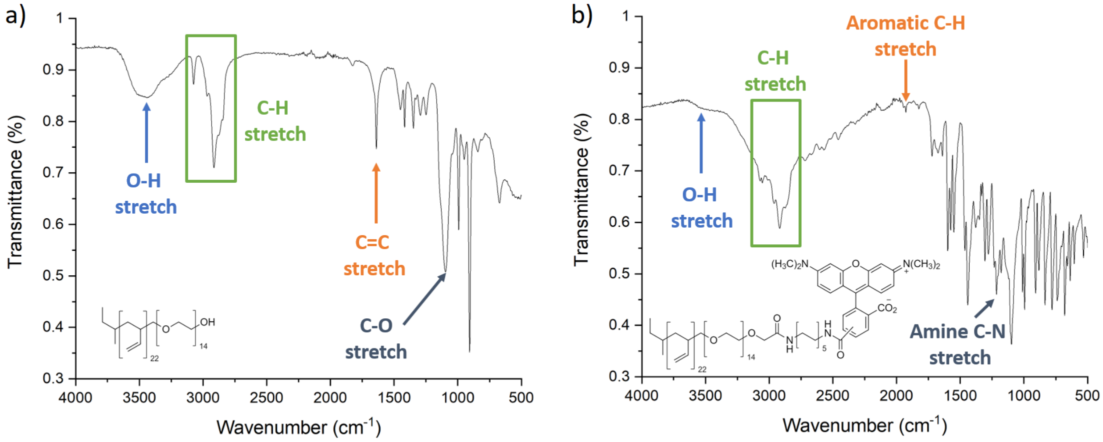

Figure 3.2: IR spectra for PBd$_{22}$-PEO$_{14}$ and PBd$_{22}$-PEO$_{14}$-TMR. IR spectrum for a) PBd$_{22}$-PEO$_{14}$ has a distinct hydroxy peak, which is diminished in the spectra for b) PBd$_{22}$-PEO$_{14}$-TMR, suggesting this functional group is not longer present in the final product.

Amphiphilic block copolymer PBd$_{22}$-PEO$_{14}$ has a hydroxy-terminal group that was used to form a peptide bond with tetramethyl rhodamine cadaverine (tetramethylrhodamine cadaverine) to give a fluorescently labelled polymer, PBd$_{22}$-PEO$_{14}$-TMR. This hydroxide bond stretch of this hydroxy-terminal functional group can be clearly seen in Figure 3.2a of PBd$_{22}$-PEO$_{14}$ but is diminished in Figure 3.2b of PBd$_{22}$-PEO$_{14}$-TMR suggesting this functional group no longer exists in final product from the synthesis procedure.

Peak assignations of the spectra shown in Figure 3.2a of PBd$_{22}$-PEO$_{14}$ can be found in Appendices A1.1 and A1.2.

LC-MS spectrum of PBd$_{22}$-PEO$_{14}$, tetramethylrhodamine cadaverine and PBd$_{22}$-PEO$_{14}$-TMR were obtained. Compound 4 of PBd$_{22}$-PEO$_{14}$ shown in the chromatogram of Figure 3.3a has the greatest intensity. The mass spectrum for this compound agrees with the m/z value expected for the polybutadiene block of PBd$_{22}$-PEO$_{14}$ (1200 $\mathrm{g\,mol^{-1}}$).

Figure 3.3b shows that TMR starting material was pure, as it only contains one compound with a m/z value of approximately 514 $\mathrm{g\,mol^{-1}}$ which agrees with the molecular mass of TMR. Figure 3.3c shows that Compound 3 has the greatest intensity in the chromatogram. Although compound 1 in Figure 3.3c has the same placement as compound 1 in Figure 3.3b, the mass spectrum for compound 1 does not contain m/z values that agree with the molecular weight of TMR, suggesting that the purification step was successful at removing excess TMR.

The m/z value 2472 in Compound 3 of Figure 3.3c agrees with the expected molecular mass of PBd$_{22}$-PEO$_{14}$-TMR (2314 $\mathrm{g\,mol^{-1}}$). From the relative intensity values of the chromatogram, an approximate concentration of successfully fluorescently tagged polymer can be found. The concentration was calculated to be 0.083 mM, which is roughly 20% of the initial concentration (1 $\mathrm{mg\,mL^{-1}}$, 0.415 mM).

The structure of PBd$_{22}$-PEO$_{14}$-TMR was further confirmed by correlated spectroscopy-nuclear magnetic resonance (COSY-NMR) as shown in Figure 3.4. The dye molecule was expected to form an amide bond with the hydroxy terminal of the polymer, which is shown as a peak observed at $\sim 7\ ppm$.The correlation between these peaks and other peaks on the spectrum indicate the formation of an amide bond between PBd$_{22}$-PEO$_{14}$ and tetramethylrhodamine cadaverine.

PBd$_{22}$-PEO$_{14}$-TMR (**1**): ^{1}H NMR (CDCl$_3$ with 5% w/w TMS, 500 MHz): δ_H 12.12 (1H, s, 7.25, RCOOH), 9.23 (1H, s, 7.25, H-CO-R), 8.19 (2H, m, 7.25, aromatic), 8.10 (1H, s, aromatic), 7.47 (3H, s, aromatic), 7.25 (526, m, amide, aromatic, deuterated chloroform), 7.05 (3H, s, aromatic), 6.22 (3H, s, 7.25, R-CO-NH-R), 4.92 (2H, m, RC=C-H), 3.65 (35H, m, O-C-H), 2.37 (1H, s, 7.25, RN-C-H), 1.54 (98H, m, R-CH), 1.25 (4H, m, R-CH3), 0.97 (2H, m, R-CH3).

3.2.8 Giant unilamellar vesicle formation

GUVs were prepared using the electroformation method from 6.57 mM POPC and PBd-b-PEO solutions with 0.5 mol% 1,2- dioleoyl -sn- glycero -3- phosphoethanolamine -N-(lissamine rhodamine B sulfonyl) (ammonium salt) (Rh-PE) dissolved in chloroform for fluctuation spectroscopy experiments, 0.5 mol% 6-Dodecanoyl -2- Dimethylaminonaphthalene (Laurdan) for membrane hydration measurements, or 2 mol% 3,3′-dioctadecyloxacarbocyanine perchlorate (DiO)and 10 mol% Poly 1,2-butadiene(1200)-block-polyethylene oxide(600) with 5-(and-6-)-((N-(5-aminopentyl) amino) carbonyl) tetramethylrhodamine fluorescent tag (PBd_{22}-PEO_{14}-TMR) for FRAP and lipid-polymer ratio experiments. Briefly, 18 µL of a lipid solution was deposited as a thin layer over the conductive side of two Indium titanium oxide (ITO)-coated glass slides (surface resistivity 8-12 $\Omega\,m^{-2}$) and allowed to dry. The ITO slides were then assembled into an electroformation chamber each in contact with copper tape and separated by a Teflon spacer. The chamber was filled with a 300 mM sucrose solution (300 $mOsm\,kg^{-1}$) and connected to a function generator to apply an AC electric field. Electroformation was carried out at 10Hz at different temperatures depending on the membrane composition. The voltage changed every 10 min from 0.1 to 0.5, 1, 2 and finally 3 V peak to peak for 2 hour. 0-50 mol% PBd_{12}-PEO_{11}, electroformation was carried out at 35°C, 25 and 50 mol% PBd_{22}-PEO_{14} at 42°C, and 75 mol% and 100 mol% of both polymers at 64°C. The frequency was gradually decreased over approximately 8 min to facilitate the closure and detachment of GUVs from the surface. After electroformation, the GUVs were suspended in an isotonic 20 mM HEPES, 150 mM NaCl solution unless otherwise stated. The osmolality of the buffer was measured using a 3320 single-sample micro-osmometer (Advanced Instruments, Norwood, U.K.). The GUVs observed were between 5 and 40 µm in diameter. The GUV-based experiments were conducted at room temperature on a Zeiss LSM 880 inverted laser scanning confocal microscope. The samples were deposited on the microscope slides previously treated with a 5% BSA solution to prevent GUVs from adhering and rupturing onto the glass.

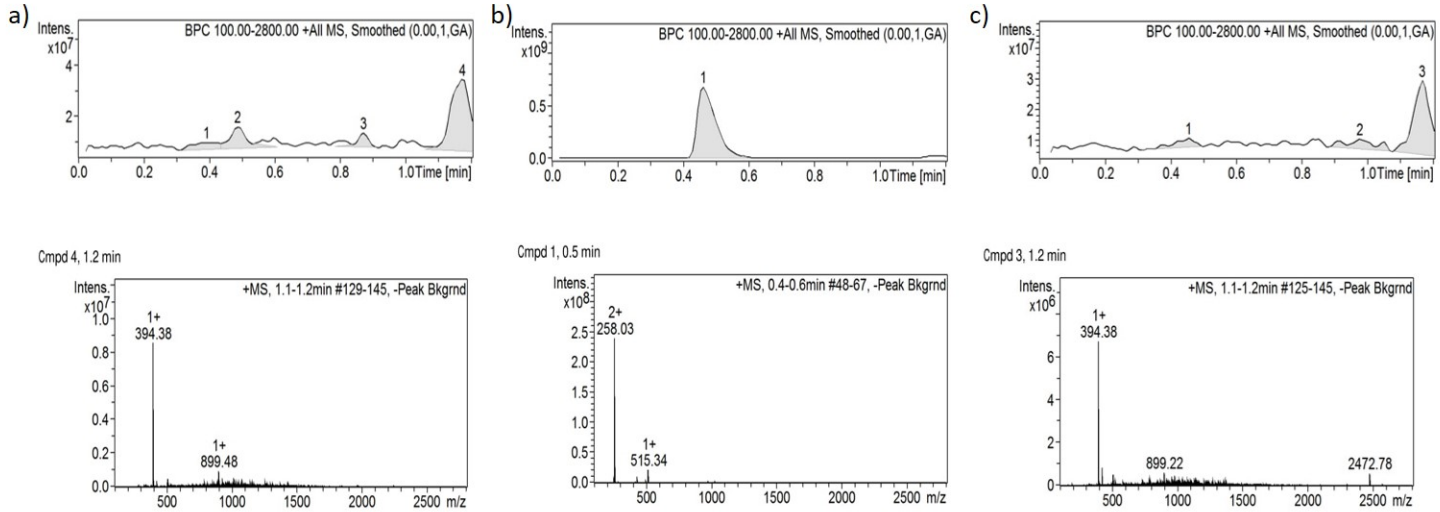

Figure 3.3: LC-MS spectra for a) PBd_{22}-PEO_{14}, b) tetramethylrhodamine cadaverine c)PBd_{22}-PEO_{14}-TMR. LC-MS spectrum for c)PBd_{22}-PEO_{14}-TMR provides evidence for a successful synthesis as the m/z value of 2472 agrees with the expected molecular mass of PBd_{22}-PEO_{14}-TMR.

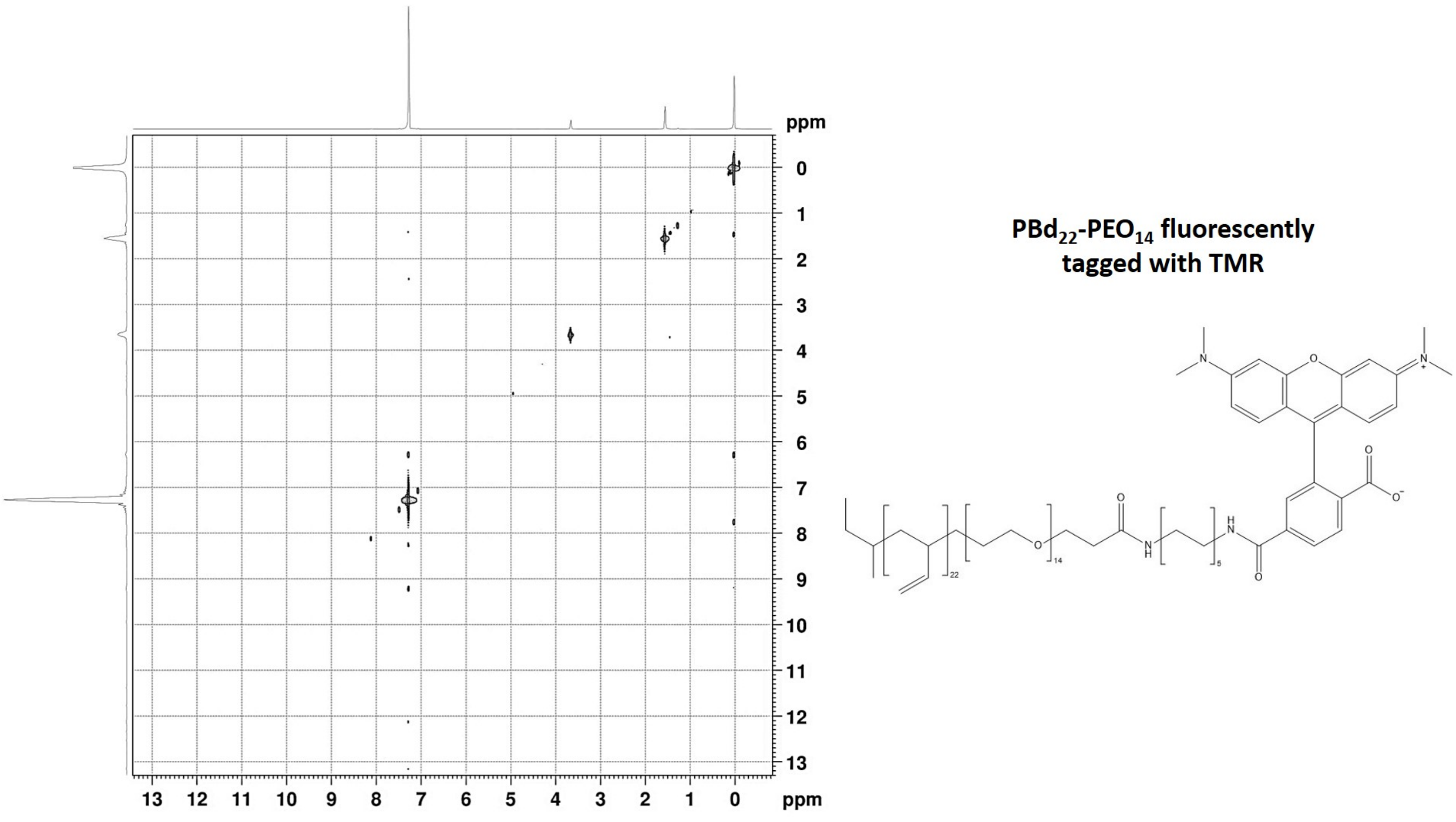

Figure 3.4: COSY-NMR spectrum for PBd_{22}-PEO_{14}-TMR. A fluorescent label has been attached by an amide bond to the PBd_{22}-PEO_{14} polymer. The peak at ~ 7 *ppm* accounts for the amide bond.

4. Membrane permeability

The properties of lipid membranes have wide-ranging effects in biology, from protein function to compartmentalisation. While lipid geometry is known to affect membrane formation (38), differences in membrane composition and phase state of the components are believed to affect membrane function, and thus have an effect on the activity of membrane associated proteins (159). It has already been shown that small variations in the structure of phospholipids in a membrane can strongly influence membrane properties such as fluidity, tension (160) permeability (86), hydration (161), and membrane protein activity (162).

Control of ion permeation is central to cell function, so any alterations in the physical properties of the bilayer is expected to have a strong effect on biological processes such as signalling dynamics and energy transduction (163). Proton permeability in particular affects biological processes from the production of energy for cellular function (108) to ion transport with membrane protein channels (86, 164). As ions are repelled by the hydrophobic region in the membrane, they cannot cross the membrane via simple diffusion, so to propagate ions such as protons across a lipid bilayer, an energetic barrier may have to be overcome. Protons can be transported across a membrane by either diffusion through the membrane using the solubility-diffusion mechanism or through transient membrane pores (165). Proton permeability also needs to be low to enable formation of electrochemical gradients across the membrane. For example, a proton gradient can be generated if the internal cellular pH is 4 and the external pH is 7, causing hydrogen ions to permeate out through the membrane and form an electrical potential (166), facilitating the transport of cations across the membrane through membrane ion channel proteins (86).

In the past, both pure liposomes (20, 167, 168, 169) and pure polymersomes (33, 170) have been used to reconstitute proteins. However, as pure systems, these materials have disadvantages such as poor mechanical stability in lipid membranes or lack of biocompatibility for polymer vesicles. More recently, hybrid bilayers composed of lipid and amphiphilic copolymers combine the advantages of both for protein reconstitution (1, 73, 77, 78, 86, 87, 88). In particular, PC/PBd-b-PEO hybrid membranes have been shown to extend functional lifetimes of incorporated membrane proteins (1, 77, 78, 86), however relatively few studies have completed experiments incrementally increasing the copolymer fraction within hybrid vesicles to determine how membrane composition affects membrane properties such as permeability. Exploring the physical properties of hybrid vesicles could reveal how the hybrid vesicles are able to facilitate an enhanced functional lifetime.

4.1 Methods

Vesicle preparation is conducted according to the protocol in 3.2.1 using a buffer of 10 mM HPTS concentration, 40 mM HEPES and 20 mM NaCl. Excess HPTS dye was removed following procedures in Section 3.2.2. The size distributions of the samples were determined using dynamic light scattering (DLS) as outlined in Section 3.2.3. The concentration of lipid was obtained from a phosphorus assay as outlined in Section 3.2.6. This method was optimised by E. Moscrop during her summer student project. Proton permeability of PBd_{12}-PEO_{11} hybrid samples were collected by G. Coates for her Master's project.

To measure the proton permeability, the absorption spectrum of 2 mL of ∼2 mM HPTS-encapsulated vesicles was measured using a UV-vis spectrometer scanning between 405 and 450 nm. To this, either 23 µL of 1.0 M NaOH or 18 µL of 1.0 M HCl was added to adjust the pH of the extravesicular solution to pH 8 or pH 7 respectively and the absorbance (between 405 and 450 nm) was monitored overnight; the first cycle scans were taken every minute over 2 hours and for the second cycle scans were taken every 10 minutes for 7 hours with constant stirring. After this, 100 µL of 10% (w/v) Triton X-100 was added to completely destabilise the vesicles and release encapsulated HPTS (so that these probes experience the pH of the extravesicular medium) before a final scan between 405 and 450 nm was completed.

A calibration curve using buffers ranging from pH 4 to pH 10 with 0.5 mM HPTS was used to determine the pH inside the encapsulated vesicles. The absorbance ratio of 450 to 405 nm ($A_{450}/A_{405} = Abs$) was plotted against pH and the data fitted to find the relationship between them. The scattering effects were taken into account by adding unencapsulated POPC vesicles to each buffer solution.

The absorbance ratio between 450 and 405 nm (Abs) was converted to pH using the calibration curve shown in Appendix A2.1:

$$pH = \ln(-\frac{A1 - Abs}{Abs - A2})dx + x_0 \tag{4.1}$$

where $A1$, $A2$, dx and x_0 are equal to 0.199, 1.791, 0.599 and 7.485 respectively. The pH was then plotted against time to show how pH changed with addition of NaOH (or HCl) and Triton X-100. The deviations between measured pH and calculated pH were observed in some hybrid vesicle systems and assumed to be caused by the restricted motion of pyranine in neutral lipid composition vesicles (171). As the pH range with these experiments is a linear function of the absorbance ratio at 450 and 405 nm, these deviations in pH were accounted for by offsetting the pH with the initial measured external buffer solution pH.

All data points in a series were offset by the same value. For example, the initial average internal pH of 100 mol% PBd$_{22}$-PEO$_{14}$ measured by HPTS gave a value of 6.74, while the average pH of the external buffer solution measured by the pH meter was 7.35. Although the internal pH and the external pH appear to be different, the rehydration buffer to form the vesicles had an identical pH measurement to the buffer used to exclude excess HPTS from the sample. Thus the internal and external pH were assumed to have identical pH values. The internal pH was offset by addition of 0.62 ($= 7.35 - 6.74$) to all data points of 100 mol% PBd$_{22}$-PEO$_{14}$ vesicles to reflect the actual pH of the external buffer solution.

Permeability coefficients were calculated by adapting a method recently reported for hybrid DOPC lipid and PBd$_{37}$-PEO$_{22}$ vesicles (86). The pH of an aqueous solution reflects the equilibrium concentration of hydroxide ions at any given time. However solutions comprising a buffer require substantially more hydroxide ions to cross the membrane to elicit a change in pH. The nominal concentration of HEPES is equal to the effective concentration of HEPES in its ionised form, so the pKb of HEPES can be used to calculate the concentration of deprotonated HEPES. The pKa (7.5) of HEPES was converted to a Kb value (-1.23), which was then used to determine a formula to find the hydroxide ion, $[^{-}OH]$, and deprotonated HEPES concentration, $[HEPES^{-}]$ of the sample throughout the experiment:

$$K_b = \frac{[^{-}OH] \times [HEPES]}{[HEPES^{-}]} \tag{4.2}$$

where the HEPES concentration, $[HEPES]$, is 40 mM, the concentration of HEPES used in the external buffer solution.

Because the change in hydroxide ion concentration is linear between 0 and 1500 seconds, the equilibrium hydroxide concentration was calculated from the linear fit of $[^{-}OH]$ over time. This was then used to determine the amount of hydroxide ions that must be added to elicit the observed change in equilibrium pH over the course of the experiment:

$$\frac{\Delta n_{^{-}OH}}{\Delta t} = \frac{([^{-}OH]_{final} + [HEPES]_{final} - [HEPES]_{intial}}{\Delta t} V_{average} \tag{4.3}$$

where $\Delta n_{^{-}OH}$ is the moles of hydroxide ions that crosses the vesicle membrane, $[^{-}OH]_{final}$ and $[HEPES]_{final}$ are the equilibrium concentrations determined using Equations 4.1 and 4.2 at $t = 1500$ seconds and $[HEPES]_{initial}$ at $t = 0$ seconds. Δt is the elapsed time and $V_{average}$ is the average internal vesicle volume calculated from the average vesicle diameter measured by DLS, with predicted membrane thickness accounted for. This yields the net rate of transfer of ^{-}OH across the vesicle membrane, $\frac{\Delta n_{-OH}}{\Delta t}$ which can be converted to the flux per unit area of the membrane:

$$J_{H^+/^-OH} = \frac{\Delta n_{^-OH}}{\Delta t} \frac{1}{S_{average}} \tag{4.4}$$

Where $S_{average}$ is the average external vesicle surface area from the DLS measured vesicle diameter. The initial net $H^+/^-OH$ flux, $J_{initialH^+/^-OH}$ was calculated from the initial concentration of ^-OH:

$$J_{initialH^+/^-OH} = \frac{[^-OH]_{t=0} + [HEPES^-]_{t=1500} - [HEPES^-]_{t=0}}{\Delta t} \times \frac{V_{average}}{S_{average}} \tag{4.5}$$

While the final net $H^+/^-OH$ flux, $J_{finalH^+/^-OH}$ was calculated from the final concentrations of ^-OH:

$$J_{finalH^+/^-OH} = \frac{[^-OH]_{t=1500} + [HEPES^-]_{t=1500} - [HEPES^-]_{t=0}}{\Delta t} \times \frac{V_{average}}{S_{average}} \tag{4.6}$$

$J_{initial}$ uses the amount of ^-OH ions at $t = 0$ seconds present while J_{final} uses the amount of ^-OH ions present at $t = 1500$ seconds.

The net flux of protons and hydroxide ions, $J_{H^+/^-OH}$, was found by subtracting $J_{initialH^+/^-OH}$ from $J_{finalH^+/^-OH}$. To find the permeability constant, P, the net flux, $J_{H^+/^-OH}$, was divided by the hydroxide ion concentration gradient, Δc formed from the addition of NaOH (or HCl).

$$J_{H^+/^-OH} = P\Delta c \tag{4.7}$$

For addition of NaOH, the pH difference is from 7.4 to 8.0, which gives a Δc of 0.75 µM, while the pH difference from addition of HCl is from 7.4 to 7, making $\Delta c = 0.15$ µM.

Although some of the permeability results appear to follow first order kinetics, analysis of the linear region was deemed more appropriate as not all the samples followed an exponential decay profile. To ensure the calculated permeability coefficients were comparable, the same analysis method was used on all samples. The average permeability and standard deviations of the permeability measurements of the hybrid and polymer vesicles were calculated from a data set of at least 3 different samples.

4.2 Results and discussion

The change in pH within the vesicle lumen of PBd_{22}-PEO_{14}/POPC vesicles after the addition of either HCl or NaOH was monitored over 10 hours using HPTS.

From Figure 4.1a , addition of NaOH initially causes a rapid increase in the pH observed, which then plateaus over time. The initial linear regions of each curve, shown in Figure 4.1c, were fitted and used to determine the net flux of protons and hydroxide ions, J_{H^+/OH^-}, using Equations 4.5, 4.6 and the permeability coefficients using Equation 4.7. The resultant permeability for each PBd$_{22}$-PEO$_{14}$/POPC sample is given in Table 4.1.

Pure POPC lipid vesicles were anticipated to have the highest permeability coefficient ($5.5 \pm 1.7 \times 10^{-11}$cm s^{-1}) amongst PBd$_{22}$-PEO$_{14}$/POPC vesicle compositions on addition of NaOH as the addition of polymer was expected to reduce membrane permeability. However, 25 mol% PBd$_{22}$-PEO$_{14}$ vesicles were found to have the greatest permeability after addition of NaOH ($11 \pm 6 \times 10^{-11}$cm s^{-1}). As PBd$_{22}$-PEO$_{14}$ mol% increased from 50 - 100 mol%, the permeability coefficients reduced from $3.3 \pm 1.8 \times 10^{-11}$cm s^{-1} to $0.8 \pm 0.6 \times 10^{-11}$cm s^{-1}. The difference in permeability between 25 mol% and 50-100 mol% PBd$_{22}$-PEO$_{14}$ compositions was statistically significant to within 95% confidence (< 0.05, Tukey and Bonferroni ANOVA).

Table 4.1: Membrane permeabilities of PBd$_{22}$-PEO$_{14}$ vesicles measured from HPTS assay following addition of 1 M HCl or NaOH.

PBd$_{22}$-PEO$_{14}$ (mol%)	1M NaOH addition (P$\times 10^{-11}$cm s^{-1})		1M HCl addition (P$\times 10^{-11}$cm s^{-1})	
	Average	Standard Deviation	Average	Standard Deviation
0	5.5	1.7	16	6.0
25	11	6.0	30	9.0
50	3.3	1.8	17	8.0
75	1.9	0.3	10	4.0
100	0.8	0.6	1.8	1.6

The same trends were seen after addition of HCl to PBd$_{22}$-PEO$_{14}$/POPC vesicles. Figure 4.1b shows addition of HCl initially causes a rapid decrease in the pH observed, which then plateaus over time. The initial linear regions of each curve, shown in Figure 4.1d, shows that 25 mol% PBd$_{22}$-PEO$_{14}$ sample has the steepest gradient, which results again in the highest permeability coefficient ($30 \pm 9 \times 10^{-11}$cm s^{-1}). As PBd$_{22}$-PEO$_{14}$ mol% increased from 50 - 100 mol%, the permeability coefficients after addition of HCl reduced from $17 \pm 8.0 \times 10^{-11}$cm s^{-1} to $1.8 \pm 1.6 \times 10^{-11}$cm s^{-1}. There is however no statistically significant difference in permeability coefficients after HCl addition (> 0.05, Tukey and Bonferroni ANOVA).

As shown by Figures 4.1a and b, 75 mol% and 100 mol% PBd_{22}-PEO_{14} vesicles in particular have extremely low permeability over 10 hours after the addition of either HCl or NaOH. Some of the initial pH changes in these samples could be due to a small amount of unencapsulated or leaked HPTS from the vesicles.

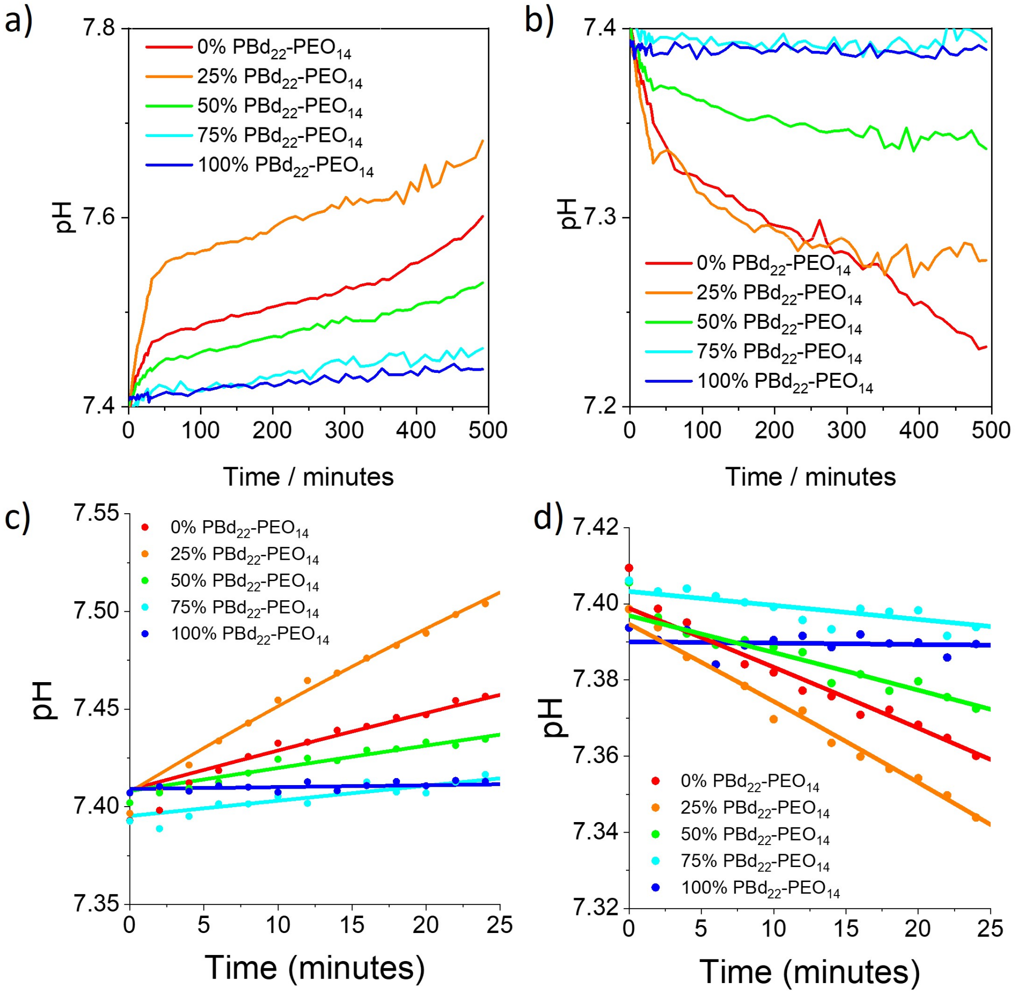

Figure 4.1: Changes in pH in PBd_{22}-PEO_{14}/POPC vesicles upon addition of acid or base. Change in pH over 10 hours upon the addition of a) NaOH or b) HCl to PBd_{22}-PEO_{14} vesicles encapsulated with HPTS. The linear regions of a) and b) were fitted with a line of best fit, shown in c) and d) respectively, to determine the net flux of protons and hydroxide ions, J_{H^+/OH^-}, using Equations 4.5, 4.6 and the permeability coefficients using Equation4.7.

Results from DLS show similar trends, where 25 mol% PBd_{22}-PEO_{14} vesicles have the smallest Z-average after HPTS encapsulation (94.21 nm, polydispersity index (PDI) 0.106). Again, as the PBd_{22}-PEO_{14} mole fraction increases from 50-100 mol% PBd_{22}-PEO_{14}, Z-average also increases from 115.9 nm (PDI 0.140) to 140.2 nm (PDI 0.544). Full DLS data can be found in Appendix A3.1.

The change in pH within the vesicle lumen of PBd$_{12}$-PEO$_{11}$/POPC vesicles after the addition of either HCl or NaOH was also monitored over 10 hours using HPTS. This data was collected by G. Coates during her Masters project.

From Figure 4.2a , addition of NaOH initially causes a rapid increase in the pH observed, which then plateaus over time. As before, the initial linear regions of each curve, shown in Figure 4.2c, were fitted and used to determine the net flux of protons and hydroxide ions, J_{H^+/OH^-}, using Equations 4.5, 4.6 and the permeability coefficients using Equation 4.7. The resultant permeability for each PBd$_{12}$-PEO$_{11}$/POPC sample is given in Table 4.2.

Table 4.2: Membrane permeabilities of PBd$_{12}$-PEO$_{11}$ vesicles measured from HPTS assay following addition of 1 M HCl or NaOH.

PBd$_{12}$-PEO$_{11}$ (mol%)	1M NaOH addition (P×10^{-11}cm s^{-1})		1M HCl addition (P×10^{-11}cm s^{-1})	
	Average	Standard Deviation	Average	Standard Deviation
0	5.5	1.7	16	6.0
25	0.9	0.2	41	1.1
50	1.2	0.2	18	5.4
75	8.5	2.7	65	4.9
100	4.8	0.6	48	3.9

For PBd$_{12}$-PEO$_{11}$/POPC compositions, 25 mol% PBd$_{12}$-PEO$_{11}$ vesicles were found to have the lowest permeability after addition of NaOH (0.9 ± 0.2 $\times 10^{-11}$cm s^{-1}). However, as PBd$_{12}$-PEO$_{11}$ mol% increased from 50 - 100 mol%, the permeability coefficients increased from 1.2 ± 0.2 $\times 10^{-11}$cm s^{-1} to 4.8 ± 0.6 $\times 10^{-11}$cm s^{-1}. 75 mol% PBd$_{12}$-PEO$_{11}$ sample, surprisingly, had the highest permeability after addition of NaOH (8.5 ± 2.7 $\times 10^{-11}$cm s^{-1}).

Similar trends were seen after addition of HCl to PBd$_{12}$-PEO$_{11}$/POPC vesicles. Figure 4.2b shows addition of HCl initially causes a rapid decrease in the pH observed, which then plateaus over time, the initial linear regions of each curve, shown in Figure 4.2d, shows that 75 mol% PBd$_{22}$-PEO$_{14}$ sample has the steepest gradient, which results in the highest permeability coefficient (65 ± 1.9 $\times 10^{-11}$cm s^{-1}) while 0 mol% and 50 mol% PBd$_{12}$-PEO$_{11}$ vesicles had the lowest permeability coefficients after addition of HCl (16 ± 6.0 $\times 10^{-11}$cm s^{-1} and 18 ± 5.4 $\times 10^{-11}$cm s^{-1} respectively) to PBd$_{12}$-PEO$_{11}$/POPC vesicle compositions. 25 mol% and 100 mol% PBd_{12}-PEO_{11} vesicles had similar permeability coefficients ($41 \pm 1.1 \times 10^{-11} \mathrm{cm\,s^{-1}}$ and $48 \pm 3.9 \times 10^{-11} \mathrm{cm\,s^{-1}}$ respectively).

Although 75 mol% PBd_{12}-PEO_{11} vesicles had the greatest initial permeability, Figures 4.2a and b show that protons continued to permeate across 50 mol% PBd_{12}-PEO_{11} vesicle membranes, causing the pH to plateau at a much higher (NaOH addition) or lower (HCl addition) pH.

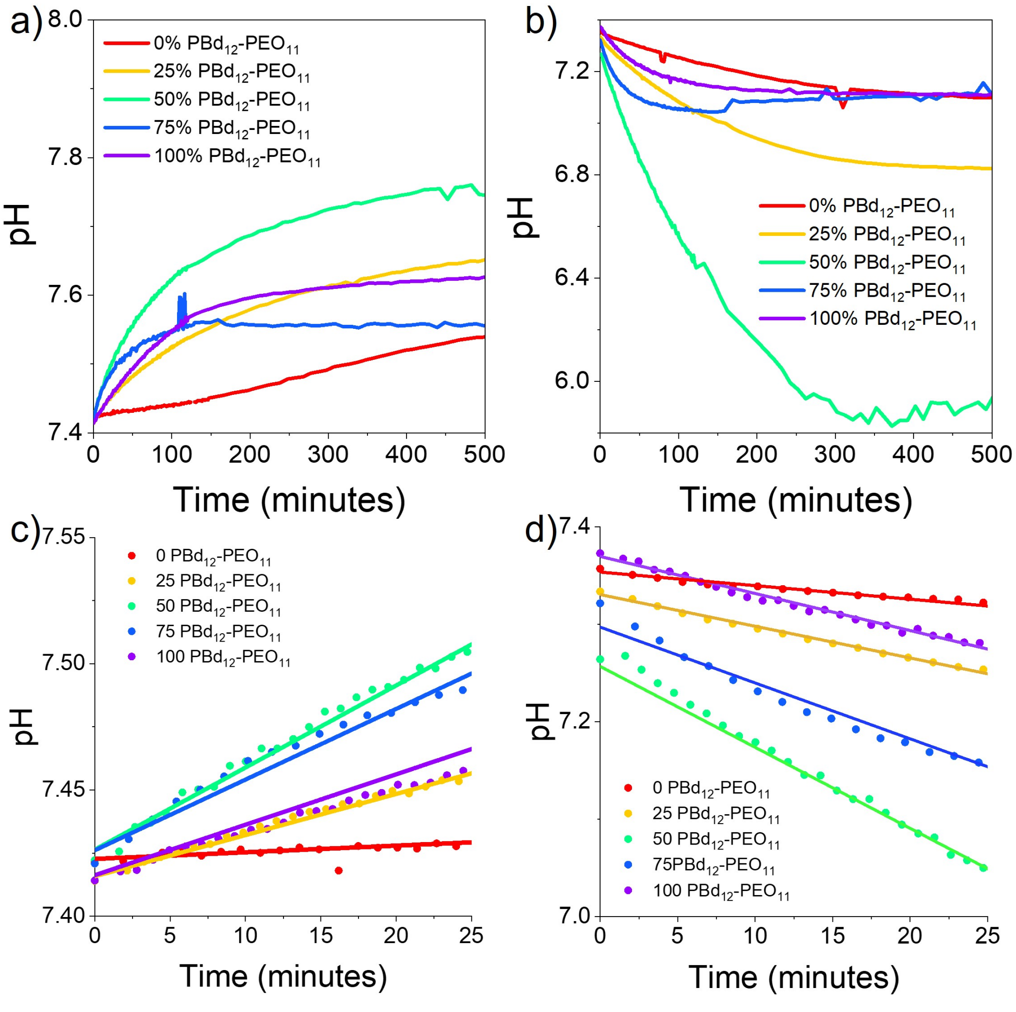

Figure 4.2: Changes in pH in PBd_{12}-PEO_{11}/POPC vesicles upon addition of acid or base. Change in pH over 10 hours upon the addition of a) NaOH or b) HCl to PBd_{12}-PEO_{11} vesicles encapsulated with HPTS. The linear regions of a) and b) were used to determine the net flux of protons and hydroxide ions, J_{H^+/OH^-}, and are shown in c) and d) respectively.

Results from DLS show that 50 mol% and 75 mol% PBd_{12}-PEO_{11} samples have the smallest Z-averages at 100.1 nm (PDI 0.173) and 101.8 nm (PDI 0.194) respectively. Although at first glance it may seem that vesicle size is also related to the permeability, 100 mol% PBd_{12}-PEO_{11} is the second most permeable sample when HCl is applied to the system yet has the largest Z-average at 135.4 nm (PDI 0.136). Full DLS data can be found in Appendix A3.2.

For all PBd_{22}-PEO_{14}/POPC and PBd_{12}-PEO_{11}/POPC vesicle compositions, the pH increased over time in two phases: an initial steep gradient, which then slowly plateaus over time. Previously, this first increase was attributed to the formation of transient pores from hydrophilic defects caused by thermal fluctuations within the membrane allowing permeation from the inner vesicle volume to the bulk solution (172). Such transient pores are believed to form when the internal pressure is higher than the membrane tension. The pores allow the vesicle content to exit, and so the tension to drops and the pore stops growing. The pore then closes, subsequently increasing the tension (173).

The second phase of pH increase was believed to be due to the solubility-diffusion mechanism where ions partition into the hydrophobic phase and then diffuse across the membrane (108, 165). Undissociated molecules use water molecules present in the hydrophobic region of the bilayer to transport themselves across the bilayer by hydrogen bond exchange (109, 174). The solubility-diffusion mechanism is thought to allow anions to permeate faster than cations of the same size, while the pore mechanism predicts that cations should permeate faster than anions (172).

Permeability coefficients upon addition of HCl to the sample for all PBd_{22}-PEO_{14}/POPC and PBd_{12}-PEO_{11}/POPC vesicle compositions were greater than the coefficients calculated after NaOH addition. As the initial change in pH is believed to be due to the pore mechanism, any hydrogen ions (cations) in solution would be expected to permeate more quickly through the membrane than the anionic hydroxide ions present in solution. Therefore when HCl is added to the sample, the permeability appears greater because there are more hydrogen ions being transferred across the membrane than when NaOH is added to the system.

As shown by Figure 4.3, PBd_{12}-PEO_{11}/POPC vesicle compositions appear to have higher permeability coefficients than PBd_{22}-PEO_{14}/POPC vesicles. The results of a previous investigation studying hybrid DOPC/PBd_{37}-PEO_{22} vesicles suggested that the difference in hydrophobic thickness made the hybrid membrane more prone to spontaneous pore formation (86). This implied that the larger molecular weight PBd_{22}-PEO_{14} polymer would form more permeable vesicles than PBd_{12}-PEO_{11} vesicles due to the larger difference in hydrophobic thickness between PBd_{22}-PEO_{14} and POPC. In this case however, PBd_{22}-

PEO_{14}/POPC vesicle compositions have overall lower permeability coefficients than PBd_{12}-PEO_{11}/POPC compositions.

Another potential reason for proton permeation is that the fluidity of the lipid bilayer can lead to the formation of transient pores that allow an influx or outpouring of molecules to or from the vesicle. So although PBd_{12}-PEO_{11} is a lower molecular weight polymer than PBd_{22}-PEO_{14}, PBd_{12}-PEO_{11} may form softer membranes and therefore be more prone to spontaneous pore formation than PBd_{22}-PEO_{14}, which have more rigid membranes.

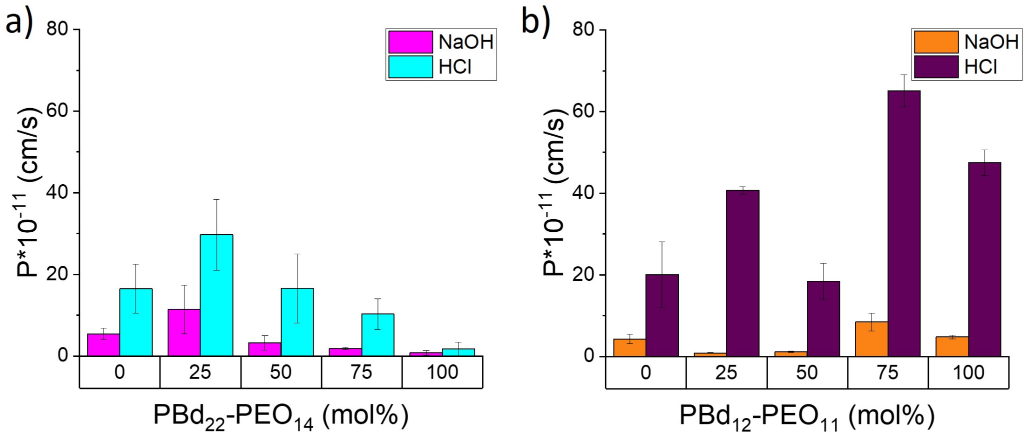

Figure 4.3: Comparison of permeability coefficients of PBd_{22}-PEO_{14}/POPC and PBd_{12}-PEO_{11}/POPC samples. Comparing permeability values after addition of 1 M HCl or NaOH to POPC vesicles with increasing a) PBd_{22}-PEO_{14} fraction and b) PBd_{12}-PEO_{11} fraction.

4.3 Conclusion

Previously, the proton permeability coefficient for lipid vesicles has been found to vary anywhere between 10^{-1} and 10^{-13} cm s^{-1} (109, 174, 175, 176). This wide range in coefficient values has been attributed to the membrane composition, the temperature and the calculation method. The rate of molecular traffic across a membrane is also dependent on the chemical and physical properties of the membrane, the number of lamellae, as well as the type of molecule being transported across the bilayer: small ions are thought to have low permeability coefficients (10^{-8} - 10^{-13} cm s^{-1}) while water has high permeability (10^{-3} cm s^{-1}) (108, 174). Here, NaOH and HCl were added to POPC vesicles with increasing mol% of PBd_{22}-PEO_{14} or PBd_{12}-PEO_{11} polymers and the resultant permeability coefficients were related to their membrane hydration.

For all the vesicle compositions, there is a net movement of ions across the membrane.

Overall, PBd_{22}-PEO_{14}/POPC vesicles were found to have lower permeability coefficients than PBd_{12}-PEO_{11}/POPC compositions. Generally, increasing PBd_{22}-PEO_{14} mole fraction decreased proton permeability, but on the other hand increasing lower molecular weight PBd_{12}-PEO_{11} mole fraction increased the permeability coefficient. Addition of HCl however, resulted in greater permeability for all compositions than addition of NaOH the the samples.

As the initial net movement of ions can be attributed to formation of transient pores from hydrophilic defects caused by thermal membrane fluctuations (172), future work could explore these mechanical membrane properties. Mechanical membrane properties such as membrane viscosity, packing and bending rigidities of PBd_{22}-PEO_{14}/POPC and PBd_{12}-PEO_{11}/POPC hybrid vesicles are explored further in Chapter 7.

5. Determining the membrane structure

In the past liposomes and polymersomes have been studied for bionanotechnology applications, however hybrid lipid-polymer vesicles could prove to be a promising alternative by combining the advantages of each material. Although there are many studies that demonstrate using hybrid vesicles for membrane protein reconstitution and drug delivery vectors, relatively few have focused on the relationship between hybrid vesicle membrane structure and membrane properties (34, 92, 95). Hybrid lipid-polymer vesicles can have multiple membrane structures depending on how well the lipid and polymer combination mix: hybrid membranes can form a well-mixed homogeneous membrane, or phase separate into domains. The polymers can also interdigitate, which reduces the thickness of the membrane. Whether the spherical membrane is phase separated or homogeneous, the bilayer can also be transversely asymmetric across the membrane, and relatedly, the curvature of the membrane might also play a role in composition across the membrane. Determining the structure of hybrid polymer/lipid vesicle membrane could help find what properties govern protein folding and stability, therefore could be used to enhance membrane protein function and durability in artificial systems.

Structure of membranes can be studied with several methods, including scattering techniques such as small angle x-ray or neutron scattering and cryogenic-transmission electron microscopy (cryo-TEM) (34). This chapter will focus on using cryo-TEM.

Lipid bilayer membranes have dipole potentials arising from the alignment of dipolar residues and water within the membrane. This is believed to affect the conformation and function of membrane proteins, although it is very difficult to measure (143, 145). The surface potential generated by lipid head groups changes the concentration of ions close to the membrane surface and ion uptake. This potential also depends on lipid structure and thus affects the permeability of ions across the membrane (145).

In cryo-TEM the image contrast is usually produced by a phase shift in the electron wave function from elastic scattering as it passes through the specimen. Neutral atoms produce contrast in electron microscopy because electrons passing through the atom electron orbitals experience a positive charge from the less-shielded nuclear charge. Additional electrostatic potentials, such as the dipole potential, adds to the contrast. The total phase shift is proportional to the integrated electrostatic potential (projected potential) along the path of the electron, making images from the microscope profiles of electrostatic potential, not electron density (143, 153) as discussed in Chapter 2. The magnitude and the profile of the dipole potential across the bilayer has previously been obtained by subtracting the contribution from the atomic potential from the cryo-TEM image intensity. Each individual membrane profile showed a consistent bilayer thickness for the liposome membranes. These profiles also displayed higher peak density in the inner leaflet which was expected from the crowding of head groups due to membrane curvature (143).

The bilayer thickness of liposomes made from phosphatidylcholine (PC) lipids with saturated and unsaturated acyl chains were measured and found to increase with increasing acyl chain length. Images show that saturated PCs have a multi-faceted morphology and a broad distribution in bilayer thickness, while unsaturated acyl PCs appear to have smooth, regular bilayers with a narrow bilayer thickness distribution (177).

Vesicles composed of polymers with increasing molecular weights were also imaged using cryo-TEM (37, 178, 179). While images of PBd-b-PEO polymers have usually just been used to confirm vesicle shape and lamellarity only (85, 178), measurements of the membrane thickness from images have also been made and compared to coarse-grain molecular dynamics (MD) simulations (179). One study even determined the hydrophobic core thickness from cryo-TEM images and found membrane thickness increased with increasing PBd-b-PEO molecular weight. Images of these polymersomes displayed Fresnel interference fringes, which were believed to correspond to abrupt changes in projected density at the inner and outer edges of the membrane so were used to determine the membrane thickness (37).

However, the majority of these studies use projection images (micrographs) taken by cryo-TEM for analysis rather than more involved cryo-TEM techniques such as cryo-electron tomography (cryo-ET) or single particle analysis methods. Even from these projection images, analyses only extend to measuring the vesicle membrane thickness, rather than an in-depth examination to determine the membrane structure. Although studies that use cryo-ET on vesicle membranes are emerging (92, 180, 181), few illuminate the structure of hybrid lipid-polymer membranes.

5.1 Method

LUVs were formed by the method outline in Section 3.2.1. The size of the vesicle was determined using DLS as detailed in Section 3.2.3. The size distributions from DLS for PBd_{22}-PEO_{14}/POPC and PBd_{12}-PEO_{11}/POPC compositions can be found in Appendices A4 and A5 respectively. The concentration of lipid was estimated by assuming full suspension of lipid film and no loss through extrusion. Cryo-TEM grids for projection images only were made as described in Section 3.2.4 and grids for tomography as outlined in Section 3.2.4. Further processing and analysis was completed on (Fiji is Just) ImageJ (FIJI).

In previous studies, membrane thickness was obtained by measuring the distance between the contrast interfaces of the inner and outer edges of the vesicle membrane (177, 179). For projection images of vesicles in all compositions, 12 measurement lines were taken across the membrane and then combined and averaged with measurements from other vesicles of the same composition.

5.1.1 Obtaining an electron intensity profile from projection images

Radial line profile

From a cryo-TEM projection image, an electron intensity profile of the membrane can be obtained manually using the radial profile plugin in FIJI, downloaded from `https://imagej.nih.gov/ij/plugins/radial-profile-ext.html`. From this profile, membrane thickness measurements can be taken as shown in Figure 5.1.

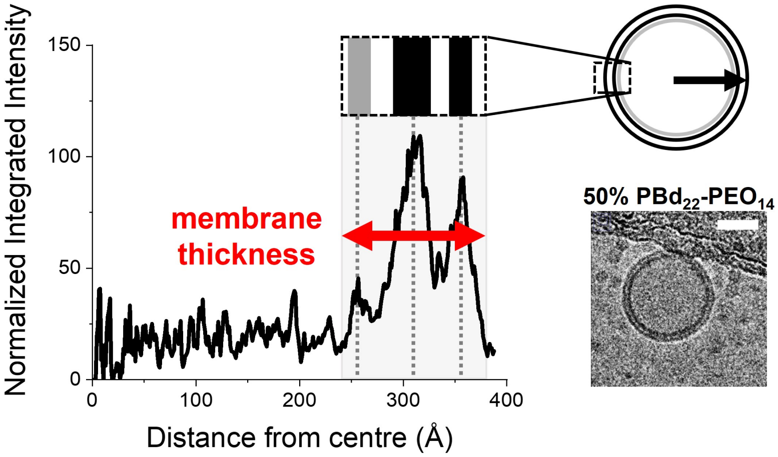

Figure 5.1: Performing radial profiles to find membrane thickness. Radial profiles of the pixel intensity on the images can be extrapolated to show the areas of high intensity in a vesicle membrane. The membrane thickness can also be obtained using this profile by measuring the distance from the start of the bilayer to the outer rim, as highlighted in green on the profile. Scale bar indicates 500 Å.

The bilayer thickness can also be extracted from the intensity profiles by taking the distance values from where the profile minima begin and end as shown by Figure 5.1.

Manual line profile

By manually choosing and drawing individual lines on projection images, the line profile positions can be changed through the slices in a stack as shown in Figure 5.2. The data has to be normalised to account for the differing ice thickness in a slice. As shown by Figures

5.2a and b, the line profiles from the vesicle centre are individually very noisy and some detail can be lost. The majority of the profile in Figure 5.2b is noise from the buffer in the lumen of the vesicle, which is unnecessary in finding the membrane structure. The vesicle radius is still uneven even within a slice, so the line profiles have to be translated so only the bilayer midpoint overlaps.

Line profiles can instead be taken just over the the membrane itself as shown in Figure 5.2c. Multiple line profiles can be measured, normalised and then translated to find the average bilayer intensity profile as shown in Figure 5.2d. In this way, data from non-spherical vesicles can also be collected.

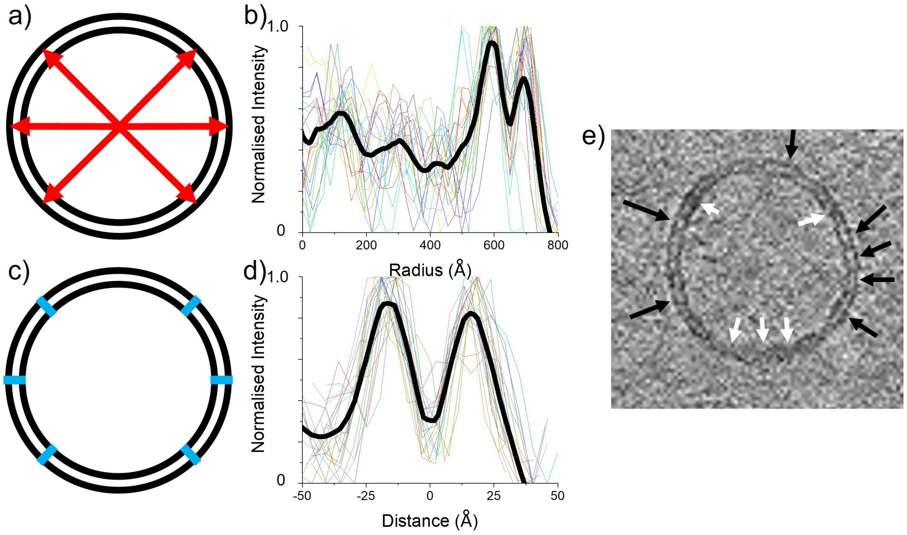

Figure 5.2: Obtaining membrane measurements using multiple line profiles. a) Several line profiles can be taken from the centre of a vesicle (red arrows) resulting in an b) electron intensity profile. c) Line profiles can also be measured across the membrane section only (blue lines). d) The line profiles profiles from c) are translated so the central minimum located between the two maxima are centred. e) The ideal regions to take line profiles are indicated by black arrows, while white arrows indicate which sections should not measured.

However, only sections of the vesicle membrane have a clear view of the membrane at the selected defocus setting, therefore the line profiles need to be taken at those sections as shown in Figure 5.2e.

Membrane measurements from tomogram images

From the electron intensity profile of each vesicle membrane within a sample, manual measurements of the membrane thickness and hydrophobic core thickness could be made.

The membrane thickness was manually measured by taking the full half width maximum (FWHM) of an intensity profile as shown in Figure 5.3. The membrane thickness values could also be determined by taking peak to peak measurements, although this might give an underestimate of the true bilayer thickness from cryo-ET images. Peak-to-peak values were assigned as the thickness of the hydrophobic core within a membrane.

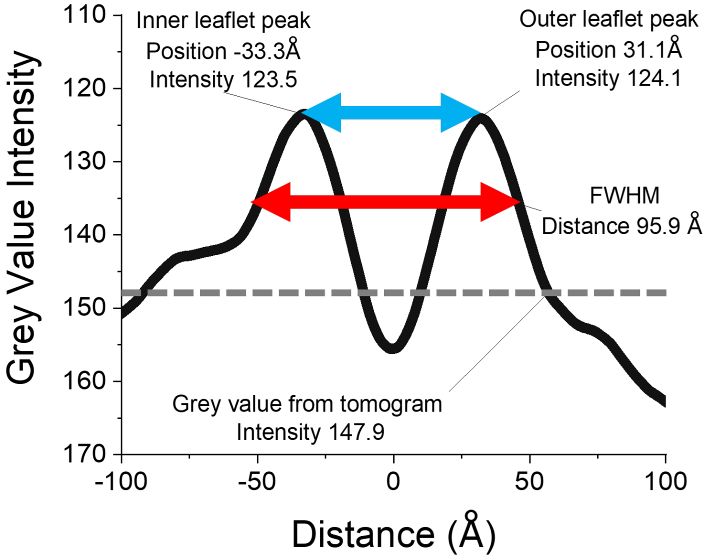

Figure 5.3: Determining the membrane thickness from an average electron intensity profile. The dashed grey line across the line profile indicates where the grey value on the tomogram lies on the profile. This number is used alongside the inner and outer leaflet y intensity values to find the y-value for the FWHM value, and thus the actual FWHM value indicated by the red arrow. The FWHM is assigned as the membrane thickness, while the peak-to-peak distance (blue arrow) indicates the hydrophobic core thickness.

To manually determine the FWHM measurement, the mean grey value of an empty area of the tomogram is found using FIJI. This mean grey value is considered the intensity of the buffer and is made the line profile baseline. Using the mean grey value, y_{grey}, and the average y value of the inner and outer leaflet peaks, y_{peak}, the y value of the FWHM can be found, y_{FWHM}, using the following equation:

$$y_{FWHM} = y_{grey} + \frac{y_{peak} - y_{grey}}{2} \tag{5.1}$$

With the resulting y_{FWHM} value, the inner and outer x values for the FWHM can be found and the bilayer thickness determined. Peak to peak measurements were also taken to find the hydrophobic core distance. As the mean grey value changes between tomograms, the average line profiles for each composition is standardised.

Automated analysis of tomogram images

An automated analysis using Python written by Dr. Caitlin Cornell was used to evaluate the presence of nanoscale domains membranes of different compositions (181). The code can be found at `https://github.com/caitlin-cornell23/cryoEMliposomes` and methods to use the code was discussed with Dr. Cornell.

Full description and mechanics of the script can be found from reference (181). Briefly, the tomogram slices were first Gaussian filtered using FIJI, and then transferred to the Python script. The script then highlights only the interfaces of high contrast at the membrane edges using a Canny-filter allowing a relative membrane thickness to be measured. This apparent bilayer thickness is defined as the minimum distance between pixels on the inner and outer leaflet. Bilayer measurements from 20-30 images of each pure vesicle composition were used to sort which observed distances in the hybrid compositions were categorised into L_o or L_d phases, or into thick and thin categories, to create a colour map.

The colour maps give the probability of the membrane thickness measurement corresponding to a thicker, extended membrane at 100% given in red, while thinner membrane thickness measurements are characterised in blue at 0%. White colour on the map indicates areas with 50% probability of a thick membrane as the measurement is the intermediate value between expected pure lipid or polymer membrane thickness. The sorted distances were mapped on to the individual tomogram images of each hybrid vesicle composition by calculating the probability of each observed distance corresponding to either the thick or thin distances. Using this method, the homogeneity of the membrane thickness within large, unilamellar hybrid PBd$_{22}$-PEO$_{14}$/POPC and PBd$_{12}$-PEO$_{11}$/POPC membranes can be extrapolated.

5.2 Results and discussion

5.2.1 Projection images

In microscopy, artefacts in the images are inherent due to the process of making the sample grids and obtaining the images. The white lines seen on the outer rim of the vesicles in Figure 5.4 were Fresnel lines and were an artefact from obtaining a high contrast image with high defocus. This means that the intensity profiles extracted from these images were not an accurate representation of the bilayers.

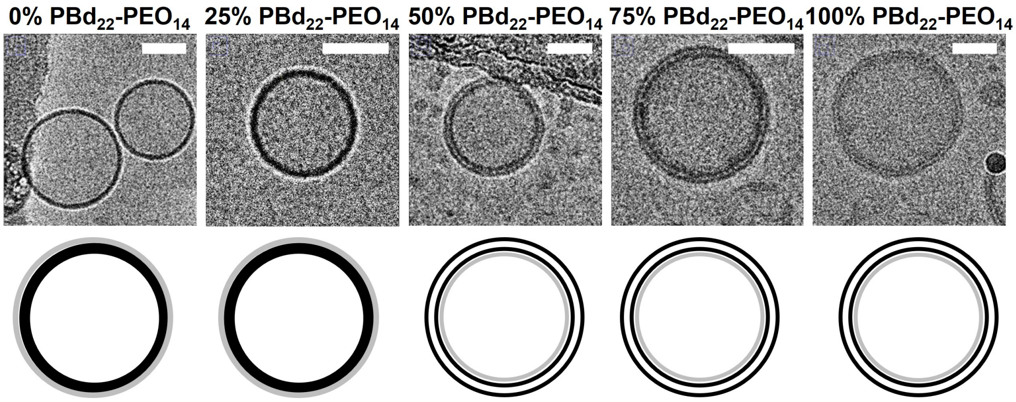

Figure 5.4: Projection images of PBd_{22}-PEO_{14}/POPC vesicle compositions. Images of PBd_{22}-PEO_{14} vesicles taken using the microscope with their graphical representations below. Images were taken at 6μm defocus and the scale bar indicates 500 Å.

Membrane thickness was obtained from these images by measuring the distance between the contrast interfaces of the inner and outer edges of the vesicle membrane. From Table 5.1 it can be seen that the bilayer thickness increases as the PBd_{22}-PEO_{14} mol% increases, with a significant rise in thickness between 25 mol% and 50 mol% PBd_{22}-PEO_{14} vesicles.

Table 5.1: Membrane thickness of hybrid PBd_{22}-PEO_{14}/POPC vesicles. Membrane thickness given here were measured by taking 12 line profiles across the vesicle membrane.

PBd_{22}-PEO_{14} (mol%)	Membrane Thickness (Å)	
	Average	Standard Deviation
0	47	7
25	51	9
50	96	12
75	87	13
100	106	14

The intensity profiles obtained using the radial profile plugin in FIJI displayed in Figure 5.5 show that as the PBd_{22}-PEO_{14} mol% increases, the membrane thickness increases and the intensity profile changes significantly. For the 50 mol% and higher mol% PBd_{22}-PEO_{14} vesicles the intensity profile is asymmetric, with a higher electron density and a third small peak present on the inner leaflet. This suggests that there is a higher intensity in the inner leaflet of the membrane however this could be due to a curvature effect of the membrane. In curved membranes, the inner leaflet is more curved than the outer leaflet, as the molecules are more tightly packed together which might give rise to a greater intensity when measured. However this feature could also be explained by the asymmetry across the bilayer, where more electron dense molecules are found in the inner leaflet of the membrane. The presence of the third small peak on the inner leaflet could also be explained by this, or it could be an artefact of using projection images for analysing bilayer structure.

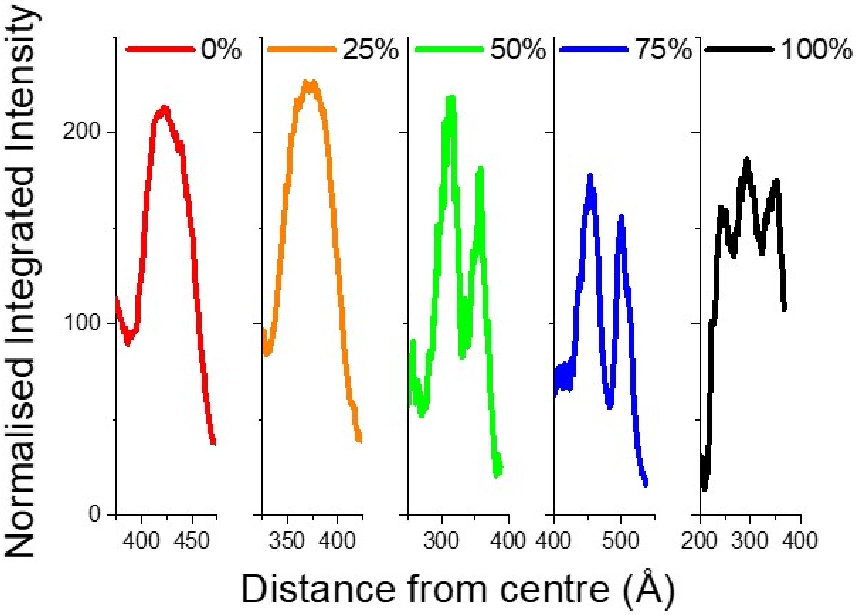

Figure 5.5: Initial radial line profiles of PBd$_{22}$-PEO$_{14}$/POPC vesicles. Radial profiles from multiple images were averaged to find the average integrated intensity distributions of hybrid PBd$_{22}$-PEO$_{14}$/POPC vesicle membranes.

5.2.2 Projection images vs tomograms

These results were collected using projection images from cryogenic grids on a Titan KRIOS microscope. The images have a high defocus of 6μm that allow the detail of the membrane intensity to be seen more clearly. The images themselves contain several artefacts which make analysing them difficult. In projection images of vesicles there can be a shadowing effect on the inner leaflet that appears because the view of the vesicle is through one focal plane, and does not take differing ice thickness into account. Coupled with the presence of Fresnel rings, and that over-focusing will increase the presence of Fresnel rings in the image, use of projection images to obtain intensity is not reliable as the images are not representative of the vesicle bilayer.

A better way of collecting data would be to collect tomograms of the cryo-grids. Here, the grids are tilted 120°, which means that the shadowing effects caused by differing ice thickness are reduced. In tomography the grid is rotated 120° so the image taken is through the centre of the sample.

With tomography, a large number of images are collected on just a few vesicles as 61 images are taken over the 120° rotation with 2° increments. Due to the rotation, vesicles previously thought to be purely spherical are shown to have prolate or oblate shapes. This means the analysis of the tomograms has to be more involved to get representative results. As with the projection images, it is possible to obtain the intensity profile for each vesicle by analysing the grey value intensity. This can be done by either using multiple line profiles across the membrane or by using the radial profile method previously mentioned.

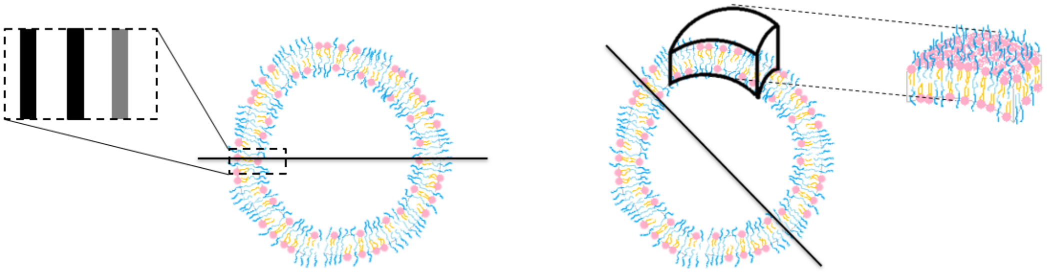

Figure 5.6: Differences between capturing projection images and tomography. Projection images show one view from the top through differing ice thickness. These images have more artefacts. In tomography the sample is rotated so there are different views of the sample resulting in 3-dimensional information. Multiple images are taken throughout the rotation and then the images are combined to form a rotational stack.

5.2.3 Tomograms

Each tomogram reconstructed with this method consists of approximately 60 slices and contains data on several vesicles. All tomogram reconstructions were carried out using the eTomo program in the IMOD suite. Tomogram reconstruction was optimised iteratively using a mixture of SIRT and back projection methods with different pixel binning values for different vesicle compositions. The ultimate aim was to find the method that resulted in high contrast images which clearly showed the features of each vesicle composition.

Initially, the tomograms were reconstructed with the SIRT method with pixel binning set to 2 for the 0 mol% PBd_{22}-PEO_{14} sample and therefore a resolution of 10.75 Å px^{-1}.

However, to be able to compare tomograms of vesicles with one composition against another, the same reconstruction and binning value had to be used. This meant compromising either how features were displayed, or image contrast. For the final analysis a filtered back projection with 10 iterations of SIRT radial filtering was used to reconstruct the tomograms. No pixels were binned to prevent artefacts in size measurements from forming. Tomogram analysis was then carried out using FIJI.

Originally radial profiles of each vesicle were taken to determine an electron intensity profile of the vesicle membrane. Figure 5.7 shows the radial profiles taken from a 100 mol% PBd_{22}-PEO_{14} vesicle from multiple slices. Figure 5.7b shows that the radial profile does deviate even between slices, which suggests that the radius is varying throughout the tomogram. From the tomogram itself it can be seen that the vesicle is not perfectly spherical and the membrane appears to be undulating, which explains why the radius is not constant in the radial profiles. Therefore using radial profiles to extract intensity data is not effective as most vesicles were imperfect spheres, and some had prolate or oblate shapes, which means the radius is not constant.

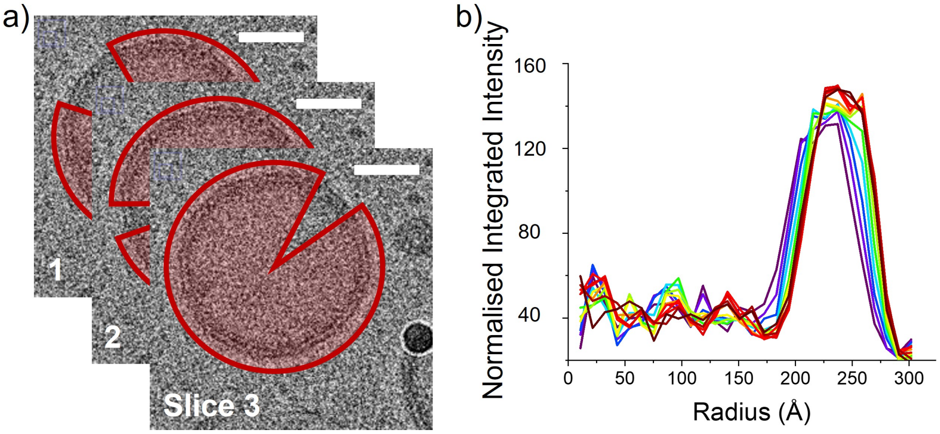

Figure 5.7: Obtaining membrane measurements using radial profile. a) Multiple radial profiles can be measured from the same vesicle if the profiles are taken from different slices. b) The profiles deviate even between slices, suggesting radius varies in a vesicle. The scale bar indicates 500 Å.

To account for membrane undulation multiple line profiles across the vesicle membrane could be used instead. However the main issue with this analysis method is that the statistical significance of the results is reduced, as instead of 360 line profiles being integrated against each other to give a radial profile, there are only a few line profiles per slice to determine the average bilayer structure for a vesicle.

To increase the statistical significance of the line profiles, more line profiles are needed per slice of a vesicle. The intensity profile of a vesicle membrane will change between vesicles, so each vesicle can therefore be treated as a separate ”experiment”. To fully represent the intensity of a vesicle composition multiple line profiles have to be drawn on each slice of a stack of images, and combined with the average line profiles of other vesicles to obtain the average intensity profile for that vesicle composition as shown by Figure 5.8.

It must be noted that the manual analysis of microscopy images is very subjective as it depends heavily on the view of the researcher.

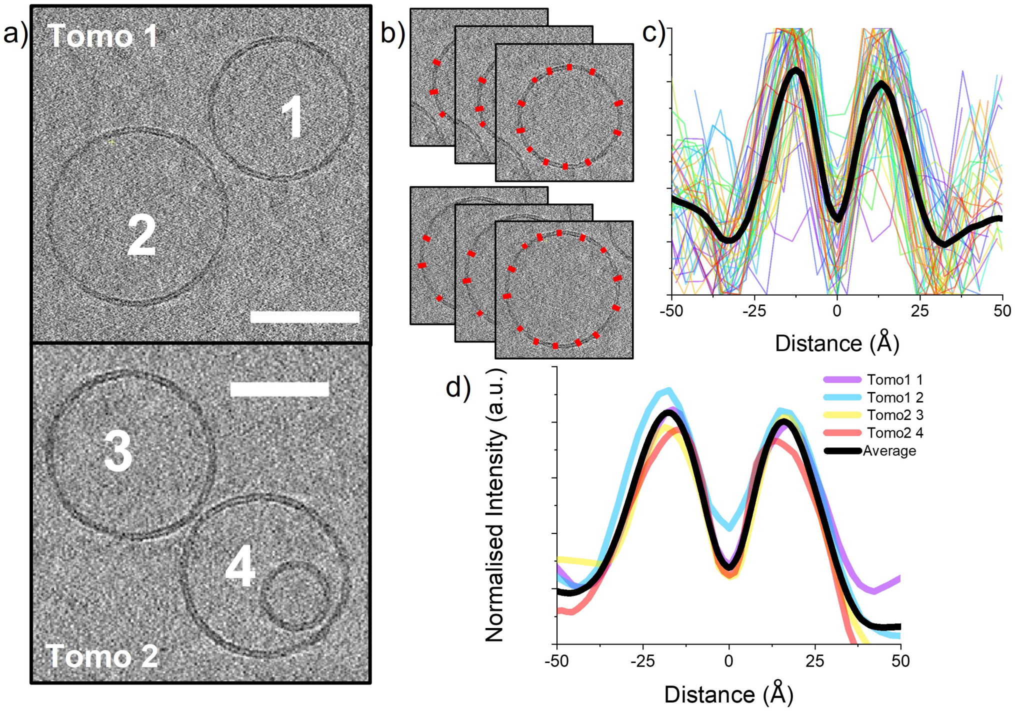

Figure 5.8: Final tomogram analysis method. a) Vesicles are selected from processed tomograms. b) Line profiles are taken across the membrane from different slices of each vesicle. c) These line profiles are translated so the minimum is centred and averaged to find the electron intensity profile for the vesicle. d) The intensity profiles from individual vesicles are combined to obtain the average electron intensity profile for that composition.

5.2.4 Bilayer measurements on tomograms

Usually, the bilayer thickness from cryo-TEM images of vesicles are measured by drawing a line from the inner and outer interfaces of high contrast (177, 179). As electron microscopy is an electron scattering technique, and has sub-angstrom resolution, it could be used to identify electron dense phosphates in lipid head groups (180). Therefore, by using cryo-ET, structural features such as bilayer thickness and hydrophobic core distance can instead be obtained by measuring the FWHM and peak-to-peak distances respectively from the resultant electron intensity profiles.

As shown by Figure 5.9g as PBd$_{22}$-PEO$_{14}$ mole fraction increases, the bilayer thickness also increases from 57.0 ± 2.8 to 97.2 ± 7.2 Å and hydrophobic core distance from 36.4 ± 2.2 to 65.8 ± 5.1 Å across 25 mol% and 100 mol% PBd$_{22}$-PEO$_{14}$ samples respectively. The increase in bilayer thickness between 0 mol% and 25 mol% PBd$_{22}$-PEO$_{14}$ samples is not statistically significant ($p > 0.05$, Tukey and Bonferroni ANOVA), suggesting PBd$_{22}$-PEO$_{14}$ polymer adapts to the lipid at low polymer fractions, while at high polymer fraction (> 25 mol%) the lipid adapts to the polymer thickness.

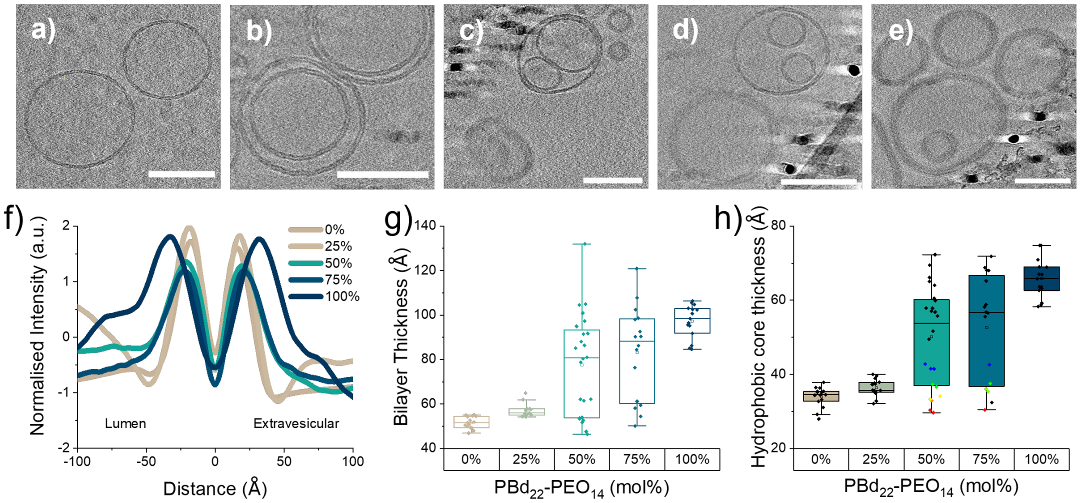

Figure 5.9: Average electron intensity profiles and associated images of PBd$_{22}$-PEO$_{14}$/POPC vesicles. Images of a) POPC, b) 25 mol%, c) 50 mol%, d) 75 mol% and e) 100 mol% PBd$_{22}$-PEO$_{14}$ vesicle compositions. Scale bar indicates 750 Å. The graphs show f) the average intensity profile, g) the individual membrane thickness measurements across the bilayer and h) the individual peak-to-peak measurements of 0-100 mol% PBd$_{22}$-PEO$_{14}$ vesicles.

While the bilayer thickness and hydrophobic core for 0 mol%, 25 mol% and 100 mol% are relatively narrow, Figure 5.9 also shows that there is a broad distribution for bilayer thickness (77.6 ± 22.3 Å , 83.2 ± 20.5 Å) and hydrophobic core (50.2 ± 13.2 Å , 52.7 ± 14.1 Å) in 50 mol% and 75 mol% PBd$_{22}$-PEO$_{14}$ samples , with some measurements grouped at thickness expected of a pure lipid membrane, while others were close to that of a pure PBd$_{22}$-PEO$_{14}$ polymer membrane. Images of individual vesicles in 50 mol% and 75 mol% compositions shown in Figure 5.9c and d. There are vesicles with two visibly different membrane thickness: in the same tomogram there are two bilayer thickness populations, population 1 with thickness < 65 Å, and population 2 with a thickness > 65 Å, indicating that the appearance of these two populations is not an artefact of the image analysis method.

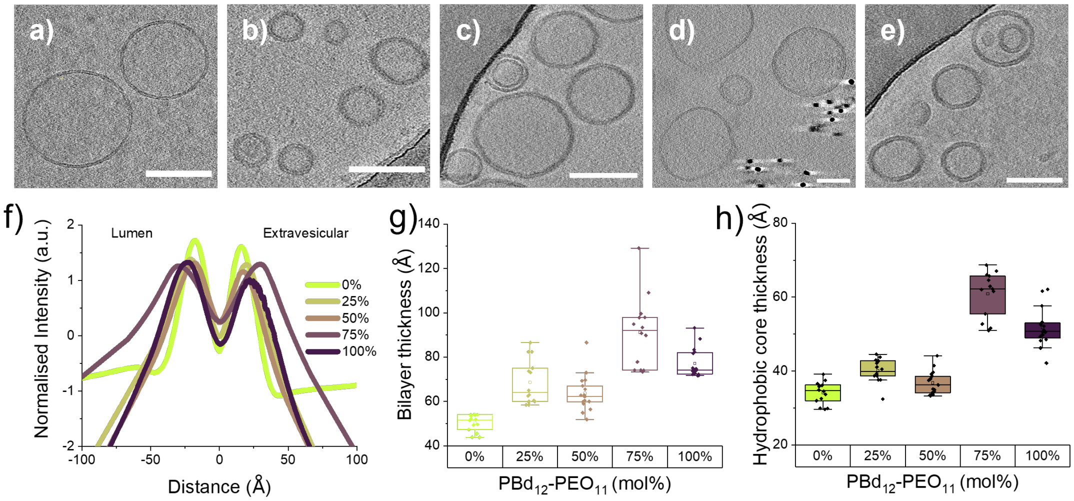

Figure 5.10: Average electron intensity profiles and associated images of PBd$_{12}$-PEO$_{11}$/POPC vesicles.Images of a) POPC, b) 25 mol%, c) 50 mol%, d) 75 mol% and e) 100 mol% PBd$_{12}$-PEO$_{11}$ vesicle compositions. Scale bar indicates 750 Å. The graphs show f) the average intensity profile and g) individual membrane thickness measurements across the bilayer and h) the individual peak-to-peak measurements of 0-100 mol% PBd$_{12}$-PEO$_{11}$ vesicles.

PBd$_{12}$-PEO$_{11}$ vesicle compositions were analysed in the same way. There was a more gradual increase in bilayer thickness and hydrophobic core distance as PBd$_{12}$-PEO$_{11}$ mole fraction increased in PBd$_{12}$-PEO$_{11}$ hybrid vesicles. However, there was a statistically significant increase between 0 mol% and 25 mol% PBd$_{12}$-PEO$_{11}$ vesicle samples (from 51.6 ± 2.5 Å to 68.6 ± 9.6 Å) and again between 50 mol% and 75 mol% PBd$_{12}$-PEO$_{11}$ compositions (from 64.8 ± 7.8 Å to 91.1 ± 15.4 Å). Surprisingly, 75 mol% PBd$_{12}$-PEO$_{11}$ vesicles appeared to have a larger bilayer thickness than 100 mol% PBd$_{12}$-PEO$_{11}$ vesicles (75.91 ± 6.4 Å). The difference in rigidity between POPC and PBd$_{12}$-PEO$_{11}$ may cause the polymer to favour extension in 25 mol% and 75 mol% samples, thus increasing the bilayer thickness and hydrophobic core measurements.

50 mol% PBd_{12}-PEO_{11} has the smallest bilayer thickness and hydrophobic core amongst the hybrid compositions, which could be due to the polymer interdigitating. This can be observed in some tomogram images where the leaflets of 50 mol% PBd_{12}-PEO_{11} are less distinctive than the 75 mol% PBd_{12}-PEO_{11} hybrid membranes. 50 mol% PBd_{12}-PEO_{11} samples also have a broad thickness distribution that encompasses both pure lipid and purePBd_{12}-PEO_{11} polymer, potentially due to the existence of 2 bilayer populations. However, no visibly distinct membrane thickness populations were observed PBd_{12}-PEO_{11} samples.

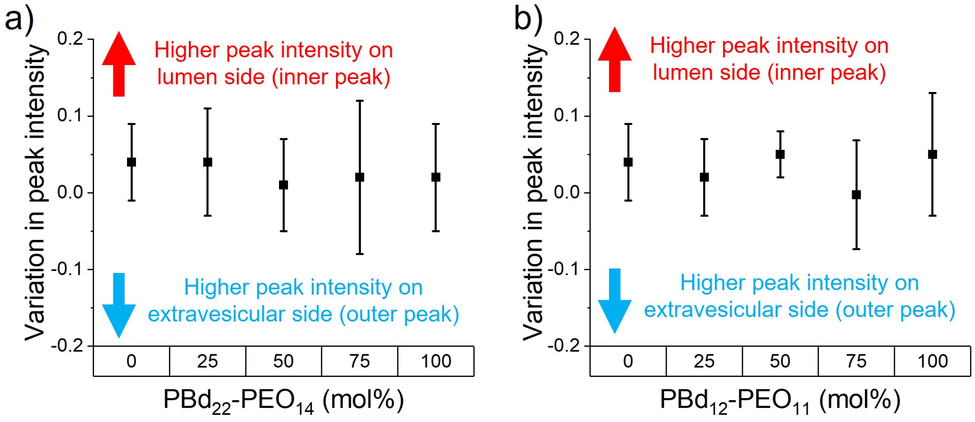

Figure 5.11: Asymmetry in hybrid vesicles. Variation in peak intensity was measured to find an asymmetry value using Equation 5.2. The asymmetry values of a) PBd_{22}-PEO_{14}/POPC and b) PBd_{12}-PEO_{11}/POPC hybrid vesicle compositions suggest no vesicles measured had transverse asymmetry.

The variation in peak intensity values in individual vesicles were used to determine asymmetry in the membrane as consistently high differences between the inner and outer peaks would imply greater electron density in one leaflet. Variation in peak intensity, and thus as asymmetry was calculated from fractional differences between the inner and outer leaflet intensities, I_{inner} and I_{outer} respectively:

$$Variation = \frac{I_{inner} - I_{outer}}{I_{inner} + I_{outer}} \tag{5.2}$$

Variation values towards 1 indicates high intensity in the inner (lumen leaflet) peak, while values towards -1 imply high peak intensities in the outer (extravesicular leaflet) peak. All variation values are above 0, indicating that the inner leaflet has a higher electron intensity overall. However, the variation values are also < 0.05 for all compositions, including 0 mol% and 100 mol% compositions as shown by Figure 5.11, suggesting that none these vesicle compositions have transverse asymmetry. The pure lipid and polymer vesicles cannot have compositional asymmetry as they are single component systems, therefore the apparent asymmetry is most likely a curvature effect. The higher inner peak intensity that leads to a variation value > 0 could be due to membrane curvature rather than transverse asymmetry within the membrane.

Lateral asymmetry and single-component domains were also not observed in either PBd_{22}-PEO_{14} and PBd_{12}-PEO_{11} polymer hybrid compositions using this analysis, implying that both lipids and polymers are present in inner and outer bilayer leaflets. The individual line profiles from different points and slices of a vesicle from a tomogram did not significantly change, suggesting that within a vesicle, the bilayer thickness remained the same. To confirm this, the relative bilayer thickness within individual membranes was measured by automated analysis, discussed in more detail below.

5.2.5 Vesicle morphology

Cryo-TEM can also be used to confirm vesicle shape and morphology. While the majority of vesicles have a spherical shape, some individual vesicles displayed interesting features. Pure POPC lipid, 0 mol% PBd_{22}-PEO_{14}, vesicles seem to be multi-lamellar or have intra-lumenal vesicles and some of the larger diameter vesicles of this composition appear faceted. While there are intra-lumenal and multi-lamellar vesicles in all compositions, the fraction of these seems to decrease with increasing PBd_{22}-PEO_{14} mole fraction. Some vesicles in 25 mol% PBd_{22}-PEO_{14} sample also appear to be faceted, however, these vesicles generally appear smaller than the 0 mol% vesicle composition. Worm-like micelles and elongated vesicular structures have also been observed in 50 mol% and 75 mol% PBd_{22}-PEO_{14} vesicle samples. As stated earlier, vesicles in the 50 mol% and 75 mol% PBd_{22}-PEO_{14} samples appear to have two different bilayer populations, and these differences can be seen clearly on the image as shown by Figure 5.12. Pure polymer PBd_{22}-PEO_{14} vesicles also have indistinct outer edges, indicative of a hydrated hydrophilic corona on the inner and outer edges of a hydrophobic core, similar to a lipid membrane.

Tomograms of 75 mol% PBd_{12}-PEO_{11} composition also display intra-lumenal vesicles alongside vesicles with unique shapes and high curvature in comparison to the anticipated spherical shape. Although worm-like micelles were present in all PBd_{12}-PEO_{11} containing vesicles, they were most prominent in the 50 mol% PBd_{12}-PEO_{11} sample.

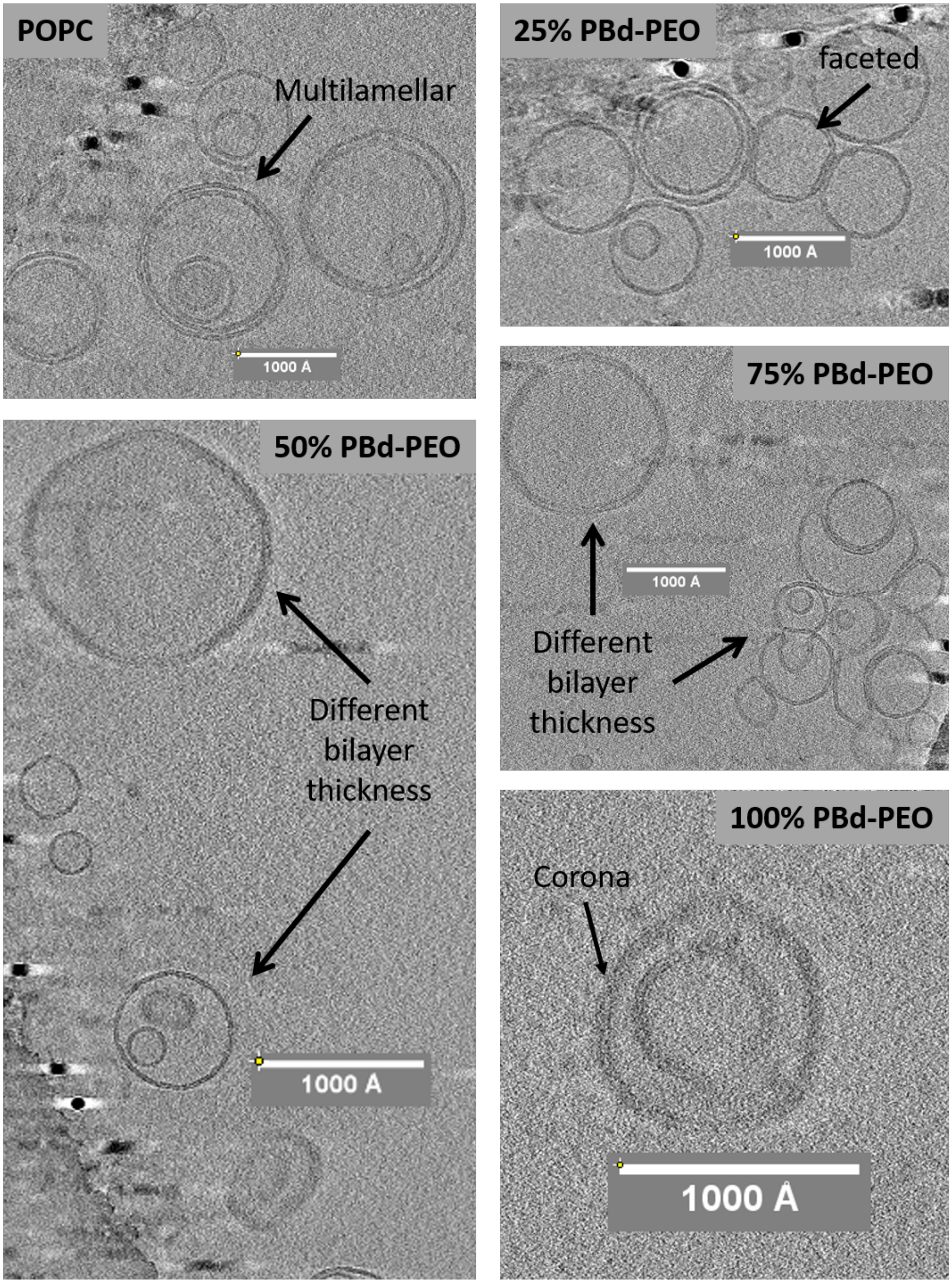

Figure 5.12: Example images of PBd_{22}-PEO_{14}/POPC hybrid vesicles. Images of a) 0 mol%, b) 25 mol% c) 50 mol% d) 75 mol% and e) 100 mol% PBd_{22}-PEO_{14} vesicles from tomograms.

5.2.6 Bilayer populations within hybrid vesicles

The bilayer thickness and hydrophobic core measurements shown in Figure 5.9 have a large standard deviation for 50 mol% and 75 mol% PBd_{22}-PEO_{14} vesicles, indicating a range of values for these compositions. Exploring more closely, two groups of vesicles with the 50 mol% and 75 mol% PBd_{22}-PEO_{14} compositions begin to emerge: population 1 in both 50 mol% and 75 mol% PBd_{22}-PEO_{14} compositions have a thin membrane thickness < 65 Å, while membrane thickness measurement of population 2 vesicles infer a thicker membrane as the values (> 90 Å). The presence of two distinct populations within hybrid samples are statistically significant to within 95% confidence (Tukey and Bonferroni ANOVA), indicating the membrane thickness values from 50 mol% and 75 mol% PBd_{22}-PEO_{14} samples do not have a broad distribution in values.

On the other hand, PBd_{12}-PEO_{11} vesicle compositions do not appear to have bilayer populations, perhaps due to the smaller difference between polymer and lipid bilayer thickness.

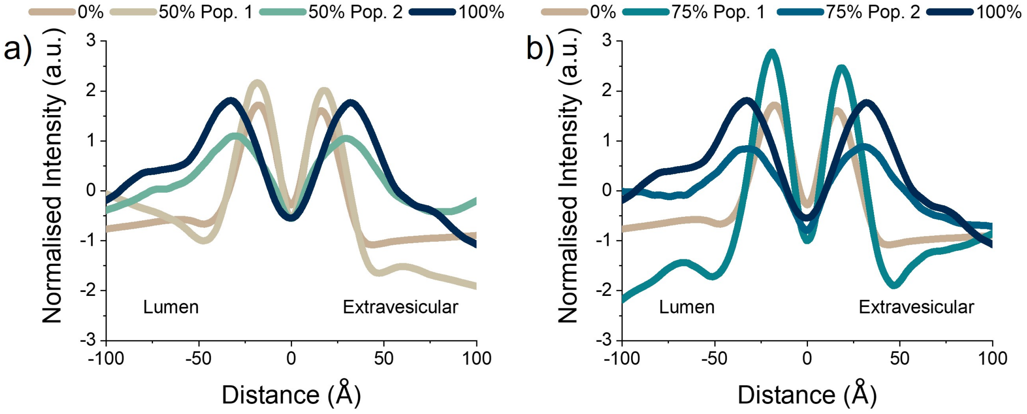

Figure 5.13: Electron intensity profiles of two bilayer populations within 50 mol% and 75 mol% PBd_{22}-PEO_{14} vesicles. Electron intensity profiles of 0 mol%, 100 mol% and population 1 and 2 of a) 50 mol% and b) 75 mol% PBd_{22}-PEO_{14} vesicle compositions. Population 1 (Pop. 1) of both 50 mol% and 75 mol% compositions has a profile like 0 mol% indicating a thin membrane, while population 2 (Pop. 2) of both compositions have thick membrane.

As demonstrated above, there appear to be two bilayer populations in 50 mol% and 75 mol% PBd_{22}-PEO_{14} tomograms. The membrane thickness of the vesicles in these samples could therefore correlate with vesicle diameter, or vice versa. As the difference in bilayer thickness of the thick and thin populations in hybrid PBd_{22}-PEO_{14} vesicles is quite large, the vesicles can be categorised into thin membranes or thick membranes, by visual observation alone. The diameters of approximately 200 vesicles in 50 mol% PBd$_{22}$-PEO$_{14}$ and 100 vesicles in 75 mol% PBd$_{22}$-PEO$_{14}$ across 5 different tomograms were measured and the resulting histograms of vesicle diameter in the thick and thin populations are shown in Figure 5.14.

As shown by Figure 5.14, in the 50 mol% PBd$_{22}$-PEO$_{14}$ sample, small vesicles appear to have both a thick and thin membrane. For this sample then, the relationship between membrane thickness and vesicle diameter is not statistically significant ($p < 0.05$, Tukey and Bonferroni ANOVA). The solid lines indicate both the thick and thin membrane populations in 50 mol% and 75 mol% PBd$_{22}$-PEO$_{14}$ samples have monomodal Gaussian distributions for the observed vesicle diameters.

However, in 75 mol% PBd$_{22}$-PEO$_{14}$ sample, small vesicles appear to have thinner membranes, while large diameter vesicles have thicker membranes. This observation is statistically significant to within 95% confidence (Tukey and Bonferroni ANOVA). PBd$_{22}$-PEO$_{14}$ membranes such as 75 mol% PBd$_{22}$-PEO$_{14}$ vesicles would be expected to have a thicker membrane and a higher bending rigidity than POPC, and so may preferentially form vesicles with diameters above a certain threshold to reduce generation of structures with high curvature.

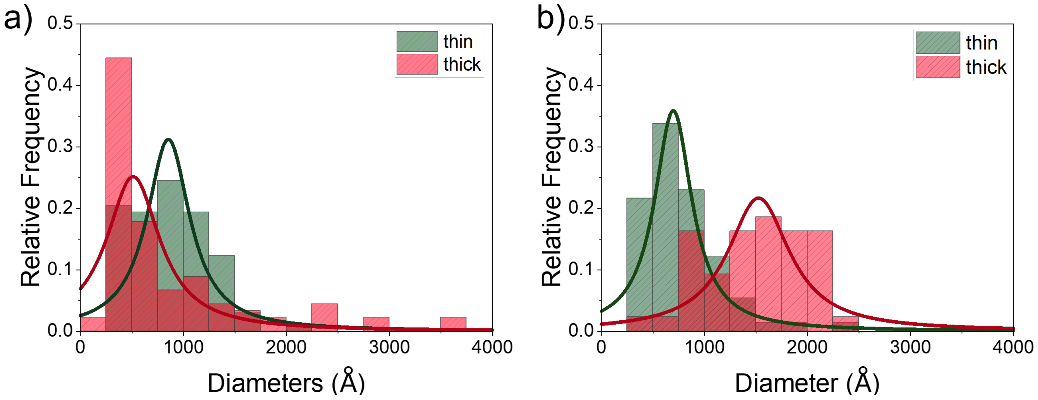

Figure 5.14: Histograms of diameters found in hybrid mol% PBd$_{22}$-PEO$_{14}$ vesicles. Histograms of the diameters of the thick and thin populations in a) 50 mol% and b) 75 mol% PBd$_{22}$-PEO$_{14}$. The solid lines indicate both the thick and thin membrane populations in 50 mol% and 75 mol% PBd$_{22}$-PEO$_{14}$ samples have monomodal Gaussian distributions for the observed vesicle diameters.

5.2.7 Automated analysis to determine phase separation

An automated analysis using Python written by Dr. Caitlin Cornell was used to evaluate the presence of nanoscale domains membranes of different compositions (181). The Python script results in a colour map that gives the probability of a membrane thickness measurement corresponding to a thicker, extended membrane, with 100% probability of a thick membrane given in red, while thin membrane thickness measurements are characterised in blue at 0% probability of a thick membrane. White colour on the map indicates areas with 50% probability of a thick membrane as the measurement is the intermediate value between thick and thin membrane thickness categories.

For all PBd_{22}-PEO_{14} hybrid vesicle compositions, the colour maps reveal that the bilayer thickness is consistent throughout the vesicle, representative maps displayed in Figure 5.15. The absence of different colours, and therefore membrane thickness, implies a homogenous distribution of POPC and PBd_{22}-PEO_{14} polymer within the membrane. However, occasionally measurements were taken along one leaflet rather than between two leaflets, culminating in an anomalous phase result and colour assignation. These values were discarded by visual inspection of the measurement lines on the filtered images.

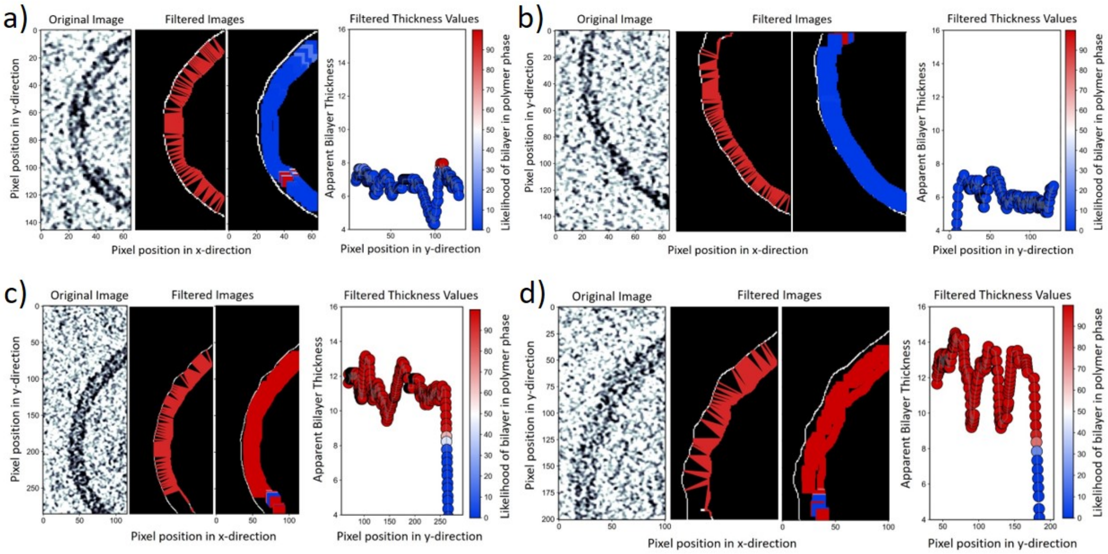

Figure 5.15: Results from automated analysis on PBd_{22}-PEO_{14}/POPC hybrid vesicles. The original image is the input for the code. The image is filtered and measurements taken across the bilayer to determine which "phase" the bilayer is in as a colour map of % likelihood the bilayer in a polymer phase. a) 25 mol% PBd_{22}-PEO_{14}, b) 50 mol% PBd_{22}-PEO_{14} (population 1), c) 50 mol% PBd_{22}-PEO_{14} (population 2) and d) 75 mol% PBd_{22}-PEO_{14} (Population 2).

Figure 5.15 shows thin membranes in 25 mol% PBd_{22}-PEO_{14} and population 1 of 50 mol% PBd_{22}-PEO_{14} samples have a low proportion of thick measurements within the membrane; the membrane is thin. On the other hand, population 2 of 50 mol% and 75 mol% PBd_{22}-PEO_{14} samples have a high proportion of thick membrane measurements existing in the membrane. The same automated analysis was also carried out on the shorter chain PBd_{12}-PEO_{11} hybrid compositions. Their analysis was carried out by G. Coates during her Master's project.

From Figure 5.10 the average bilayer thickness for 25 mol% and 75 mol% PBd_{12}-PEO_{11} vesicles is higher than pure POPC membranes. The automated analysis confirms this as these vesicle compositions have a high proportion of thick membrane measurements. Considering Figure 5.10 again for 50 mol% PBd_{12}-PEO_{11} sample, the distribution of bilayer thickness values, although small, encompasses both pure lipid and pure polymer bilayer thickness. The automated analysis shows that 36% of 50 mol% PBd_{12}-PEO_{11} vesicles had thin or intermediate bilayer thickness, while 64% appeared thicker or with an intermediate bilayer thickness, implying presence of 2 bilayer thickness populations within 50 mol% PBd_{12}-PEO_{11} samples.

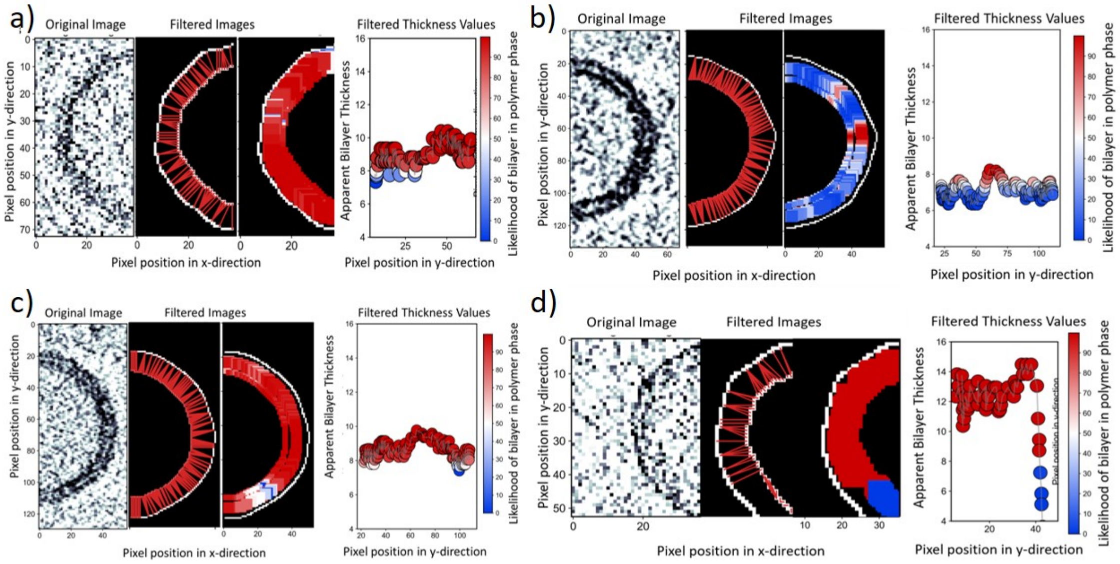

Figure 5.16: Results from automated analysis on PBd_{12}-PEO_{11}/POPC hybrid vesicles. The original and filtered images with the measurement lines and determined phase as a colour map of % likelihood the bilayer in a polymer phase of a) 25 mol% PBd_{12}-PEO_{11}, b) 50 mol% PBd_{12}-PEO_{11} (population 1) c) 50 mol% PBd_{12}-PEO_{11} (population 2) and d) 75 mol% PBd_{12}-PEO_{11}.

Although the script automates the image analysis and gives a visual evaluation of the hybrid lipid/polymer membrane thickness, the manual analysis method still has advantages. To generate good results from the automated script, the tomogram slices have to carefully filtered, causing some of the structural details to be lost from the image. In the manual line profile method, no image adjustments are required, so subtle structural details can be retained and captured. The final results from the automated script are also relative thickness values rather than the absolute thickness values obtained by the manual line profile method. However, with further optimisation, this automated script could be a powerful tool to analyse tomography images of hybrid lipid/polymer vesicle membranes.

5.3 Conclusion

Electron microscopy (EM) allows the high resolution observation of small objects by using accelerated electrons. The electrons interact with the sample to produce a phase shift that is dependent on the electron potential across the sample. The electron exiting the grid is measured by a detector which then produces an image. In cryo-transmission electron microscopy (cryo-TEM), samples are fixed in vitreous ice, which allows the sample to remain in its native state while it is being imaged. Previous studies on vesicles use projection images, or micrographs, to view and confirm the presence of vesicles in the samples (177, 182, 183). However these micrographs cannot be used for structural analysis by themselves as they contain imaging artefacts such as shadowing from out of plane features. During tomography, the sample grid is tilted to image the sample with a low electron dose at different rotations, which reduces some of the artefacts from imaging on a single plane. The pixels in the resulting images contain intensity values related to the atomic potentials across the sample. Line profiles can be drawn across the image to find the intensity values across the vesicle membrane, which can then be used to determine the possible membrane structure.

Here, POPC phospholipid has been mixed with PBd_{22}-PEO_{14} and PBd_{12}-PEO_{11} amphiphilic block copolymers to form hybrid membranes. Depending on the lipid-polymer composition, the membrane can form a well-mixed homogeneous membrane, or phase separate into domains. The polymers can also interdigitate, which reduces the thickness of the membrane.

For vesicles, the bilayer thickness of the membrane can be determined by averaging multiple line profiles at different slices of each vesicle. Then average line profiles of each vesicle can be combined together to give the average intensity profile for a vesicle composition. Using these line profiles, the FWHM (bilayer thickness) and peak-to-peak (hydrophobic core) of each vesicle could be measured.

Generally, membrane thickness was found to increase with increasing polymer fraction, from 51.6 Å for a pure lipid system to 97.2 Å in pure PBd_{22}-PEO_{14} vesicles and 75.9 Å for small molecular weight PBd_{12}-PEO_{11} vesicles. In 50 mol% and 75 mol% PBd_{22}-PEO_{14}

hybrid vesicles, two bilayer populations were found: vesicles could be categorised by a visibly thick or thin membrane and homogeneity within these populations were confirmed using an automated analysis. This presence of two populations within PBd$_{22}$-PEO$_{14}$ hybrid samples suggests an uneven distribution of lipids and polymers in each vesicle. This is discussed in more detail in Chapter 6.

Surprisingly, automated analysis distinguished vesicles within 50 mol% PBd$_{12}$-PEO$_{11}$ into thin and thick membrane categories, even though no bilayer populations within this sample were observed in the line profiles and tomogram images themselves. The steep increase in membrane thickness at 25 mol% and 75 mol% PBd$_{12}$-PEO$_{11}$ vesicles indicate that the difference in material rigidity between POPC and PBd$_{12}$-PEO$_{11}$ may cause the polymer to favour extension in these samples, thus increasing the bilayer thickness and hydrophobic core measurements.

Cryo-ET can provide a lot of information on the structure of a sample and revealed an electron intensity profile of membranes for different vesicle compositions, the bilayer thickness and the presence of different bilayer thickness populations. The results are unique as small details and features are made visible, but are perhaps not representative of the entire sample. Combining cryo-ET with another technique such as SAXS would provide more insight into the average hybrid lipid-polymer membrane structure found in a sample.

6. Combining techniques to probe membrane structure

In Chapter 5 the structure of hybrid vesicles was studied with cryogenic transmission electron microscopy (cryo-TEM). Small angle x-ray scattering (SAXS) has historically also been used to obtain structural information about lipid membranes using large unilamellar vesicles (LUV) or multi lamellar vesicles (MLV) (137, 184, 185, 186). The scattering profile collected using SAXS can be fitted with a model that can be transformed into an electron density profile for the membrane.

In lipid membranes, changes to the membrane structure caused by vesicle composition (187, 188), lamellarity (189), temperature (190) and vesicle size (132) have been monitored by SAXS. For DOPS lipid vesicles with sizes less than 620 Å, the bilayer was found by SAXS and small angle neutron scattering (SANS) to be symmetric, however for vesicle sizes of 1220 Å, DOPS was shown to have an asymmetric membrane, thought to form due to geometrical constraints and electrostatic interactions rather than curvature alone (132, 187). Combining the results of scattering profiles of DOPC, DMPC and DLPC LUV and MLV membranes showed that increasing the chain length of the lipid does increase the thickness of the hydrophobic core region in the electron density profiles (189).

Polymer membranes have also been investigated using SAXS to observe how polymer architecture affects membrane structure. Transmission electron microscopy (TEM) was used in conjunction with SAXS to determine the PEO brush length and hydration of poly(butylene oxide)-block-poly(ethylene oxide) (PBO-b-PEO) membranes with different molecular weights. The study showed that there was an increase in PEO corona length with increasing polymerisation, however uranyl acetate was used stain the sample to improve image contrast, which may bias the results. In this study, using uranyl acetate allowed measurements of the PEO brush length to be taken and compared to the degree of PBO-b-PEO polymerisation (191). Although uranyl acetate can be used to improve contrast, it can create image artefacts by causing a fine grain in the image as uranyl ions bind to functional groups within the membrane, generating only an outline of the particle and losing all internal information (156, 192). In applying the stain, another layer of carbon is deposited, which increases background noise (156). In addition to this, uranyl acetate is very sensitive towards light and will precipitate if exposed, potentially causing drying artefacts and flattening the object (156, 192). Cryo-TEM provides more detail of a membrane without causing dehydration and staining artefacts to occur. It has been used to confirm the shape and lamellarity of vesicle samples and compare alongside SAXS results (85, 178).

The advantage of SAXS is that it is an ensemble technique that provides an average structure for an object. However, the scattering pattern can be problematic to model without some known structural information (193) and smaller local structural details about the sample are not available. As demonstrated in Chapter 5, use of cryogenic electron tomography (cryo-ET) for examination of the bilayer provides high-resolution information about the imaged object, however the results are always specific with respect to analysed vesicles rather than representative of the whole sample. With single particle analysis (SPA), distributions of a vesicle membrane can be observed and not just average membrane structure of the entire sample. However, electron microscopy techniques are only able to analyse $10^1 - 10^3$ vesicles at one time, whereas SAXS can collect data from the entire sample, approximately ranging from $10^{10} - 10^{13}$ vesicles at once.

On their own, these techniques are powerful but have their limitations. Used together however, the information gained from one technique can be used to inform and optimise the other. SAXS gives a radial average of a scattering pattern of the sample, unveiling the structure in 1D, providing information on both the vesicle diameter and the membrane architecture whereas cryo-ET can yield a 3D density map of similar resolution after post-acquisition computation (193, 194). Scattering profiles from SAXS must be fitted with a model, which usually contains an ensemble of solutions, some of which would not represent the structure (193). To determine robust measurements of the bilayer thickness and peak-to-peak distances, the details found using cryo-ET can be used to ensure and fine tune a fitting model for SAXS scattering curves.

Previously, the planar correlations from unaligned cryo-TEM images have been related to SAXS profiles using an Abel transform (193). Fully reconstructed 3D structures obtained using cryo-TEM have also been used to obtain theoretical SAXS curves and compared to experimental SAXS profiles (194). The SAXS scattering pattern is the result of a Fourier transform of the electronic density correlation function and reveals low resolution sample features (194). Used in conjunction with cryo-TEM, the ensemble of solutions suggested by SAXS can then be trimmed to give the most probable sample structure for subsequent refinement steps.

Electron intensity line profiles from cryo-ET can be used to constrain the model for SAXS to create a model for hybrid membranes. In this case information about the bilayer thickness, the presence of different bilayer populations and the possible fraction of each bilayer population can be used to inform the decisions made when creating a model for SAXS data.

6.1 Methods

6.1.1 Small angle x-ray scattering

Vesicles were prepared as described in Section 3.2.1. The same vesicles formed for cryogenic electron tomography (cryo-ET) experiments were used for the collection of small angle x-ray scattering (SAXS) scattering profiles. Vesicle samples were also characterised by size using dynamic light scattering (DLS) as outlined in Section 3.2.3. The size characterisation results can be found in Appendix A4. Samples were prepared for SAXS as described in Section 3.2.5.

Scattering profiles from SAXS must be fitted with a model, which should reflect the known structural knowledge on the studied system as appropriately as possible (193). The resolution of the SAXS information is governed by the maximum q that you can measure above the noise level. The bilayer thickness of the hybrid vesicles provided by analysis of cryo-ET tomograms in Chapter 5 were used to inform the refinement process and reduce the number of possible model solutions to give the most probable sample structure. The samples used for SAXS were dilute, with a polydispersity index < 0.250, so no contribution from a structure factor was anticipated and the scattering profiles can be modelled with a form factor alone. Full explanation for the form factors can be found in Section 2.2.2.

As previously outlined in Section 2.2.2, the form factor usually used to model lipid bilayers uses 2 Gaussians to represent polar head groups at positions $\pm z_H$ and methyl groups at the centre of the lipid bilayer, $z = 0$, given by Equation 2.23. This 2-Gaussian model can be made more complex by expanding to 3, or even 4-Gaussians, as described by Equation 2.25, potentially to account for interdigitation within the polymer membranes shown by Figure 6.1. Initially, the 2-Gaussian model in Equation 2.23 was used on all PBd_{22}-PEO_{14} membrane compositions. Equation 2.25 was then introduced to fit the pure PBd_{22}-PEO_{14} vesicles.

For hybrid samples, the fitting functions from Equations 2.23 and 2.25 for the pure lipid and polymer membranes were combined. A weighting factor, w, was applied to find the fraction of thin membrane and thick membrane vesicles in the hybrid sample:

$$F_{hybrid} = (1 - w)F_{2G} + wF_{4G} \tag{6.1}$$

The output to Equation 6.1 gives two electron density profiles, which correspond to thin and thick membrane vesicles within the hybrid samples.

Equation 2.20 in Section 2.2.2 giving the ”Bilayered Vesicle” model from SASfit analysis program was also applied to the 100 mol% PBd_{22}-PEO_{14} polymer vesicle scattering intensity profiles, the results of which are presented in Appendix A7.1.

The 4-Gaussian and hybrid models to fit the SAXS scattering intensity patterns of polymer and hybrid vesicles was created in collaboration with Prof. Michael Rappolt, Chair in Lipid Biophysics, and Dr. Amin Sadeghpour, teaching fellow within the School of Food Science and Nutrition. Prof. Michael Rappolt performed the fitting analysis using the Gaussian models on the PBd$_{22}$-PEO$_{14}$/POPC vesicle SAXS data.

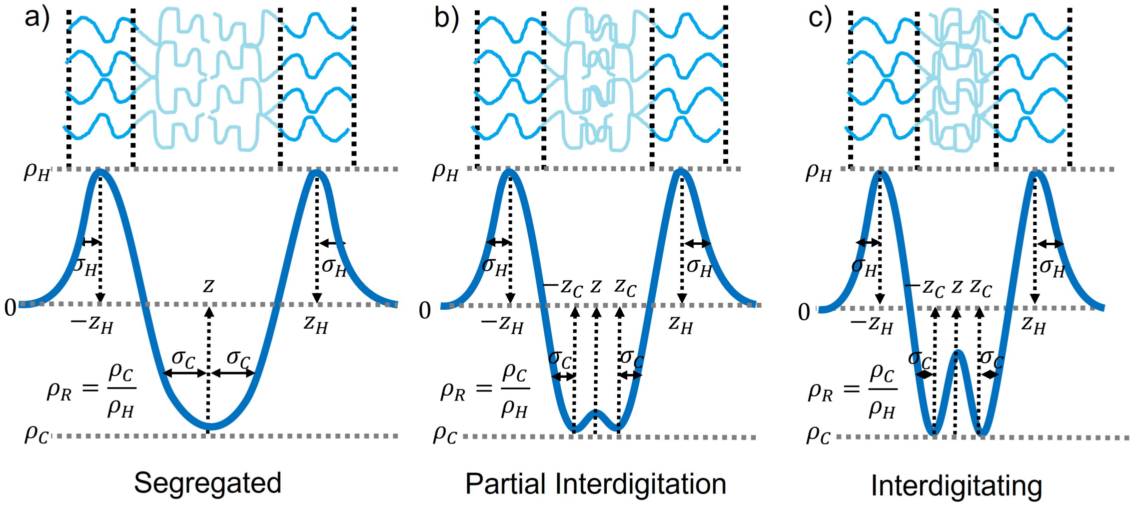

Figure 6.1: Example electron density profile models of polymer membranes from SAXS scattering patterns. The electron density profile of a polymer membrane can be retrieved from scattering intensity curves obtained by SAXS. The scattering curves for polymer membranes bilayers can be fitted with a a) 2-Gaussian model, which can be expanded into a 4-Gaussian model to account for b) partial or c) fully interdigitating membranes. The electron density profiles provide valuable insight into the structure of the membrane.

6.1.2 Fourier transforms of cryo-ET images

The images of 100 mol% PBd$_{22}$-PEO$_{14}$ vesicles collected using cryo-ET were used to generate a line profile by Fourier transformation of the image. Using FIJI, tomogram images of 100 mol% PBd$_{22}$-PEO$_{14}$ vesicles were processed by creating a fast Fourier transform (FFT) of the image as shown in Figure 6.2. The background was then subtracted, the brightness and contrast adjusted and a threshold applied to reduce image background noise. To obtain a radial line profile, the radial profile plugin for FIJI was used. This plugin can be downloaded from `https://imagej.nih.gov/ij/plugins/radial-profile-ext.html`

Once a line profile was obtained, it was transferred to OriginPro for further processing. The x-axis on the line profile is initially in Å, which first needs to be converted to cycle number (cycle(n)) by dividing by the scale, here 8.06 Å px^{-1}, and then into q (Å^{-1}) units in order to compare the FFT line profile with SAXS scattering curves. The units can be converted by applying:

$$q = 2\pi \frac{cycle(n)}{d_{max}} \tag{6.2}$$

where cycle(n) is the pixel cycle number and d_{max} is the value of Å/cycle(n) at cycle 1, in this case 2036.36 Å/cycle.

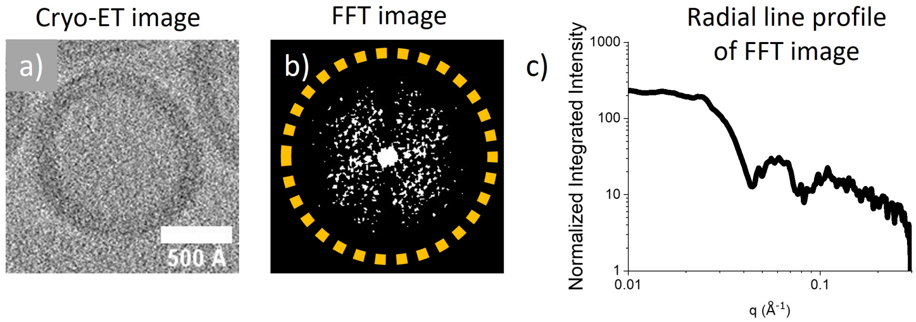

Figure 6.2: Method to obtain a scattering curve from cryo-ET images. From a)a cryo-ET image of 100 mol% PBd$_{22}$-PEO$_{14}$ vesicle with a scale (here, 8.06 Å px^{-1}) applied, an b) FFT of the image of 256 × 256 pixels can be extracted using FIJI. The FFT image brightness and contrast is adjusted, and a threshold applied. Using the radial profile plugin in FIJI, a c) line profile for the FFT image is obtained.

Once the x-axis has been converted to q, the SAXS model for the sample is used to fit the FFT line profile. FFT profiles from 15 cryo-ET images of 100 mol% PBd$_{22}$-PEO$_{14}$ vesicles were averaged and then Equation 2.25 was applied to compare the electron density profile from SAXS with the FFT profile from cryo-ET images.

6.1.3 Single particle analysis

In addition to cryo-ET and SAXS analysis on all PBd$_{22}$-PEO$_{14}$ vesicle compositions, single particle analysis (SPA) was performed on 100 mol% PBd$_{22}$-PEO$_{14}$ sample to confirm the polymer membrane structure. Vesicles were prepared as described in Section 3.2.1. The grids for SPA were prepared as outlined in Section 3.2.4. SPA data was collected and processed by Dr. Rebecca Thompson and Dr. Daniel Maskell, senior support scientists at the Astbury Biostructure Laboratory at the University of Leeds.

From the 2D projection images of 100 mol% PBd$_{22}$-PEO$_{14}$ vesicles, 1300 sections of the membrane were manually picked by Dr. Daniel Maskell using RELION software. The images were grouped into three classes of 100 mol% PBd$_{22}$-PEO$_{14}$ membrane section which were then combined to reconstruct an image of the polymer membrane structure. This image was then analysed by drawing 16 line profiles across the membrane using FIJI as described in Section 5.1.1 to find the electron intensity profile from SPA.

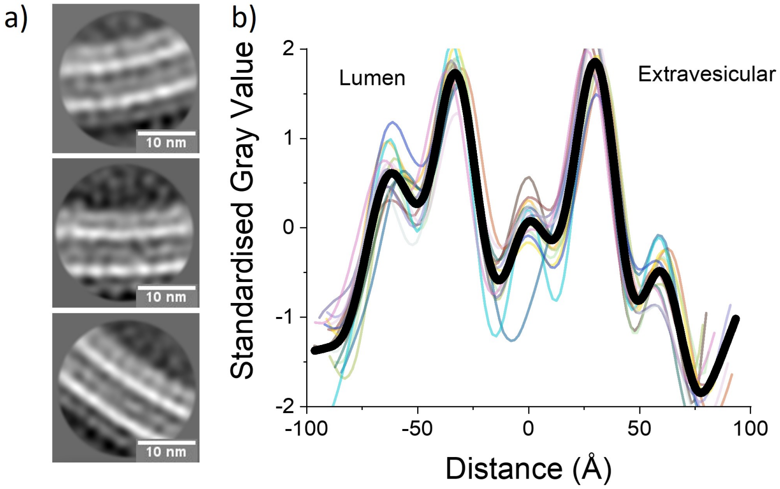

Figure 6.3: Results of single particle analysis. 1300 membrane sections of 100 mol% PBd_{22}-PEO_{14} polymer membranes were manually picked using RELION software and grouped into a) three classes. These images were then analysed with FIJI by measuring 16 line profiles across the membrane to obtain an b) average electron intensity profile of 100 mol% PBd_{22}-PEO_{14} membranes.

6.2 Results and discussion

6.2.1 Scattering contributions

Figure 6.4 shows that as the polymer mole fraction increases, at low q (< 0.08 Å^{-1}) scattering contributions in the SAXS profiles appear, and increase in intensity. As the electron intensity profiles from cryo-ET images of the 100 mol% PBd_{22}-PEO_{14} displayed shoulders against each peak, a 4-Gaussian SAXS model was created and utilised to fit the SAXS scattering profile of the 100 mol% PBd_{22}-PEO_{14} sample. The membrane thickness and peak-to-peak measurements from cryo-ET described in Chapter 5 were used to constrain the SAXS model and lead the refinement process, a single form factor was applied to pure POPC and pure PBd_{22}-PEO_{14} membranes. Initially, a single form factor was applied to hybrid PBd_{22}-PEO_{14} vesicles as well; however, as cryo-ET revealed the presence of two bilayer populations within hybrid PBd_{22}-PEO_{14}/POPC samples, both the pure lipid and pure polymer form factors were applied, culminating in electron density profile (EDP) displaying thick and thin membranes for each hybrid PBd$_{22}$-PEO$_{14}$ sample as shown in Figure 6.4. An outline of how the SAXS models were constrained using cryo-ET results can be found in Appendix A6.1.

While the resultant electron density profiles for thin membranes from hybrid PBd$_{22}$-PEO$_{14}$ samples appear unchanged with increasing PBd$_{22}$-PEO$_{14}$ mole fraction, the trough depth increases with increasing PBd$_{22}$-PEO$_{14}$ mole fraction in the electron density profiles of thick hybrid membranes. The electron dense phosphate headgroups would lower the ratio of the minimum/maximum electron density contrast $\rho_R = \rho_C/\rho_H$, reducing the trough depth with increasing lipid fraction, implying that lipids are present in the thick membranes.

The fraction of thick and thin membranes in each hybrid sample was also fitted, and compared to the percentage of thick and thin membranes found from cryo-ET images as shown in Table 6.1. Fractions of thick and thin membrane vesicles in tomograms each hybrid sample were determined by categorisation through visual observation of cryo-ET images. Although cryo-ET showed no populations in 25 mol% PBd$_{22}$-PEO$_{14}$ sample, SAXS indicates that there were two thickness populations within this hybrid sample. The fraction of thin membranes in each composition decreased as PBd$_{22}$-PEO$_{14}$ mole fraction increased, from 56% in the 25 mol% PBd$_{22}$-PEO$_{14}$ sample to 15% in the 75 mol% PBd$_{22}$-PEO$_{14}$ sample.

The discrepancy between fractions obtained from analysing cryo-ET and SAXS results could be explained by variations in ice thickness on cryo-ET grids, which sort vesicles by size and concentrate the smaller vesicles in thinner regions. As demonstrated earlier, large vesicle diameters correspond to thicker membranes in 75 mol% PBd$_{22}$-PEO$_{14}$ samples. These thicker membranes are less likely to be captured in thin ice or a cryo-ET grid, which could skew the fraction of thick and thin membrane vesicles observed in hybrid samples.

Table 6.1: The fractions of thick and thin membranes in PBd$_{22}$-PEO$_{14}$ vesicle compositions found by cryo-ET and SAXS analysis. Fractions of thick and thin membranes in cryo-ET images were found by categorising individual vesicles by visual observation. Fractions of thick and thin membranes in SAXS scattering profiles were determined using Equation 6.1

PBd$_{22}$-PEO$_{14}$(mol%)	Cryo-ET		SAXS	
	Thin (%)	Thick (%)	Thin (%)	Thick (%)
0	100	0	100	0
25	100	0	56	44
50	58	42	25	75
75	63	37	15	85
100	0	100	0	100

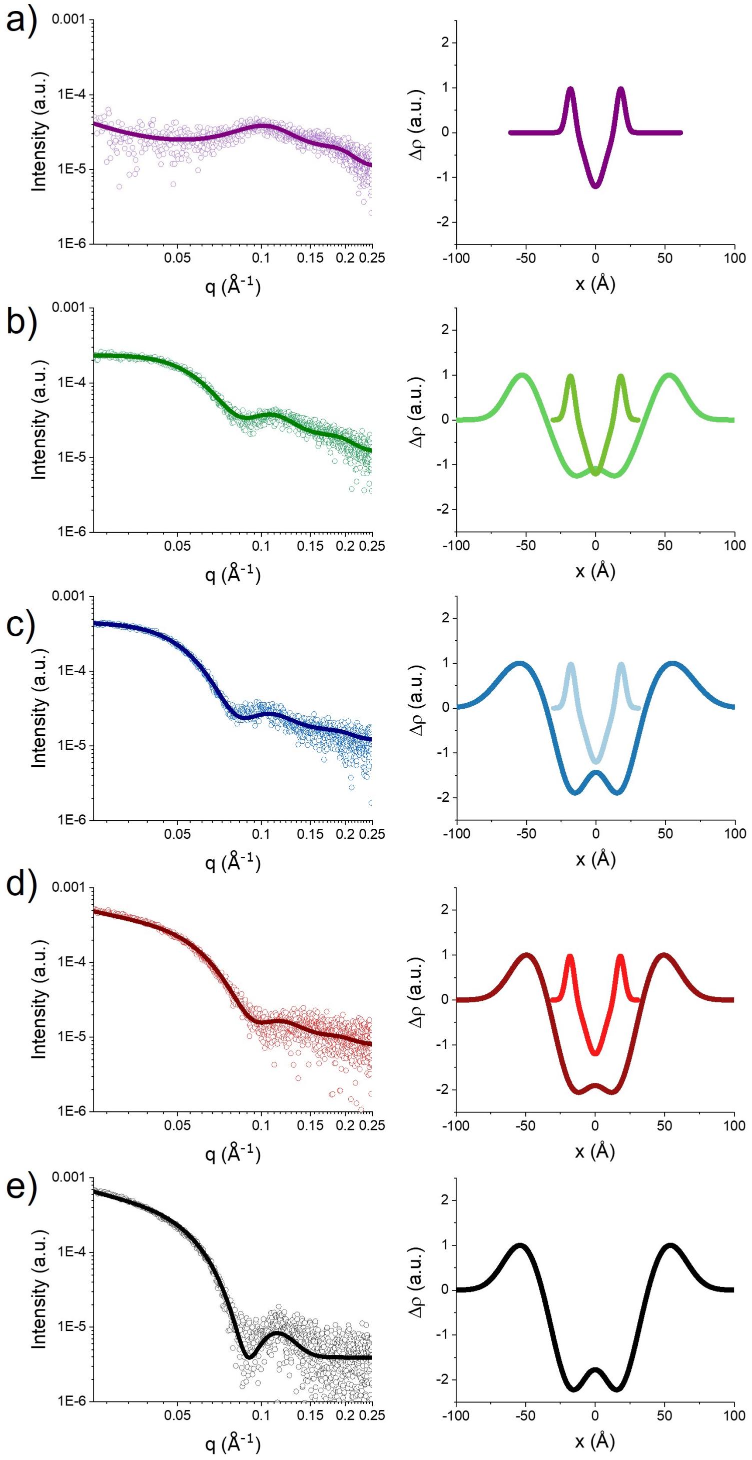

Figure 6.4: SAXS scattering curves and the resultant electron density profiles. The measurements of the full width half maximum (FWHM), peak-to-peak were taken from cryo-ET electron intensity profiles and used to constrain the SAXS model fits and obtain a bilayer electron density profile for a) 0 mol%, b) 25 mol% c) 50 mol% d) 75 mol% and e) 100 mol% PBd_{22}-PEO_{14} vesicles.

6.2.2 Comparing results from SAXS, cryo-ET and SPA

Comparing the electron density profiles from SAXS with the electron intensity profiles attained using cryo-ET, excellent correspondence can be seen in the profiles of pure POPC lipid, where peak positions are closely aligned as shown by Figure 6.5a. In the SAXS profile, the peak-to-peak distances in POPC lipid membranes is 36.4 Å, while for the cryo-ET profile, the peak-to-peak distance is 33.9 Å. These measurements are comparable to the bilayer thickness of POPC lipid membranes (peak-to-peak) found previously using SAXS and cryo-TEM: in SAXS, the peak-to-peak distance was estimated to be $\sim$ 38 Å (185, 186, 188), while measurements of cryo-TEM images gives a membrane thickness of 37 Å (177). Usually membrane thickness from cryo-TEM projection images is measured by the distance between the outer edges of the contrast interfaces.

While SAXS analysis also confirms that the polymer membranes are significantly thicker than the POPC membranes, the profiles have significant disparities. In particular, the SAXS data indicates much larger peak-to-peak distances compared to the cryo-ET profiles (108 Å and 65.8 Å, respectively), as shown by Figure 6.5b. Both SAXS and cryo-ET do reveal two bilayer populations within the PBd$_{22}$-PEO$_{14}$ hybrid samples, one population presenting a thinner membrane <65 Å, and the other with a thicker membrane > 65 Å.

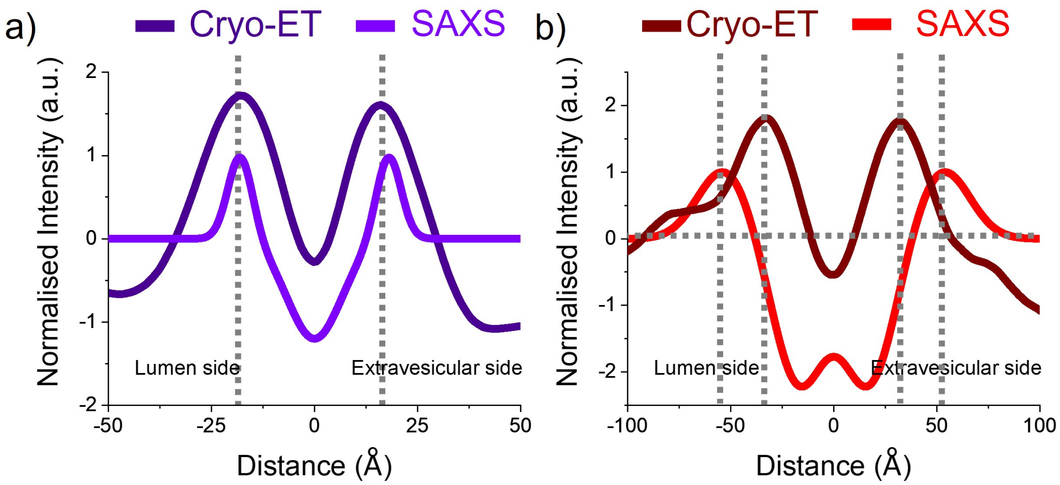

Figure 6.5: Comparing results from SAXS and cryo-ET. Comparing the electron intensity profiles obtained from cryo-ET with the electron density profiles from SAXS of a) pure POPC vesicles and b) pure PBd$_{22}$-PEO$_{14}$ vesicles.

To explore this discrepancy between SAXS and cryo-ET in 100 mol% PBd$_{22}$-PEO$_{14}$ membranes, a FFT of the cryo-ET images was obtained resulting in a line profile similar to the SAXS scattering curve for 100 mol% PBd$_{22}$-PEO$_{14}$ vesicles. This scattering curve was fitted with the 4-Gaussian form factor Equation 2.25, which produced another electron intensity profile from the cryo-ET images of 100 mol% PBd$_{22}$-PEO$_{14}$. As shown by Figures 6.6b and f, the peak-to-peak distance in the profile from the FFT correspond to the peaks found from the SAXS scattering curves (108 Å from both techniques). A closer inspection also reveals a small electron dense peak in the centre of the trough region, where the hydrophobic core is expected to be. This suggests that the information collected by SAXS is present in the cryo-ET images, but it is too noisy to be clearly resolved during real-space analysis.

Another reconstruction technique utilising cryo-TEM images was used to explore 100 mol% PBd$_{22}$-PEO$_{14}$ membrane structure. For SPA, multiple cryo-TEM projection images of the vesicles were obtained and then membrane sections were specifically picked from those images and grouped together to give a high-resolution image of the membrane. This image can then be compared to the electron profiles from cryo-ET and SAXS by using FIJI to obtain an intensity profile across the membrane.

The SAXS electron density profile and FFT profile of 100 mol% PBd$_{22}$-PEO$_{14}$ in Figures 6.6b and f revealed a small electron dense peak in the centre of the trough region, where the hydrophobic core is expected to be. Although this feature is not observed in the cryo-ET profile, the SPA profile in Figure 6.6h shows a small electron dense peak within the centre of the trough region. This is indicative of some polymer interdigitation, as polymers in both the inner and outer bilayer leaflets would tangle and thus have a higher electron density than if the polymer leaflets were completely segregated.

Figure 6.6b also shows that the position of full width half maximum of the trough in the SAXS EDP (59.2Å) corresponds with the inner peak-to-peak distance in cryo-ET and SPA profiles in Figures 6.6d and h (65.8 Å and 63.4 Å, respectively). In SAXS, the hydrophobic core is defined as the region which has a lower density than water (< 0.33 e^{-} Å^{-3}) in the the electron density profile. For example, the methyl chains in lipid bilayers have an electron density of 0.16 e^{-} Å^{-3} while hydrocarbon tails have a density of 0.30 e^{-} Å^{-3} (195). However, in measurements of in lipid membrane from cryo-TEM images, the hydrophobic core is often not considered separately and only membrane thickness is measured (177, 179, 191).

Theoretically, the hydrophobic core thickness in an interdigitated polymer bilayer conformation could be estimated using a polymer random walk model, where the root mean squared end-to-end distance of the hydrophobic block in the amphiphilic block copolymer, $\sqrt{\langle R^2 \rangle}$:

$$\sqrt{\langle R^2 \rangle} = N^v b \tag{6.3}$$

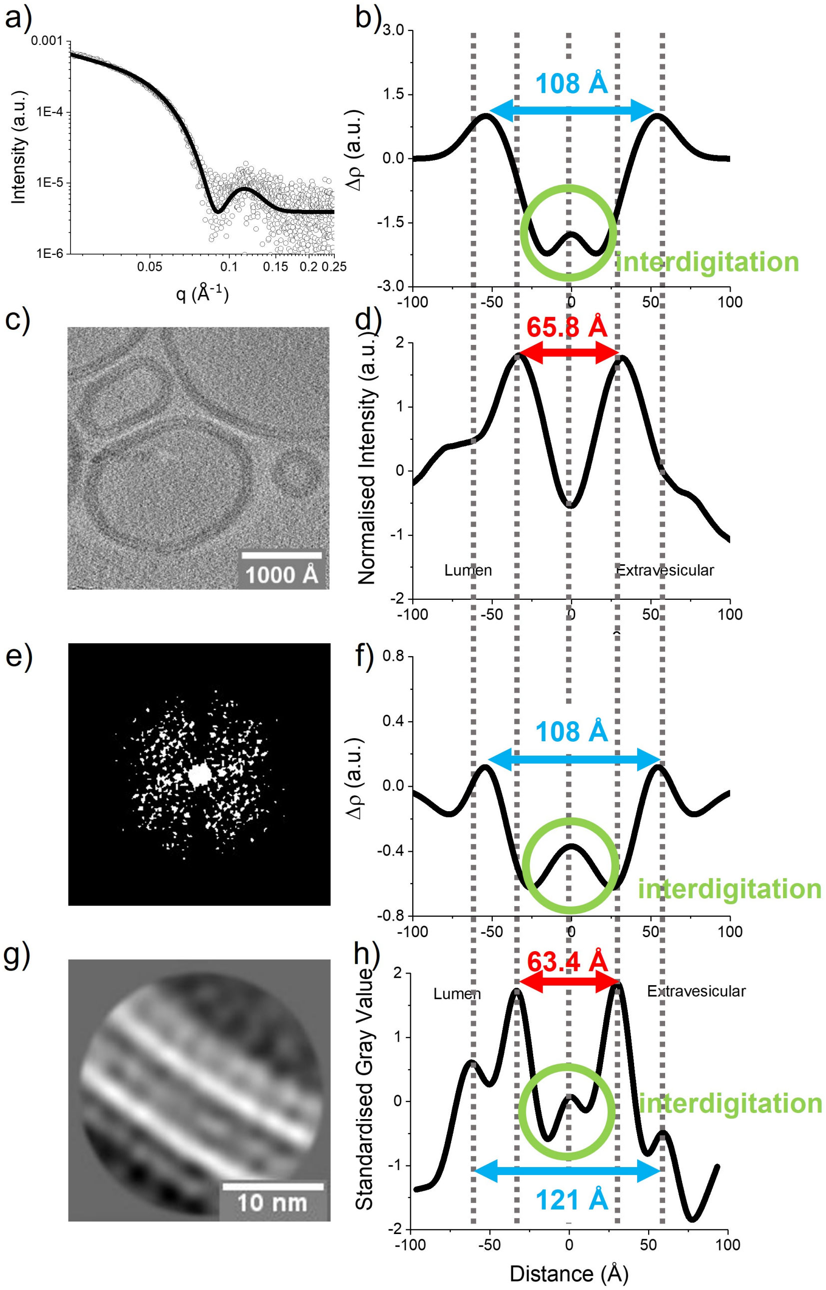

Figure 6.6: Comparing results of 100 mol% PBd$_{22}$-PEO$_{14}$ sample from SAXS, cryo-ET and SPA. The a) SAXS scattering curves of 100 mol% PBd$_{22}$-PEO$_{14}$ and b) corresponding electron density profile for the membrane. Analysis of the c) cryo-ET images of 100 mol% PBd$_{22}$-PEO$_{14}$ results in d) an electron intensity profile that has smaller peak-to-peak distances than the SAXS electron density profile. The trough in b) also has a small electron dense peak, not observed in d), which could indicate polymer interdigitation within the bilayer. An e) FFT of the cryo-ET image results in a f) electron intensity profile that corresponds to the SAXS electron density profile. The g) final image from SPA gives h) an intensity profile which appears to correspond to features seen in both b) and d). Inner peak positions in h) correspond to peak positions in d), and there is also a small electron dense peak within the trough region of h) which is also observed in b).

where N is the number of Kuhn segments in the hydrophilic block, v is the Flory exponent and b is the Kuhn length of the hydrophilic block.

For hydrophobic polybutadiene, (1,2 addition), the Kuhn length is thought to be 13.7 Å (196). Assuming polybutadiene is acting as ideal chains that interdigitate, the Flory exponent $v = 0.5$, gives a hydrophobic core of 55 Å for PBd_{22}-PEO_{14} membranes. If the polymers leaflets in the membrane are segregated, the Flory exponent $v = 1$, which gives a hydrophobic core of 110 Å. These give the potential physical limits for membrane hydrophobic core measurements. However, PBd_{22}-PEO_{14} polymer membranes could undergo partial interdigitation as well, where the Flory exponent $v = 0.66$, giving a hydrophobic core thickness of 69.6 Å. However, using random walk models in this way must be done with care.

The measurements of the hydrophobic core from SAXS, cryo-ET and SPA profiles are all below the predicted hydrophobic thickness for fully segregated polymer leaflets, but above the thickness calculated from fully interdigitated membranes, implying PBd_{22}-PEO_{14} forms partially interdigitating membranes. Generally, the number of Kuhn segments, N, in a random walk must be large enough to allow the non-identical steps in the walk to sum to zero. However, as a polymer membrane consists of many polymers, the large N could come from the collective behaviours of many polymers rather than the length of individual polymers within a membrane.

The cryo-ET profile also shows a shoulder forming on the outer edges of these peaks at approximately ± 80 Å. Although the position of this shoulder does not align with the outer peak at ± 58.5 Å in the SPA profile of Figure 6.6h, this outer peak in the SPA profile is directly between the peak and shoulder positions in the cryo-ET profile. This same observation can be made when comparing the SAXS profile with the cryo-ET profile, where the SAXS peak position at ± 54.0 Å is directly between the peak and shoulder in the cryo-ET profile. The SAXS model used here for PBd_{22}-PEO_{14} membranes does not account for these two additional positive electron density contributions in this structural region, which is why this particular feature cannot be reproduced. The inner peaks of the SPA profile in Figure 6.6h could represent the hydrophobic/hydrophilic interface between the hydrophobic polybutadiene (PBd) and hydrophilic polyethylene oxide (PEO) blocks, while the outer peak may represent the centre of the PEO corona.

Figure 6.6h appears asymmetric in the outer peak intensities and widths of the lumen and extravesicular sides. The peak intensity of the outer peak on the lumen side is larger, and the width wider, than the outer peak on the extravesicular side. This may suggest a curvature asymmetry effect where there is a higher density of PEO PBd_{22}-PEO_{14} chains, but the chains are extended, on the lumen side of the curved membrane, while the PEO chains on the extravesicular membrane side would have greater free volume to coil in resulting in a smaller peak intensity and narrower peak width. As SPA was conducted on 100 mol% PBd_{22}-PEO_{14} vesicles, the asymmetry is not due to composition.

Although only 100 mol% PBd_{22}-PEO_{14} has been investigated using SAXS, cryo-ET and SPA, as shown by Figures 6.4 and 6.6, the SAXS electron density profiles of population 2 of hybrid PBd_{22}-PEO_{14}/POPC samples corresponds closely to the pure PBd_{22}-PEO_{14} model, so observations about 100 mol% membranes are anticipated to be similar for hybrid samples. The SPA profile has features that correspond with positions of features observed in both SAXS and cryo-ET profiles showing that both cryo-ET and SAXS are required to obtain a complete picture of the structure within hybrid PBd_{22}-PEO_{14}/POPC membranes.

Although on first inspection both cryo-ET and SAXS would be expected to produce identical profiles as they are both generally measuring electron density, the techniques are based on different principles as explained in Chapter 2. Cryo-ET picks up features that vary in electron potential, while in SAXS electron density is measured. SAXS results are model dependent, and cryo-TEM results depend mainly on the data reduction techniques for retrieving intensity profiles. This explains slightly the different features within the membrane, resulting in varying profiles seen in Figure 6.6. Adding too many fitting parameters to the SAXS model also does not improve the fit to the scattering data due to its limited resolution. A 4-Gaussian model was used to fit 100 mol% PBd_{22}-PEO_{14} membranes, but increasing this to a 6-Gaussian model would be over-parameterising, and gave the same result with peak positions between the peaks seen by cryo-ET and SPA.

6.3 Conclusion

Small angle x-ray scattering (SAXS) is an ensemble technique that has commonly been used to determine the average electron density profile of lipid membranes (197, 137, 198). However, the resultant scattering pattern is often difficult to model without some structural information (193). As demonstrated earlier, cryo-ET was successfully used to probe the membrane structure of hybrid lipid-polymer vesicles, revealing an electron intensity profile for each compositions, and two bilayer thickness populations with PBd_{22}-PEO_{14} hybrid vesicle samples. Here the information gained from cryo-ET was used to inform and optimise the model for SAXS scattering patterns.

Usually in cryo-TEM analysis of lipid membranes, the bilayer thickness is defined by the distance between the outer edges of the contrast interfaces while the hydrophobic core is often not specifically considered (177, 179, 191). Other studies have utilised small angle neutron scattering (SANS) and Förster resonance energy transfer (FRET) to determine nanoscale domains as small as 5 nm with large unilamellar vesicles and found polymer architecture has an effect on the mixing behaviours of components in a hybrid lipid-polymer membrane (98). Although cryo-ET has been used previously to determine structures of PBd_{22}-PEO_{14}/POPC hybrid vesicles (tubular and vesicular structures in 15-85 mol% PBd_{22}-PEO_{14} compositions), the study suggested that the polymer accumulates in the outer leaflet in the hybrid membrane, whereas the lipid is more likely to reside in the inner leaflet (92).

Here, two bilayer populations in 50 mol% and 75 mol% PBd_{22}-PEO_{14} hybrid vesicles were revealed by cryo-ET and confirmed by SAXS. While these populations could be perceived as polymer-rich and lipid-rich vesicles with hybrid PBd_{22}-PEO_{14}/POPC samples, these results could also indicate the polymer forms a segregated, bilayer conformation or an interdigitated conformation as these two conformations are energetically similar. Population 1 within hybrid PBd_{22}-PEO_{14} samples, which have a thin membrane (< 65 Å from measurements of cryo-ET images), may have polymers that are fully interdigitating, while in population 2 (bilayer thickness from cryo-ET measuements > 65 Å) the polymers may form a bilayer conformation with only partial interdigitation within the hydrophobic core. Comparison of the hydrophobic core thickness from cryo-ET, FFT, SAXS and SPA electron density profiles with theoretical calculations using a random walk model also suggest that PBd_{22}-PEO_{14} is partially interdigitating in the membrane.

Inspection of SAXS electron density profiles of population 2 in hybrid PBd_{22}-PEO_{14}/POPC samples show that relative electron density of the hydrophobic core region reduces as the polymer fraction increases, implying population 2 comprises mixed membranes. Analysis of cryo-ET images of hybrid PBd_{22}-PEO_{14}/POPC vesicles in Chapter 5 has also shown the electron intensity profiles of thick and thin membrane populations do differ to the profiles for pure lipid and pure polymer vesicles. This implies an uneven distribution of lipids and polymers in each vesicle is causing the differences in membrane thickness, rather than the presence of polymer-rich and lipid-rich vesicle populations in each hybrid sample. There is no evidence from analysis of either SAXS profiles or cryo-ET images of phase separation into nanoscale polymer-rich and lipid-rich domains within individual vesicles of hybrid samples, indicating all compositions have homogenous membranes.

However to fully confirm the formation of hybrid PBd_{22}-PEO_{14}/POPC membranes contain an uneven distribution of lipids and polymers that are homogeneously mixed within the membrane further analysis is required. Potentially, by labelling the lipid and the polymer, contributions from each labelled component can then be used to verify membrane homogeneity by another method, as well as determine the proportion of lipid and polymer in each hybrid vesicle. This is discussed further in Chapter 7.

Although cryo-ET and SAXS electron profiles have excellent correspondence for peak positions in pure POPC lipid membranes, these two techniques appear to highlight different features within a PBd_{22}-PEO_{14} polymer membrane. This makes a quantitative comparison of hydrophobic core and bilayer thickness using the same definition for all compositions difficult. However details such as hydrophobic thickness of the membrane, previously not assessed by cryo-TEM, have been resolved by cryo-ET and SAXS has been used to produce an electron density profile of a polymer membrane. A FFT of the cryo-ET images also confirmed the peak positions found in the SAXS electron density profile. Cryo-ET is an excellent tool for assessing heterogeneities and unique features within samples, but it can also be used to build and refine models for SAXS. Utilising the results from cryo-ET to inform and optimise the fits for models, SAXS can then be used with confidence to find ensemble structural details with low statistical error.

SPA however was able to distinguish all features seen by both cryo-ET and SAXS. With the additional advantage of being able to observe a distribution of structures within a sample and not just the average structure, this technique could be used more in the future to determine the structure of hybrid lipid-polymer membranes.

7. Hybrid membrane properties from GUV image analysis

Biological membranes comprise a mixture of lipids and their composition controls essential cell membrane properties such as fluidity, mechanical stability and membrane protein function (16). As biological membranes have multiple components, they are believed to have lateral heterogeneities and nano-scale domains that contribute to the inherent properties and behaviours of the membrane (65, 199). Giant unilamellar vesicles (GUV) have similar sizes to biological cells (1-100 µm) and are valuable cell membrane models to observe membrane dynamics using a light microscope (23, 200).

Phase separation has been observed in GUVs by incorporating fluorescently labelled polymers or lipids within the membrane and monitoring the spatial localisation of their fluorescence using confocal microscopy. For GUVs comprising binary polymer mixtures, polymer mixing and phase separation within the sample was predicted by investigating the fluorescence from BODIPY and BODIPY-FL fluorophores within the initial polymer films, before the films are electroformed into GUVs. Where the films showed no mixing between the fluorophores, the resultant GUVs had separated into pure component vesicles, while films that indicated mixing between the florophores gave GUVs with homogenous, mixed membranes (65). However, confocal images of GUV formation from poly((2-methacryloyloxy)ethyl phosphorylcholine)-block-poly(2-(diisopropyl-amino)ethyl methacrylate) (PMPC-PDPA) and PBd-b-PEO binary polymer mixture demonstrated the kinetics of formation of hybrid polymer-polymer membranes is very slow, with phase separation only clearly forming after 12 hours of electroformation (64).

Binary lipid membranes can be used to generate phase-separated lipid membranes depending on whether the lipid components are in a fluid-, gel-, liquid-ordered or liquid disordered phases, with phase-separation occurring if one of the components is in the gel-state (201). Previous studies have observed that hybrid vesicles can be either homogeneous or inhomogeneous with lateral domains (22, 29, 79, 91, 99). POPC/PBd-b-PEO membranes composed of lower molecular weight polymers were more likely to form hybrid vesicles (82). Domains have even been induced to form in hybrid POPC/PBd-b-PEO GUVs by biotinylation of one of the components and cross-linking with the protein, NeutraAvidin. The domain pattern depended on whether the polymer or lipid was biotinylated; polymer cross-linking resulted in a large single domain, while lipid cross-linking gave many small, lipid-rich domains within a polymer matrix (29).

Lateral phase separation alters the membrane curvature energy, and its occurrence is determined by the hydrophobic thickness of the components, the chemical compatibilities between the polymers as well as the component phase states (22, 34). Studies have also found that line tension at POPC or DPPC/PDMS-PEO boundaries could be finely tuned by the copolymer molar mass and architecture, resulting in the formation of stable lipid domains with different sizes and morphologies in hybrid GUVs (98). A high thickness mismatch was also believed to result in a high line tension that drove PDMS-PEO/POPC and PDMS-PEO/DPPC vesicle morphologies towards patch domains or the formation of separated liposomes and polymersomes (22, 34). The bending rigidity of these polymer domains was shown to be larger than that of the lipid domains. An equilibrium between the line tension and bending energy was thought to be more easily achieved for small polymer-rich domains, while small lipid-rich domains were believed to require a large curvature increase followed by membrane fission into separated vesicles to balance line tension with bending energy (34). Line tension and membrane elasticity was also observed to affect the phase separation in PDMS-co-PEO/DPPC or DOPC membranes (75).

The ability of domains to coalesce is dependent on the viscosity of the continuous phase, while attractive or repulsive interactions between them depend on membrane elasticity (29). Fluorescence recovery after photobleaching (FRAP) has been used in the past to monitor membrane fluidity and viscosity: for POPC/PBd_{46}-PEO_{30} GUVs, FRAP showed that the diffusion coefficient decreased with increasing polymer fraction (29). The intermediary value of the diffusion coefficient between pure POPC and pure PBd_{46}-PEO_{30} of an asymmetric giant hybrid vesicle was believed to indicate polymer interdigitation (199). FRAP experiments have been combined with micropipette aspiration techniques to investigate the relationship between membrane tension and fluidity (29, 96). Flicker spectroscopy has also been used in combination with FRAP, and is another option in the determination of membrane tension and bending rigidity in lipid membranes (124, 202, 203). To further complement FRAP results, membrane probes such as Laurdan can also be used to visualise membrane fluidity. Recently, Laurdan has been employed to report relative values of membrane packing, used to extrapolate membrane order and hydration in lipid mixtures (119, 204, 205).

Although PC and PBd_{22}-PEO_{14} hybrid membranes have been shown to extend functional lifetimes of incorporated membrane proteins (1, 77, 78), relatively few studies have completed experiments incrementally increasing the copolymer fraction within hybrid vesicles to determine surface morphologies (membrane homogeneity or phase separation), membrane viscosity and mechanical properties, and then relating membrane composition to those results. Therefore there is a need to systematically investigate PC/PBd_{22}-PEO_{14} membrane compositions.

7.1 Methods

7.1.1 Determination of polymer-lipid ratio

10 mol% of the resultant fluorescently labelled polymer dye was used alongside 2 mol% 3,3'-dioctadecyloxacarbocyanine perchlorate (DiO) to determine the polymer-lipid ratio. As all the hybrid vesicles contained both 2 mol% DiO and 10 mol% PBd_{22}-PEO_{14}-TMR, their compositions were altered as shown in Table 7.1. Going forwards, compositions will continue to be referred to by the sample label in Table 7.1.

Table 7.1: True mole fractions of POPC, PBd-b-PEO, DiO and PBd_{22}-PEO_{14}-TMR in PBd_{22}-PEO_{14} and PBd_{12}-PEO_{11} GUV compositions. The addition of 2 mol% DiO and 10 mol% PBd_{22}-PEO_{14}-TMR to the hybrid vesicles alters their composition.

Sample label (mol%)	POPC (mol%)	PBd-b-PEO (mol%)	DiO (mol%)	PBd_{22}-PEO_{14}-TMR (mol%)
0	98.0	–	2.0	–
25	66.5	22.5	1.8	9.2
50	43.6	45.4	1.8	9.2
75	22.7	66.5	1.8	9.0
100	–	90	–	10

Giant unilamellar vesicles (GUV) were formed using the method outlined in 3.2.8. Confocal laser scanning microscopy was used to determine absolute intensity of 2 mol%DiO and 10 mol% PBd_{22}-PEO_{14}-TMR dyes in hybrid membranes. Imaging was conducted with a Zeiss LSM880 + Airyscan inverted confocal microscope within 1 hour of GUV formation.

The microscope tile scanning option was used to scan large areas of the sample and facilitate the acquisition of statistical data and the images were analysed using the FIJI software (National Institutes of Health, Bethesda, MD). Förster resonance energy transfer (FRET) was not expected as the tile scan option excites each dye individually before compiling the multichannel image. The image was split into channels, representing the intensity contribution from each fluorescent dye as shown in Figure 7.1. The image from the PBd_{22}-PEO_{14}-TMR channel was duplicated to create the mask. First this duplicate was adjusted for brightness and contrast, and a threshold applied. Then a mask was created to ensure only vesicles greater than > 10 µm were measured using the automatic particle analysis tool. This size was chosen to prevent selection of non-vesicular aggregates. The mask created regions of interest around selected vesicles of a particular size. These regions of interest were then applied to the split channel images with intensity contributions from each dye to retrieve their intensity values.

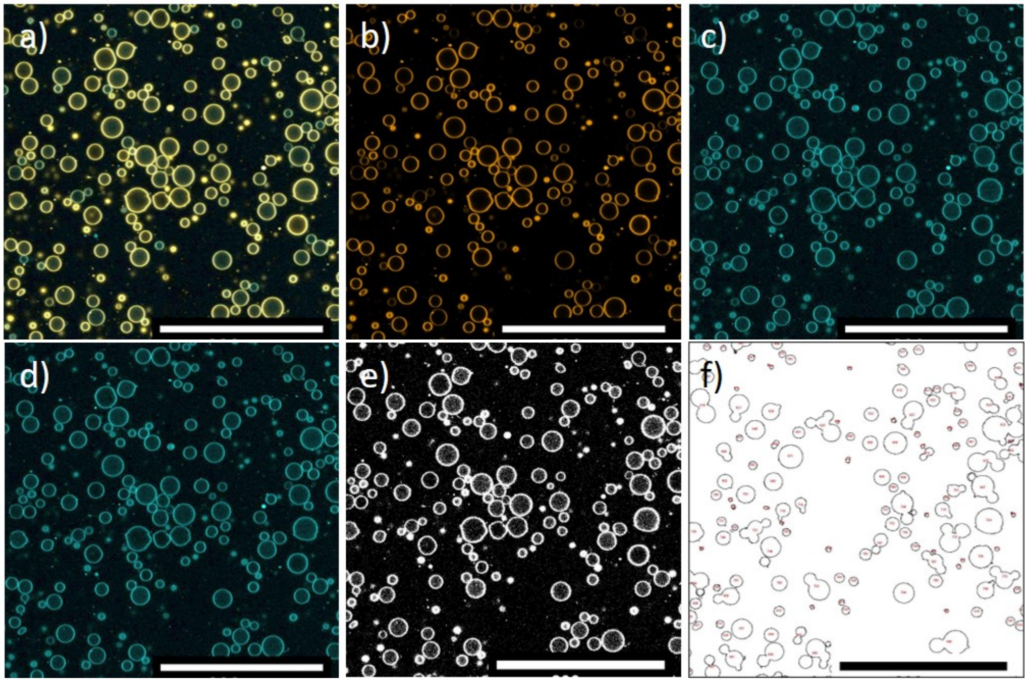

Figure 7.1: Method for determining polymer-lipid ratio. The a) tile scan of the hybrid lipid-polymer vesicles (25 mol% PBd_{12}-PEO_{11}) is split into channels of intensity contributions from b) DiO fluorescent lipid and c) PBd_{22}-PEO_{14}-TMR fluorescent polymer only. The image of PBd_{22}-PEO_{14}-TMR intensity is d) duplicated and brightness and contrast adjusted before e) a threshold is applied. Finally, a f) mask is created, created regions of interest around vesicles of diameters > 10 µm. The black outlines in f) represent the unmasked areas where intensity will be measured, while white indicates the masked areas where no intensity measurements are taken. These regions of interest in f) are then applied to b) and c) to find the intensity contributions from each dye separately.

The intensity values from each dye image are normalised to the mean plus standard deviation value. The relative intensity ratio, R, between the intensity contributions from DiO, I_{DiO}, and PBd_{22}-PEO_{14}-TMR, $I_{PBd_{22}-PEO_{14}-TMR}$, was calculated using:

$$R = \frac{I_{PBd_{22}-PEO_{14}-TMR} - I_{DiO}}{I_{PBd_{22}-PEO_{14}-TMR} + I_{DiO}} \tag{7.1}$$

This gives a normalised value between -1 and 1, where -1 indicates the intensity contributions in hybrid vesicles are from DiO only: 1 indicates the intensity contributions in the hybrid vesicles are entirely from PBd_{22}-PEO_{14}-TMR, while an intensity ratio of 0 indicates equal fluorescence intensity contributions in hybrid vesicles from both PBd_{22}-PEO_{14}-TMR and DiO. The resultant histograms are then fitted with a normal distribution curve.

7.1.2 Fluorescence recovery after photobleaching

10 mol% of the PBd_{22}-PEO_{14}-TMR polymer dye was used alongside 2 mol% DiO to investigate changes in membrane viscosity by Fluorescence recovery after photobleaching (FRAP). As all the hybrid GUVs contained both 2 mol% DiO and 10 mol% PBd_{22}-PEO_{14}-TMR, their compositions were altered as shown in Table 7.1. Going forwards, compositions will continue to be referred to by the sample label in Table 7.1. GUV were formed using the method outlined in 3.2.8. Confocal laser scanning microscopy was used to determine FRAP of 2 mol%DiO and 10 mol% PBd_{22}-PEO_{14}-TMR dyes in hybrid GUV membranes. Imaging was conducted with a Zeiss LSM880 + Airyscan inverted confocal microscope within 1 hour of GUV formation.

FRAP consists of bleaching irreversibly a particular region of interest (ROI) with a 100% intensity for all laser beams (405, 458, 514, 561 and 633 nm) and then monitoring with a 2% intensity laser beam (for 488 nm for DiO excitation and 561 nm for PBd_{22}-PEO_{14}-TMR excitation). The rate of fluorescence recovery that represents the time needed for the surrounding fluorescent molecules to diffuse into that region of interest. FRAP experiments were performed on the top pole of GUVs where a circular region of interest with a 5 ± 0.5 µm diameter was exposed to five bleaching scans at 100 mol% laser power, and the recovery was monitored by recording time series of 13 frames of size 256 × 256 pixel per second, with the confocal pinhole adjusted to 3.1 µm. The recovery curves were fitted with Origin Pro using the classic fluorescence recovery model:

$$f(t) = A[exp(-\frac{2\tau_D}{t})[I_0(\frac{2\tau_D}{t}) + I_t(\frac{2\tau_D}{t})]] \tag{7.2}$$

where t is the time, A is the recovery level, τ_D is the half recovery time, and I_0 and I_1 are modified Bessel functions of the first kind. The diffusion coefficient (D) can then be calculated from the recovery times and the radius of the bleached region (r) using:

$$D = \frac{r^2}{4\tau_D} \tag{7.3}$$

7.1.3 Spectral imaging

0.5 mol% 6-Dodecanoyl -2- Dimethylaminonaphthalene (Laurdan) was added to the lipid-polymer thin film mixtures to investigate changes to membrane hydration. GUV were then formed using the method outlined in 3.2.8. A Zeiss LSM880 + Airyscan inverted confocal laser scanning microscope was used to image the GUVs within 1 hour of formation.

Spectral imaging of Laurdan fluorescence in the different membrane samples was performed using the microscope 32-channel GaAsP detector array. Laser light at 405 nm was selected for fluorescence excitation of Laurdan. The lambda detection range was set between 412 and 555 nm with intervals of 8.9 nm, allowing simultaneous coverage of the whole spectrum. The confocal pinhole aperture was adjusted to 3.1 µm, and to increase the scan speed, single GUVs were maximally magnified to allow the whole vesicle to be imaged. The images of resolution 512 × 512 pixels were saved in .lsm file format and filtered with a Gaussian blur before being analysed to find the general polarisation value of each pixel by using a custom plug-in compatible with FIJI, found at `https://github.com/dwaithe/GP-plugin`. Spectral images can be found in Appendix A9.1.

$$GP = \frac{I_{444} - I_{488}}{I_{444} + I_{488}} \tag{7.4}$$

7.1.4 Flicker spectroscopy

The mechanical properties of GUVs were determined using flicker spectroscopy. This is a non-invasive image analysis technique that quantifies the amplitude of membrane thermal fluctuations $\langle | u_q^2 | \rangle$ as a function of their wavenumber ($q = \frac{2\pi}{l}$) along the length (l) of the GUV contour. For these experiments, the GUVs were osmotically relaxed by being incubated overnight at 4 °C with a hyperosmotic buffer (320 $\mathrm{mOsm\,kg^{-1}}$). A time series over 5 min at a frame rate of 3.3 frames per second at a resolution of 1024 × 1024 pixels were taken of the equatorial plane of individual GUVs. The confocal pinhole aperture was adjusted to 0.7 µm (1 Airy unit), and to increase the scan speed, single GUVs were maximally magnified, which allows imaging of the whole vesicle. The data were analysed using MATLAB contour analysis software kindly provided by P. Cicuta and co-workers at the University of Cambridge (Cambridge, U.K.). This program analyses each frame of the time series and quantifies the membrane tension (σ) and bending rigidity modulus (κ_b) by fitting the fluctuation spectrum with the following equation:

$$\langle | u_q^2 | \rangle = \frac{k_B T}{2\sigma}\left(\frac{1}{q} - \frac{1}{\sqrt{\frac{\sigma}{\kappa_b} + q^2}}\right) \tag{7.5}$$

where k_B is the Boltzmann constant and T is the temperature.

7.2 Results and discussion

7.2.1 Membrane composition

Combining POPC with PBd$_{22}$-PEO$_{14}$ or PBd$_{12}$-PEO$_{11}$ to create GUVs was successful in varying degrees for all compositions as shown by Figure 7.2. DiO was used as the fluorescent probe for lipids, while PBd$_{22}$-PEO$_{14}$-TMR, synthesised from PBd$_{22}$-PEO$_{14}$, was expected to partition into the polymer. The hybrid vesicles contain both 2 mol% DiO and 10 mol% PBd$_{22}$-PEO$_{14}$-TMR while 0 mol% and 100 mol% PBd$_{22}$-PEO$_{14}$ compositions contain only 2 mol% DiO or 10 mol% PBd$_{22}$-PEO$_{14}$-TMR respectively. The true mole fractions of POPC, PBd-b-PEO (representing both PBd$_{22}$-PEO$_{14}$ and PBd$_{12}$-PEO$_{11}$), DiO and PBd$_{22}$-PEO$_{14}$-TMR within these mixed vesicles can be found earlier in Table 7.1.

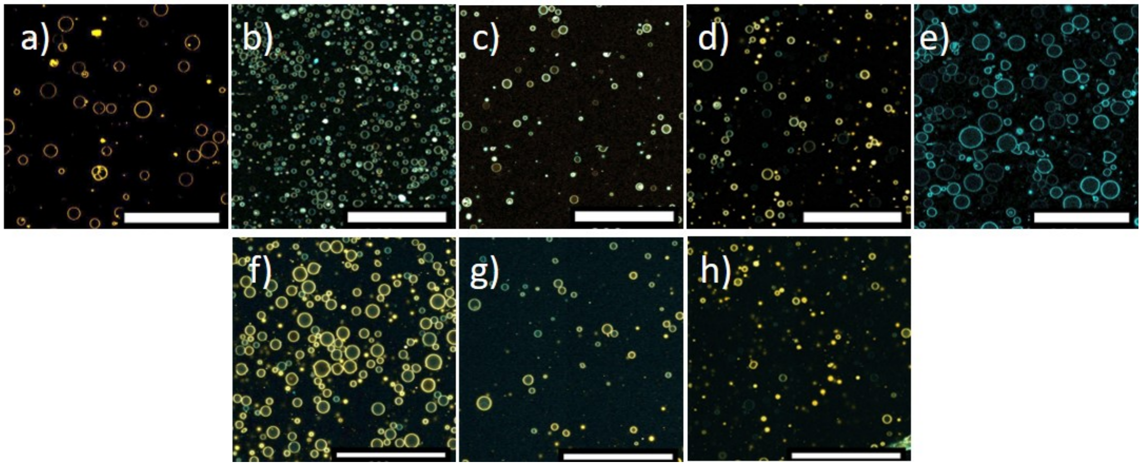

Figure 7.2: Tile scans of PBd$_{22}$-PEO$_{14}$ and PBd$_{12}$-PEO$_{11}$ composition GUVs. Tile scans a) POPC, b) 25 mol% PBd$_{22}$-PEO$_{14}$, c) 50 mol% PBd$_{22}$-PEO$_{14}$, d) 75 mol% PBd$_{22}$-PEO$_{14}$, e) 100 mol% PBd$_{22}$-PEO$_{14}$, f) 25 mol% PBd$_{12}$-PEO$_{11}$, g) 50 mol% PBd$_{12}$-PEO$_{11}$ and h) 75 mol% PBd$_{12}$-PEO$_{11}$ compositions were taken. To obtain good images of 100 mol% and 75 mol% PBd$_{22}$-PEO$_{14}$ GUVs, the samples were diluted × 2 to reduce saturation. The hybrid vesicles contain both 2 mol% DiO and 10 mol% PBd$_{22}$-PEO$_{14}$-TMR while 0 mol% and 100 mol% PBd$_{22}$-PEO$_{14}$ compositions contain only 2 mol% DiO or 10 mol% PBd$_{22}$-PEO$_{14}$-TMR respectively. The scale bar is 200 µm.

100 mol% and 75 mol% PBd$_{22}$-PEO$_{14}$ samples consistently formed many large (10-50 µm) GUVS, with minimal method optimisation required and × 2 dilution required to reduce image saturation and obtain good images. However 0 mol%, 25 mol% and 50 mol% PBd$_{22}$-PEO$_{14}$ usually generated smaller vesicles (1-20 µm) and several optimisation iterations were required to achieve the images shown in Figure 7.2, compared to 75 mol%

and 100 mol% PBd_{22}-PEO_{14} compositions. On the other hand, 25 mol% PBd_{12}-PEO_{11} sample consistently formed many large GUVs (10-35 µm), while 50 mol%, 75 mol% and 100 mol% PBd_{12}-PEO_{11} samples formed fewer, smaller vesicles (1-20 µm).

While the majority of vesicles were uni-lamellar, some multi-lamellar and intra-lumenal vesicles were observed in all samples. 0 mol% and 25 mol% vesicle compositions especially, contained vesicles with very small intra-lumenal vesicles. All hybrid compositions appeared homogenous, and no phase separation was observed in any vesicles.

While blending POPC lipid with either PBd_{22}-PEO_{14} and PBd_{12}-PEO_{11} polymers was expected to form homogenous hybrid membranes due to the similar Hildebrand solubilities of the two materials, there could still be phase separation from differences in component hydrophobic thickness. To verify hybrid vesicle samples have formed blended membranes and not phase separated into distinct lipid-only or polymer-only populations, the relative intensities of a fluorescently labelled lipid (DiO) and polymer (PBd_{22}-PEO_{14}-TMR) for each vesicle were measured. In Figure 7.3, intensity values tending towards 1 indicate a higher polymer dye intensity within the membrane and implies a polymer-rich vesicle, while values tending towards -1 indicate a higher lipid dye intensity, implying a lipid-rich membrane. An intensity ratio of 0 indicates equal fluorescence intensity contributions in hybrid vesicles from both PBd_{22}-PEO_{14}-TMR and DiO.

As shown by Figure 7.3a the relative intensity ratios of hybrid PBd_{22}-PEO_{14} GUVs have a monomodal distribution centred around 0, indicating most GUVs in hybrid PBd_{22}-PEO_{14} samples have equal fluorescence intensity contributions from DiO and PBd_{22}-PEO_{14}-TMR. There are no distributions around -1 or 1, showing there are no vesicles with only DiO or PBd_{22}-PEO_{14}-TMR present in the membrane. This suggests these membranes are homogenous and there are no populations of pure PBd_{22}-PEO_{14} polymer or pure POPC lipid vesicles.

Figure 7.3h also shows that the relative intensity ratios of 25 mol% and 75 mol% hybrid PBd_{12}-PEO_{11} GUVs have a monomodal distribution centred around 0 and there are no distributions around -1 or 1. Again, this indicates most GUVs in 25 mol% and 75 mol% PBd_{12}-PEO_{11} samples have equal fluorescence intensity contributions from DiO and PBd_{22}-PEO_{14}-TMR, and that there are no populations of POPC- or PBd_{12}-PEO_{11}-only GUVs, therefore membranes composed of PBd_{12}-PEO_{11} are homogenous. Although 50 mol% PBd_{12}-PEO_{11} has the broadest distribution tending towards 1 and therefore indicating slightly more polymer-rich membranes, the distribution is still monomodal rather than bi-modal, indicating there are no populations of pure PBd_{12}-PEO_{11} polymer or pure POPC lipid vesicles.

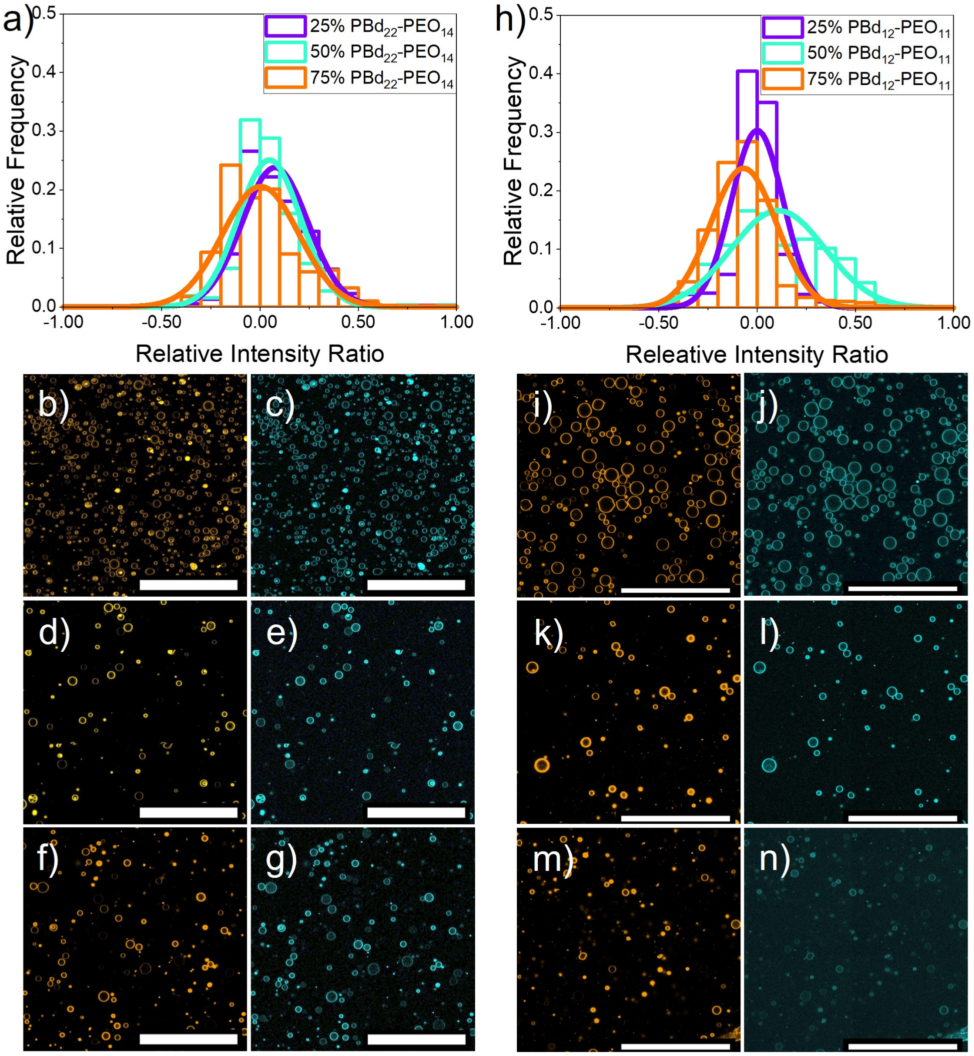

Figure 7.3: Intensity contributions from DiO and PBd$_{22}$-PEO$_{14}$-TMR in hybrid GUVs. A histogram of relative intensity ratios in a) PBd$_{22}$-PEO$_{14}$/POPC hybrid GUVs, fitted with a normal distribution curve, shows the ratios are centred around 0, suggesting a mixed membrane. Images below show intensity contributions from: b) DiO and c) PBd$_{22}$-PEO$_{14}$-TMR in 25 mol% PBd$_{22}$-PEO$_{14}$; d) DiO and e) PBd$_{22}$-PEO$_{14}$-TMR in 50 mol% PBd$_{22}$-PEO$_{14}$; f) DiO and g) PBd$_{22}$-PEO$_{14}$-TMR in 75 mol% PBd$_{22}$-PEO$_{14}$. The histogram of relative intensity ratios in h) PBd$_{12}$-PEO$_{11}$/POPC hybrid GUVs, again fitted with a normal distribution curve, shows the ratios are also centred around 0, suggesting a mixed membrane. Images below show intensity contributions from: i) DiO and j) PBd$_{22}$-PEO$_{14}$-TMR in 25 mol% PBd$_{12}$-PEO$_{11}$; k) DiO and l) PBd$_{22}$-PEO$_{14}$-TMR in 50 mol% PBd$_{12}$-PEO$_{11}$; m) DiO and n) PBd$_{22}$-PEO$_{14}$-TMR in 75 mol% PBd$_{12}$-PEO$_{11}$. The scale bar is 200 µm.

As the two fluorophores present in the hybrid lipid-polymer membranes have overlapping emission and excitation spectra, Förster resonance energy transfer (FRET) between them could occur, altering the intensity contribution from each dye and providing an inaccurate, non-representative result. The contribution from the lipid fluorophore, DiO, would decrease during FRET, shifting the intensity ratio towards 1 and resulting in a conclusion of a polymer-rich membrane in all vesicle compositions, which is not seen in Figure 7.3. The tile scan option on the microscope excites and images fluorescence from each probe sequentially, meaning the emission from DiO would not affect the fluorescence of PBd_{22}-PEO_{14}-TMR. The normalising the fluorescence intensity contributions from each dye before calculating the ratio would also negate any effects from FRET that could impact the result.

The results from observations and relative fluorescence intensity ratios show no obvious phase separation within the individual vesicles was observed. However lipid-rich and polymer-rich domains that are smaller than the microscope spatial resolution (~ 200 nm) may have formed in the hybrid membranes. To determine whether the hybrid PBd_{22}-PEO_{14} and PBd_{12}-PEO_{11} vesicles have nano-scale domains, cryo-electron tomography on LUV membranes of these lipid-polymer blends was performed as discussed in Chapter 5. Using visual observation, manual line profile analysis and an automated membrane thickness analysis, no nano-scale domains within hybrid vesicles composed of POPC and PBd_{22}-PEO_{14} or PBd_{12}-PEO_{11} were found.

7.2.2 Membrane viscosity

Changes to lipid lateral mobility with increasing polymer fraction were investigated using fluorescence recovery after photobleaching (FRAP). The diffusion coefficients were extrapolated from the fluorescence recovery times of a bleached area in the upper pole of a vesicle by calculating the mobility of the fluorescent lipid (DiO) and the fluorescent polymer (PBd_{22}-PEO_{14}-TMR) within the GUV membrane. As before, hybrid vesicles contain both 2 mol% DiO and 10 mol% PBd_{22}-PEO_{14}-TMR while 0 mol% and 100 mol% PBd_{22}-PEO_{14} compositions contain only 2 mol% DiO or 10 mol% PBd_{22}-PEO_{14}-TMR respectively. The true mole fractions of POPC, PBd-b-PEO (representing both PBd_{22}-PEO_{14} and PBd_{12}-PEO_{11}), DiO and PBd_{22}-PEO_{14}-TMR within these hybrid vesicles can be found earlier in Table 7.1. The fluorescence recovery data was modelled using a single diffusion coefficient for all membrane compositions. Between 15 and 20 GUVs were analysed for each composition and the average values shown in Figure 7.4.

The fluorophore DiO was included in 0-75 mol% polymer membrane compositions and was expected to partition into the lipid matrix of a hybrid membrane. The diffusion coefficient from DiO fluorescence recovery decreased with increasing polymer fraction, from 3.31 ± 0.56 $\mu m\,s^{-1}$ for a pure POPC lipid membrane to 0.46 ± 0.15 $\mu m\,s^{-1}$ in 75 mol% PBd_{22}-PEO_{14} hybrid vesicles and 0.68 ± 0.23 $\mu m\,s^{-1}$ in 75 mol% PBd_{12}-PEO_{11} hybrid vesicles. In PBd_{22}-PEO_{14} vesicle compositions, only the difference between 0 mol% and 25 mol% PBd_{22}-PEO_{14} is statistically significant. However for all PBd_{12}-PEO_{11} hybrid vesicle compositions, the differences in DiO fluorescence recovery is statistically significant ($p <$ 0.05, Tukey and Bonferroni ANOVA).

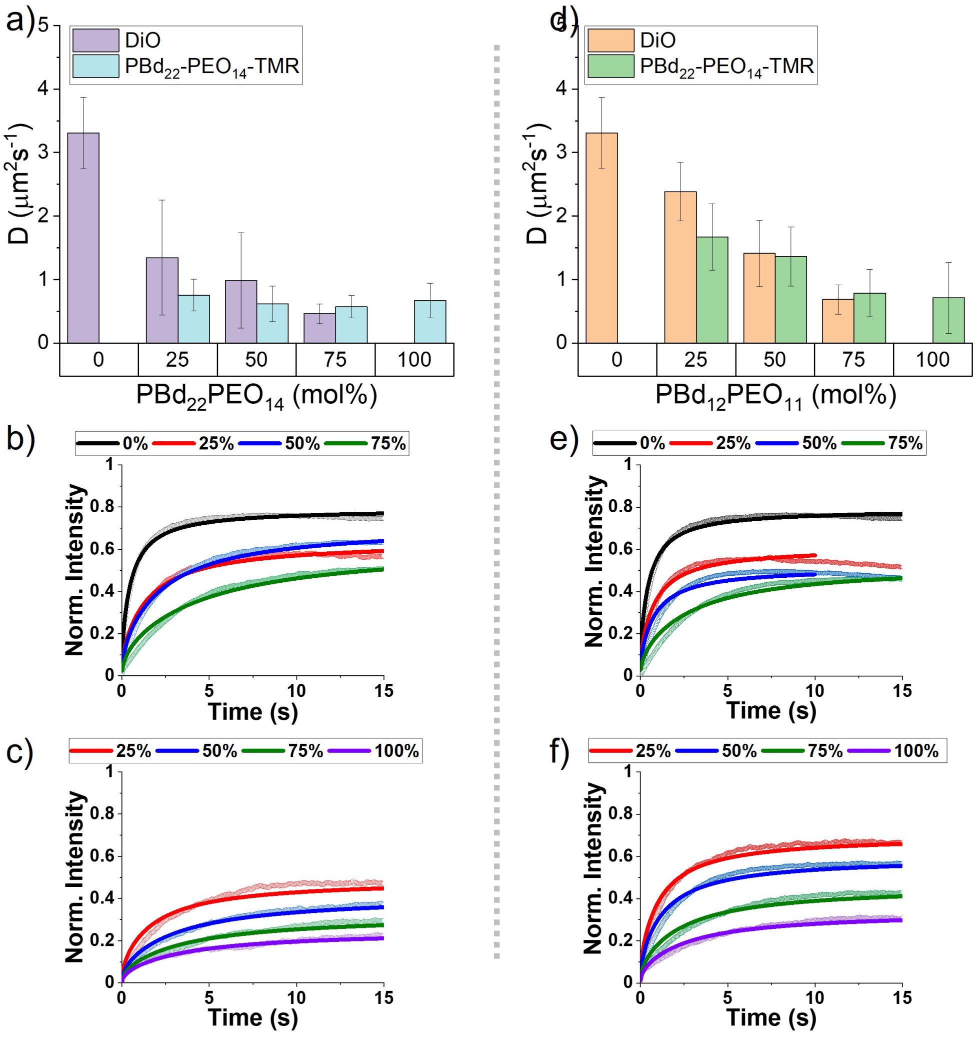

Figure 7.4: Comparing diffusion coefficients of PBd_{22}-PEO_{14}/POPC samples with PBd_{12}-PEO_{11}/POPC samples. The diffusion coefficients of a) PBd_{22}-PEO_{14} vesicles and d) PBd_{12}-PEO_{11} vesicles as well as the fluorescence recovery after photobleaching profiles from b),e) DiO and c),f) PBd_{22}-PEO_{14}-TMR fluorescent dyes in each composition.

The diffusion of polymers through the hybrid matrix was also monitored using a fluorescently labelled polymer, PBd_{22}-PEO_{14}-TMR, included in 25-100 mol% polymer compositions. The diffusion coefficient from PBd_{22}-PEO_{14}-TMR fluorescence recovery decreased with increasing polymer fraction, from $0.75 \pm 0.25\ \mu m\, s^{-1}$ for 25 mol% PBd_{22}-PEO_{14} vesicles to $0.67 \pm 0.28\ \mu m\, s^{-1}$ in 100 mol% PBd_{22}-PEO_{14} hybrid vesicles and 1.67 $\pm$ 0.52 $\mu m\, s^{-1}$ in 25 mol% PBd_{12}-PEO_{11} hybrid vesicles to $0.71 \pm 0.56\ \mu m\, s^{-1}$ in 100 mol% PBd_{12}-PEO_{11} vesicles. Although polymer diffusion through the hybrid matrix also decreased with increasing polymer fraction in PBd_{22}-PEO_{14} and PBd_{12}-PEO_{11} hybrid compositions, this decrease is not statistically significant ($p < 0.05$, Tukey and Bonferroni ANOVA) except between 50 mol% and 75 mol% PBd_{12}-PEO_{11}.

Overall, the diffusion of both DiO and PBd_{22}-PEO_{14}-TMR through either a PBd_{22}-PEO_{14} or PBd_{12}-PEO_{11} membrane decreases with increasing polymer mol%. This reduction in both DiO and PBd_{22}-PEO_{14}-TMR mobility appears to correlate with the polymer causing a significant drop in lipid mobility in 25 mol% PBd_{22}-PEO_{14} vesicles. Except in the 25 mol% PBd_{22}-PEO_{14} sample, there is no statistical significance between the diffusion coefficients of DiO or PBd_{22}-PEO_{14}-TMR in hybrid vesicles composed of either PBd_{22}-PEO_{14} or PBd_{12}-PEO_{11}, ($p < 0.5$, Tukey and Bonferroni ANOVA). This drop in DiO mobility in 25 mol% PBd_{22}-PEO_{14} vesicles correlates with hydrogen ion permeability results discussed previously in Chapter 4, where 25 mol% PBd_{22}-PEO_{14} vesicles were found to be more permeable than pure POPC vesicles.

7.2.3 Membrane hydration

Changes in membrane hydration with increasing polymer fraction in PBd_{22}-PEO_{14}/POPC and PBd_{12}-PEO_{11}/POPC vesicle compositions was monitored using the fluorescent probe Laurdan. The shift in fluorescence emission between 444 nm and 488 nm is used in Equation 7.4 to calculate a GP value that can be used as a quantitative measure for lipid packing as previous studies on hydration in lipid membranes have shown that lipids in the fluid phase are more hydrated, while lipids in the gel phase have more restricted motion, and are less hydrated (121). A GP value of 1 indicates an ordered membrane with little to no solvent within the hydrophobic region, while a GP of -1 indicates Laurdan is completely exposed to the bulk media and the membrane is disordered as shown in Figures 7.5a and b.

GUVs were used to obtain GP values from 15-20 individual vesicles using the confocal microscope. Higher molecular weight PBd_{22}-PEO_{14} membranes were anticipated to have more rigid membranes and so have greater membrane order than PBd_{12}-PEO_{11} membranes. Surprisingly, all compositions GP values were < 0 indicating a hydrated disordered membrane, with a marginal increase in GP value as polymer fraction increases as shown in Figure 7.5c. The marginally higher GP value in 100 mol% PBd_{22}-PEO_{14} sample is not statistically significant ($p > 0.05$, Tukey and Bonferroni ANOVA), therefore both PBd_{22}-PEO_{14} and PBd_{12}-PEO_{11} form GUV membranes with the same membrane order.

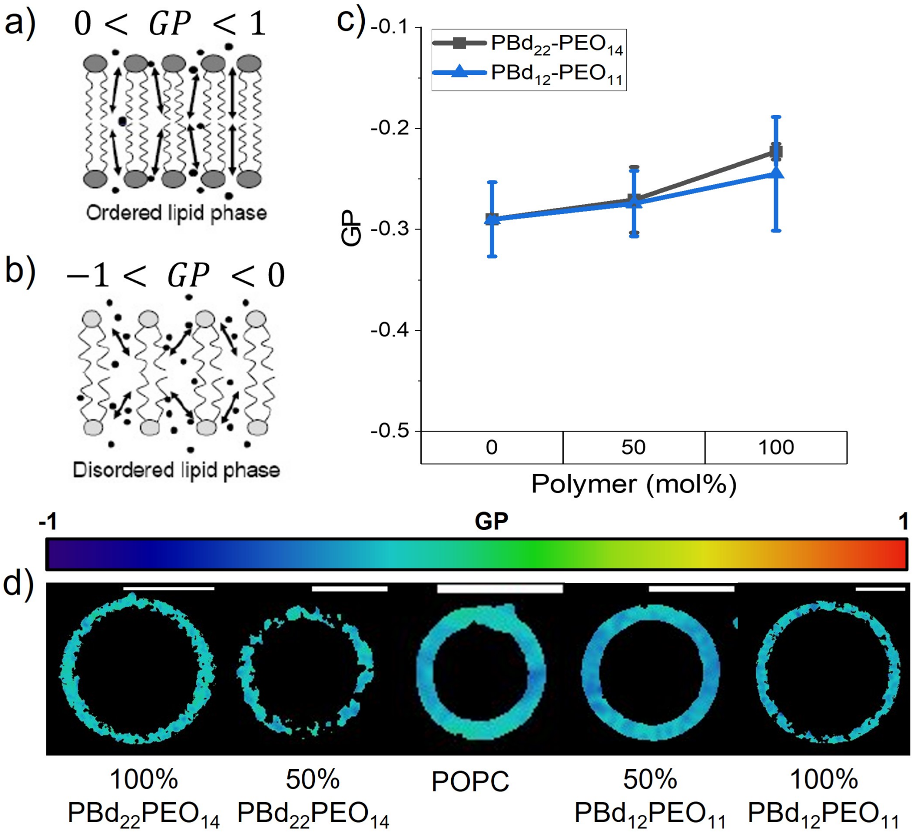

Figure 7.5: Comparison of membrane hydration obtained by fluorescence spectroscopy and spectral imaging. General polarisation (GP) values give an indication of packing in membranes: a) a positive GP value indicates an ordered membrane with little to no solvent while b) a negative GP value indicates a disordered membrane. c) GP values of GUVs increases slightly as polymer fraction increases in PBd_{22}-PEO_{14} and PBd_{12}-PEO_{11} vesicles. For all the compositions, there is very little variation in GP value in individual vesicles. d) The colour maps indicating GP values in images of each vesicle composition. The black spots on the colour map indicate no spectral data at those points. All spectral images can be found in Appendix A9.1. Scale bar indicates 10 µm.

7.2.4 Membrane rigidity

Flicker spectroscopy experiments were performed to quantify the membrane bending modulus (κ_b) of 0 mol%, 50 mol% and 100 mol% polymer GUVs with 0.5 mol% Rh-PE. Although the resolution of this technique does not allow accurate calculation of the membrane fluctuation amplitudes, $\langle|u(q)|^2\rangle$, of high-tension GUVs at a range of wavenumbers (q), the GUVs can be osmotically relaxed to decrease the tension of the membrane (124) to take these measurements. In doing so, the thermal undulations increases, increasing the membrane fluctuation amplitude, allowing for a more reliable fitting of the resultant power spectrum. The GUVs were chosen for flicker spectroscopy by visual observation; large GUVs with membranes that were clearly undulating were chosen over small GUVs or GUVs with apparently static membranes.

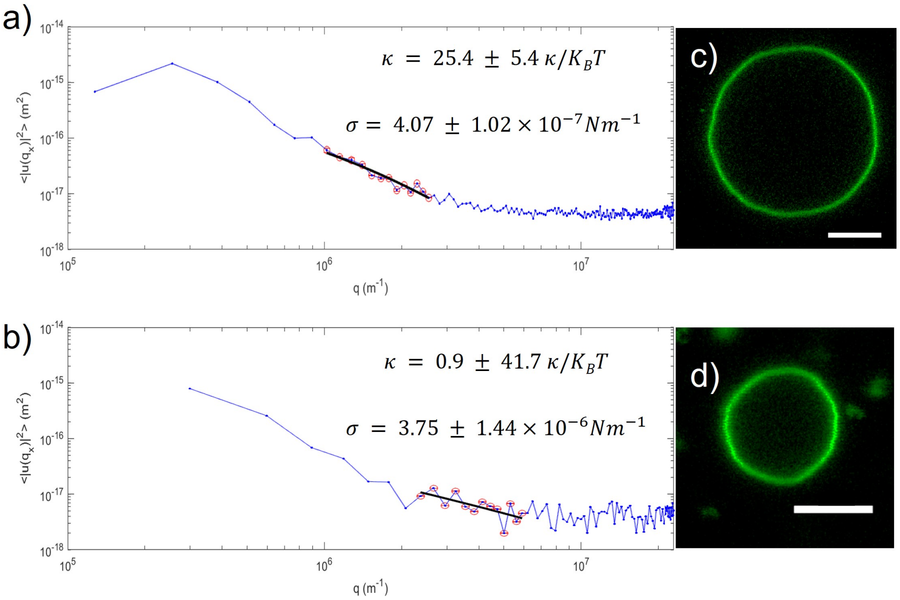

Figure 7.6: Outputs from MATLAB script. The output of a) 100 mol% PBd$_{22}$-PEO$_{14}$ vesicles show these vesicles have a much lower tension σ, and greater bending rigidity κ_b with a smaller error than b) 100 mol% PBd$_{12}$-PEO$_{11}$ vesicles. The images of c) 100 mol% PBd$_{22}$-PEO$_{14}$ sample shows that these vesicles are also larger (16 µm) than d) 100 mol% PBd$_{12}$-PEO$_{11}$ (7 µm), which may also affect the output from the MATLAB script. Scale bars are 5 µm.

For 0 mol% and 100 mol% PBd$_{22}$-PEO$_{14}$, and 50 mol% PBd$_{12}$-PEO$_{11}$ vesicle compositions, the difference in osmotic pressure between the internal and external media was 15-20 mOsm kg^{-1}. Unfortunately, despite increasing the osmotic difference across the membrane to 25-30 mOsm kg^{-1}, the lateral membrane tension was too high in 50 mol%

PBd$_{22}$-PEO$_{14}$ and 100 mol% PBd$_{12}$-PEO$_{11}$ vesicles, resulting in inconsistent bending rigidity values with high error for these samples. This may partially be due to the diameter of 100 mol% PBd$_{12}$-PEO$_{11}$ and 50 mol% PBd$_{22}$-PEO$_{14}$ vesicles being, on average, smaller than the other compositions measured for their undulations to be captured using the MATLAB script. High membrane tension would also reduce the amplitude of membrane fluctuations, making the fluctuations too small to be observed. As the membrane fluctuations would fall outside the resolution of the microscope, the undulations not be captured during image analysis.

As expected, pure polymer vesicles composed of the higher molecular weight PBd$_{22}$-PEO$_{14}$ polymer have the highest average bending rigidity, 37.3 ± 6.3 κ_b/K_BT, measured as shown by Figure 7.7.

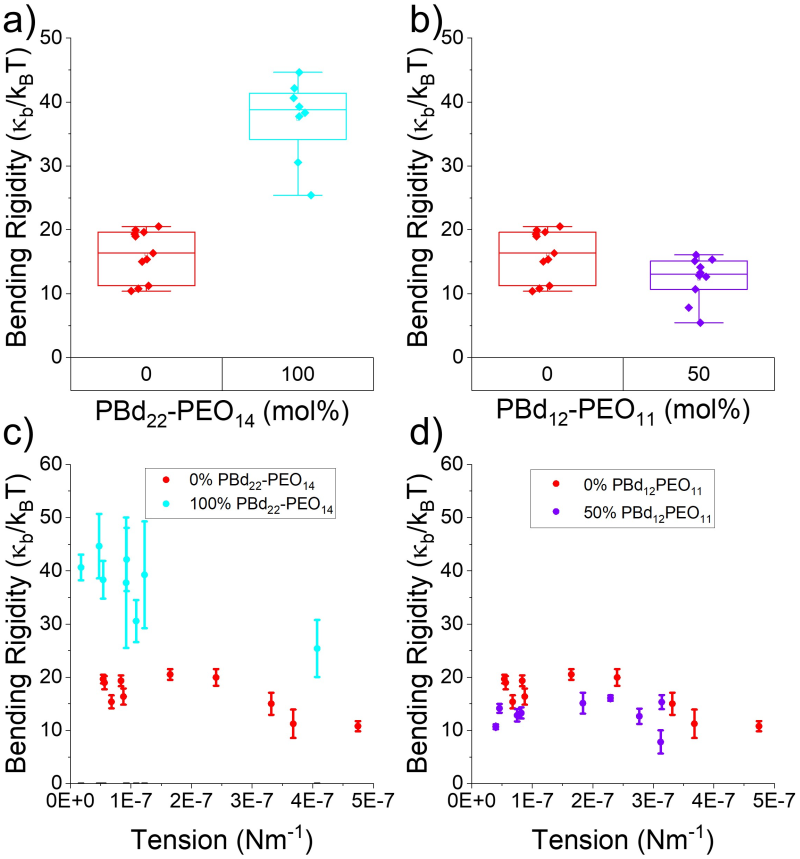

Figure 7.7: Bending rigidity and tension of hybrid lipid polymer membranes. The bending rigidity values taken by flicker spectroscopy on a) PBd$_{22}$-PEO$_{14}$ and b) PBd$_{12}$-PEO$_{11}$vesicle compositions as well as the bending rigidity vs lateral membrane tension in c)PBd$_{22}$-PEO$_{14}$ and d) PBd$_{12}$-PEO$_{11}$ compositions.

Although the values appear similar, 50 mol% PBd_{12}-PEO_{11} vesicles have a lower bending rigidity than pure POPC membranes ($12.3 \pm 3.4\ \kappa_b/K_BT$ and $16.1 \pm 3.9\ \kappa_b/K_BT$ respectively). Based on previous experiments 100 mol% PBd_{12}-PEO_{11} vesicles are anticipated to have a similar, or even lower bending rigidity compared to POPC membranes.

Lateral membrane tension was measured simultaneously with bending rigidity but no statistically significant difference between any composition was found ($p > 0.05$, Tukey and Bonferroni ANOVA).

7.3 Conclusion

POPC and PBd-b-PEO polymers were combined to form hybrid giant unilamellar vesicles. As polymer molar mass is thought to control the membrane thickness and therefore the membrane properties (103), different PBd-b-PEO polymer molecular weights were evaluated and their properties were compared. Even though the higher molecular weight PBd_{22}-PEO_{14} polymer would be expected to form more rigid, ordered membranes than PBd_{12}-PEO_{11}, well-mixed, homogenous membranes can be predicted as PBd_{46}-PEO_{30}, with a greater molecular weight than PBd_{22}-PEO_{14}, was successfully combined with POPC to form GUVs with homogenous membranes (90). The alkane chains in POPC also has a similar Hildebrande solubility to polybutadiene found in PBd-b-PEO, indicating homogeneous membrane formation (79, 100).

No macroscale phase separation was observed by visual inspection of the images of hybrid vesicle compositions. Analysing the relative fluorescence intensity ratios from DiO and PBd_{22}-PEO_{14}-TMR in both PBd_{22}-PEO_{14}/POPC and PBd_{12}-PEO_{11}/POPC hybrid vesicles indicate the membranes are well-mixed and homogenous, and that separate liposome and polymersome populations do not exist within any hybrid composition. Nanoscale domains were not expected as demonstrated by previously shown cryo-electron tomography studies in Chapter 5.

Fluorophore diffusion provides an indication of membrane viscosity. The few studies that have explored diffusion through polymer/lipid membranes found that diffusion of polymers through a membrane is much slower than for lipids (29) and that for higher molecular weight polymers, increasing the polymer fraction decreased the diffusion coefficient (96), corresponding to the results discussed in this chapter. On average the combined DiO and PBd_{22}-PEO_{14}-TMR fluorophore diffusion through hybrid PBd_{12}-PEO_{11} membranes was greater than hybrid PBd_{22}-PEO_{14} membranes, implying hybrid PBd_{22}-PEO_{14} membranes are more viscous than hybrid PBd_{12}-PEO_{11} membranes. However using PBd_{22}-PEO_{14}-TMR to measure membrane viscosity in PBd_{12}-PEO_{11}/POPC hybrid vesicles may not produce a representative result as diffusion of the PBd_{22}-PEO_{14}-TMR probe through the membrane is measured, rather than the diffusion of unlabelled PBd_{12}-PEO_{11}. PBd_{22}-PEO_{14}-TMR is fluorescently labelled PBd_{22}-PEO_{14} polymer, so has a higher molecular weight than PBd_{12}-PEO_{11} so the hybrid PBd_{12}-PEO_{11}/POPC samples are now ternary rather than binary mixtures (assuming DiO component has negligible effect).

This was mirrored in the general polarisation values of LUV and GUV membranes. Overall, the GP values indicate membranes of all PBd_{22}-PEO_{14} and PBd_{12}-PEO_{11} compositions are disordered and fluid, with only a marginal increase in GP as polymer fraction increases, suggesting similar hydration between POPC and both PBd_{22}-PEO_{14} and PBd_{12}-PEO_{11}.

Although a complete dataset could not be obtained due to high tension within some samples, 100 mol% PBd_{22}-PEO_{14} vesicles have the highest bending rigidity, indicating more rigid membrane structure. 50 mol% PBd_{12}-PEO_{11} have a low bending rigidity, implying a soft membrane. This corresponds to a previous study where reducing the polymer molecular weight in hybrid PBd-b-PEO/POPC vesicles resulted in vesicles that were more prone to deformation (206).

Although previous studies have shown PBd-b-PEO/POPC membranes increase functional lifetimes of incorporated membrane proteins (1, 77, 78), relatively few investigations have determined membrane phase separation, viscosity and fluidity and related the membrane compositions to these properties. Here, hybrid PBd-b-PEO/POPC GUVs were shown to form well-mixed, homogenous membranes, which have tunable viscosity and fluidity by altering the membrane composition.

8. Sterilisation and preservation

Since their discovery in the 1960s, the potential of lipid vesicles as drug delivery vesicles has been explored (9, 207, 208, 209). Most recently, lipid vesicles have been used as a key component in Pfizer/BioNTech and Moderna COVID-19 vaccines, protecting and transporting messenger ribonucleic acid (mRNA) molecules to the cells (210). Polymer vesicles have also been investigated as an alternative option for drug delivery due to their enhanced structural stability compared to their lipid counterparts (211, 212, 213, 214). Despite the advantages of block copolymers, they lack the natural biocompatibility and biofunctionality of phospholipids. By blending these two materials into a hybrid system, the advantages of both are combined and use of hybrid lipid-polymer vesicles as drug delivery vehicles are beginning to emerge (10, 215).

To be a viable option for drug delivery applications, hybrid lipid-polymer vesicles must be sterilised to make them safe for public use (216), and also be easy to transport, or at least withstand the temperature fluctuations that occur during transport (217) from the manufacturing site to their final destination without releasing their contents. Sterilisation is the process by which all forms of life are destroyed, removed or permanently inactivated. Instead of an absolute measure of sterilisation, pharmaceutical industries use processes that reduces the probability of the survival of undesired organisms to a negligible level. Currently, pharmaceutical companies use thermal, filtration and irradiation techniques to sterilise their products (216, 218). Thermal sterilisation, by using an autoclave, is the most common and the most reliable as it achieves destruction of microorganisms by irreversible denaturation of enzymes (218). During thermal sterilisation, the heat imparted could damage the structure of the vesicles or their payload. Filtration through a maximum of 0.22 µm membrane is usually used for thermally labile solutions and sterilisation of active ingredients or medical devices can be achieved by irradiation (216). During filtration, vesicles undergo shear stress when passing through the filter membrane channels. With the addition of high flow through the channel, high shear stress could cause vesicles to deform and even induce transient pore formation in the vesicle membrane, which might lead to the vesicles leaking or even rupturing. Irradiation also has the potential to damage lipids and/or polymers.

The vesicle formulations must also be stable during their storage and transportation between primary and secondary manufacturing locations, or between the manufacturer and end-user. Even once the formulations have reached the end-user, they may be stored for some time before they are finally used. Cold-chain transportation is often used to maintain the stability and activity of medicinal products and labile formulations. Liquid formulations can be frozen for preservation, but extended freezing can cause ice crystal formation that could damage the membrane during freezing and subsequent thawing (219). Potential damage from ice crystals aside, vesicles will become stressed by the expansion of water in their lumen upon freezing. Water volume increases by $\sim 9\%$ when frozen, which will extend the area of the vesicle membrane by $\sim 6\%$, which exceeds the lysis strain lipid membranes can withstand. Freeze-thaw cycles in LUV formation protocols are used intentionally rupture liposomes for this reason. During manufacture, transport and storage, formulation may experience several freeze-thaw cycles. During transport, many pharmaceutical products are stored and shipped at improper temperatures. Fluctuations in temperature can also hit products with temperatures that they cannot withstand causing some samples to reach their destination past their shelf life, which can make some formulations ineffective or even harmful (217, 220). This variation in temperature could be emulated by numerous freeze-thaw-vortex (FTV) cycles; the release of encapsulated material can be monitored over several cycles of FTV.

Lyophilisation (freeze-drying) can be used to maintain the stability of lipids during transportation. During the freeze-drying process the product is frozen, thus immobilising the sample and allowing it to retain its original form, and then the water is evaporated by sublimation, preventing microbial growth (221). For lipids, the absence of water would minimise the rate of hydrolysis during storage (222). However for lyophilisation of liposomes additives are often required to maintain encapsulation and structural stability, even though their efficacy can be inconsistent (222).

Hybrid lipid-polymer vesicles have been shown to exhibit the biocompatibility of lipid systems as well as the mechanical stability of polymersomes, making them a viable drug delivery vehicle (10, 215). However, for drug delivery applications, the vesicles also need to withstand sterilisation processes and the rigours of transport. Very few studies have explored the stability of hybrid lipid-polymer vesicles under these conditions, so the material properties of hybrid PBd_{22}-PEO_{14}/POPC and PBd_{12}-PEO_{11}/POPC vesicles presented in this chapter could help design vesicles as drug delivery vehicles with controlled encapsulation and release.

8.1 Methods

Large unilamellar vesicles were formed as outlined in 3.2.1 using 60 mM 5(6)- carboxyfluorescein (CF), 40 mM HEPES and 20 mM sodium chloride as the buffer, adjusted the pH to 7.4 by dropwise addition of sodium hydroxide. Suspensions were extruded 11 times though a 100 or 400 nm pore size polycarbonate membrane filters using a LiposoFast Basic

Extruder. The samples were run on a Sephadex G50 column under gravity using 40 mM HEPES and 20 mM sodium chloride buffered to pH 7.4 as the mobile phase to remove unencapsulated CF dye as outlined in 3.2.2, and size characterisation carried out as detailed in 3.2.3. Size distributions were also measured after the processing steps described below to assess the colloidal stability of these vesicle formulations under these conditions.

8.1.1 CF leakage assay

The 100 nm sized hybrid vesicle samples were split into 4 fractions of 500 µL (vesicle concentration $\sim$ 2 mM). Fraction 1 was thermally sterilised using an autoclave at 121 °C) for 15 min. Fraction 2 was lyophilised using a VirTis Benchtop Pro Lyophiliser (Wolf Laboratories Ltd., York, UK) for 24 h after freezing the sample in nitrogen. Fraction 3 underwent 5 filtration cycles through a 13 mM PTFE 200 nm syringe filter device (Fisher Scientific Ltd, Hampton, New Hampshire, USA) with polypropylene housing. Fraction 4 was frozen in liquid nitrogen, thawed in a water bath at 60 °C and then vortexed for 3s. The samples in Fraction 4 were treated by 4 of these freeze-thaw-vortex (FTV) cycles. 400 nm sized vesicles were also filtered through a PTFE 200 nm syringe filter device (Fisher Scientific Ltd, Hampton, New Hampshire, USA) with a polypropylene housing 5 times.

CF is self-quenching at high concentrations ($>$ 40 mM) (11, 111) , so the emission intensity at this concentration was often very low. The CF was encapsulated at 60 mM, so the control samples would have a low emission intensity. When the vesicles released the encapsulated CF, the CF was diluted by the external buffer and the fluorescence intensity increased. To measure the CF release, 0.5 mL fractions were diluted to 2 mL (vesicle concentration $\sim$ 18 µM) and the fluorescence emission at 519 nm of CF-encapsulated vesicles was measured with excitation set to 492 nm using a Horiba Scientific Fluoromax Plus (Horiba Ltd., Kyoto, Japan). Measurements were made on initial vesicle fractions and between every processing cycle for each fraction. The initial vesicle preparations were ruptured with 50 µL of 10% (w/v) Triton X-100 (end concentration 0.91% (w/v)) to completely destabilise the vesicles and release the encapsulated CF before a final fluorescence emission at 519 nm was measured. The CF% release was calculated by

$$CF\%\ release = \frac{I_i - I_0}{I_t - I_0} \times 100\% \tag{8.1}$$

Where I_0 is the initial intensity of the sample, I_i is the intensity of the sample after each processing cycle (from autoclaving, lyophilisation, FTV or filtering), and I_t is the intensity after the initial sample is burst with Triton X-100.

8.1.2 Cryogenic transmission electron microscopy

Vesicles of 50 mol% PBd_{22}-PEO_{14} at 100 nm and 400 nm were imaged before and after the final freeze-thaw-vortex and filtration cycles respectively. Minor changes to the methods outlined in Section 3.2.4 were made: for 100 nm vesicles, 400 mesh 2/2 Cu Quantifoil grids were used, while for 400 nm vesicles 400 mesh Cu Lacey grids were used.

Samples (3μL, $\sim$ 2 mM) were placed directly onto the grid using a FEI Vitrobot mkIV. The samples were kept in closed pucs under nitrogen until required. To image the grids, FEI Titan KRIOS microscope with an accelerating voltage of 300 kV was used with a defocussing of 3 μm at a magnification of $\times$ 75000. The pixel resolution for these images were 1.069 $\text{Å}\,\text{px}^{-1}$.

8.2 Results and discussion

The hybrid vesicles were investigated under conditions designed to mimic the sterilisation and preservation processes used in industry. The full range of compositions from pure lipid to pure polymer of both PBd_{22}-PEO_{14} and PBd_{12}-PEO_{11} diblock copolymers were formed and loaded with CF. The encapsulation stability was studied using fluorescent spectroscopy through the release of CF. The colloidal stability of the vesicle formulations was determined from their hydrodynamic size distributions obtained from the DLS.

8.2.1 Sterilisation

Autoclaving

Autoclaving of hybrid vesicles would be the preferred choice for sterilisation for these formulations. First, vesicles composed of the pure system were investigated: 100 mol% POPC, 100 mol% PBd_{22}-PEO_{14} and 100 mol% PBd_{12}-PEO_{11}. As 100% CF release was observed in all pure lipid or polymer vesicles as shown in Figure 8.1, it was considered extremely unlikely that hybrid compositions would perform any better.

To observe the colloidal stability of the vesicles DLS size distributions were collected before and after autoclaving as shown in Figure 8.1. The auto-correlation function associated with the size profiles are shown in Appendix A10.1. The delayed exponential decay shown in the auto-correlation functions indicate aggregation or structural instabilities in all the vesicles (except 100 mol% POPC) after autoclaving. The presence of larger micron-sized sedimenting particles is also suggested by the auto-correlation function not reaching the baseline.

Autoclaving as a method of sterilisation proved to be too destructive, causing the vesicles to release their entire contents. As these vesicles were unstable under autoclaving, other potential methods of sterilisation were also investigated. However, this does not mean that autoclaving these hybrid vesicles is impossible: the vesicle formulations could be optimised with additional additives to the buffer, such as sugars or polyols, to help protect the vesicle structure during autoclaving (223).

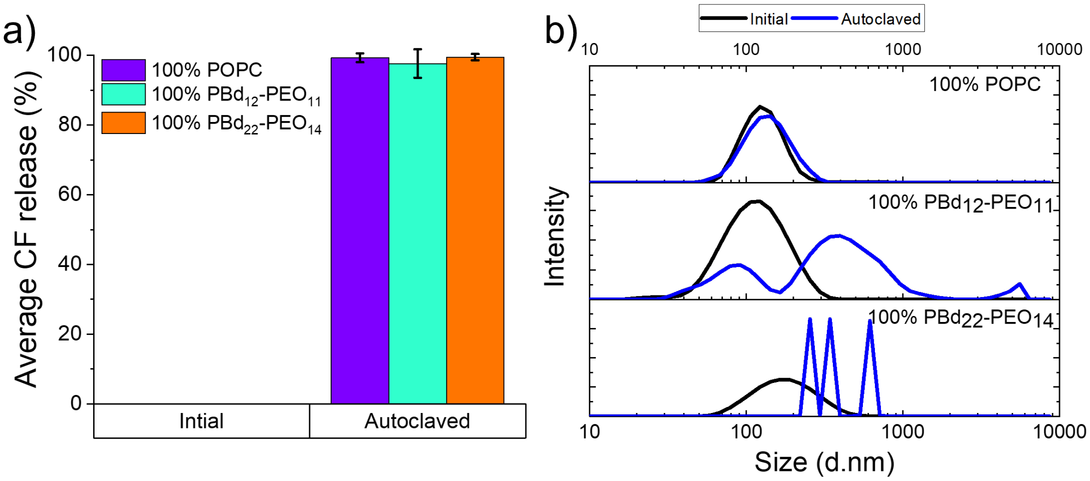

Figure 8.1: CF release and size distributions of 100 nm hybrid vesicles after autoclaving. a) CF release and b) DLS distributions of the hydrodynamic diameters of 100 nm extruded PBd_{12}-PEO_{11} and PBd_{22}-PEO_{14} hybrid vesicles before and after autoclaving cycles. The CF intensity increases when the 100 mol% vesicle compositions are autoclaved indicating that the CF contents is fully released.

Filtration

Sterilisation can also be achieved by filtration through a membrane with a maximum pore size of 0.22 µm. Here, a 0.20 µm pore size membrane was used in five filtration cycles at room temperature of hybrid vesicles between 0 and 100 mol% block copolymer content in 25 mol% increments for both PBd-b-PEO polymers. Across the five filtration cycles the average contents release reached at most 10% for both PBd-b-PEO polymers as shown by Figures 8.2 a and b. There is no statistical significance ($p < 0.05$ Tukey and Bonferroni) between the different vesicle compositions studied. Contrary to expectations, the only statistically significant difference is in the greater contents release of 100 mol% PBd_{22}-PEO_{14} polymersomes compared to all other membrane compositions. As this membrane comprises the larger PBd_{22}-PEO_{14} polymer, the previous expectation was that these vesicles would be more mechanically stable. However, the % release is only marginally greater than 10% for the fourth and fifth filtration cycle in the 100 mol% PBd_{22}-PEO_{14} membranes, which is still low even after several filtration cycles.

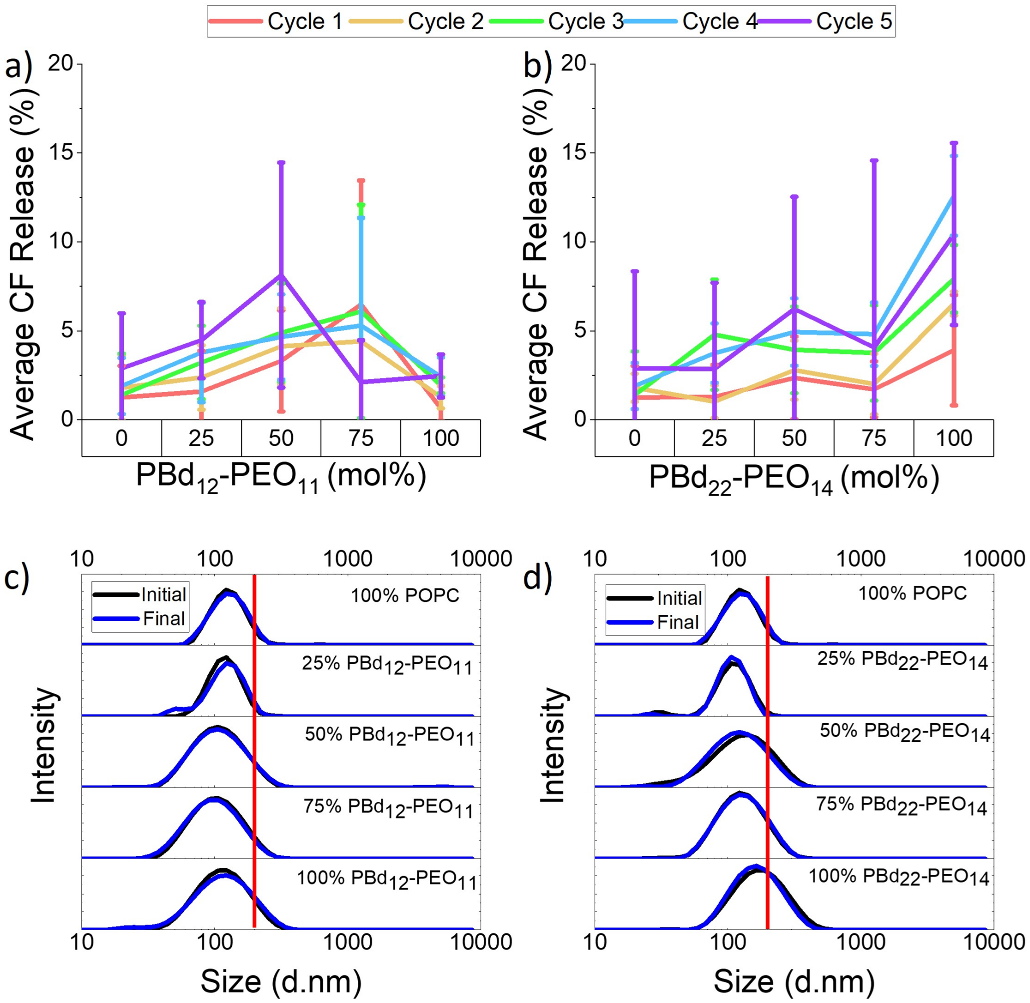

Figure 8.2: CF release and size distributions of 100 nm extruded hybrid vesicles before and after filtration through a 200 nm pore. Encapsulated CF % release following filtration plotted against membrane composition for hybrid vesicles composed of POPC and a) PBd_{12}-PEO_{11} or b) PBd_{22}-PEO_{14}. Data is shown for between one to five filtration cycles through a 0.2 μm pore size filter membrane. Each measurement was performed in triplicate and the errors data points represent mean ± s.d. The red line on these graphs indicate the filter pore size of 200 nm. The DLS distributions of the hydrodynamic diameters of 100 nm extruded c) PBd_{12}-PEO_{11} and d) PBd_{22}-PEO_{14} hybrid vesicles before and after five filtration cycles.

The DLS size distributions of 100 nm extruded vesicles before and after five filtration cycles was similar between vesicle compositions in both PBd-b-PEO polymers. Vesicles with higher polymer content have a tail in their size distribution that extends beyond the filtration pore size. 100 nm sized vesicles can pass the filter without any major changes in their size however as the size distribution extends beyond the filtration pore size suggests that the probability of transient pore formation in the vesicle membrane increases when vesicle size is greater than the filter pore size as the vesicle must deform to propagate through the filter pore channel. There was no evidence of aggregation or sedimentation as shown by Appendix A10.2 and A10.3. Since the majority of the 100nm extruded vesicles were smaller than the 200nm filter size, a more stringent test of hybrid vesicle stability under filtration was completed by using 400nm extruded vesicles. For this set of experiments, only the pure lipid and PBd-b-PEO vesicles plus the 50 mol% polymer hybrid compositions of both polymers were investigated.

The contents release from 400 nm extruded vesicles was significantly greater than from 100 nm extruded vesicles as shown in Figure 8.3. The shorter PBd_{12}-PEO_{11} polymer membranes appear to slightly reduce the CF release observed with increasing polymer mol%, although this difference is not statistically significant. The only statistically significant difference in contents release is observed for pure PBd_{22}-PEO_{14} polymer vesicles, which show reduced encapsulation stability compared to the POPC liposomes and 50 mol% polymer hybrid vesicles 8.3b. However, overall contents release after five filtration cycles remains small, less than 15% for all compositions except the 100 mol% PBd_{22}-PEO_{14} vesicles, where contents release is approximately 25% after five filter passes.

Filtering the 100 mol% PBd_{22}-PEO_{14} vesicles was more difficult than the filtration of other vesicle compositions, as higher pressures had to be applied to force the vesicle sample through the filter. This suggests that the vesicles composed of the thicker polymers are more rigid and have a high bending stiffness. The higher pressure required during filtrations is probably the cause of the greater CF release from the 100 mol% PBd_{22}-PEO_{14} vesicles as high pressure is more likely to induce more shear stress during filtration. The shorter PBd_{12}-PEO_{11} polymer vesicles might have a lower bending resistance, which could impart some enhanced elasticity, allowing these vesicle samples to pass through the filter more easily.

All the samples contained some vesicles that were much smaller in size than the 400 nm pore size of the extrusion membrane for vesicle preparation as shown in Figure 8.3. However, a large proportion of vesicles are larger than the 200 nm filter size, meaning that these vesicles would need to deform or break-up to pass through the filter.

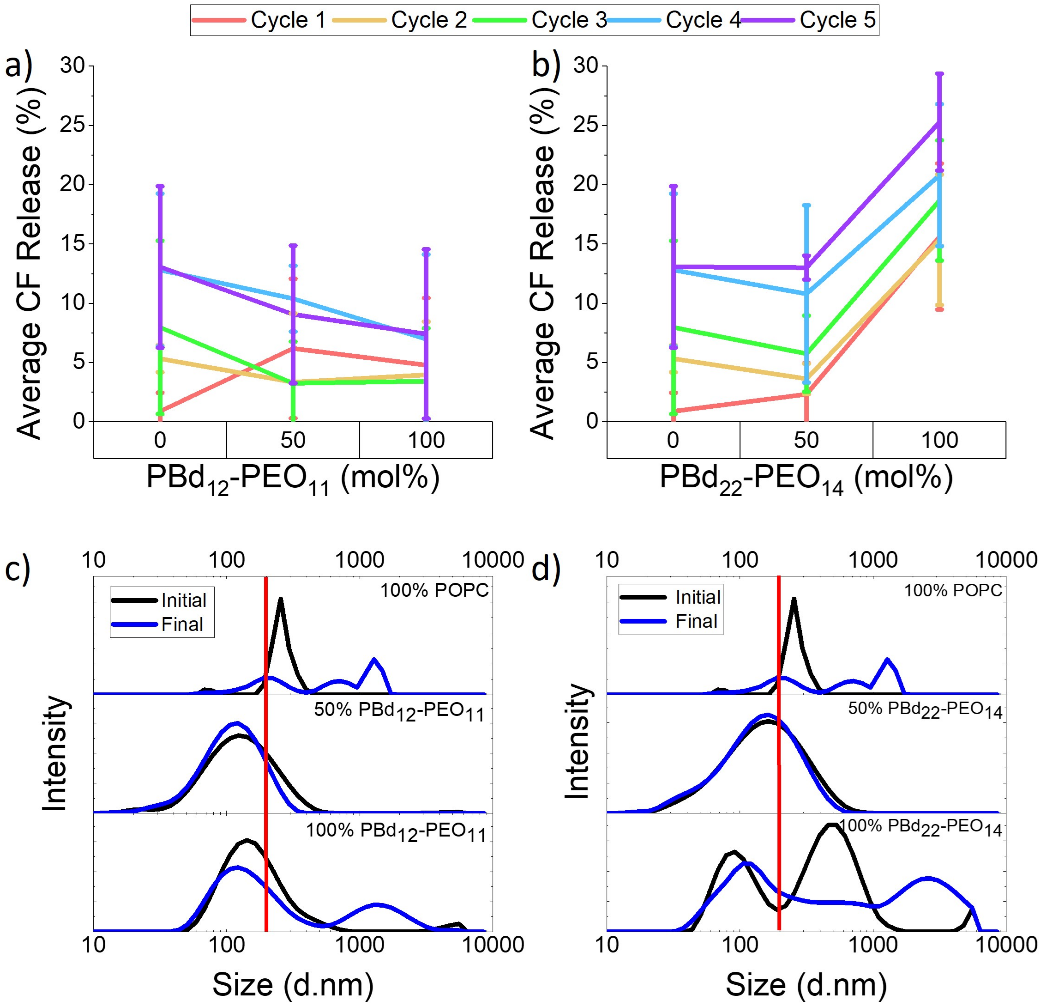

Figure 8.3: CF release and size distributions of 400 nm extruded hybrid vesicles before and after filtration through a 200 nm pore. Encapsulated CF % release following filtration plotted against membrane composition for hybrid vesicles composed of POPC and a) PBd$_{12}$-PEO$_{11}$ or b) PBd$_{22}$-PEO$_{14}$. Data is shown for between one to five filtration cycles through a 0.2 µm pore size filter membrane. Each measurement was performed in triplicate and the errors data points represent mean ± s.d. The red line on these graphs indicate the filter pore size of 200 nm. The DLS distributions of the hydrodynamic diameters of 400 nm extruded c) PBd$_{12}$-PEO$_{11}$ and d)PBd$_{22}$-PEO$_{14}$ hybrid vesicles before and after five filtration cycles.

All pure component vesicles, lipid or polymer, showed multimodal size distributions after five filtration cycles, indicating aggregation and loss of colloidal stability. The 50 mol% polymer hybrid vesicle formulations fared best under filtration, which might be due to the enhanced colloidal stability of blended lipid-polymer hybrid membrane. However, it is also possible that this is simply due to the smaller initial size of these hybrid vesicles (145 nm for 50 mol% PBd_{12}-PEO_{11} hybrid vesicles and 182 nm for 50 mol% PBd_{22}-PEO_{14} hybrid vesicles) compared to the pure component vesicles. As good colloidal stability was observed for the 100 nm extruded vesicles, this latter explanation seems the most likely. The smaller initial size of 50 mol% polymer hybrid vesicles could be because of this composition has a preferred curvature that limits the maximum vesicle size.

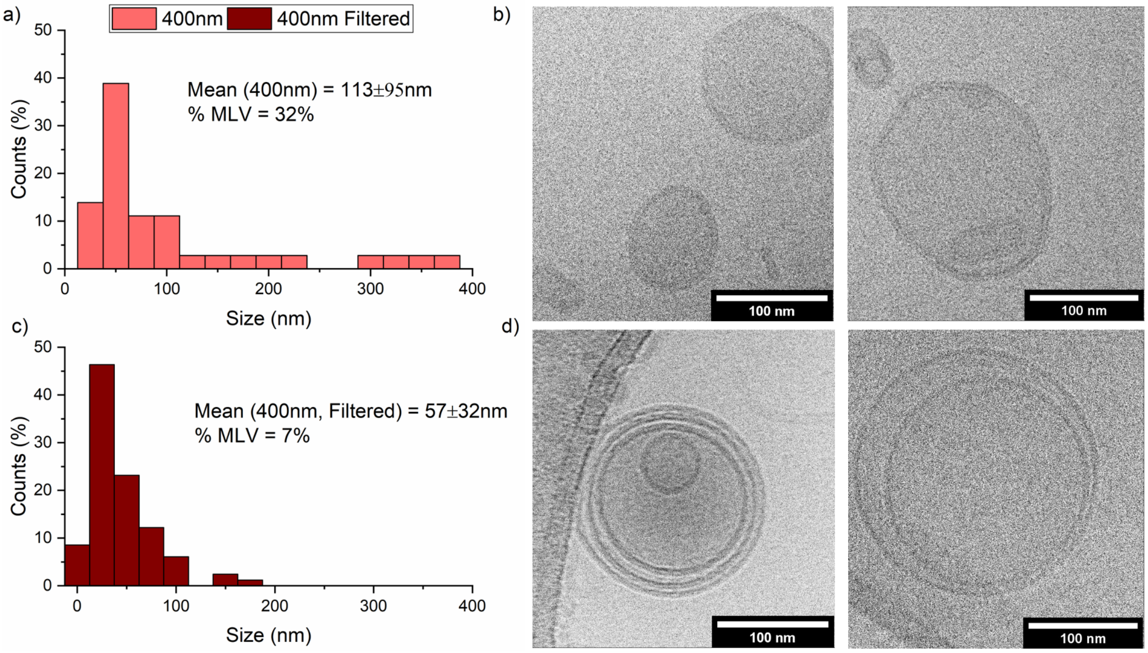

Figure 8.4: Cryo-TEM images of 400 nm extruded vesicles before and after five filtration cycles through a 200 nm pore. Cryo-transmission electron microscopy (Cryo-TEM) of 50 mol% PBd_{22}-PEO_{14} hybrid vesicle (400 nm extrusion membrane) before and after five filtration cycles. a) Histogram of initial vesicle sizes from cryo-TEM images; b) representation images of vesicles before filtration; c) histogram of vesicle sizes after filtration from cryo-TEM images; d) representation images of vesicles after filtration. Scale bars represent 100 nm. The image was taken from reference (2).

400 nm 50 mol% PBd_{22}-PEO_{14} vesicles were imaged before and after filtration using cryo-transmission electron microscopy. Diameter measurements from cryo-TEM images show that initially 50 mol% PBd_{22}-PEO_{14} vesicles have an average diameter of 113 ± 95 nm and 32% of vesicles were observed to be multilamellar. This is similar to the DLS analysis which gave a Z-average of 124 nm (PDI 0.279) for the initial 50 mol% PBd_{22}-PEO_{14} sample. However after filtration the size measurements differ between cryo-TEM and DLS analyses: cryo-TEM analysis gave an average vesicle size of 57 ± 32 nm with 7% of

vesicles found to be multilamellar while DLS showed a post-filtration Z-average of 120 nm (PDI 0.269). From the histograms of vesicle size from cryo-TEM in Figures 8.4a and c, this reduction in average size might be due to the rupturing of larger $>$ 200 nm vesicles from the post-filtered samples, which would also explain the lower fraction of multilamellar vesicles observed in the cryo-TEM images.

As shown in Figure 2.14, ice thickness can vary depending on the particle dimensions, but usually ranges from a few nanometres to a few hundred nanometres (138). The thicker the ice, the worse the resolution (224), however if the ice is too thin than the particles are pushed towards the grid hole edges, leaving the grid hole empty of sample an potentially causing particle aggregation (225). Variations in ice thickness can also sort the vesicles by size, concentrating the larger vesicles in thicker ice (145). Lacey carbon-coated copper grids have a higher percentage of open area than traditional grids, which allows larger objects to protrude over the edges of the grid holes and be seen at a higher resolution (2, 226). Although variations in ice thickness can sort the vesicles by size and exclude the larger vesicles from the thin ice found in the EM grid holes thus giving a smaller size distribution from cryo-TEM compared to DLS, the difference between the pre-and post-filtered hybrid vesicles by cryo-TEM appears to be significant. The disassembly of some larger and multilamellar vesicles during filtration would likely account for the $\sim$15% leakage of vesicle contents observed in Figure 8.3.

8.2.2 Preservation

Lyophilisation

Lyophilisation of hybrid vesicles would be the preferred choice for preservation if these formulations can be made to be stable under these conditions. When the samples were lyophilised, only vesicles composed of the pure components were investigated initially: 100 mol% POPC, 100 mol% PBd_{22}-PEO_{14} and 100 mol% PBd_{12}-PEO_{11}. As 100% CF release was observed in all cases as shown in Figure 8.5, it was considered extremely unlikely that hybrid blends would perform any better.

To observe the colloidal stability of the vesicles DLS size distributions were collected before and after lyophilisation as shown in Figure 8.5. The auto-correlation function associated with the size profiles are shown in Appendix A10.6. The delayed exponential decay shown in the auto-correlation functions indicate aggregation or structural instabilities in all the vesicles. The presence of larger micron-sized sedimenting particles is also suggested by the auto-correlation function not reaching the baseline, leading to poor fits of the auto-correlation function and non-Guassian-like traces shown in Figure 8.5b.

Lyophilisation as a preservation method proved to be too destructive, causing the vesicles to release their entire contents, so other potential methods of preservation were also investigated. However, lyophilisation of hybrid vesicles is not impossible: the vesicle formulations could be optimised with additional additives such cryoprotectants to the buffer to help protect the vesicle structure during lyophilisation (227).

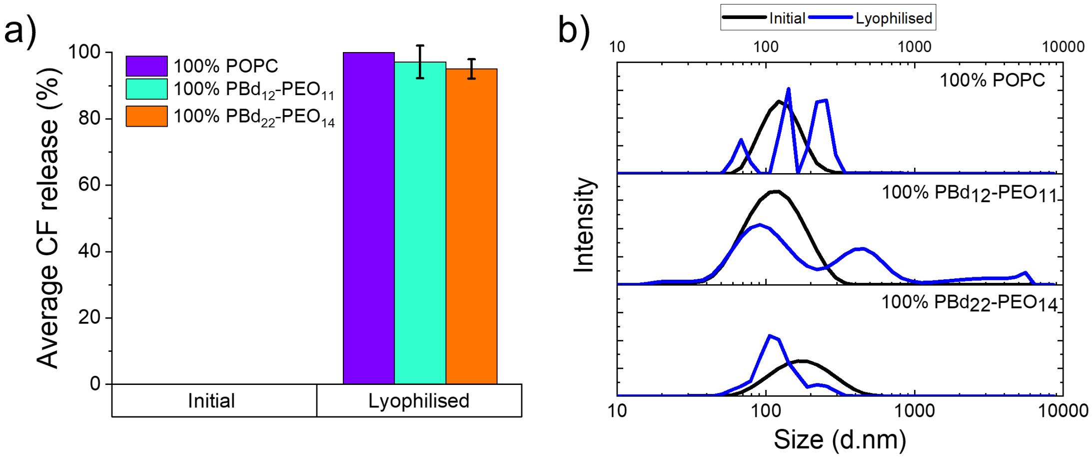

Figure 8.5: CF release and size distributions of 100 nm extruded vesicles before and after lyophilisation. a) CF release and b) DLS distributions of the hydrodynamic diameters of 100 nm extruded PBd$_{12}$-PEO$_{11}$ and PBd$_{22}$-PEO$_{14}$ hybrid vesicles before and after lyophilisation. The CF intenstiy increases when the pure component vesicles are lyophilised indicating that the CF contents is fully released.

Freeze-thaw-vortex

Vesicle samples can also be frozen in the liquid state without sublimation of excess water as alternative to lyophilisation. The formulations would need to withstand several cycles of freeze-thawing without releasing their contents to be a viable storage method during transportation. Here, the stability of the vesicles were investigated following four freeze-thaw-vortex (FTV) cycles. The vortexing step is necessary to ensure the vesicles are fully resuspended in the liquid state.

Figure 8.6 shows that pure POPC vesicles are unstable even after one FTV cycle, which is expected as the freeze-thaw technique is often used for passive loading in lipid vesicle preparation protocols as it temporarily makes the membrane permeable. Vesicles with increasing PBd$_{22}$-PEO$_{14}$ mol% were observed to be more stable maintain their encapsulated CF than those with increasing mol% of PBd$_{12}$-PEO$_{11}$. The 100 mol% PBd$_{22}$-PEO$_{14}$ vesicle had the highest encapsulation stability over other hybrid formulations across four FTV cycles. As PBd$_{22}$-PEO$_{14}$ is the larger block copolymer, it is thought to have a thicker, more elastic membrane that allows the membrane to stretch without rupturing from the volume expansion of freezing. These thicker membranes might also protect the vesicles from damage caused by the formation of ice crystals during freezing.

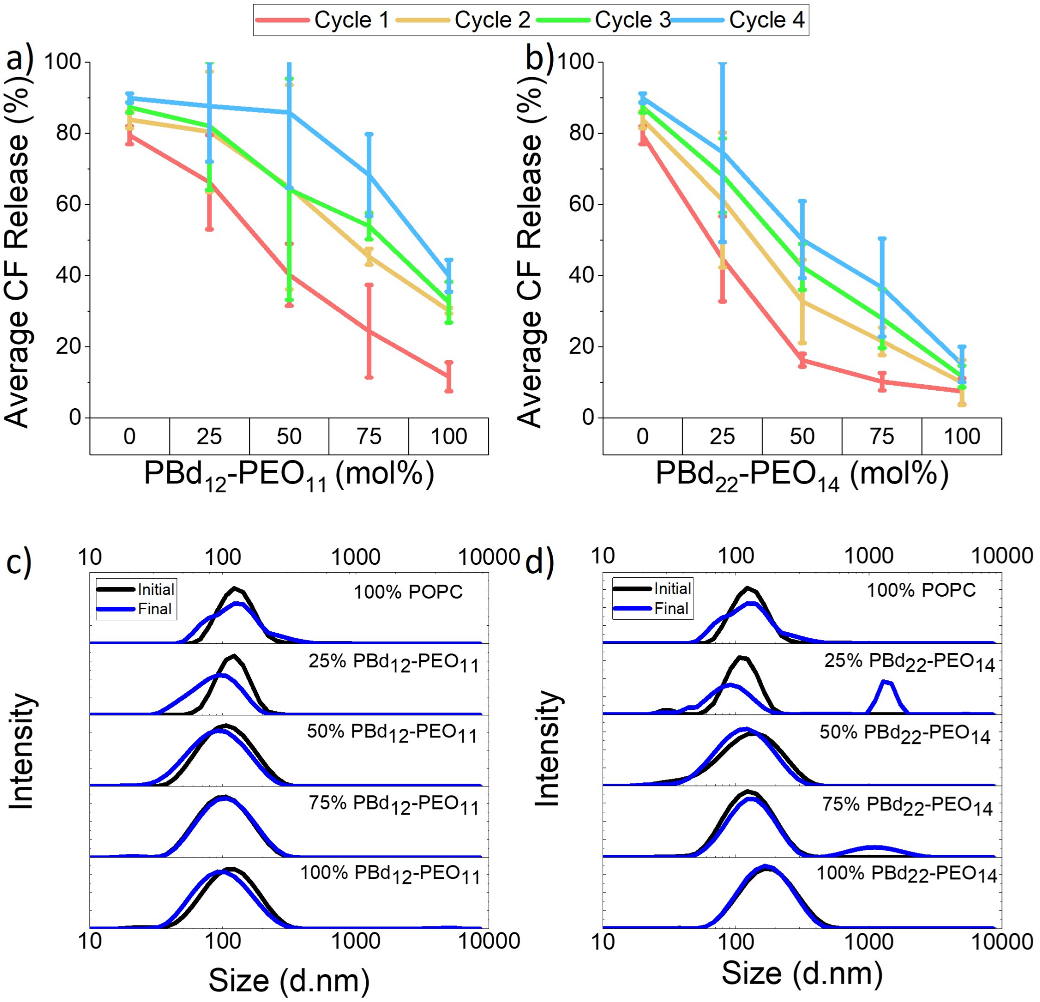

Figure 8.6: CF release and size distributions of 100 nm extruded vesicles before and after four FTV cycles. Encapsulated CF % release following four FTV cycles plotted against membrane composition for hybrid vesicles composed of POPC and a) PBd_{12}-PEO_{11} or b) PBd_{22}-PEO_{14}. Data is shown for one to five filtration cycles through a 0.2 µm pore size filter membrane. Each measurement was performed in triplicate and the errors data points represent mean ± s.d. The DLS distributions of the hydrodynamic diameters of 100 nm extruded c) PBd_{12}-PEO_{11} and d) PBd_{22}-PEO_{14} hybrid vesicles before and after four FTV cycles.

The DLS size distributions from Figure 8.6c and d show that the FTV cycles had the most impact on the colloidal stability on the lipid-rich vesicles: for lipid-rich compositions the size distributions broaden following four FTV cycles while for hybrid vesicles with ≥50 mol% polymer content were similar before and after four FTV cycles.

Cryo-TEM was used again to investigate the effect of freeze-thaw action on the size and morphology of 50 mol% PBd_{22}-PEO_{14} hybrid vesicles shown in Figure 8.7. The vesicles appear to have similar size before and after the FTV cycles (59 ± 38 vs. 60 ± 24 nm), and multilamellarity seems to increase slightly following the FTV cycles (from 15% vs. 24%). However the size distribution from cryo-TEM does not agree with the z-average measurements from the DLS (108 nm vs. 101 nm, PDI 0.213 and 0.191 respectively), which could be explained by the cryo-TEM grid preparation. Again, variations in ice thickness sorts the vesicles by size, favouring smaller vesicles in the cryo-TEM grid holes and larger vesicles on the carbon-coated support.

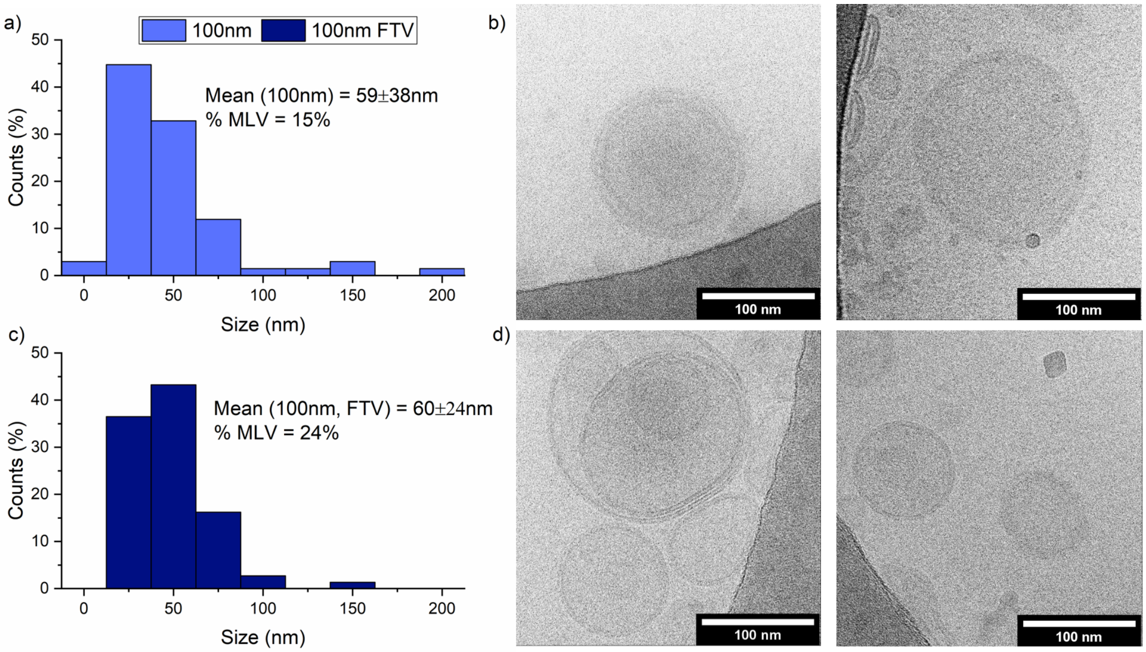

Figure 8.7: Cryo-TEM images of 100 nm extruded vesicles before and after four FTV cycles. Cryo-transmission electron microscopy (Cryo-TEM) of 50 mol% PBd_{12}-PEO_{11} hybrid vesicle (400 nm extrusion membrane) before and after five filtration cycles. a) Histogram of initial vesicle sizes from cryo-TEM images; b) representation images of vesicles before filtration; c) histogram of vesicle sizes after filtration from cryo-TEM images; d) representation images of vesicles after filtration. Scale bars represent 100 nm. The image was taken from reference (2).

8.3 Conclusion

For pure, single-component lipid and polymer vesicles, sterilisation using an autoclave results in the total release of the encapsulated CF. Autoclaving involves exposure to high temperature, which is thought to be detrimental to lipid vesicles by causing aggregation (223, 228). The aggregation after heat sterilisation has been suggested to lead to instability in lipid vesicles by electrolytes causing dehydration of the hydrophilic moiety (223). However, in a previous study, it was found that egg or saturated lipid vesicles without encapsulated drugs could be sterilised by autoclaving (228). It was expected that the polymeric vesicles would be more resistant to heat exposure as polymers membranes are believed to be more robust than lipids. Autoclaving polymersomes with thick membranes (PEE_{31}-PEO_{40} and PBd_{46}-PEO_{26}) has previously shown encapsulation and colloidal stability, although there was shift to a smaller size distribution indicating aggregated or ruptured vesicles (229). However, the block copolymers PBd_{22}-PEO_{14} and PBd_{12}-PEO_{11} used here release their full contents after they are autoclaved. Furthermore, the DLS shows that the size distribution before and after autoclaving varies considerably, suggesting aggregation of the polymer samples has taken place. To enhance the stability of the vesicles during heat sterilisation, it has been suggested that sugars or polyols could be used to stabilise the vesicles (223) and the drug could be encapsulated after vesicles have been autoclaved (228).

Lyophilisation, also known as freeze-drying, also caused complete contents release in all pure component lipid and PBd-b-PEO vesicles, with the size distribution from the DLS also indicating ruptured or aggregated vesicles. The initial freezing step causes ice crystals to form that could potentially pierce the membrane. Expansion of the internal aqueous volume could also cause the vesicle membrane to rupture. However, the polymer-rich vesicle compositions are stable after several freeze-thaw cycles, indicating that the freezing action during lyophilisation is not solely responsible for the loss of colloidal and encapsulation stability of these vesicles. During the second step of lyophilisation, water is removed by sublimation. It is believed that this dehydration step could lead to the the structural instabilities that causes the vesicles to aggregate and rupture as water is essential to the self-assembly of amphiphiles into vesicles. The enhanced stability of block copolymers alone was expected to increase their stability during lyophilisation, however this was not the case under conditions used here. The damaging effects of lyophilisation can be minimised by addition of cryoprotectants, such as glycerol or trehalose or other carbohydrates, to the aqueous phase before freezing to prevent aggregation, fusion and leakage. Cryoprotectants have been successfully used to enhance the stability of liposomes to lyophilisation and rehydration (222). However, there is potential for the cryoprotectants to interact with block copolymers in the hybrid vesicles making further investigation necessary.

While autoclaving and lyophilisation of hybrid vesicles with additional preservatives in the bulk aqueous phase needs further investigation, filtration and freeze-thaw processes appear to be more viable processes for sterilisation and preservations protocols. Overall, sterilisation by filtration through a 200 nm pore resulted in low overall contents, especially in 100 nm extruded vesicles. The DLS size distributions suggest only a small fraction of the vesicles are larger than the filter pore size, which explains these vesicles having overall good colloidal stability. However, hydrodynamic shear stress from passing through the filter pore might still cause some membrane destabilisation and contents release.

400 nm extruded vesicles were also filtered through a 200 nm pore filter as a more stringent test of vesicle stability under filtration. The majority of these vesicles were larger than the 200 nm filter pore size, and their size distributions were not maintained after several filtration cycles. Contents release was higher in the 400 nm extruded membranes compared to the 100 nm extruded membranes (up to 25% vs. 15%) and there appeared to be loss of colloidal stability from aggregation and membrane rupture. Only the 50 mol% PBd_{12}-PEO_{11} and 50 mol% PBd_{22}-PEO_{14} vesicles appeared to maintain their initial size after filtration through a 200 nm pore. However, that may be due to the 50 mol% polymer hybrid vesicles having an initial size of less than 200 nm despite being extruded through a 400 nm pore membrane.

Converse to the initial hypothesis of vesicles with high mol% of the larger PBd_{22}-PEO_{14} block copolymer being more stable under filtration due to greater mechanical robustness, 100 mol% PBd_{22}-PEO_{14} vesicles fared the worst. This is thought to be due to the higher bending rigidity of the thicker membranes of the polymer-rich vesicles, which have higher resistance towards the deformations required to pass through the filter membrane. A previous study on POPC and PBd-b-PEO membranes of different molecular weights also showed that reducing the polymer molecular weight resulted in vesicles that were more prone to deformation (206). This explains why higher pressures were required to force these vesicle samples across the filter membranes. This higher pressure is likely to have a severe impact on the encapsulation stability of the PBd_{22}-PEO_{14} hybrid vesicles as high pressure is more likely to induce shear stress during filtration. On the other hand, the smaller PBd_{12}-PEO_{11} polymer does not appear to lose encapsulation stability, probably because it has a low bending rigidity similar to pure lipid vesicles. The PBd_{12}-PEO_{11} hybrid vesicles may also have enhanced membrane elasticity and improved toughness, although this is not a statistically significant observation.

The polymer-rich vesicles can also withstand several FTV cycles making this a better alternative for sample preservation to lyophilisation. While the contents release increased with the number of FTV cycles, it decreased as the polymer mol% increased. This might be due to high polymer content imparting greater membrane elasticity and lysis strain to the hybrid vesicle membranes.

In conclusion, filtration and freeze-thaw are the most viable routes to sterilising and preserving hybrid vesicles while maintaining their encapsulation and colloidal stability. Although filtration is sufficient to sterilise small vesicle samples, larger vesicles are less stable to filtration so more investigation into developing a viable autoclave method is still worthwhile. Lyophilised vesicles would also be advantageous to reduce economic and environmental costs. Therefore, further efforts to enhance hybrid vesicle stability to these harsher processes are still of significant interest.

9. Conclusion and Outlook

Pure lipid and polymer vesicles have been used for a variety of applications, from acting as microreactors for compartmentalized chemistry (3, 4, 5), or sensors if the membrane surface is functionalised with proteins (6, 7), to drug delivery vectors by encapsulation or insertion of the drug molecules (9, 13) and cell membrane models (14, 15). However, the pure systems do have some disadvantages: although biocompatible, lipid membranes have poor long-term stability while the opposite is often true of polymer membranes. A previous study showed that by blending these materials to form a hybrid vesicle, the durability from the polymers can be combined with the biocompatibility of lipids, and that these hybrid vesicles can also be used to reconstitute a membrane protein (1) that retains its functionality after 500 days.

In the research described in this thesis, 1- palmitoyl -2- oleoyl -sn- glycero -3- phosphocholine (POPC) lipid (MW = 760.09 $\mathrm{g\,mol^{-1}}$) was mixed with poly 1,2-butadiene -block-polyethylene oxide (PBd-b-PEO) of two different molecular weights ($\mathrm{PBd_{22}}$-$\mathrm{PEO_{14}}$, MW = 1800 $\mathrm{g\,mol^{-1}}$ and $\mathrm{PBd_{12}}$-$\mathrm{PEO_{11}}$, MW = 1150 $\mathrm{g\,mol^{-1}}$) to determine how polymer molecular weight affects the structure and membrane properties of the hybrid vesicles. This amphiphilic block copolymer was used because it has a similar Hildebrande solubility parameter to POPC (100, 101); butadiene mimics the long alkyl chains of a phospholipid, while ethylene oxide mimics the hydrophilic phosphate head group (102). PEO is also known to improve the pharmacokinetic properties of vesicles due to a stealth effect it causes that hinders recognition of the vesicle as a foreign body by the immune system (91). Polymer molecular weight is also thought to control the membrane thickness and therefore the membrane mechanical properties (103). A combination of techniques were used to probe the material properties and structure of hybrid POPC lipid and PBd-b-PEO polymer membranes.

Synthetic lipid membranes are known to age rapidly, resulting in the formation of transient pores and aggregation. Unlike a lipid membrane however, polymer membranes are more colloidally stable, robust and have low permeability (37, 103, 230). Fluorescence spectroscopy was used to determine the proton permeability of these POPC/PBd-b-PEO membranes. Overall, increasing polymer composition decreases membrane permeability in large unilamellar vesicles (LUVs). However, while the larger $\mathrm{PBd_{22}}$-$\mathrm{PEO_{14}}$ polymer would be expected to have a high permeability coefficient due to the potential size mismatch with POPC, the average permeability coefficients for hybrid $\mathrm{PBd_{12}}$-$\mathrm{PEO_{11}}$ are in fact greater, despite the similarity in molecular weight between $\mathrm{PBd_{12}}$-$\mathrm{PEO_{11}}$ and POPC. This greater permeability in the smaller $\mathrm{PBd_{12}}$-$\mathrm{PEO_{11}}$ vesicle compositions could be due to the formation of a softer, more flexible membrane. However, differences in permeability could also be attributed to the coexistence of worm-like micelles with vesicles within PBd$_{12}$-PEO$_{11}$/POPC samples, which has the potential for a dynamic equilibrium between the vesicles and micelles, and so have a substantial impact on the permeability measurements (86).

To determine the relationship between polymer molecular weight to hydrophobic thickness, the membrane structure and membrane properties of the hybrid vesicles, bilayer measurements were obtained using cryo-electron tomography (cryo-ET) and the results used to inform small angle x-ray scattering (SAXS) fitting models. Profiles across the hybrid membranes acquired by both cryo-ET and SAXS indicate a symmetric membrane, where the polymer is interdigitating in the hybrid and pure polymer vesicles. Bilayer thickness measurements taken at the full width half maximum (FWHM) were also found to increase with increasing polymer mole fraction. However two membrane thickness populations exist within the PBd$_{22}$-PEO$_{14}$ hybrid samples, one population displaying a thin membrane, and the other with a thick membrane. While this could suggest the formation polymer-rich and lipid-rich populations with hybrid PBd$_{22}$-PEO$_{14}$/POPC samples, it could also be indicative of the polymer forming either a segregated, bilayer conformation or an interdigitated conformation, as these two conformations are energetically similar.

In the electron density profiles of PBd$_{22}$-PEO$_{14}$/POPC hybrids resulting from SAXS, the electron density contrast ratio increases in the thick membrane model implying that lipids are present in these thick membranes, and that as the lipid fraction in the sample decreases, their presence in the membrane also decreases. Although no statistical significance exists between bilayer thickness and vesicle size in the 50 mol% polymer sample, there is a correspondence between thin membranes and smaller vesicles in the 75 mol% PBd$_{22}$-PEO$_{14}$ sample. Automated analysis of cryo-ET images confirmed that individual hybrid vesicles within each thickness population were homogenous. The steep increases in bilayer measurements of PBd$_{12}$-PEO$_{11}$ hybrid vesicles indicate that vesicle compositions of 25 mol% and 75 mol% difference in POPC and PBd$_{12}$-PEO$_{11}$ rigidity may cause the polymer to favour extension in these samples, increasing their bilayer thickness measurements. The trends in bilayer thickness measurements of both PBd$_{22}$-PEO$_{14}$ and PBd$_{12}$-PEO$_{11}$ vesicle samples are also mirrored in the permeability coefficients of these samples, implying a relationship between membrane thickness and proton permeability. All compositions presented not only unilamellar vesicles, but multi-lamellar and intra-lumenal vesicles as well as worm-like micelles.

Relative intensity ratios of fluorescently labelled polymer, PBd$_{22}$-PEO$_{14}$-TMR, and labelled lipid, DiO show that all hybrid PBd$_{22}$-PEO$_{14}$/POPC and PBd$_{12}$-PEO$_{11}$/POPC giant unilamellar vesicle (GUV) samples have monomodal distributions centred around 0. This implies that the membranes are well-mixed and homogeneous as there are no vesicles with only DiO or PBd$_{22}$-PEO$_{14}$-TMR present in the membrane and therefore there are no pure polymer or pure lipid vesicles within these GUV samples. However, cryo-ET and SAXS results show that there are two distinct membrane populations in PBd$_{22}$-PEO$_{14}$/POPC hybrid LUVs. As speculated earlier, these populations could be indicative of the polymer forming either a segregated, bilayer conformation or an interdigitated conformation as these two conformations are energetically similar. Cryo-ET also showed that there was correspondence between thick membranes and larger vesicles in 75 mol% PBd$_{22}$-PEO$_{14}$ sample, it could be hypothesised that as GUVs have much larger diameters than LUVs, GUVs may favour the thicker membrane structure.

Fluorophore diffusion can provide an indication of membrane viscosity. Overall, diffusion of DiO fluorophore through hybrid PBd$_{22}$-PEO$_{14}$/POPC and PBd$_{12}$-PEO$_{11}$/POPC GUVs decreased with increasing polymer mole fraction. However, the diffusion coefficients for the fluorescent polymer PBd$_{22}$-PEO$_{14}$-TMR in hybrid membranes did not change with increasing polymer content, suggesting that while increasing polymer fraction reduces movement of lipid through a polymer-rich matrix, the polymer diffusion is unaffected. DiO diffusion through PBd$_{12}$-PEO$_{11}$/POPC membranes was greater than through hybrid PBd$_{22}$-PEO$_{14}$/POPC membranes, implying PBd$_{22}$-PEO$_{14}$ forms more viscous membranes than PBd$_{12}$-PEO$_{11}$. As PBd$_{22}$-PEO$_{14}$ is a higher molecular weight polymer and forms thicker membranes than PBd$_{12}$-PEO$_{11}$, it could be speculated PBd$_{22}$-PEO$_{14}$ forms a more rigid membrane than PBd$_{12}$-PEO$_{11}$, and so is more difficult to diffuse through.

General polarisation values of hybrid PBd$_{22}$-PEO$_{14}$/POPC and PBd$_{12}$-PEO$_{11}$/POPC GUV membranes show both blends form a disordered, hydrated membrane, and increasing polymer mole fraction increases membrane order in both PBd$_{22}$-PEO$_{14}$ and PBd$_{12}$-PEO$_{11}$ vesicle compositions.

Material interactions might also play a role in membrane elasticity. Trends seen in FRAP experiments agree with flicker spectroscopy results: 100 mol% PBd$_{22}$-PEO$_{14}$ vesicles have the highest bending rigidity and lowest diffusion coefficient across all compositions. The higher molecular weight block copolymer, PBd$_{22}$-PEO$_{14}$, provides a more rigid membrane structure due to the more viscous nature of its matrix compared to PBd$_{12}$-PEO$_{11}$, resulting in low diffusion of lipids and polymers through the membrane and a high bending rigidity. Potentially due to the similar solubility parameters between the materials, and the overall fluidity of PBd-b-PEO block copolymers being similar to that of POPC, no macroscale domains were observed in the hybrid compositions.

Characterising the material properties of hybrid lipid-polymer vesicles could help design vesicles for bionanotechnology applications with controlled encapsulation and release. Although hybrid vesicles composed of POPC and PBd_{22}-PEO_{14} or PBd_{12}-PEO_{11} were not stable under autoclaving and lyophilisation, they were found to retain encapsulated cargo after several filtration and freeze-thaw cycles, and increasing the polymer mole fraction decreased the contents release. However, hydrodynamic shear stress from passing through the 200 nm filter pore might cause membrane destabilisation and contents release, as 400 nm extruded vesicles had a greater contents release compared to 100 nm extruded vesicles of both polymer compositions. Initially, vesicles with higher mole fraction of PBd_{22}-PEO_{14} were believed to have a greater mechanical robustness from their higher bending rigidity, however 100 mol% PBd_{22}-PEO_{14} vesicles actually fared the worst. The mechanical robustness of PBd_{22}-PEO_{14} increased the resistance to deformation required to pass through the filter membrane, which explains why higher pressures were required to force these vesicles through the filter. On the other hand, PBd_{12}-PEO_{11} membranes did not appear to lose encapsulation stability, because it may have bending rigidity similar to POPC vesicles (2).

The aim of this investigation was to understand the relationship between membrane structure and properties. For POPC and PBd-b-PEO blends, the hybrid membranes appear to be well-mixed, homogenous symmetric membranes, with different proportions of lipid to polymer within individual vesicles. Although the PBd-b-PEO polymers have a similar membrane order to POPC, the larger PBd_{22}-PEO_{14} membrane does exhibit greater bending rigidity and resistance to deformation than PBd_{12}-PEO_{11} membranes. For PBd_{22}-PEO_{14}/POPC lipid-polymer blends, increasing the polymer fraction appears to increase membrane order, bilayer thickness and reduce membrane permeability and diffusion of molecules through the membrane.

Previous studies have already shown that PBd-b-PEO/PC hybrid membranes do extend the functional lifetime of incorporated membrane proteins (1, 77, 78, 86) making this blend a viable choice for applications in bionanotechnology. The results found during this project show that membrane properties such as permeability, contents release, viscosity and bending rigidity can be tuned to fit a specific purpose by altering the membrane composition in PBd_{22}-PEO_{14}/POPC and PBd_{12}-PEO_{11}/POPC membranes.

Outlook

Other techniques and methods can be used to complement and further explore the material properties of hybrid lipid-polymer vesicles, and how their properties relate to structure.

For example, there are an arsenal of scattering techniques available to probe membrane structure which have not been used in this investigation. X-ray scattering of aligned lamellar bilayers can not only be used to find lamellar repeat distance at small scattering angles (231), but also to determine coexisting liquid ordered and liquid disordered phases by changes in the average chain tilt orientation at wide scattering angles (232). Wide angle x-ray scattering (WAXS) can interrogate bilayer structures that are in the order of 3–4 Å ($q \leq 2.0$ Å $^{-1}$) (233), and the scattering pattern can usually be obtained in conjunction with SAXS measurements. WAXS has been used in the past to explore molecular distance and packing of head group and acyl chain regions of phospholipids containing alcohols and polyalcohols, providing important details on vesicle microscopic structure, such as phospholipid phase and packing (234). This could provide insight into interdigitation of polymers within hybrid lipid-polymer membranes. Small angle neutron scattering (SANS) is another popular scattering technique and has certain advantages over x-rays utilised in SAXS and WAXS. Neutrons have a greater penetration depth but the sample does not typically suffer from beam damage (235). SANS also allows contrast variation experiments where different parts of the sample can be selectively highlighted by isotopic labelling (236) and are relatively insensitive to the size of the vesicle, so can provide very accurate measurements of bilayer thickness for both multilamellar vesicles and unilamellar vesicles (237). SAXS and SANS data of asymmetric POPC/DPPC vesicles have even been analysed simultaneously to fully exploit the benefits of contrast variation in SANS (238).

However, there are challenges to data analysis of both scattering results as the curves are smooth and one-dimensional so contain quite a limited amount of information. This leads to either over-fitting of structural models to scattering patterns, or constraining the model too much alongside other issues (236). Molecular dynamics (MD) has been used to overcome some of these problems, by directly comparing the simulated properties with primary experimental data to provide a realistic description of the membrane properties. In one study, GROMACS simulation package was used to determine the volume and area per lipid, as well as the WAXS spectra of DPPC and DMPC lipid membranes, with good agreement between the experimental and simulated spectra (239). Coarse-grain MD simulations on GROMACS have also been used to predict mechanical properties of a range of lipid membranes (240, 241). Coarse-grain MD was used to successfully predict the membrane thickness, area per chain, polymer stretching and electron density of PBd-b-PEO and PEE-b-PEO polymer membranes with increasing molecular weights (179). Even hybrid membranes have been simulated to determine how hydrophobic thickness mismatch can affect phase separation behaviours of lipids and polymers with different molecular weights (95). Therefore MD studies on hybrid lipid-polymer vesicles could be used to augment practical experiments and extract membrane structure and properties more easily.

Förster resonance energy transfer (FRET) has also often been used in combination with scattering techniques as it provides insight into the membrane structure of hybrid vesicles, especially in the determination of nano-domains between the lipid and polymer phases with sizes between $<$ 50-100 nm (34, 99, 98). The donor probe used was expected to partition into the polymer phase, while the acceptor probe was mainly in the lipid phase. No energy would transfer between the probes if the hybrid sample was a mixture of pure liposomes or polymersomes, so detection of the FRET phenomenon would indicate the presence of hybrid vesicles. Then, FRET efficiency is used to elucidate the homogeneity of the membrane: a decrease in FRET efficiency is thought to be synonymous with phase formation within a membrane as the average distance between the FRET donor and acceptor would be larger than the Förster radius of the FRET pair. In this way, stable nano-domains were discovered in DPPC/PDMS-g-$(PEO)_2$ and POPC/PDMS-g-$(PEO)_2$ hybrid lipid polymer vesicles (99). Ultra nano-domains were found using FRET on lipid mixtures by using two domain-detecting FRET pairs with small Förster radii ($<$ 5 nm) (242). However, as demonstrated in Chapters 5, 6 and 7, PBd_{22}-PEO_{14}/POPC and PBd_{12}-PEO_{11}/POPC vesicles do not appear phase separate, so FRET experiments would not be useful beyond confirming this.

For many bionanotechnology applications it is also desirable for the system to incorporate biofunctional molecules for biomimetic membrane-based technologies. Hybrid PBd_{22}-PEO_{14}/POPC lipid-polymer blends have already been shown to provide a stable, durable, homogenous environment for cytochrome bo_3 (1). Blending PBd_{22}-PEO_{14} with other lipids besides POPC, such as complicated lipid mixtures like *E. coli* lipids, could also be investigated. However there has been no investigation into the stability or durability of integrated membrane proteins in to PBd_{12}-PEO_{11} hybrid vesicles. In addition to the ubiquinol assay previously used on cytochrome bo_3 reconstituted PBd_{22}-PEO_{14} hybrid vesicles, oxygen concentration and proton permeability can also be monitored to determine and compare the protein activity in the different hybrid lipid-polymer compositions (78, 88).

Biological cellular functions, such as signal transduction, that rely on membrane proteins also appear to be affected by biological membrane morphologies (243). In artificial cells such as vesicles, deformations are believed to be due in part to ion-membrane interactions (47, 85). An investigation using SAXS and cryo-TEM imaging has shown triblock copolymer PEO-PDMS-PEO membranes to be affected by high salt concentrations (up to 500 mM), with the overall hydrodynamic diameter and membrane thickness increasing with increasing salt concentration. Different vesicle morphologies were also observed with increasing salt concentration, evolving from spherical shapes to prolates and finally oblates (85). Membrane interactions with salts at a range of concentrations and their relationship with membrane properties may be useful in tuning the size, morphology and properties of hybrid lipid-polymer vesicles.

The results described in this thesis show that by blending these PBd$_{22}$-PEO$_{14}$ or PBd$_{12}$-PEO$_{11}$ with POPC, vesicle properties can be tuned through varying their relative mixing ratio and could help design vesicles for bionanotechnology applications with controlled encapsulation and release. These hybrid lipid-polymer blends could be developed further however to provide a stable, durable, homogenous environment for certain membrane proteins in order to create artificial cells.

Although the results offer detailed fundamental understanding on PBd$_{22}$-PEO$_{14}$/POPC and PBd$_{12}$-PEO$_{11}$/POPC membrane compositions and some of their bulk physicochemical properties, utilising the full potential of scattering techniques in combination with molecular dynamics simulations would allow greater insight into vesicle structure. For many bionanotechnology applications it is also desirable for the system to incorporate biofunctional molecules for biomimetic membrane-based technologies, therefore more work needs to be done to further optimise the hybrid membrane environment for a wider range of membrane proteins or different bionanotechnology applications by blending PBd-b-PEO with more complex lipid mixtures. This thesis provides some of the groundwork for further advances in vesicle engineering for emerging applications, such as nanoreactors, drug delivery vectors and biosensors.

Bibliography

(1) Khan, S., Li, M., Muench, S., Jeuken, L., Beales, P., Durable proteo-hybrid vesicles for the extended functional lifetime of membrane proteins in bionanotechnology. *Chemical Communications*, 2016, **52**(73), pp. 11020–11023.

(2) Seneviratne, R., Jeuken, L.J., Rappolt, M., Beales, P.A., Hybrid vesicle stability under sterilisation and preservation processes used in the manufacture of medicinal formulations. *Polymers*, 2020, **12**(4), p. 914.

(3) Hindley, J.W., Elani, Y., McGilvery, C.M., Ali, S., Bevan, C.L., Law, R.V., Ces, O., Light-triggered enzymatic reactions in nested vesicle reactors. *Nature Communications*, 2018, **9**(1), pp. 1–6.

(4) Trantidou, T., Friddin, M., Elani, Y., Brooks, N.J., Law, R.V., Seddon, J.M., Ces, O., Engineering compartmentalized biomimetic micro-and nanocontainers. *ACS Nano*, 2017, **11**(7), pp. 6549–6565.

(5) Tsumoto, K., Nomura, S.i.M., Nakatani, Y., Yoshikawa, K., Giant liposome as a biochemical reactor: transcription of DNA and transportation by laser tweezers. *Langmuir*, 2001, **17**(23), pp. 7225–7228.

(6) Sunami, T., Sato, K., Matsuura, T., Tsukada, K., Urabe, I., Yomo, T., Femtoliter compartment in liposomes for *in vitro* selection of proteins. *Analytical Biochemistry*, 2006, **357**(1), pp. 128–136.

(7) Wu, J., Zawistowski, A., Ehrmann, M., Yi, T., Schmuck, C., Peptide functionalized polydiacetylene liposomes act as a fluorescent turn-on sensor for bacterial lipopolysaccharide. *Journal of the American Chemical Society*, 2011, **133**(25), pp. 9720–9723.

(8) Huang, T., Hou, Z., Xu, Q., Huang, L., Li, C., Zhou, Y., Polymer vesicle sensor for visual and sensitive detection of SO_2 in water. *Langmuir*, 2017, **33**(1), pp. 340–346.

(9) Elsayed, M.M., Abdallah, O.Y., Naggar, V.F., Khalafallah, N.M., Lipid vesicles for skin delivery of drugs: reviewing three decades of research. *International Journal of Pharmaceutics*, 2007, **332**(1-2), pp. 1–16.

(10) Khan, S., McCabe, J., Hill, K., Beales, P.A., Biodegradable hybrid block copolymer–lipid vesicles as potential drug delivery systems. *Journal of Colloid and Interface Science*, 2020, **562**, pp. 418–428.

(11) Meng, F., Engbers, G.H., Feijen, J., Biodegradable polymersomes as a basis for artificial cells: encapsulation, release and targeting. *Journal of Controlled Release*, 2005, **101**(1-3), pp. 187–198.

(12) Molinaro, R., Corbo, C., Martinez, J.O., Taraballi, F., Evangelopoulos, M., Minardi, S., Yazdi, I.K., Zhao, P., De Rosa, E., Sherman, M., *et al.*, Biomimetic proteolipid vesicles for targeting inflamed tissues. *Nature Materials*, 2016, **15**(9), pp. 1037–1046.

(13) Torchilin, V.P., Recent advances with liposomes as pharmaceutical carriers. *Nature Reviews Drug discovery*, 2005, **4**(2), pp. 145–160.

(14) Rigaud, J.L., Lévy, D., *Reconstitution of membrane proteins into liposomes*, vol. 372. Elsevier, 2003.

(15) Papahadjopoulos, D., Kimelberg, H.K., Phospholipid vesicles (liposomes) as models for biological membranes: their properties and interactions with cholesterol and proteins. *Progress in Surface Science*, 1974, **4**, pp. 141–232.

(16) Binder, W.H., Barragan, V., Menger, F.M., Domains and rafts in lipid membranes. *Angewandte Chemie International Edition*, 2003, **42**(47), pp. 5802–5827.

(17) Singer, S.J., Nicolson, G.L., The fluid mosaic model of the structure of cell membranes. *Science*, 1972, **175**(4023), pp. 720–731.

(18) Lombard, J., Once upon a time the cell membranes: 175 years of cell boundary research. *Biology Direct*, 2014, **9**(1), pp. 1–35.

(19) Hunte, C., Specific protein–lipid interactions in membrane proteins. *Biochemical Society Transactions*, 2005, **33**(5), pp. 938–942.

(20) Shen, H.H., Lithgow, T., Martin, L., Reconstitution of membrane proteins into model membranes: seeking better ways to retain protein activities. *International Journal of Molecular Sciences*, 2013, **14**(1), pp. 1589–1607.

(21) Sessa, G., Weissmann, G., Phospholipid spherules (liposomes) as a model for biological membranes. *Journal of Lipid Research*, 1968, **9**(3), pp. 310–318.

(22) Chemin, M., Brun, P.M., Lecommandoux, S., Sandre, O., Le Meins, J.F., Hybrid polymer/lipid vesicles: fine control of the lipid and polymer distribution in the binary membrane. *Soft Matter*, 2012, **8**(10), pp. 2867–2874.

(23) Walde, P., Cosentino, K., Engel, H., Stano, P., Giant vesicles: preparations and applications. *ChemBioChem*, 2010, **11**(7), pp. 848–865.

(24) Gurtovenko, A.A., Vattulainen, I., Ion leakage through transient water pores in protein-free lipid membranes driven by transmembrane ionic charge imbalance. *Biophysical Journal*, 2007, **92**(6), pp. 1878–1890.

(25) Marrink, S., Jähnig, F., Berendsen, H., Proton transport across transient single-file water pores in a lipid membrane studied by molecular dynamics simulations. *Biophysical Journal*, 1996, **71**(2), pp. 632–647.

(26) Powell, K.T., Weaver, J.C., Transient aqueous pores in bilayer membranes: a statistical theory. *Bioelectrochemistry and Bioenergetics*, 1986, **15**(2), pp. 211–227.

(27) Meyer, C.E., Abram, S.L., Craciun, I., Palivan, C.G., Biomolecule–polymer hybrid compartments: combining the best of both worlds. *Physical Chemistry Chemical Physics*, 2020, pp. 11197–11218.

(28) Schulz, M., Glatte, D., Meister, A., Scholtysek, P., Kerth, A., Blume, A., Bacia, K., Binder, W.H., Hybrid lipid/polymer giant unilamellar vesicles: effects of incorporated biocompatible PIB–PEO block copolymers on vesicle properties. *Soft Matter*, 2011, **7**(18), pp. 8100–8110.

(29) Nam, J., Beales, P.A., Vanderlick, T.K., Giant phospholipid/block copolymer hybrid vesicles: mixing behavior and domain formation. *Langmuir*, 2011, **27**(1), pp. 1–6.

(30) Discher, D.E., Eisenberg, A., Polymer vesicles. *Science*, 2002, **297**(5583), pp. 967–973.

(31) Muhammad, N., Dworeck, T., Fioroni, M., Schwaneberg, U., Engineering of the *E. coli* outer membrane protein FhuA to overcome the hydrophobic mismatch in thick polymeric membranes. *Journal of Nanobiotechnology*, 2011, **9**(1), pp. 1–9.

(32) Stoenescu, R., Graff, A., Meier, W., Asymmetric ABC-triblock copolymer membranes induce a directed insertion of membrane proteins. *Macromolecular Bioscience*, 2004, **4**(10), pp. 930–935.

(33) Itel, F., Najer, A., Palivan, C.G., Meier, W., Dynamics of membrane proteins within synthetic polymer membranes with large hydrophobic mismatch. *Nano Letters*, 2015, **15**(6), pp. 3871–3878.

(34) Dao, T.P.T., Fernandes, F., Ibarboure, E., Ferji, K., Prieto, M., Sandre, O., Le Meins, J.F., Modulation of phase separation at the micron scale and nanoscale in giant

polymer/lipid hybrid unilamellar vesicles (GHUVs). *Soft Matter*, 2017, **13**(3), pp. 627–637.

(35) Poon, W.C., Andelman, D., *Soft condensed matter physics in molecular and cell biology*. CRC Press, 2006.

(36) He, F., Tong, Y.W., A mechanistic study on amphiphilic block co-polymer poly (butadiene-b-(ethylene oxide)) vesicles reveals the water permeation mechanism through a polymeric bilayer. *RSC Advances*, 2014, **4**(29), pp. 15304–15313.

(37) Bermudez, H., Brannan, A.K., Hammer, D.A., Bates, F.S., Discher, D.E., Molecular weight dependence of polymersome membrane structure, elasticity, and stability. *Macromolecules*, 2002, **35**(21), pp. 8203–8208.

(38) Israelachvili, J.N., *Intermolecular and surface forces*. Academic Press, 2011.

(39) Boal, D.H., *Mechanics of the Cell*. Cambridge University Press - M.U.A, 2012.

(40) Jouhet, J., Importance of the hexagonal lipid phase in biological membrane organization. *Frontiers in Plant Science*, 2013, **4**, p. 494.

(41) Eze, M.O., Phase transitions in phospholipid bilayers: lateral phase separations play vital roles in biomembranes. *Biochemical Education*, 1991, **19**(4), pp. 204–208.

(42) Schulz, M., Olubummo, A., Binder, W.H., Beyond the lipid-bilayer: interaction of polymers and nanoparticles with membranes. *Soft Matter*, 2012, **8**(18), pp. 4849–4864.

(43) Lim Soo, P., Eisenberg, A., Preparation of block copolymer vesicles in solution. *Journal of Polymer Science Part B: Polymer Physics*, 2004, **42**(6), pp. 923–938.

(44) Du, J., O'Reilly, R.K., Advances and challenges in smart and functional polymer vesicles. *Soft Matter*, 2009, **5**(19), pp. 3544–3561.

(45) Mai, Y., Eisenberg, A., Self-assembly of block copolymers. *Chemical Society Reviews*, 2012, **41**(18), pp. 5969–5985.

(46) Israelachvili, J.N., *Intermolecular and surface forces*. Academic press, 2011.

(47) Antonietti, M., Förster, S., Vesicles and liposomes: a self-assembly principle beyond lipids. *Advanced Materials*, 2003, **15**(16), pp. 1323–1333.

(48) Gauthier, N.C., Masters, T.A., Sheetz, M.P., Mechanical feedback between membrane tension and dynamics. *Trends in Cell Biology*, 2012, **22**(10), pp. 527–535.

(49) Mui, B., Döbereiner, H., Madden, T., Cullis, P., Influence of transbilayer area asymmetry on the morphology of large unilamellar vesicles. *Biophysical Journal*, 1995, **69**(3), pp. 930–941.

(50) Evans, E.A., Bending resistance and chemically induced moments in membrane bilayers. *Biophysical Journal*, 1974, **14**(12), pp. 923–931.

(51) Peiró-Salvador, T., Ces, O., Templer, R.H., Seddon, A.M., Buffers may adversely affect model lipid membranes: a cautionary tale. *Biochemistry*, 2009, **48**(47), pp. 11149–11151.

(52) Soubias, O., Teague, W.E., Hines, K.G., Gawrisch, K., The role of membrane curvature elastic stress for function of rhodopsin-like G protein-coupled receptors. *Biochimie*, 2014, **107**, pp. 28–32.

(53) Bochicchio, D., Monticelli, L., The membrane bending modulus in experiments and simulations: a puzzling picture. *Advances in Biomembranes and Lipid Self-Assembly*, 2016, **23**, pp. 117–143.

(54) Campelo, F., Arnarez, C., Marrink, S.J., Kozlov, M.M., Helfrich model of membrane bending: from Gibbs theory of liquid interfaces to membranes as thick anisotropic elastic layers. *Advances in Colloid and Interface Science*, 2014, **208**, pp. 25–33.

(55) Koynova, R., Caffrey, M., Phases and phase transitions of the phosphatidylcholines. *Biochimica et Biophysica Acta (BBA)-Reviews on Biomembranes*, 1998, **1376**(1), pp. 91–145.

(56) Heberle, F.A., Feigenson, G.W., Phase separation in lipid membranes. *Cold Spring Harbor perspectives in biology*, 2011, **3**(4), p. a004630.

(57) Battaglia, G., Ryan, A.J., Bilayers and interdigitation in block copolymer vesicles. *Journal of the American Chemical Society*, 2005, **127**(24), pp. 8757–8764.

(58) Bates, F.S., Fredrickson, G.H., Block copolymer thermodynamics: theory and experiment. *Annual Review of Physical Chemistry*, 1990, **41**(1), pp. 525–557.

(59) Le Meins, J.F., Sandre, O., Lecommandoux, S., Recent trends in the tuning of polymersomes' membrane properties. *The European Physical Journal E*, 2011, **34**(2), pp. 1–17.

(60) Itel, F., Chami, M., Najer, A., Lörcher, S., Wu, D., Dinu, I.A., Meier, W., Molecular organization and dynamics in polymersome membranes: A lateral diffusion study. *Macromolecules*, 2014, **47**(21), pp. 7588–7596.

(61) Matsen, M.W., Bates, F.S., One-component approximation for binary diblock copolymer blends. *Macromolecules*, 1995, **28**(21), pp. 7298–7300.

(62) Matsen, M.W., Effect of architecture on the phase behavior of AB-type block copolymer melts. *Macromolecules*, 2012, **45**(4), pp. 2161–2165.

(63) J. Nam, T. Vanderlick, P.B., Formation and dissolution of phospholipid domains with varying hybrid lipo-polymersomes. *Soft Matter*, 2012, **8**, pp. 7982–7988.

(64) LoPresti, C., Massignani, M., Fernyhough, C., Blanazs, A., Ryan, A.J., Madsen, J., Warren, N.J., Armes, S.P., Lewis, A.L., Chirasatitsin, S., *et al.*, Controlling polymersome surface topology at the nanoscale by membrane confined polymer/polymer phase separation. *ACS Nano*, 2011, **5**(3), pp. 1775–1784.

(65) Rideau, E., Wurm, F.R., Landfester, K., Membrane engineering: phase separation in polymeric giant vesicles. *Small*, 2020, **16**(27), p. 1905230.

(66) Anderson, R.G., Jacobson, K., A role for lipid shells in targeting proteins to caveolae, rafts, and other lipid domains. *Science*, 2002, **296**(5574), pp. 1821–1825.

(67) Raucher, D., Sheetz, M.P., Characteristics of a membrane reservoir buffering membrane tension. *Biophysical Journal*, 1999, **77**(4), pp. 1992–2002.

(68) Morris, C., Homann, U., Cell surface area regulation and membrane tension. *The Journal of Membrane Biology*, 2001, **179**(2), pp. 79–102.

(69) García-Sáez, A.J., Chiantia, S., Schwille, P., Effect of line tension on the lateral organization of lipid membranes. *Journal of Biological Chemistry*, 2007, **282**(46), pp. 33537–33544.

(70) Nagle, J.F., Tristram-Nagle, S., Lipid bilayer structure. *Current Opinion in Structural Biology*, 2000, **10**(4), pp. 474–480.

(71) Nagle, J.F., Tristram-Nagle, S., Structure of lipid bilayers. *Biochimica et Biophysica Acta (BBA)-Reviews on Biomembranes*, 2000, **1469**(3), pp. 159–195.

(72) Schulz, M., Binder, W.H., Mixed hybrid lipid/polymer vesicles as a novel membrane platform. *Macromolecular Rapid Communications*, 2015, **36**(23), pp. 2031–2041.

(73) Bieligmeyer, M., Artukovic, F., Nussberger, S., Hirth, T., Schiestel, T., Müller, M., Reconstitution of the membrane protein OmpF into biomimetic block copolymer–phospholipid hybrid membranes. *Beilstein Journal of Nanotechnology*, 2016, **7**(1), pp. 881–892.

(74) Fauquignon, M., Ibarboure, E., Carlotti, S., Brûlet, A., Schmutz, M., Le Meins, J.F., Large and giant unilamellar vesicle (s) obtained by self-assembly of poly (dimethylsiloxane)-b-poly (ethylene oxide) diblock copolymers, membrane properties and preliminary investigation of their ability to form hybrid polymer/lipid vesicles. *Polymers*, 2019, **11**(12), p. 2013.

(75) Chen, D., Santore, M.M., Hybrid copolymer–phospholipid vesicles: phase separation resembling mixed phospholipid lamellae, but with mechanical stability and control. *Soft Matter*, 2015, **11**(13), pp. 2617–2626.

(76) Miele, Y., Mingotaud, A.F., Caruso, E., Malacarne, M.C., Izzo, L., Lonetti, B., Rossi, F., Hybrid giant lipid vesicles incorporating a PMMA-based copolymer. *Biochimica et Biophysica Acta (BBA)-General Subjects*, 2021, **1865**(4), p. 129611.

(77) Rottet, S., Iqbal, S., Beales, P.A., Lin, A., Lee, J., Rug, M., Scott, C., Callaghan, R., Characterisation of hybrid polymersome vesicles containing the efflux pumps naatm1 or p-glycoprotein. *Polymers*, 2020, **12**(5), p. 1049.

(78) Kleineberg, C., Wölfer, C., Abbasnia, A., Pischel, D., Bednarz, C., Ivanov, I., Heitkamp, T., Börsch, M., Sundmacher, K., Vidakovic-Koch, T., Light-driven ATP regeneration in diblock/grafted hybrid vesicles. *ChemBioChem* , 2020.

(79) Hamada, N., Gakhar, S., Longo, M.L., Hybrid lipid/block copolymer vesicles display broad phase coexistence region. *Biochimica et Biophysica Acta (BBA)-Biomembranes*, 2021, **1863**(4), p. 183552.

(80) Tahir, N., Madni, A., Li, W., Correia, A., Khan, M.M., Rahim, M.A., Santos, H.A., Microfluidic fabrication and characterization of sorafenib-loaded lipid-polymer hybrid nanoparticles for controlled drug delivery. *International Journal of Pharmaceutics*, 2020, **581**, p. 119275.

(81) Pott, T., Bouvrais, H., Méléard, P., Giant unilamellar vesicle formation under physiologically relevant conditions. *Chemistry and Physics of Lipids*, 2008, **154**(2), pp. 115–119.

(82) Lim, S.K., de Hoog, H.P., Parikh, A.N., Nallani, M., Liedberg, B., Hybrid, nanoscale phospholipid/block copolymer vesicles. *Polymers*, 2013, **5**(3), pp. 1102–1114.

(83) Winzen, S., Bernhardt, M., Schaeffel, D., Koch, A., Kappl, M., Koynov, K., Landfester, K., Kroeger, A., Submicron hybrid vesicles consisting of polymer–lipid and polymer–cholesterol blends. *Soft Matter*, 2013, **9**(25), pp. 5883–5890.

(84) Ong, S.G.M., Chitneni, M., Lee, K.S., Ming, L.C., Yuen, K.H., Evaluation of extrusion technique for nanosizing liposomes. *Pharmaceutics*, 2016, **8**(4), p. 36.

(85) Perera, R.M., Gupta, S., Li, T., Bleuel, M., Hong, K., Schneider, G.J., Influence of NaCl on shape deformation of polymersomes. *Soft Matter*, 2021.

(86) Paxton, W.F., McAninch, P.T., Achyuthan, K.E., Shin, S.H.R., Monteith, H.L., Monitoring and modulating ion traffic in hybrid lipid/polymer vesicles. *Colloids and Surfaces B: Biointerfaces*, 2017, **159**, pp. 268–276.

(87) Ruysschaert, T., Sonnen, A.F., Haefele, T., Meier, W., Winterhalter, M., Fournier, D., Hybrid nanocapsules: interactions of ABA block copolymers with liposomes. *Journal of the American Chemical Society*, 2005, **127**(17), pp. 6242–6247.

(88) Otrin, L., Marušič, N., Bednarz, C., Vidakovic-Koch, T., Lieberwirth, I., Landfester, K., Sundmacher, K., Toward artificial mitochondrion: mimicking oxidative phosphorylation in polymer and hybrid membranes. *Nano Letters*, 2017, **17**(11), pp. 6816–6821.

(89) J. Nam, P. Beales, T.V., Giant phospholipid/block copolymer hybrid vesicles: Mixing behaviour and domain formation. *Langmuir*, 2011, **27**(1), pp. 1–6.

(90) Nam, J., Vanderlick, T.K., Beales, P.A., Formation and dissolution of phospholipid domains with varying textures in hybrid lipo-polymersomes. *Soft Matter*, 2012, **8**(30), pp. 7982–7988.

(91) Magnani, C., Montis, C., Mangiapia, G., Mingotaud, A.F., Mingotaud, C., Roux, C., Joseph, P., Berti, D., Lonetti, B., Hybrid vesicles from lipids and block copolymers: Phase behaviour from the micro-to the nano-scale. *Colloids and Surfaces B: Biointerfaces*, 2018, **168**, pp. 18–28.

(92) Lim, S.K., Wong, A.S., de Hoog, H.P.M., Rangamani, P., Parikh, A.N., Nallani, M., Sandin, S., Liedberg, B., Spontaneous formation of nanometer scale tubular vesicles in aqueous mixtures of lipid and block copolymer amphiphiles. *Soft Matter*, 2017, **13**(6), pp. 1107–1115.

(93) Khan, A.K., Ho, J., Roy, S., Liedberg, B., Nallani, M., Facile mixing of phospholipids promotes self-assembly of low-molecular-weight biodegradable block co-polymers into functional vesicular architectures. *Polymers*, 2020, **12**(4), p. 979.

(94) Fauquignon, M., Ibarboure, E., Le Meins, J.F., Membrane reinforcement in giant hybrid polymer lipid vesicles achieved by controlling the polymer architecture. *Soft Matter*, 2021, **17**(1), pp. 83–89.

(95) Hu, S.W., Huang, C.Y., Tsao, H.K., Sheng, Y.J., Hybrid membranes of lipids and diblock copolymers: From homogeneity to rafts to phase separation. *Physical Review E*, 2019, **99**(1), p. 012403.

(96) Dao, T., Fernandes, F., Fauquignon, M., Ibarboure, E., Prieto, M., Le Meins, J.F., The combination of block copolymers and phospholipids to form giant hybrid unilamellar vesicles (GHUVs) does not systematically lead to "intermediate" membrane properties. *Soft Matter*, 2018, **14**(31), pp. 6476–6484.

(97) Shen, W., Hu, J., Hu, X., Impact of amphiphilic triblock copolymers on stability and permeability of phospholipid/polymer hybrid vesicles. *Chemical Physics Letters*, 2014, **600**, pp. 56–61.

(98) Dao, T.T., Brûlet, A., Fernandes, F., Er-Rafik, M., Ferji, K., Schweins, R., Chapel, J.P., Fedorov, A., Schmutz, M., Prieto, M., *et al.*, Mixing block copolymers with phospholipids at the nanoscale: from hybrid polymer/lipid wormlike micelles to vesicles presenting lipid nanodomains. *Langmuir*, 2017, **33**(7), pp. 1705–1715.

(99) Dao, T.T., Fernandes, F., Er-Rafik, M., Salva, R., Schmutz, M., Brûlet, A., Prieto, M., Sandre, O., Le Meins, J.F., Phase separation and nanodomain formation in hybrid polymer/lipid vesicles. *ACS Macro Letters*, 2015, **4**(2), pp. 182–186.

(100) Barton, A.F., *Handbook of polymer-liquid interaction parameters and solubility parameters*. CRC press, 1990.

(101) Barton, A.F., *CRC handbook of solubility parameters and other cohesion parameters*. Routledge, 2017.

(102) Zaba, C., Ritz, S., Tan, C.W.D., Zayni, S., Müller, M., Reuning, U., Sinner, E.K., Functional cell adhesion receptors (integrins) in polymeric architectures. *ChemBioChem*, 2015, **16**(12), pp. 1740–1743.

(103) LoPresti, C., Lomas, H., Massignani, M., Smart, T., Battaglia, G., Polymersomes: nature inspired nanometer sized compartments. *Journal of Materials Chemistry*, 2009, **19**(22), pp. 3576–3590.

(104) Ghiran, I.C., Introduction to fluorescence microscopy. In: *Light microscopy*, Springer, 2011, pp. 93–136.

(105) Atkins, P., De Paula, J., Friedman, R., *Quanta, matter, and change: a molecular approach to physical chemistry*. Oxford University Press, 2009.

(106) Atkins, P., De Paula, J., *Elements of physical chemistry*. Oxford University Press, USA, 2013.

(107) Lakowicz, J., Solvent and environmental effects. *Principles of Fluorescence Spectroscopy* , 2006, **3**, pp. 205–231.

(108) Kuyper, C.L., Kuo, J.S., Mutch, S.A., Chiu, D.T., Proton permeation into single vesicles occurs via a sequential two-step mechanism and is heterogeneous. *Journal of the American Chemical Society*, 2006, **128**(10), pp. 3233–3240.

(109) Nichols, J.W., Deamer, D.W., Net proton-hydroxyl permeability of large unilamellar liposomes measured by an acid-base titration technique. *Proceedings of the National Academy of Sciences*, 1980, **77**(4), pp. 2038–2042.

(110) Clement, N.R., Gould, J.M., Pyranine (8-hydroxy-1, 3, 6-pyrenetrisulfonate) as a probe of internal aqueous hydrogen ion concentration in phospholipid vesicles. *Biochemistry*, 1981, **20**(6), pp. 1534–1538.

(111) Goldbach, P., Brochart, H., Wehrlé, P., Stamm, A., Sterile filtration of liposomes: retention of encapsulated carboxyfluorescein. *International Journal of Pharmaceutics*, 1995, **117**(2), pp. 225–230.

(112) Hiraoka, Y., Sedat, J.W., Agard, D.A., Determination of three-dimensional imaging properties of a light microscope system. partial confocal behavior in epifluorescence microscopy. *Biophysical Journal* , 1990, **57**(2), pp. 325–333.

(113) Thorn, K., A quick guide to light microscopy in cell biology. *Molecular Biology of the Cell*, 2016, **27**(2), pp. 219–222.

(114) Webb, R.H., Theoretical basis of confocal microscopy. In: *Methods in Enzymology*, vol. 307, Elsevier, 1999, pp. 3–20.

(115) Dunst, S., Tomancak, P., Imaging flies by fluorescence microscopy: principles, technologies, and applications. *Genetics*, 2019, **211**(1), pp. 15–34.

(116) Inoué, S., Foundations of confocal scanned imaging in light microscopy. In: *Handbook of Biological Confocal Microscopy*, Springer, 2006, pp. 1–19.

(117) Parasassi, T., Krasnowska, E.K., Bagatolli, L., Gratton, E., Laurdan and prodan as polarity-sensitive fluorescent membrane probes. *Journal of Fluorescence*, 1998, **8**(4), pp. 365–373.

(118) Lúcio, A.D., Vequi-Suplicy, C.C., Fernandez, R.M., Lamy, M.T., Laurdan spectrum decomposition as a tool for the analysis of surface bilayer structure and polarity: a study with DMPG, peptides and cholesterol. *Journal of Fluorescence*, 2010, **20**(2), pp. 473–482.

(119) Amaro, M., Reina, F., Hof, M., Eggeling, C., Sezgin, E., Laurdan and di-4-aneppdhq probe different properties of the membrane. *Journal of Physics D: Applied Physics*, 2017, **50**(13), p. 134004.

(120) Harris, F.M., Best, K.B., Bell, J.D., Use of laurdan fluorescence intensity and polarization to distinguish between changes in membrane fluidity and phospholipid order. *Biochimica et Biophysica Acta (BBA)-Biomembranes*, 2002, **1565**(1), pp. 123–128.

(121) Sánchez, S.A., Tricerri, M., Gunther, G., Gratton, E., *et al.*, Laurdan generalized polarization: from cuvette to microscope. *Modern Research and Educational Topics in Microscopy*, 2007, **2**, pp. 1007–1014.

(122) Owen, D.M., Rentero, C., Magenau, A., Abu-Siniyeh, A., Gaus, K., Quantitative imaging of membrane lipid order in cells and organisms. *Nature Protocols*, 2012, **7**(1), p. 24.

(123) Soumpasis, D., Theoretical analysis of fluorescence photobleaching recovery experiments. *Biophysical Journal*, 1983, **41**(1), pp. 95–97.

(124) Rautu, S.A., Orsi, D., Di Michele, L., Rowlands, G., Cicuta, P., Turner, M.S., The role of optical projection in the analysis of membrane fluctuations. *Soft Matter*, 2017, **13**(19), pp. 3480–3483.

(125) Stetefeld, J., McKenna, S.A., Patel, T.R., Dynamic light scattering: a practical guide and applications in biomedical sciences. *Biophysical Reviews*, 2016, **8**(4), pp. 409–427.

(126) Pencer, J., Hallett, F.R., Effects of vesicle size and shape on static and dynamic light scattering measurements. *Langmuir*, 2003, **19**(18), pp. 7488–7497.

(127) Goldburg, W., Dynamic light scattering. *American Journal of Physics*, 1999, **67**(12), pp. 1152–1160.

(128) Frisken, B.J., Revisiting the method of cumulants for the analysis of dynamic light-scattering data. *Applied Optics*, 2001, **40**(24), pp. 4087–4091.

(129) Schnablegger, H., Singh, Y., The SAXS guide. *Anton Paar GmbH* , 2013.

(130) Tyler, A.I., Law, R.V., Seddon, J.M., X-ray diffraction of lipid model membranes. In: *Methods in membrane lipids*, Springer, 2015, pp. 199–225.

(131) Li, N.Y.D., Perutková, Š., Iglič, A., Rappolt, M., My first electron density map: a beginner's guide to small angle x-ray diffraction. *Elektrotehniski Vestnik*, 2017, **84**(3), p. 69.

(132) Kučerka, N., Pencer, J., Sachs, J.N., Nagle, J.F., Katsaras, J., Curvature effect on the structure of phospholipid bilayers. *Langmuir*, 2007, **23**(3), pp. 1292–1299.

(133) Seddon, J.M., Templer, R.H., Warrender, N.A., Huang, Z., Cevc, G., Marsh, D., Phosphatidylcholine–fatty acid membranes: effects of headgroup hydration on the phase behaviour and structural parameters of the gel and inverse hexagonal (hii) phases. *Biochimica et Biophysica Acta (BBA)-Biomembranes*, 1997, **1327**(1), pp. 131–147.

(134) Liu, Y., Nagle, J.F., Diffuse scattering provides material parameters and electron density profiles of biomembranes. *Physical Review E*, 2004, **69**(4), p. 040901.

(135) Breßler, I., Kohlbrecher, J., Thünemann, A.F., SASfit: a tool for small-angle scattering data analysis using a library of analytical expressions. *Journal of Applied Crystallography*, 2015, **48**(5), pp. 1587–1598.

(136) Riabtseva, A., Kaberov, L.I., Noirez, L., Ryukhtin, V., Nardin, C., Verbraeken, B., Hoogenboom, R., Stepanek, P., Filippov, S.K., Structural characterization of nanoparticles formed by fluorinated poly (2-oxazoline)-based polyphiles. *European Polymer Journal*, 2018, **99**, pp. 518–527.

(137) Brzustowicz, M.R., Brunger, A.T., X-ray scattering from unilamellar lipid vesicles. *Journal of Applied Crystallography*, 2005, **38**(1), pp. 126–131.

(138) Milne, J.L., Borgnia, M.J., Bartesaghi, A., Tran, E.E., Earl, L.A., Schauder, D.M., Lengyel, J., Pierson, J., Patwardhan, A., Subramaniam, S., Cryo-electron microscopy–a primer for the non-microscopist. *The FEBS Journal*, 2013, **280**(1), pp. 28–45.

(139) Cowley, J., Spence, J., Tanaka, M., Vainshtein, B., Zvyagin, B., Penczek, P., Dorset, D., Electron diffraction and electron microscopy in structure determination. *International Tables for Crystallography*, 2006, pp. 297–402.

(140) Ercius, P., Alaidi, O., Rames, M.J., Ren, G., Electron tomography: A three-dimensional analytic tool for hard and soft materials research. *Advanced Materials*, 2015, **27**(38), pp. 5638–5663.

(141) Danev, R., Baumeister, W., Cryo-EM single particle analysis with the volta phase plate. *Elife*, 2016, **5**, p. 13046.

(142) Vulović, M., Ravelli, R.B., van Vliet, L.J., Koster, A.J., Lazić, I., Lücken, U., Rullgård, H., Öktem, O., Rieger, B., Image formation modeling in cryo-electron microscopy. *Journal of Structural Biology*, 2013, **183**(1), pp. 19–32.

(143) Wang, L., Bose, P.S., Sigworth, F.J., Using cryo-em to measure the dipole potential of a lipid membrane. *Proceedings of the National Academy of Sciences*, 2006, **103**(49), pp. 18528–18533.

(144) Singer, A., Mathematics for cryo-electron microscopy. *arXiv preprint arXiv:1803.06714*, 2018.

(145) Sejwal, K., Chami, M., Baumgartner, P., Kowal, J., Müller, S.A., Stahlberg, H., Proteoliposomes–a system to study membrane proteins under buffer gradients by cryo-em. *Nanotechnology Reviews*, 2017, **6**(1), pp. 57–74.

(146) Krämer, K., Cryo-EM: a cold, hard look at biology. *Chemistry World* , 2017, **14**(11), pp. 14–15.

(147) Chi-Ming, J., Hai-Feng, D., Real-space observation of individual skyrmions in helimagnetic nanostripes. *Chinese Physics B*, 2015, **24**(12), p. 128501.

(148) Kuchel, R., Images of a holey film on a 200 Cu grid. [online], 2012 Available from, URL `https://myscope.training/legacy/tem/background/concepts/imagegeneration/stigmationfocus.php`, [Accessed 25 April 2019].

(149) Leigh, K.E., Navarro, P.P., Scaramuzza, S., Chen, W., Zhang, Y., Castaño-Díez, D., Kudryashev, M., Subtomogram averaging from cryo-electron tomograms. *Methods in Cell Biology*, 2019, **152**, pp. 217–259.

(150) Wade, R., A brief look at imaging and contrast transfer. *Ultramicroscopy* , 1992, **46**(1-4), pp. 145–156.

(151) Xiong, Q., Morphew, M.K., Schwartz, C.L., Hoenger, A.H., Mastronarde, D.N., CTF determination and correction for low dose tomographic tilt series. *Journal of Structural Biology*, 2009, **168**(3), pp. 378–387.

(152) Karlsson, L., *Transmission Electron Microscopy of III-V Nanowires and Nanotrees*. Lund University, 2007.

(153) Sigworth, F.J., Principles of cryo-EM single-particle image processing. *Microscopy*, 2016, **65**(1), pp. 57–67.

(154) Smith, S.W., *et al.*, The scientist and engineer's guide to digital signal processing, 1997.

(155) Boekema, E.J., Folea, M., Kouřil, R., Single particle electron microscopy. *Photosynthesis Research*, 2009, **102**(2), pp. 189–196.

(156) Lyumkis, D., Challenges and opportunities in cryo-EM single-particle analysis. *Journal of Biological Chemistry*, 2019, **294**(13), pp. 5181–5197.

(157) Rosenthal, P.B., Henderson, R., Optimal determination of particle orientation, absolute hand, and contrast loss in single-particle electron cryomicroscopy. *Journal of Molecular Biology*, 2003, **333**(4), pp. 721–745.

(158) Elands, J., Skoglund, U., Cryo electron microscopy and electron tomography will play a crucial role in the future of drug development. *Drug Discovery* , 2005, p. 81.

(159) Kimelberg, H., *The influence of membrane fluidity on the activity of membrane-bound enzymes*. Elsevier, 1977.

(160) Lee, A.G., How lipids affect the activities of integral membrane proteins. *Biochimica et Biophysica Acta (BBA)-Biomembranes*, 2004, **1666**(1-2), pp. 62–87.

(161) Jurkiewicz, P., Sỳkora, J., Humpolíčková, J., Hof, M., *et al.*, Solvent relaxation in phospholipid bilayers: principles and recent applications. *Journal of Fluorescence*, 2005, **15**(6), pp. 883–894.

(162) McIntosh, T.J., Simon, S.A., Roles of bilayer material properties in function and distribution of membrane proteins. *Annu. Rev. Biophys. Biomol. Struct.*, 2006, **35**, pp. 177–198.

(163) Zhang, Y.L., Frangos, J.A., Chachisvilis, M., Laurdan fluorescence senses mechanical strain in the lipid bilayer membrane. *Biochemical and Biophysical Research Communications*, 2006, **347**(3), pp. 838–841.

(164) Lomora, M., Itel, F., Dinu, I.A., Palivan, C.G., Selective ion-permeable membranes by insertion of biopores into polymersomes. *Physical Chemistry Chemical Physics*, 2015, **17**(24), pp. 15538–15546.

(165) Paula, S., Volkov, A., Van Hoek, A., Haines, T., Deamer, D.W., Permeation of protons, potassium ions, and small polar molecules through phospholipid bilayers as a function of membrane thickness. *Biophysical Journal*, 1996, **70**(1), pp. 339–348.

(166) Cullis, P., Bally, M., Madden, T., Mayer, L., Hope, M., pH gradients and membrane transport in liposomal systems. *Trends in Biotechnology*, 1991, **9**(1), pp. 268–272.

(167) Choi, S.K., Schurig-Briccio, L., Ding, Z., Hong, S., Sun, C., Gennis, R.B., Location of the substrate binding site of the cytochrome bo_3 ubiquinol oxidase from *escherichia coli*. *Journal of the American Chemical Society*, 2017, **139**(24), pp. 8346–8354.

(168) Geertsma, E.R., Mahmood, N.N., Schuurman-Wolters, G.K., Poolman, B., Membrane reconstitution of ABC transporters and assays of translocator function. *Nature Protocols*, 2008, **3**(2), pp. 256–266.

(169) Rigaud, J.L., Pitard, B., Levy, D., Reconstitution of membrane proteins into liposomes: application to energy-transducing membrane proteins. *Biochimica et Biophysica Acta (BBA)-Bioenergetics*, 1995, **1231**(3), pp. 223–246.

(170) Goers, R., Thoma, J., Ritzmann, N., Di Silvestro, A., Alter, C., Gunkel-Grabole, G., Fotiadis, D., Müller, D.J., Meier, W., Optimized reconstitution of membrane proteins into synthetic membranes. *Communications Chemistry*, 2018, **1**(1), pp. 1–10.

(171) Kano, K., Fendler, J.H., Pyranine as a sensitive pH probe for liposome interiors and surfaces. pH gradients across phospholipid vesicles. *Biochimica et Biophysica Acta (BBA)-Biomembranes*, 1978, **509**(2), pp. 289–299.

(172) Paula, S., Volkov, A., Deamer, D., Permeation of halide anions through phospholipid bilayers occurs by the solubility-diffusion mechanism. *Biophysical Journal*, 1998, **74**(1), pp. 319–327.

(173) Kostina, N., Wagner, A.M., Haraszti, T., Rahimi, K., Xiao, Q., Klein, M.L., Percec, V., Rodriguez-Emmenegger, C., Unravelling topology-induced shape transformations in dendrimersomes. *Soft Matter*, 2020.

(174) Nozaki, Y., Tanford, C., Proton and hydroxide ion permeability of phospholipid vesicles. *Proceedings of the National Academy of Sciences*, 1981, **78**(7), pp. 4324–4328.

(175) Deamer, D.W., Proton permeation of lipid bilayers. *Journal of Bioenergetics and Biomembranes*, 1987, **19**(5), pp. 457–479.

(176) Nagle, J.F., Theory of passive proton conductance in lipid bilayers. *Journal of Bioenergetics and Biomembranes*, 1987, **19**(5), pp. 413–426.

(177) Tahara, Y., Fujiyoshi, Y., A new method to measure bilayer thickness: cryo-electron microscopy of frozen hydrated liposomes and image simulation. *Micron*, 1994, **25**(2), pp. 141–149.

(178) Rodriguez-Garcia, R., Mell, M., López-Montero, I., Netzel, J., Hellweg, T., Monroy, F., Polymersomes: smart vesicles of tunable rigidity and permeability. *Soft Matter*, 2011, **7**(4), pp. 1532–1542.

(179) Kowalik, M., Schantz, A.B., Naqi, A., Shen, Y., Sines, I., Maranas, J.K., Kumar, M., Chemically specific coarse-grained models to investigate the structure of biomimetic membranes. *RSC Advances*, 2017, **7**(86), pp. 54756–54771.

(180) Heberle, F.A., Doktorova, M., Scott, H.L., Skinkle, A.D., Waxham, M.N., Levental, I., Direct label-free imaging of nanodomains in biomimetic and biological membranes by cryogenic electron microscopy. *Proceedings of the National Academy of Sciences*, 2020, **117**(33), pp. 19943–19952.

(181) Cornell, C.E., Mileant, A., Lee, K.K., Keller, S.L., Direct imaging of lipid domains in nanoscale vesicles by cryo-EM. *Biophysical Journal*, 2020, **118**(3), p. 228a.

(182) Frederik, P.M., Hubert, D., Cryo-electron microscopy of liposomes. *Methods in Enzymology*, 2005, **391**, pp. 431–448.

(183) Won, Y.Y., Brannan, A.K., Davis, H.T., Bates, F.S., Cryogenic transmission electron microscopy (cryo-TEM) of micelles and vesicles formed in water by poly (ethylene oxide)-based block copolymers. *The Journal of Physical Chemistry B*, 2002, **106**(13), pp. 3354–3364.

(184) Jousma, H., Talsma, H., Spies, F., Joosten, J., Junginger, H., Crommelin, D., Characterization of liposomes. the influence of extrusion of multilamellar vesicles through polycarbonate membranes on particle size, particle size distribution and number of bilayers. *International Journal of Pharmaceutics*, 1987, **35**(3), pp. 263–274.

(185) Pabst, G., Rappolt, M., Amenitsch, H., Laggner, P., Structural information from multilamellar liposomes at full hydration: full q-range fitting with high quality x-ray data. *Physical Review E*, 2000, **62**(3), p. 4000.

(186) Pabst, G., Katsaras, J., Raghunathan, V.A., Rappolt, M., Structure and interactions in the anomalous swelling regime of phospholipid bilayers. *Langmuir*, 2003, **19**(5), pp. 1716–1722.

(187) Kučerka, N., Nieh, M.P., Pencer, J., Harroun, T., Katsaras, J., The study of liposomes, lamellae and membranes using neutrons and x-rays. *Current Opinion in Colloid & Interface Science*, 2007, **12**(1), pp. 17–22.

(188) Rappolt, M., Bilayer thickness estimations with "poor" diffraction data. *Journal of Applied Physics*, 2010, **107**(8), p. 084701.

(189) Kučerka, N., Liu, Y., Chu, N., Petrache, H.I., Tristram-Nagle, S., Nagle, J.F., Structure of fully hydrated fluid phase DMPC and DLPC lipid bilayers using x-ray scattering from oriented multilamellar arrays and from unilamellar vesicles. *Biophysical Journal*, 2005, **88**(4), pp. 2626–2637.

(190) Kučerka, N., Nieh, M.P., Katsaras, J., Fluid phase lipid areas and bilayer thicknesses of commonly used phosphatidylcholines as a function of temperature. *Biochimica et Biophysica Acta (BBA)-Biomembranes*, 2011, **1808**(11), pp. 2761–2771.

(191) Smart, T.P., Mykhaylyk, O.O., Ryan, A.J., Battaglia, G., Polymersomes hydrophilic brush scaling relations. *Soft Matter*, 2009, **5**(19), pp. 3607–3610.

(192) Pandithage, R., Brief introduction to contrasting for EM sample preparation. *Leica Contrast Manual*, 2013, pp. 1–16.

(193) Kim, J.S., Afsari, B., Chirikjian, G.S., Cross-validation of data compatibility between small angle x-ray scattering and cryo-electron microscopy. *Journal of Computational Biology*, 2017, **24**(1), pp. 13–30.

(194) Jiménez, A., Jonic, S., Majtner, T., Otón, J., Vilas, J.L., Maluenda, D., Mota, J., Ramírez-Aportela, E., Martínez, M., Rancel, Y., *et al.*, Validation of electron microscopy initial models via small angle x-ray scattering curves. *Bioinformatics*, 2019, **35**(14), pp. 2427–2433.

(195) Harper, P., Gruner, S., Lewis, R., McElhaney, R., Electron density modeling and reconstruction of infinite periodic minimal surfaces (IPMS) based phases in lipid-water systems. II. Reconstruction of D surface based phases. *The European Physical Journal E*, 2000, **2**(3), pp. 229–245.

(196) Fetters, L., Lohse, D., Colby, R., Chain dimensions and entanglement spacings. In: *Physical properties of polymers handbook*, Springer, 2007, pp. 447–454.

(197) Kučerka, N., Nagle, J.F., Sachs, J.N., Feller, S.E., Pencer, J., Jackson, A., Katsaras, J., Lipid bilayer structure determined by the simultaneous analysis of neutron and x-ray scattering data. *Biophysical Journal*, 2008, **95**(5), pp. 2356–2367.

(198) Su, C.J., Wu, S.S., Jeng, U.S., Lee, M.T., Su, A.C., Liao, K.F., Lin, W.Y., Huang, Y.S., Chen, C.Y., Peptide-induced bilayer thinning structure of unilamellar vesicles and the related binding behaviour as revealed by x-ray scattering. *Biochimica et Biophysica Acta (BBA)-Biomembranes*, 2013, **1828**(2), pp. 528–534.

(199) Peyret, A., Ibarboure, E., Le Meins, J.F., Lecommandoux, S., Asymmetric hybrid polymer–lipid giant vesicles as cell membrane mimics. *Advanced Science*, 2018, **5**(1), p. 1700453.

(200) Döbereiner, H.G., Properties of giant vesicles. *Current Opinion in Colloid & Interface Science*, 2000, **5**(3-4), pp. 256–263.

(201) Bagatolli, L., Gratton, E., Two photon fluorescence microscopy of coexisting lipid domains in giant unilamellar vesicles of binary phospholipid mixtures. *Biophysical Journal*, 2000, **78**(1), pp. 290–305.

(202) Amjad, O.A., Mognetti, B.M., Cicuta, P., Di Michele, L., Membrane adhesion through bridging by multimeric ligands. *Langmuir*, 2017, **33**(5), pp. 1139–1146.

(203) Arribas Perez, M., Moriones, O.H., Bastús, N.G., Puntes, V., Nelson, A., Beales, P.A., Mechanomodulation of lipid membranes by weakly aggregating silver nanoparticles. *Biochemistry*, 2019, **58**(47), pp. 4761–4773.

(204) Sezgin, E., Waithe, D., De La Serna, J.B., Eggeling, C., Spectral imaging to measure heterogeneity in membrane lipid packing. *ChemPhysChem*, 2015, **16**(7), p. 1387.

(205) Gaus, K., Zech, T., Harder, T., Visualizing membrane microdomains by laurdan 2-photon microscopy. *Molecular Membrane Biology*, 2006, **23**(1), pp. 41–48.

(206) Bello, G., Cavallini, F., Dailey, L.A., Ehmoser, E.K., Supported polymer/lipid hybrid bilayers formation resembles a lipid-like dynamic by reducing the molecular weight of the polymer. *Biochimica et Biophysica Acta (BBA)-Biomembranes*, 2021, **1863**(1), p. 183472.

(207) Allen, T.M., Liposomes. *Drugs*, 1997, **54**(4), pp. 8–14.

(208) Magee, W.E., Miller, O.V., Liposomes containing antiviral antibody can protect cells from virus infection. *Nature*, 1972, **235**(5337), pp. 339–341.

(209) McDougall, I.R., Dunnick, J.K., Goris, M.L., Kriss, J.P., In vivo distribution of vesicles loaded with radiopharmaceuticals: a study of different routes of administration. *Journal of Nuclear Medicine*, 1975, **16**(6), pp. 488–491.

(210) Kulkarni, J.A., Thomson, S.B., Zaifman, J., Leung, J., Wagner, P.K., Hill, A., Tam, Y.Y.C., Cullis, P.R., Petkau, T.L., Leavitt, B.R., Spontaneous, solvent-free entrapment of SiRNA within lipid nanoparticles. *Nanoscale*, 2020, **12**(47), pp. 23959–23966.

(211) Wang, Y., Wang, L., Li, B., Cheng, Y., Zhou, D., Chen, X., Jing, X., Huang, Y., Compact vesicles self-assembled from binary graft copolymers with high hydrophilic fraction for potential drug/protein delivery. *ACS Macro Letters*, 2017, **6**(11), pp. 1186–1190.

(212) Palivan, C.G., Goers, R., Najer, A., Zhang, X., Car, A., Meier, W., Bioinspired polymer vesicles and membranes for biological and medical applications. *Chemical Society Reviews*, 2016, **45**(2), pp. 377–411.

(213) Lee, J.S., Feijen, J., Polymersomes for drug delivery: design, formation and characterization. *Journal of Controlled Release* , 2012, **161**(2), pp. 473–483.

(214) Meng, F., Zhong, Z., Feijen, J., Stimuli-responsive polymersomes for programmed drug delivery. *Biomacromolecules*, 2009, **10**(2), pp. 197–209.

(215) Cheng, Z., Elias, D.R., Kamat, N.P., Johnston, E.D., Poloukhtine, A., Popik, V., Hammer, D.A., Tsourkas, A., Improved tumor targeting of polymer-based nanovesicles using polymer–lipid blends. *Bioconjugate Chemistry*, 2011, **22**(10), pp. 2021–2029.

(216) Organisation, W.H., Methods of sterilisation. *The International Pharmacopoeia*, 2019, pp. 1–3.

(217) Sykes, C., Time-and temperature-controlled transport: supply chain challenges and solutions. *Pharmacy and Therapeutics*, 2018, **43**(3), p. 154.

(218) Armenante, P., Kirpekar, A., Sterilization in the pharmaceutical and biotechnology industry. In: *Handbook of Downstream Processing*, Springer, 1997, pp. 261–308.

(219) Jang, T.H., Park, S.C., Yang, J.H., Kim, J.Y., Seok, J.H., Park, U.S., Choi, C.W., Lee, S.R., Han, J., Cryopreservation and its clinical applications. *Integrative Medicine Research*, 2017, **6**(1), pp. 12–18.

(220) Cuhadar, S., Koseoglu, M., Atay, A., Dirican, A., The effect of storage time and freeze-thaw cycles on the stability of serum samples. *Biochemia Medica*, 2013, **23**(1), pp. 70–77.

(221) de Castro, M.D.L., García, J.L.L., Analytical freeze-drying. In: *Techniques and Instrumentation in Analytical Chemistry*, vol. 24, Elsevier, 2002, pp. 11–41.

(222) Khan, I., Elhissi, A., Shah, M., Alhnan, M.A., Ahmed, W., Liposome-based carrier systems and devices used for pulmonary drug delivery. In: *Biomaterials and Medical Tribology*, Elsevier, 2013, pp. 395–443.

(223) Kikuchu, H., Carlsson, A., Yachi, K., Hirota, S., Possibility of heat sterilization of liposomes. *Chemical and Pharmaceutical Bulletin*, 1991, **39**(4), pp. 1018–1022.

(224) Rice, W.J., Cheng, A., Noble, A.J., Eng, E.T., Kim, L.Y., Carragher, B., Potter, C.S., Routine determination of ice thickness for cryo-EM grids. *Journal of Structural Biology*, 2018, **204**(1), pp. 38–44.

(225) Drulyte, I., Johnson, R.M., Hesketh, E.L., Hurdiss, D.L., Scarff, C.A., Porav, S.A., Ranson, N.A., Muench, S.P., Thompson, R.F., Approaches to altering particle distributions in cryo-electron microscopy sample preparation. *Acta Crystallographica Section D: Structural Biology*, 2018, **74**(6), pp. 560–571.

(226) Karlsson, G., Thickness measurements of lacey carbon films. *Journal of Microscopy*, 2001, **203**(3), pp. 326–328.

(227) Toh, M.R., Chiu, G.N., Liposomes as sterile preparations and limitations of sterilisation techniques in liposomal manufacturing. *Asian Journal of Pharmaceutical Sciences*, 2013, **8**(2), pp. 88–95.

(228) Zuidam, N.J., Lee, S.S., Crommelin, D.J., Sterilization of liposomes by heat treatment. *Pharmaceutical Research*, 1993, **10**(11), pp. 1591–1596.

(229) Lee, J.C.M., Bermudez, H., Discher, B.M., Sheehan, M.A., Won, Y.Y., Bates, F.S., Discher, D.E., Preparation, stability, and in vitro performance of vesicles made with diblock copolymers. *Biotechnology and Bioengineering*, 2001, **73**(2), pp. 135–145.

(230) Seneviratne, R., Khan, S., Moscrop, E., Rappolt, M., Muench, S.P., Jeuken, L.J., Beales, P.A., A reconstitution method for integral membrane proteins in hybrid lipid-polymer vesicles for enhanced functional durability. *Methods*, 2018, **147**, pp. 142–149.

(231) Uppamoochikkal, P., Tristram-Nagle, S., Nagle, J.F., Orientation of tie-lines in the phase diagram of DOPC/DPPC/cholesterol model biomembranes. *Langmuir*, 2010, **26**(22), pp. 17363–17368.

(232) Mills, T.T., Tristram-Nagle, S., Heberle, F.A., Morales, N.F., Zhao, J., Wu, J., Toombes, G.E., Nagle, J.F., Feigenson, G.W., Liquid-liquid domains in bilayers detected by wide angle x-ray scattering. *Biophysical Journal* , 2008, **95**(2), pp. 682–690.

(233) Braun, A.R., Sachs, J.N., Extracting experimental measurables from molecular dynamics simulations of membranes. In: *Annual Reports in Computational Chemistry*, vol. 7, Elsevier, 2011, pp. 125–150.

(234) Manca, M.L., Castangia, I., Matricardi, P., Lampis, S., Fernàndez-Busquets, X., Fadda, A.M., Manconi, M., Molecular arrangements and interconnected bilayer formation induced by alcohol or polyalcohol in phospholipid vesicles. *Colloids and Surfaces B: Biointerfaces*, 2014, **117**, pp. 360–367.

(235) Hollamby, M.J., Practical applications of small-angle neutron scattering. *Physical Chemistry Chemical Physics*, 2013, **15**(26), pp. 10566–10579.

(236) Hub, J.S., Interpreting solution x-ray scattering data using molecular simulations. *Current Opinion in Structural Biology*, 2018, **49**, pp. 18–26.

(237) Pencer, J., Hallett, F., Small-angle neutron scattering from large unilamellar vesicles: an improved method for membrane thickness determination. *Physical Review E*, 2000, **61**(3), p. 3003.

(238) Eicher, B., Heberle, F.A., Marquardt, D., Rechberger, G.N., Katsaras, J., Pabst, G., Joint small-angle x-ray and neutron scattering data analysis of asymmetric lipid vesicles. *Journal of Applied Crystallography*, 2017, **50**(2), pp. 419–429.

(239) Sega, M., Garberoglio, G., Brocca, P., Cantù, L., Microscopic structure of phospholipid bilayers: comparison between molecular dynamics simulations and wide-angle x-ray spectra. *The Journal of Physical Chemistry B*, 2007, **111**(10), pp. 2484–2489.

(240) Eid, J., Razmazma, H., Jraij, A., Ebrahimi, A., Monticelli, L., On calculating the bending modulus of lipid bilayer membranes from buckling simulations. *The Journal of Physical Chemistry B*, 2020, **124**(29), pp. 6299–6311.

(241) Hossein, A., Deserno, M., Spontaneous curvature, differential stress, and bending modulus of asymmetric lipid membranes. *Biophysical Journal*, 2020, **118**(3), pp. 624–642.

(242) Pathak, P., London, E., The effect of membrane lipid composition on the formation of lipid ultrananodomains. *Biophysical Journal*, 2015, **109**(8), pp. 1630–1638.

(243) McMahon, H.T., Gallop, J.L., Membrane curvature and mechanisms of dynamic cell membrane remodelling. *Nature*, 2005, **438**(7068), pp. 590–596.

Appendices

A1 Infrared spectra peak assignations

Table A1.1: Assignations of peaks in PBd$_{22}$-PEO$_{14}$ IR spectrum.

Observed wavenumber (cm)	Assignation			Assigned bond wavenumber (cm)
3457	O-H	Stretching	Alcohol	3550-3200
3073	C-H	Stretching	Alkene	3100-3000
2965	C-H	Stretching	Alkane	3000-2840
2915	C-H	Stretching	Alkane	3000-2840
1637	C=C	Stretching	Alkene	1662-1626
1451	C-H	Stretching	Alkane (methyl)	1450
1414	O-H	Bending	Alcohol	1420-1330
1344	O-H	Bending	Alcohol	1420-1330
1087	C-O	Stretching	Alcohol (2ndary)	1124-1087
922	C=C	Bending	Alkene (mono)	995-985
943	C=C	Bending	Alkene (trans)	980-960

Table A1.2: Assignations of peaks in PBd_{22}-PEO_{14}-TMR IR spectrum.

Observed wavenumber (cm)	Assignation			Assigned bond wavenumber (cm)
3077	C-H	Stretching	Alkene	3100-3000
3056	C-H	Stretching	Alkene	3100-3000
2965	C-H	Stretching	Alkane	3000-2840
2915	C-H	Stretching	Alkane	3000-2840
2874	C-H	Stretching	Alkane	3000-2840
2717	C-H	Stretching	Aldehyde	2830-2695
1927	C-H	Bending	Aromatic	2000-1650
1832	C=O	Stretching	Anhydride	1818
1592	N-H	Bending	Amine	1650-1580
1439	O-H	Bending	Carboxylic	1440-1395
1384	O-H	Bending	Phenol	1390-1310
1215	C-N	Stretching	Amine	1250-1020
1093	C-N	Stretching	Amine	1250-1020
989	C=C	Bending	Alkene (mono)	995-985
830	C=C	Bending	Alkene (tri)	840-790

A2 HPTS calibration curve

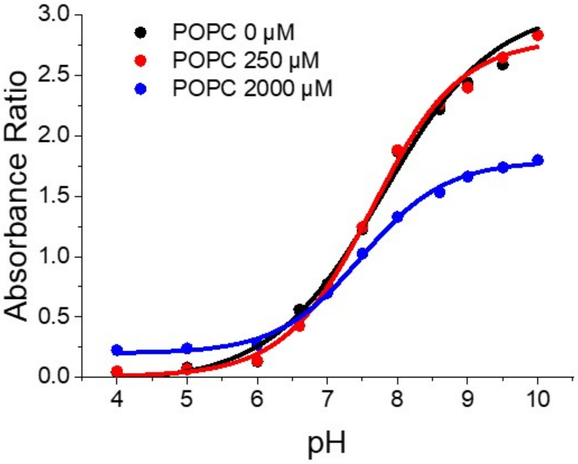

Figure A2.1: Calibration curve of absorbance ratio against pH. The absorbance ratio from absorbances at 450 and 405 nm were plotted against pH was used to determine the pH of the HPTS solution inside lipid, hybrid and polymer vesicles. Lipid POPC vesicles were added to the calibration solutions to observe the affect of vesicles on the collected absorbance ratio. The curves were fitted with a form of the Henderson-Hasselbalch relation using OriginPro.

Three calibration curves were measured to determine the effect of vesicles on HPTS absorbance. As shown by Figure A2.1, increasing the concentration of vesicles from 0 µM to 2000 µM flattens the calibration curve. This flattening could be due to vesicle scattering. As 2 mM vesicle solutions were used for the experiment, calibration curve using 2000 µM was used to determine pH of the internal vesicle solutions from the absorbance ratios.

The data were fit to the following equation with the same functional form as the Henderson-Hasselbalch relation, to find the pH from UV-vis absorbance ratio values $Abs = \frac{A_{450}}{A_{405}}$ from the intensities at 450 nm, A_{450}, and 405 nm, A_{405} :

$$pH = \ln\left(-\frac{A1 - Abs}{Abs - A2}\right)dx + x_0 \tag{1}$$

where $A1$, $A2$, dx and x_0 are equal to 0.199, 1.791, 0.599 and 7.485 respectively for 2000 µM vesicle solutions.

A3 Size distributions of HPTS encapsulated hybrid vesicles

Table A3.1: Size distribution of HPTS encapsulated PBd_{22}-PEO_{14} vesicles.

PBd_{22}-PEO_{14} (mol%)	Z-average (d.nm)	PDI	Size (d.nm)	Standard Deviation
0	113.4	0.073	120.9	32.51
25	94.21	0.106	106.8	27.87
50	115.9	0.140	136.0	54.95
75	121.1	0.092	134.3	44.62
100	140.2	0.544	148.0	32.20

Table A3.2: Size distribution of HPTS encapsulated PBd_{12}-PEO_{11} vesicles.

PBd_{12}-PEO_{11} (mol%)	Z-average (d.nm)	PDI	Size (d.nm)	Standard Deviation
0	111.6	0.137	128.7	47.64
25	109.1	0.112	124.2	44.89
50	100.1	0.173	122.4	50.00
75	101.8	0.194	128.7	62.46
100	135.4	0.136	158.7	63.34

A4 Membrane measurements of PBd$_{22}$-PEO$_{14}$ vesicles

Table A4.1: The FWHM, peak to peak and FWHM to peak measurements of POPC vesicles with increasing mol% of PBd$_{22}$-PEO$_{14}$.

PBd$_{22}$-PEO$_{14}$ (mol%)	FWHM (Å)		Peak to Peak (Å)		FWHM to Peak (Å)	
	Average	Standard Deviation	Average	Standard Deviation	Average	Standard Deviation
0	51.6	2.5	33.9	2.6	8.8	1.1
25	57.0	2.8	36.4	2.2	10.3	1.3
50	77.6	22.3	50.2	13.2	12.9	4.4
75	83.2	20.5	52.7	14.1	14.7	6.8
100	97.2	7.2	65.8	5.1	15.7	3.2

Table A4.2: FWHM, peak to peak and FWHM to peak measurements of the all the vesicles (total) and populations 1 and 2 (pop 1 and pop 2)measured in both 50 mol% and 75 mol% PBd$_{22}$-PEO$_{14}$ samples.

PBd$_{22}$-PEO$_{14}$ (mol%)	FWHM (Å)		Peak to Peak (Å)		FWHM to Peak (Å)	
	Average	Standard Deviation	Average	Standard Deviation	Average	Standard Deviation
50 (Total)	77.6	22.3	50.2	13.2	12.9	4.4
50 (Pop 1)	54.5	5.4	36.0	4.5	9.3	1.1
50 (Pop 2)	94.1	13.4	60.3	6.2	15.6	4.0
75 (Total)	83.2	20.5	52.7	14.1	14.7	6.8
75 (Pop 1)	56.7	4.0	36.4	3.9	10.1	2.2
75 (Pop 2)	95.3	11.7	60.0	10.4	16.7	7.2

Table A4.3: DLS size distributions of the PBd_{22}-PEO_{14} vesicle samples used in cryo-ET.

PBd_{22}-PEO_{14} (mol%)	Z-average (d.nm)	PDI	Size (d.nm)	Standard Deviation
0	130.8	0.106	139.2	40.04
25	104.2	0.184	133.1	43.01
			48.24	7.962
50	116.7	0.236	154.9	81.73
75	139.2	0.098	155.3	53.24
100	140.5	0.097	157.5	55.15

A5 Membrane measurements of PBd$_{12}$-PEO$_{11}$ vesicles

Table A5.1: The FWHM, peak to peak and FWHM to peak measurements of POPC vesicles with increasing mol% of PBd$_{12}$-PEO$_{11}$.

PBd$_{12}$-PEO$_{11}$ (mol%)	FWHM (Å)		Peak to Peak (Å)		FWHM to Peak (Å)	
	Average	Standard Deviation	Average	Standard Deviation	Average	Standard Deviation
0	51.6	2.5	33.9	2.6	8.8	1.1
25	68.6	9.6	40.0	3.1	14.3	4.3
50	64.8	7.8	36.8	3.0	14.0	4.1
75	91.1	15.4	60.9	5.9	15.8	5.2
100	75.9	6.4	50.6	5.0	12.6	1.6

Table A5.2: DLS size distributions of the PBd$_{12}$-PEO$_{11}$ vesicle samples used in cryo-ET.

PBd$_{12}$-PEO$_{11}$ (mol%)	Z-average (d.nm)	PDI	Size (d.nm)	Standard Deviation
0	130.8	0.106	139.2	40.04
25	107.8	0.120	122.5	33.70
50	105.5	0.123	121.8	47.42
75	110.0	0.134	126.9	46.00
100	117.2	0.108	131.8	44.91

A6 Using Cryo-ET measurements to refine SAXS models

Table A6.1: How results from cryo-ET described in Chapter 5 were used to constrain and refine the SAXS models as described in Chapter 6.

Cryo-ET	SAXS
Electron intensity profile across membrane	Use of 2-Gaussian or 4-Gaussian model
Bilayer thickness from FWHM	Constrain and refine Gaussian widths
Hydrophobic core thickness from peak-to-peak	Constrain and refine Gaussian positions
Two bilayer populations in hybrid samples	Two models required to fit hybrid vesicle scattering
Proportion of thick and thin membranes in sample	Constrain weighting of combined Gaussian model

A7 Profiles obtained using strip-function and 4-Gaussian models

In Chapter 6, the scattering profiles were fitted using both the in-house 4-Gaussian model using MatLAB code created by Dr. A. Sadeghpour, as well as SASFit's strip-function bilayer model. As can be seen by Figure A7.1, the electron density profile of 100 mol% PBd_{22}-PEO_{14} vesicle composition provided by strip-function is comparable to with the peak-to-peak and trough widths of the 4-Gaussian model. The remaining compositions were treated with the 4-Gaussian model.

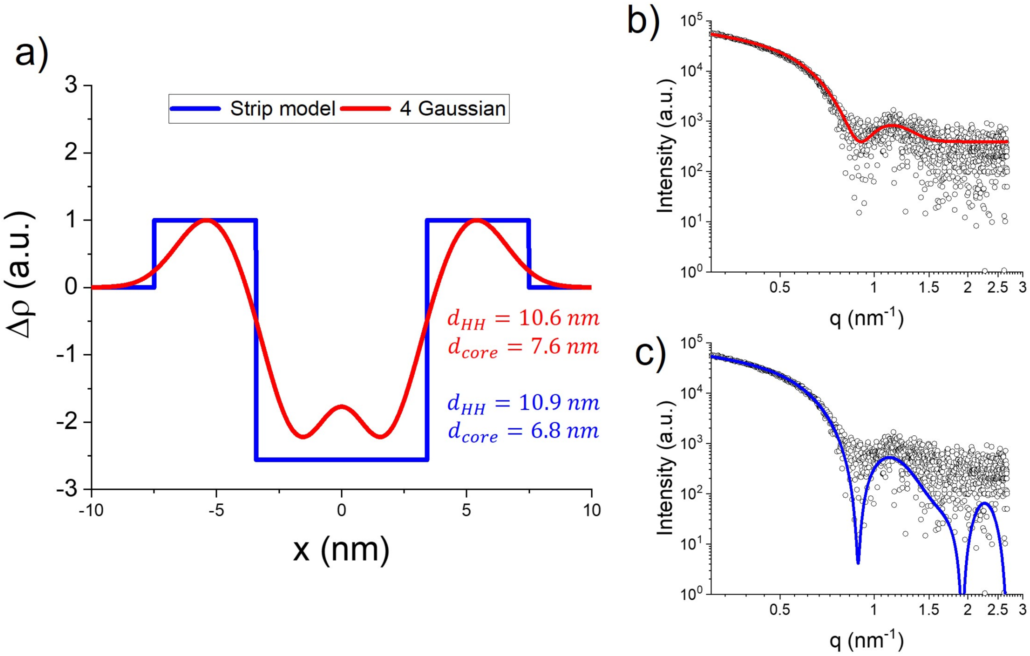

Figure A7.1: Electron density profiles using different form factor fitting models. The a) electron density profiles of 100 mol% PBd_{22}-PEO_{14} obtained by a strip-function and 4-Gaussian model, and the model fit using b) a 4-Gaussian model or c) a strip-function model.

Prof. Michael Rappolt performed the fitting analysis using the SASfit strip model on the PBd_{22}-PEO_{14} SAXS data.

A8 SAXS scattering profiles at 4 °C and 25 °C

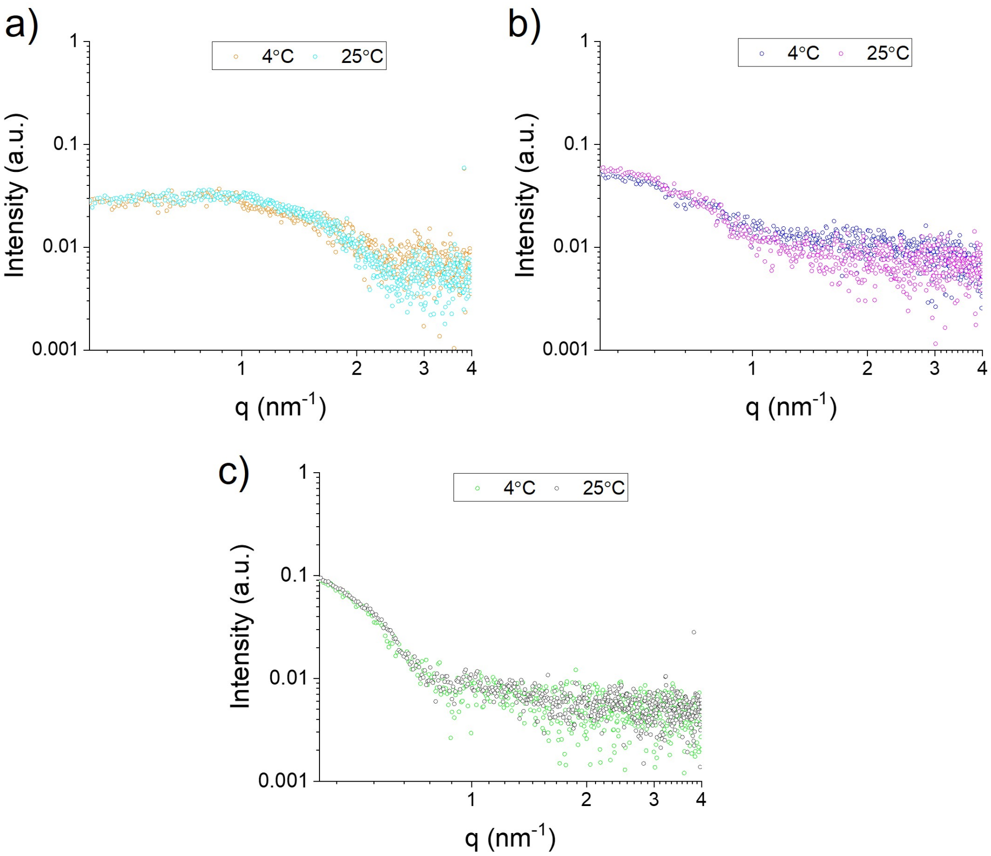

Figure A8.1: Scattering profiles at 4°C and 25 °C. The scattering profiles obtained at 4 °C and 25 °C of a) POPC, b) 100 mol% PBd$_{12}$-PEO$_{11}$ and c) 100 mol% PBd$_{22}$-PEO$_{14}$ vesicle compositions show that there is negligible difference in scattering indicating the samples are not affected strongly by temperature.

In Chapter 6, Tomograms of each vesicle composition were obtained by forming vitreous ice on copper carbon grids at 4 °C, while SAXS scattering profiles were obtained at 25 °C. To ensure that temperature did not play a role in the differences between the final bilayer thickness and hydrophobic core measurements of the electron profiles, SAXS scattering profiles were obtained at both 4 °C and 25 °C. Figure A8.1 shows that there is minimal difference between the scattering profiles with the difference in temperature.

A9 Spectral imaging of Laurdan GUVs

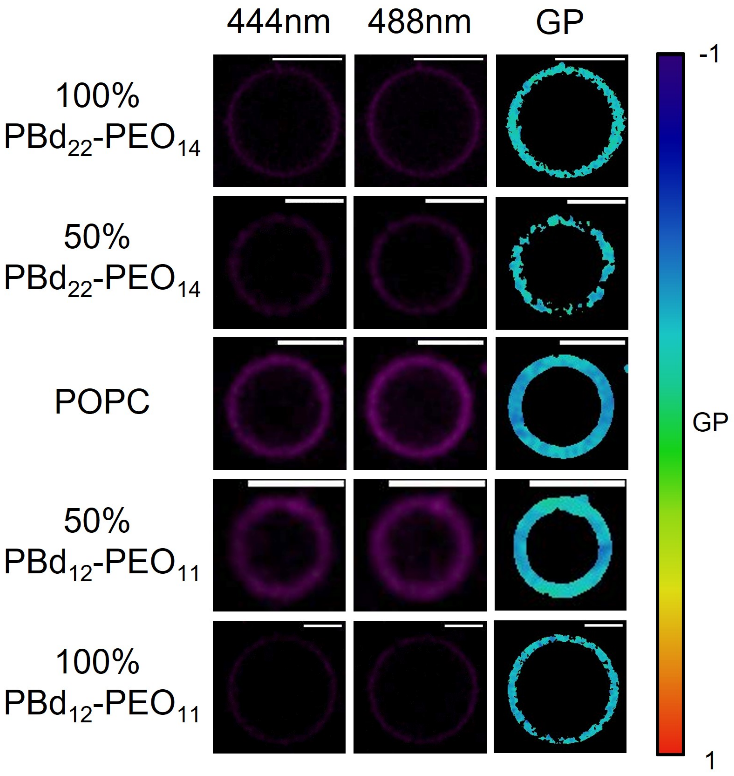

Figure A9.1: Colour maps of Laurdan GP values on GUVs. The images of GUVs containing 0.25 mol% at wavelengths 44 nm and 488 nm that contribute to the final GP result in Figure 7.5. Scale bars indicate 10 µm.

In Chapter 7, 0.25 mol% Laurdan was incorporated into 0 mol%, 50 mol% and 100 mol% PBd_{22}-PEO_{14} and PBd_{12}-PEO_{11} compositions. The brighter GUVs at 444 and 488 nm emission give a more intense GP image. Although the same fraction of each composition was Laurdan, the distribution of Laurdan in individual vesicles may cause the difference in brightness.

A10 Size distributions and CONTIN fits in CF encapsulated vesicles

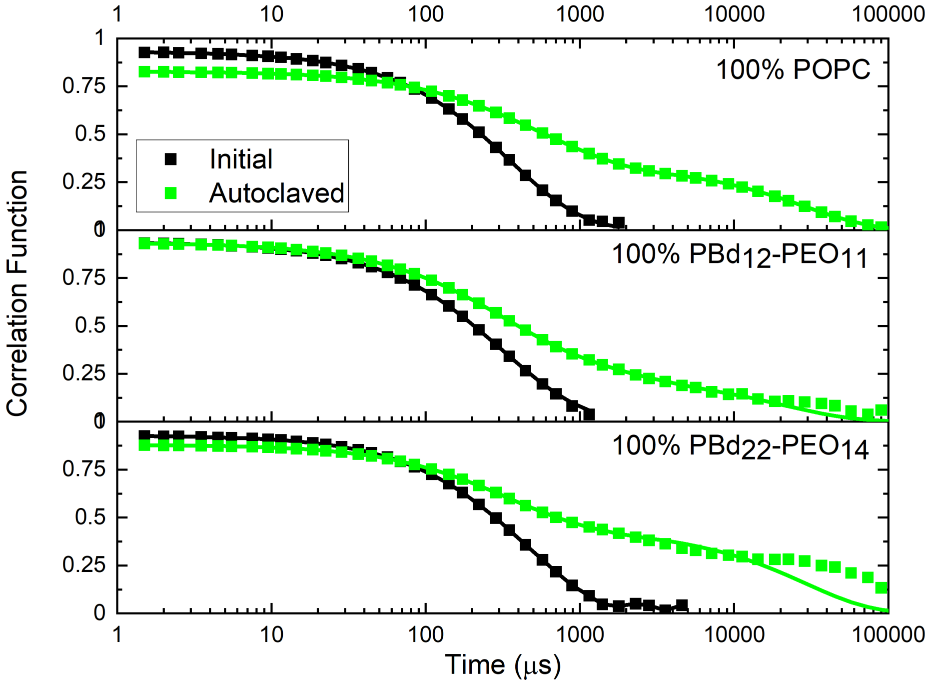

Figure A10.1: The CONTIN fit size distributions before and after autoclaving from the DLS profiles shown in Figure 8.1and their fitted autocorrelation functions.

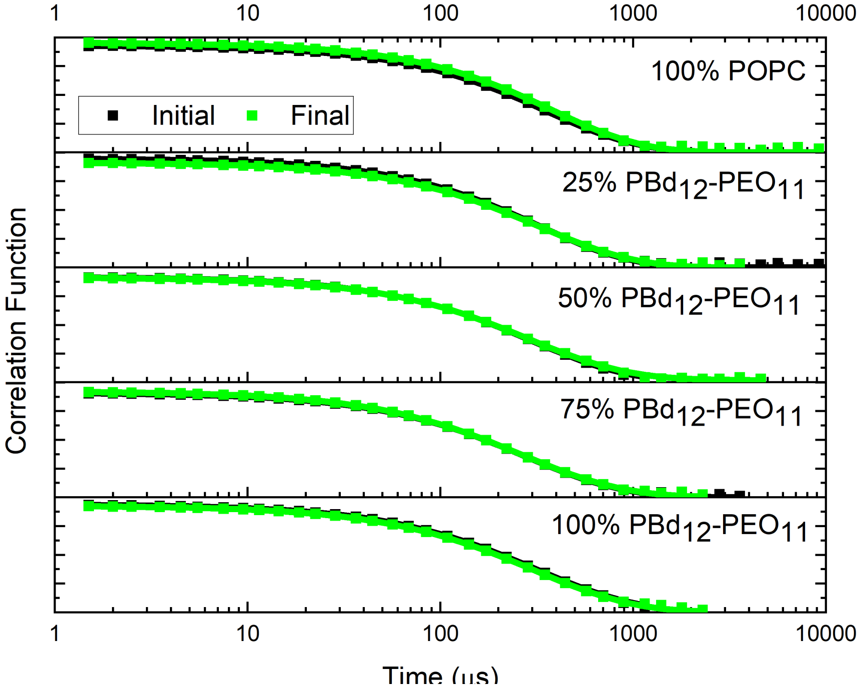

Figure A10.2: The CONTIN fit size distributions of 100 nm extruded PBd_{12}-PEO_{11} vesicles before and after five filtration cycles from the DLS profiles shown in Figure 8.2 and their fitted autocorrelation functions.

Table A10.1: DLS fitting data of 100 nm extruded PBd_{12}-PEO_{11} hybrid vesicles before five filtration cycles.

PBd_{12}-PEO_{11} (mol%)	Z-average (d.nm)		Average Intensity Diameter (d.nm)		PDI	
	Average	Standard Deviation	Average	Standard Deviation	Average	Standard Deviation
0	123.2	120.0	131.9	7.7	0.096	0.018
25	107.8	0.1	122.5	0.6	0.120	0.011
50	95.7	4.3	115.2	4.6	0.163	0.014
75	90.4	1.8	110.6	1.8	0.174	0.003
100	99.8	3.8	122.7	6.8	0.183	0.015

Table A10.2: DLS fitting data of 100 nm extruded PBd_{12}-PEO_{11} hybrid vesicles after five filtration cycles.

PBd_{12}-PEO_{11} (mol%)	Z-average (d.nm)		Average Intensity Diameter (d.nm)		PDI	
	Average	Standard Deviation	Average	Standard Deviation	Average	Standard Deviation
0	121.8	9.3	132.0	7.8	0.085	0.024
25	107.6	1.7	126.3	5.3	0.134	0.002
50	96.1	5.3	1595.4	2643.2	0.180	0.017
75	124.0	57.7	287.8	306.4	0.218	0.083
100	99.6	1.2	127.4	0.7	0.204	0.011

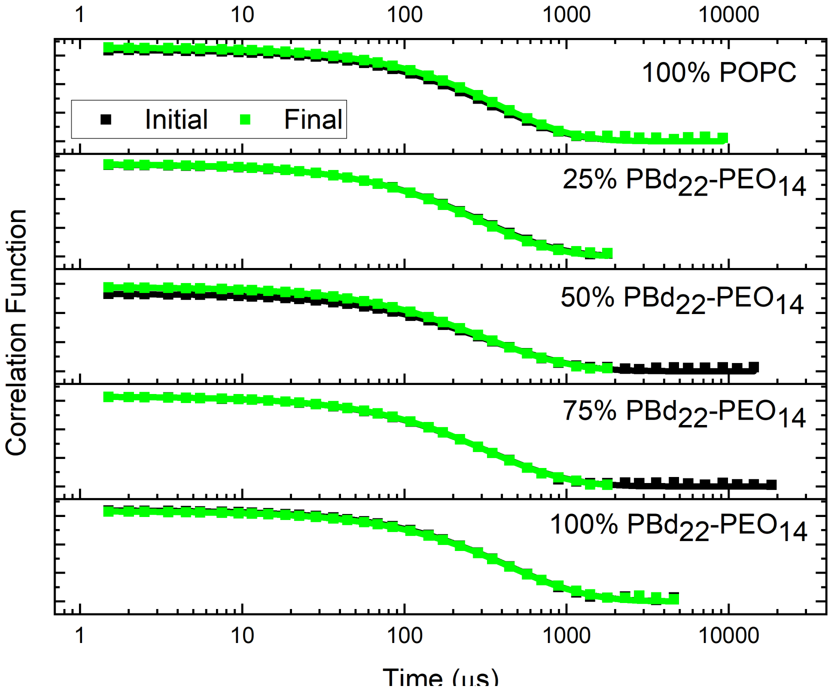

Figure A10.3: The CONTIN fit size distributions of 100 nm extruded PBd_{22}-PEO_{14} vesicles before and after five filtration cycles from the DLS profiles shown in Figure 8.2 and their fitted autocorrelation functions.

Table A10.3: DLS fitting data of 100 nm extruded PBd_{22}-PEO_{14} hybrid vesicles before five filtration cycles.

PBd_{22}-PEO_{14} (mol%)	Z-average (d.nm)		Average Intensity Diameter (d.nm)		PDI	
	Average	Standard Deviation	Average	Standard Deviation	Average	Standard Deviation
0	123.2	120.0	131.9	7.7	0.096	0.018
25	97.2	1.5	114.5	6.0	0.154	0.003
50	108.0	2.1	138.9	2.4	0.213	0.022
75	114.8	5.4	135.3	5.8	0.145	0.018
100	160.8	17.0	189.0	21.1	0.16	0.044

Table A10.4: DLS fitting data of 100 nm extruded PBd_{22}-PEO_{14} hybrid vesicles after five filtration cycles.

PBd_{22}-PEO_{14} (mol%)	Z-average (d.nm)		Average Intensity Diameter (d.nm)		PDI	
	Average	Standard Deviation	Average	Standard Deviation	Average	Standard Deviation
0	121.8	9.3	132.0	7.8	0.085	0.024
25	96.1	0.8	111.2	2.5	0.147	0.013
50	105.9	2.0	132.4	1.0	0.185	0.015
75	116.8	4.8	137.2	5.9	0.137	0.010
100	149.1	1.8	176.0	3.3	0.145	0.011

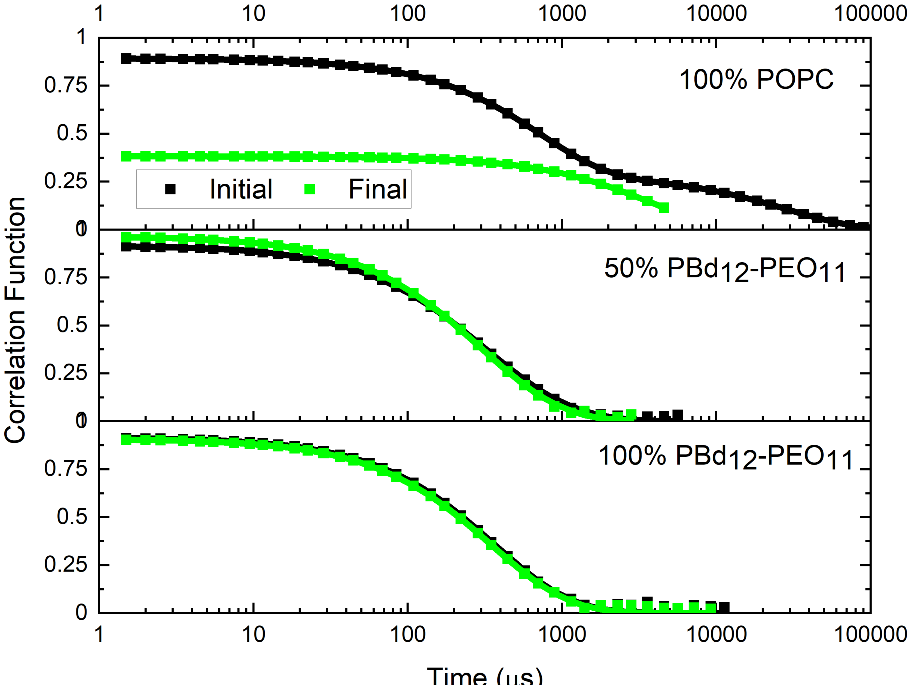

Figure A10.4: The CONTIN fit size distributions of 400 nm extruded PBd_{12}-PEO_{11} vesicles before and after five filtration cycles from the DLS profiles shown in Figure 8.2 and their fitted autocorrelation functions.

Table A10.5: DLS fitting data of 400 nm extruded PBd_{12}-PEO_{11} hybrid vesicles before five filtration cycles.

PBd_{12}-PEO_{11} (mol%)	Z-average (d.nm)		Average Intensity Diameter (d.nm)		PDI	
	Average	Standard Deviation	Average	Standard Deviation	Average	Standard Deviation
0	318.8	36.5	263.5	34.5	0.417	0.050
50	106.9	1.0	1588.6	850.9	0.247	0.002
100	160.6	68.5	2448.7	1354.4	0.221	0.135

Table A10.6: DLS fitting data of 400 nm extruded PBd_{12}-PEO_{11} hybrid vesicles after five filtration cycles.

PBd_{12}-PEO_{11} (mol%)	Z-average (d.nm)		Average Intensity Diameter (d.nm)		PDI	
	Average	Standard Deviation	Average	Standard Deviation	Average	Standard Deviation
0	318.8	36.5	263.5	34.5	0.417	0.050
50	106.9	1.0	1588.6	850.9	0.247	0.002
100	160.6	68.5	2448.7	1354.4	0.221	0.135

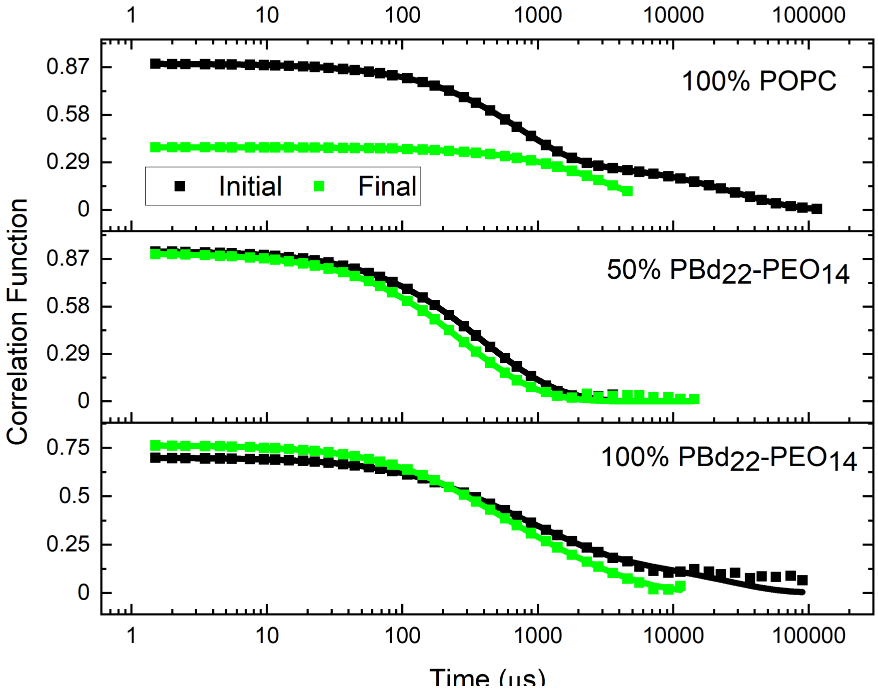

Figure A10.5: The CONTIN fit size distributions of 400 nm extruded PBd_{22}-PEO_{14} vesicles before and after five filtration cycles from the DLS profiles shown in Figure 8.2 and their fitted autocorrelation functions.

Table A10.7: DLS fitting data of 400 nm extruded PBd_{22}-PEO_{14} hybrid vesicles before five filtration cycles.

PBd_{22}-PEO_{14} (mol%)	Z-average (d.nm)		Average Intensity Diameter (d.nm)		PDI	
	Average	Standard Deviation	Average	Standard Deviation	Average	Standard Deviation
0	318.8	36.5	263.5	34.5	0.417	0.050
50	123.7	0.9	182.2	8.5	0.279	0.014
100	261.4	87.4	1447.4	948.3	0.491	0.055

Table A10.8: DLS fitting data of 400 nm extruded PBd_{22}-PEO_{14} hybrid vesicles after five filtration cycles.

PBd_{22}-PEO_{14} (mol%)	Z-average (d.nm)		Average Intensity Diameter (d.nm)		PDI	
	Average	Standard Deviation	Average	Standard Deviation	Average	Standard Deviation
0	822.9	856.1	719.9	555.9	0.493	0.444
50	119.8	30.2	164.9	47.9	0.269	0.029
100	579.4	707.4	798.75	699.9	0.524	0.225

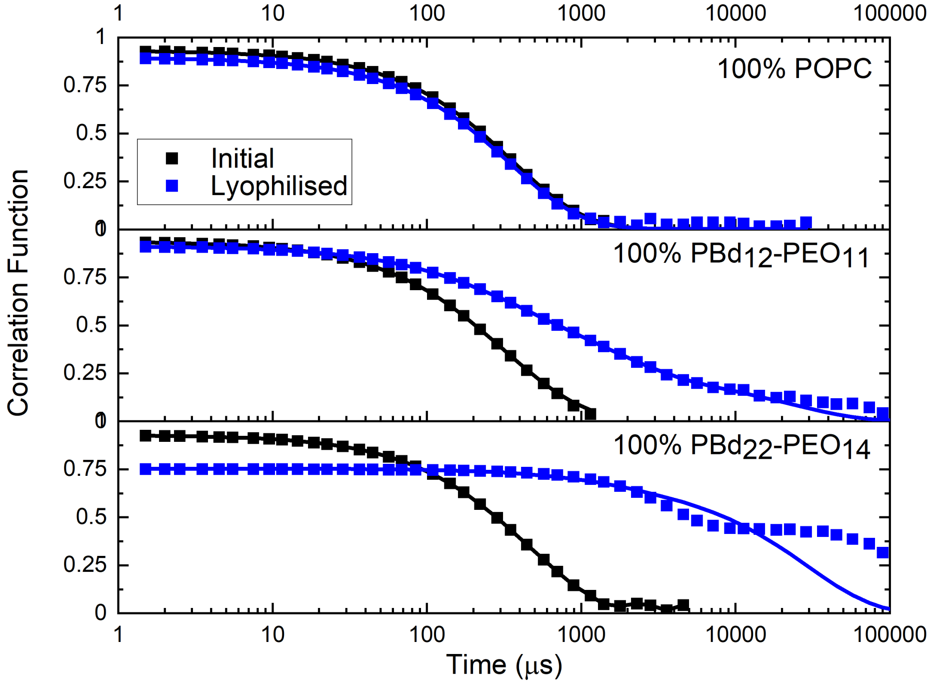

Figure A10.6: The CONTIN fit size distributions before and after lyophilisation from the DLS profiles shown in Figure 8.5 and their fitted autocorrelation functions.

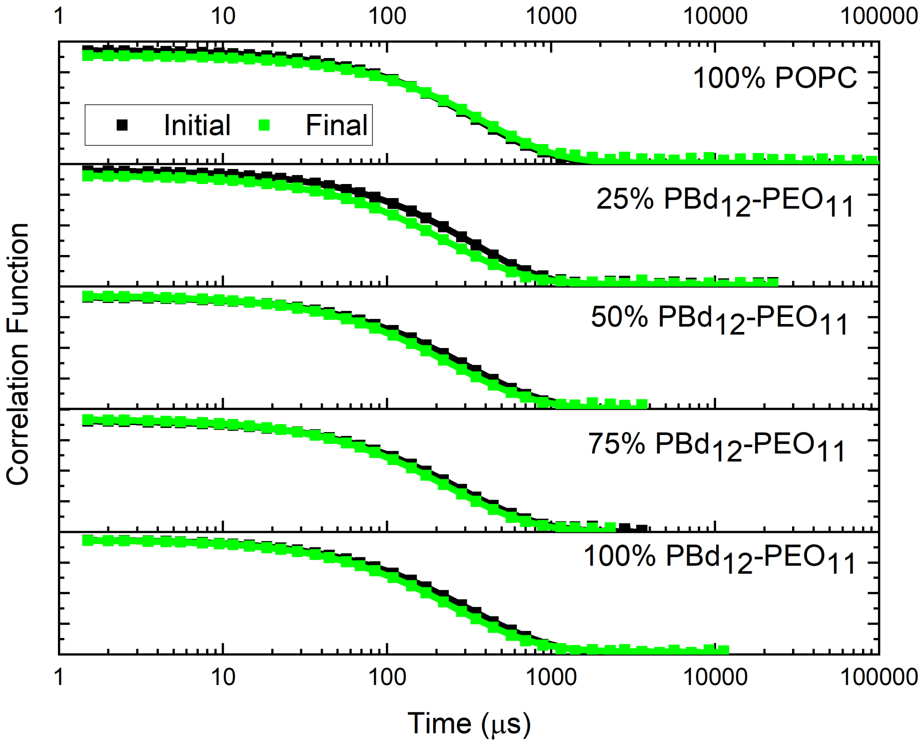

Figure A10.7: The CONTIN fit size distributions of 100 nm extruded PBd$_{12}$-PEO$_{11}$ vesicles before and after four FTV cycles from the DLS profiles shown in Figure 8.6 and their fitted autocorrelation functions.

Table A10.9: DLS fitting data of 100 nm extruded PBd$_{12}$-PEO$_{11}$ hybrid vesicles before four FTV cycles.

PBd$_{12}$-PEO$_{11}$ (mol%)	Z-average (d.nm)		Average Intensity Diameter (d.nm)		PDI	
	Average	Standard Deviation	Average	Standard Deviation	Average	Standard Deviation
0	123.2	120.0	131.9	7.7	0.096	0.018
50	107.8	0.1	122.5	0.6	0.120	0.011
100	95.7	4.3	115.2	4.6	0.163	0.014
75	90.4	1.8	110.6	1.8	0.174	0.003
100	99.8	3.8	122.7	6.8	0.183	0.015

Table A10.10: DLS fitting data of 100 nm extruded PBd$_{12}$-PEO$_{11}$ hybrid vesicles after four FTV cycles.

PBd$_{12}$-PEO$_{11}$ (mol%)	Z-average (d.nm)		Average Intensity Diameter (d.nm)		PDI	
	Average	Standard Deviation	Average	Standard Deviation	Average	Standard Deviation
0	116.8	19.5	136.2	32.9	0.135	0.074
50	82.3	5.3	93.5	2.5	0.168	0.009
100	81.7	2.0	100.5	2.3	0.178	0.007
75	80.6	2.0	98.4	0.9	0.172	0.009
100	90.9	1.6	109.6	7.4	0.177	0.015

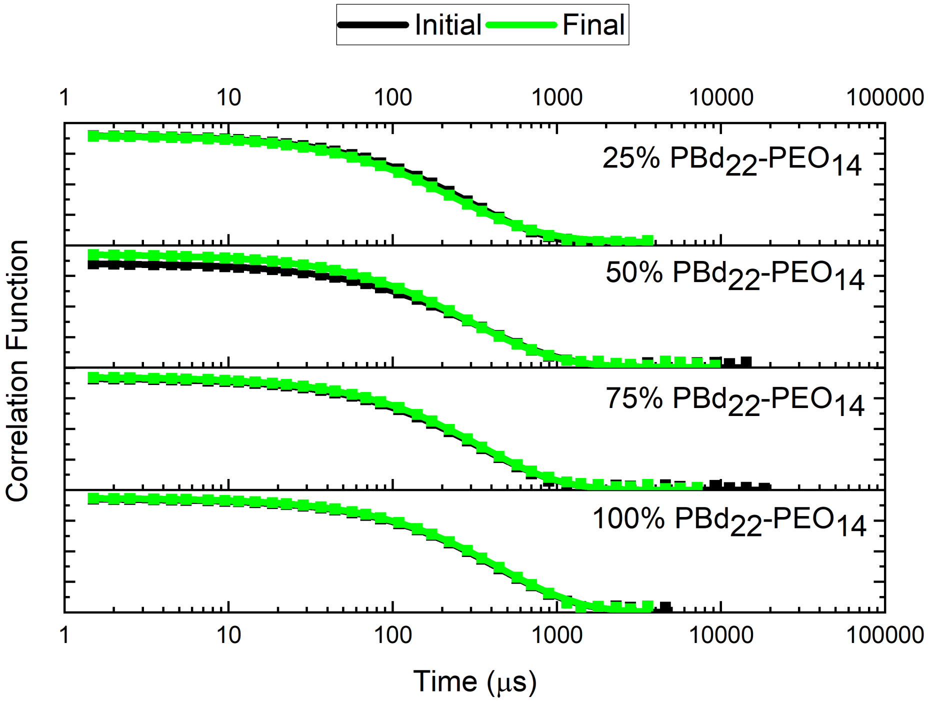

Figure A10.8: The CONTIN fit size distributions of 100 nm extruded PBd_{22}-PEO_{14} vesicles before and after four FTV cycles from the DLS profiles shown in Figure 8.6 and their fitted autocorrelation functions.

Table A10.11: DLS fitting data of 100 nm extruded PBd_{22}-PEO_{14} hybrid vesicles before four FTV cycles.

PBd_{22}-PEO_{14} (mol%)	Z-average (d.nm)		Average Intensity Diameter (d.nm)		PDI	
	Average	Standard Deviation	Average	Standard Deviation	Average	Standard Deviation
0	123.2	120.0	131.9	7.7	0.096	0.018
50	97.2	1.5	114.5	6.0	0.154	0.003
100	108.0	2.1	138.9	2.4	0.213	0.022
75	114.8	5.4	135.3	5.8	0.145	0.018
100	160.8	17.0	189.0	21.1	0.16	0.044

Table A10.12: DLS fitting data of 100 nm extruded PBd_{22}-PEO_{14} hybrid vesicles after four FTV cycles.

PBd_{22}-PEO_{14} (mol%)	Z-average (d.nm)		Average Intensity Diameter (d.nm)		PDI	
	Average	Standard Deviation	Average	Standard Deviation	Average	Standard Deviation
0	116.8	19.5	136.2	32.9	0.135	0.074
50	379.3	511.2	863.8	886.8	0.26	0.119
100	101.0	1.4	125.4	1.1	0.191	0.016
75	157.2	75.0	313.5	312.5	0.260	0.210
100	154.2	4.8	181.4	8.0	0.139	0.015